This is to certify that the
dissertation entitled

EXPLORATORY SYNTHESIS IN MOLTEN SALTS: CHARACTERIZATION, NONLINEAR OPTICAL AND PHASE-CHANGE PROPERTIES OF NEW CHALCOPHOSPHATE COMPOUNDS

presented by

IN CHUNG

has been accepted towards fulfillment
of the requirements for the

Doctoral degree in Chemistry

Major Professor's Signature

8/12/2008

Date

EXPLORATORY SYNTHESIS IN MOLTEN SALTS: CHARACTERIZATION, NONLINEAR OPTICAL AND PHASE-CHANGE PROPERTIES OF NEW CHALCOPHOSPHATE COMPOUNDS

By

IN CHUNG

A DISSERTATION

Submitted to
Michigan State University
in partial fulfillment of the requirements
for the degree of

DOCTOR OF PHILOSOPHY

CHEMISTRY

2008

ABSTRACT

EXPLORATORY SYNTHESIS IN MOLTEN SALTS: CHARACTERIZATION, NONLINEAR OPTICAL AND PHASE-CHANGE PROPERTIES OF NEW CHALCOPHOSPHATE COMPOUNDS

By

IN CHUNG

The polychalcophosphate flux technique has played an important role in discovery of new chalcophosphate compounds via access to low and intermediate temperature of 160 – 600 °C. Chalcophosphates are compounds that possess phosphorus and chalcogen atoms with P-Q bond, where Q = S, Se, or Te. The structural diversity within the class of metal chalcophosphates is extensive, and members of this family can exhibit technologically important ion-exchange, intercalation, magnetic, electrical, and optical properties.

In the present work exploratory synthesis of chalcophosphate compounds using polychalcophosphate molten salt method and characterization of physicochemical properties that are mainly concentrate upon nonlinear optical properties and crystal-glass phase-change behavior are described. Chapters 2-6 focus on the effort of systematic study of alkali metal selenophosphate ternary compounds. The first family of this class is one-dimensional compounds, $APSe_6$ (A = K, Rb, Cs) and $A_2P_2Se_6$ (A =K, Rb). The compounds adopt noncentrosymmetric polar space group and exhibited remarkably strong second harmonic generation response in both crystalline and glassy phases. They

also show a reversible crystal-glass phase-change behavior. By coupling noncentrosymmetry in crystal structure and phase-change behavior, we proposed general fabrication strategy for optical glassy fibers that yield strong, intrinsic, second-order nonlinear optical properties. The $APSe_6$ (A=K, Rb) glassy optical fiber exhibited waveguided second harmonic and difference frequency generation. The second family of this class is phosphorus-rich, novel molecular complex salts of $Rb_4P_6Se_{12}$, $Cs_4P_6Se_{12}$, and $Cs_5P_5Se_{12}$. All compounds feature low valent P in two different formal oxidation states. We attempted rational synthetic conditions to stabilize less oxidized phosphorus compounds by utilizing excess P in the flux. The polychalcophosphate flux also produced rare phosphorus telluride compound. The new compound $K_4P_8Te_4$ featuring P-Te bonding exhibited reversible crystal-glass phase-change behavior, dissolution process to photoluminescent solution with hydrazine, and evolution of nanosphere by precipitating the resulting solution with alcohol. Finally stabilizing Bi metal with selenophosphate flux at high temperature gave naturally growing flexible nanowires of $Cs_5BiP_4Se_{12}$ that can be dispersed in alcohol. The compound that adopts the noncentrosymmetric polar space group exhibited strong near-IR second harmonic generation response.

To my wife

Hyun Young

ACKNOWLEDGEMENTS

First of all, I would like to thank my advisor Prof. Kanatzidis for incredible supports and never giving me up. His research philosophy deeply impressed me to study solid-state and materials chemistry. Scientific discussion with him was priceless. He frequently provided deeper insight into my findings and let me progress to higher standards. One valuable lessons from him was how important interdisciplinary collaborations are in solid-state chemistry. Thanks to Prof. Kanatzidis and his supports, he could successfully collaborated with many coworkers in Physics and Electrical Engineering.

I determined to study solid-state chemistry when I listened to Prof. Jin-Ho Choy's class in undergraduate school. His endless passion for new chemistry has been a role model to me. Dr. Jung-Hwan Do, a former postdoc in our group, greatly helped and advised me to start my research work and everyday life when I first joined this group. I learned every basic lab skill and fundamental knowledge including how to solve single crystal structure. My doctoral degree work could not be finish without my excellent collaborators. Dr. Jung-Hwan Song in Prof. Freeman group in Northwestern University never stopped to solve challenging problems for electronic structure calculations. Dr. Joon I. Jang in Prof. Ketterson group in Northwestern University helped me greatly to measure nonlinear optical properties. They provided a kind explanation concerting their fields. I also have to thank M. Gave, C. Canlas, and A. Karst in Prof. Weliky group in

Michigan State University for solid-state NMR measurements. Christos, a labmate, helped PDF analysis study. I cannot forget all helps from the former and present members of Prof. Kanatzidis Lab for their valuable discussion.

Finally, I deeply thank my family's all supports and love. And this work is dedicated to my dearest wife, Hyun Young.

TABLE OF CONTENTS

LIST OF TABLES

LIST OF FIGURES

LIST OF ABBREAVIATIONS

CCD	Charge Coupled Device
DTA	Differential Thermal Analysis
TGA	Thermogravimetric Analysis
EDS	Energy Dispersive Spectroscopy
SEM	Scanning Electron Microscopy
TEM	Transmission Electron Microscopy
UV/vis	Ultraviolet/visible
IR	Infrared
PDF	Pair Distribution Function
NLO	Nonlinear Optical
SHG	Second Harmonic Generation
DFG	Difference Frequency Generation
FLAPW	Full-potential Linearized Augmented Plane Wave
GGA	Generalized Gradient Approximation
sx-LDA	screened exchange Local Density Approximation
DFT	Density Functional Theory
DOS	Density of States
VBM	Valence Band Maximum
CBM	Conduction Band Maximum
SOC	Spin Orbital Coupling

BZ	Brillouin Zone
DFT	Density Functional Theory
PL	Photoluminescence

Chapter 1

Introduction to Chalcophosphate Compounds and Their Representative Properties.

1. Introduction to Chalcophosphate Compounds

Solid state materials have provided many technologically important properties such as superconductivity, giant magnetoresistance, ferroelectricity, photovoltaic energy conversion and nonlinear optics. Much attention has been paid on the exploration of new materials as well as studies on existing materials to discover enhanced or novel properties. To achieve this, exploratory synthesis is a powerful approach because it is almost impossible to predict the final product of solid state compounds. Phosphorus, in general, has been known to combine with nearly all elements including chalcogenides. Indeed, the structural and compositional diversity in known chalcophosphates is prominent and they show attractive physicochemical properties as described in this chapter. In this regard, the chalcophosphate class of compounds is the great target for exploratory synthesis to discover new compound and study their physical and chemical properties.

The chalcophosphate family $M_xP_yQ_z$ (M = metal; Q = S, Se) has been an important class because of its interesting properties and great structural variety. In 1960's, the first example of chalcophosphate family was synthesized and characterized. The crystal structure of $AlPS_4$ and BPS_4 was determined by Weiss and Schäfer.[1] Transition metal thiophosphate MPS_3 family was discovered by Hahn and Klingen five years later.[2]

The analogous Se chemistry began and showed similar crystal structures and physical properties in the early 70's.[3] During this era, new chalcophosphates were synthesized by traditional solid state synthetic methods, that is, direct stoichiometric reaction of elements or binaries as starting materials at high temperature of ~500 – 900 °C. The compounds mostly possess the ethane-like $[P_2Q_6]^{4-}$ or the tetrahedral $[PQ_4]^{3-}$ anionic building block, which are currently regarded as classical chalcophosphate anions. The MPQ_3 (Q = S, Se) family[1,3,4,5,6,7] shows two dimensional layered structure (CdI_2 or $CdCl_2$-type structure) with the $[P_2Q_6]^{4-}$ anion.

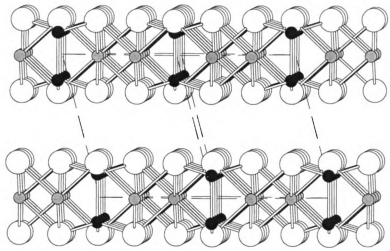

Figure 1-1. Typical structure of layered MPQ_3 compound. Grey circle denotes M, black circle phosphorus, and white circle Q atom.

Monovalent (Li, Ag), divalent (Cd, Sn, Hg, Fe, Pb, Fe, V, etc) and trivalent (In) cations[1,3,4,5,6,7] have been incorporated in the compounds. Many compounds showed important properties. For example, $Sn_2P_2S_6$ crystallizes in the noncentrosymmetric (NCS) space group *Pc* and undergoes a second order, exothermic phase transition from ferroelectric to paraelectric ($P2_1/c$) at 60 °C.[8a] The compound is promising ferroelectric material for potential use in nonvolatile memory device.[8b] SnP_2S_6 crystallizes in the acentric *R*-3 space group represents significant second harmonic generation (SHG) efficiency.[9] $CuInP_2S_6$ displays a paraelectric-ferroelectric phase transition near room temperature.[10] $In_{1.33}P_2Se_6$ shows photoconductivity and is potentially useful for solar energy conversion.[11] Due to layered structure of the MPQ_3 family, rich intercalation chemistry and properties of the resulting compounds have been extensively studied. For example, $Mn_2P_2S_6$[12] intercalated with an organic dye displays both strong nonlinear optical (NLO) properties and spontaneous magnetization up to a high temperature (T_C ~ 40 K). Some members have been studied specifically for their use as cathode materials in secondary lithium batteries.[13]

The chalcophosphates containing the $[PQ_4]^{3-}$ anionic building unit have been relatively less studied but show notable properties. At 261 °C α-Na_3PS_4 undergoes a phase transition to β-Na_3PS_4. Above 490 °C there is evidence for a second high temperature phase; however, this phase has not been fully studied. Both α-Na_3PS_4 and β-Na_3PS_4 have shown to be good ion conductors.[14] Cu_3PS_4 and Cu_3PS_3Se were found to be active as cathodes for the photoelectrolysis of water.[15] $InPS_4$[16] crystallizes in the NCS tetragonal space group *I*-4 which gives rise to nonlinear optical susceptibility and piezo-coefficients.[17] SHG and optical activity have been detected in $Pb_3(PS_4)_2$,[18] which

crystallizes in the NCS cubic space group $P2_13$. Members of the rare earth metal compounds, $LnPS_4$ (Ln = Y, La, Ce, Pr, Nd, Sm, Gd, Tb, Er, Tm and Yb),[19] have been studied for luminescence under UV-excitation. Tl_3PSe_4[20] is a promising material for use in acoustooptic devices such as optical filters, laser modulators and signal processors.

To that date, the ternary chalcophosphate compounds MPQ_3 (M = divalent), A_3PQ_4 and MPQ_4 (M = trivalent metal) were predominant. They were typically synthesized by direct combination of the elements and/or binaries at high temperature of 500-800 °C, mainly giving thermodynamic phases. Although a number of interesting compounds were synthesized using this conventional solid state synthetic method, the number of compounds and their structural types was still very limited.

It was the introduction of the polychalcophosphate flux method that flourished the chalcophosphate class to quaternary phase A/M/P/Q (A = alkali metal) in the early 1990's.[21] The polychalcophosphate fluxes are formed by simple *in situ* fusion of $A_2Q/P_2Q_5/Q$. When molten $[P_xQ_y]^{n-}$ species are solubilized in excess of polychalcogenide melt, which also continues to serve as the oxidant to dissolve metallic elements into the flux. The conventional solid state synthetic method requires soaking at high temperature in order to provide sufficient diffusion between solids for a reaction to occur. This critically limits the kinetic control or the use of well-defined molecular building block in tact during reaction. In this regard, the polychalcophosphate flux method allows intermediate reaction temperature of 300-500 °C which makes possible the synthesis of not only thermodynamically stable but also metastable or kinetically stable phases.

In a low temperature flux it is possible to use intact molecular assemblies as

building blocks for incorporation into extended solids just as one does in conventional solution chemistry. Another important advantage of flux synthesis is the flexibility of the method. Changes in the composition of the flux can greatly alter the Lewis acid/base character and in turn affect the outcome of the reaction. A:P:Se ratio determines the basicity of polychalcophosphate flux $A_xP_yQ_z$. Those with a high A:P or A:Se ratio provide more basic flux (in a Lewis acid/base sense) and the resulting products tend to be shorter structural fragments or highly oxidized species. Smaller chalcogen-rich flux is more acidic than bigger chalcogen-rich flux. The trend is similar in alkali metal. For example, fully oxidized $[PS_4]^{3-}$ is a dominating ligand in thiophosphate compounds while $[P_2Se_6]^{4-}$ that possesses a P-P bonding and formally 4+ on P center is widely stabilized in selenophosphate compounds. Therefore this synthetic technique is best suited for exploratory synthesis of new phases with complex and unpredictable structural motifs and composition.

The first compounds prepared from a polychalcophosphate flux were the layered $ABiP_2S_7$ (A = K, Rb)[22], $A_3M(PS_4)_2$ (A = K, Rb, Cs; M = Sb, Bi), $Cs_3Bi_2(PS_4)_3$ and the nonstoichiometric $Na_{0.6}Bi_{1.28}P_2S_6$.[23] The great majority of new chalcophosphates, reported since this initial discovery, were synthesized via the polychalcophosphate flux technique. It was shown that with the modest changes in the composition of the $A_xP_yQ_z$ flux, the structural diversity in the Bi system ranges from the pseudo-helical one-dimensional NCS of $A_3Bi(PS_4)_2$ and the layered compounds $ABiP_2S_7$ and $Cs_3Bi_2(PS_4)_3$ to the dense three dimensional framework of $Na_{0.6}Bi_{1.28}P_2S_6$. The great multitude of coordination modes of chalcophosphates ligands gives rise to many possibilities for novel lattice construction. The thermodynamically metastable acentric compounds β-KMP_2Se_6

(M = Sb, Bi) showed rare phase transition behavior.[24] It originally formed as an amorphous phase and transformed to metastable β-KMP_2Se_6 phases upon glass transition temperature. Extended exposure to elevated temperature gave a thermodynamically stable phase. These compounds are possible candidates for phase-change optical storage and a three-stage logic gate. $SbPS_{4-x}Se_x$ grows naturally as a single wall nanotube and its band gap could by tunable by substitution of S by Se.[25]

Application of this method to Sn reveals complex chemistry with new structure-types such as the molecular $A_5Sn(PSe_5)_3$ (A = K, Rb),[26] $A_6Sn_2Se_4(PSe_5)_2$ (A = Rb, Cs), the one-dimensional $Rb_3Sn(PSe_5)(P_2Se_6)$.[27] The quinary $Rb_4Sn_2Ag_4(P_2Se_6)_3$ is an unusual layered compounds with formally Sn^{2+} and Ag^+ atoms held together by $[P_2Se_6]^{4-}$ units to feature the rare s^2-d^{10} interaction between Sn and Ag.[28] Other main group metal chalcophosphate compounds found by flux method included $APbPSe_4$,[29] $A_4Pb(PSe_4)_2$ (A = Rb, Cs), α- and β-$Na_6Pb_3(PS_4)_4$,[30] $K_4In_2(PSe_5)_2(P_2Se_6)$,[26] and $A_2ZnP_2Se_6$.[31]

Transition metal chalcophosphate compounds showed interesting properties. $KMPS_4$ (M = Ni[32], Pd[33]) and $NaV_{0.837(6)}P_2S_6$[34] exfoliated in polar solvent to give infinite anionic $^1/_\infty[MPS_4^-]$[35] and $^1/_\infty[V_{0.837(6)}P_2S_6^-]$ chains, respectively. Whereas the $^1/_\infty[NiPS_4^-]$ chains undergo autoframentation under the action of the solvent to give rise to unprecedented discrete crown-shaped $[Ni_3P_3S_{12}]^{3-}$ anions, the $^1/_\infty[PdPS_4^-]$ and $^1/_\infty[V_{0.837(6)}P_2S_6^-]$ chains are maintained in solution including complex fluid behavior and gel formation, respectively. The exfoliated vanadium compound showed induced transient birefringence and formed sol and gel, which is rare in nonoxidic system such as chalcogenides. $NaNb_2PS_{10}$ is soluble in *N*,*N*-dimethylformamide and *N*-methylformamide to generate $^1/_\infty[Nb_2PS_{10}^-]$ nanotube.

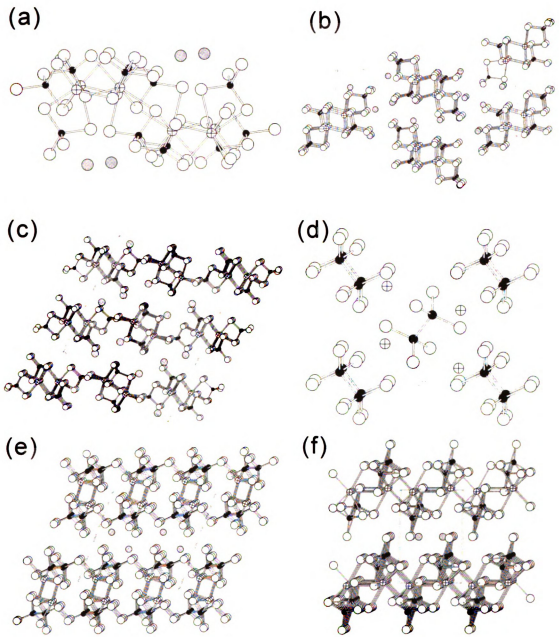

Figure 1-2. Remarkable structural variety found in the Bi chalcophosphate compounds obtained by polychalcophosphate flux method. (a) $KBiP_2S_7$, (b) $K_3Bi(PS_4)_2$, (c) $Cs_3Bi_2(PS_4)_3$, (d) $Na_{0.6}Bi_{1.28}P_2S_6$, (e) $KBiP_2Se_6$, and (f) β-$KBiP_2Se_6$. Grey circles represent alkali metal, crossed circles Bi, black circles P, and open circles S or Se. For (d), the Bi-Se bond and Na atom are omitted for clarity.

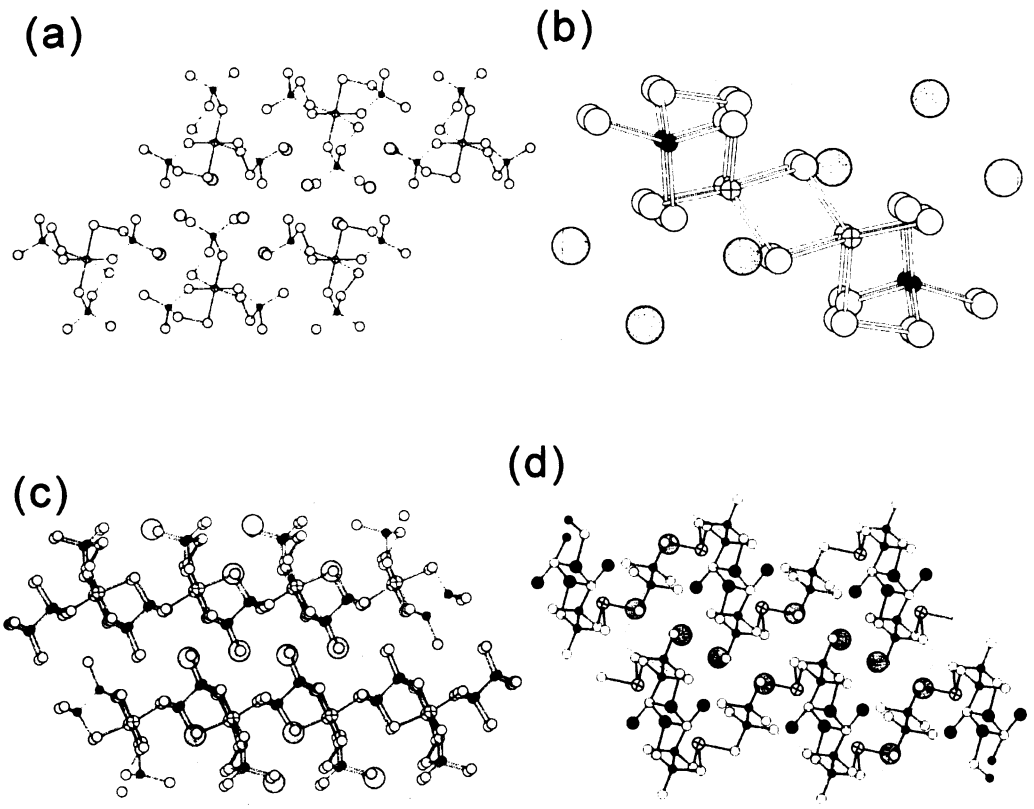

Figure 1-3. Structural diversity seen in the Sn selenophosphate compounds. (a) $Rb_5Sn(PSe_5)_3$, (b) $Rb_6Sn_2Se_4(PSe_5)_2$, (c) $Rb_3Sn(PSe_5)(P_2Se_6)$, and (d) $Rb_4Sn_2Ag_4(P_2Se_6)_3$. Crossed circles represent Sn atoms, black circles P, open circles Se, large grey circles Rb, and small grey for (d) Ag.

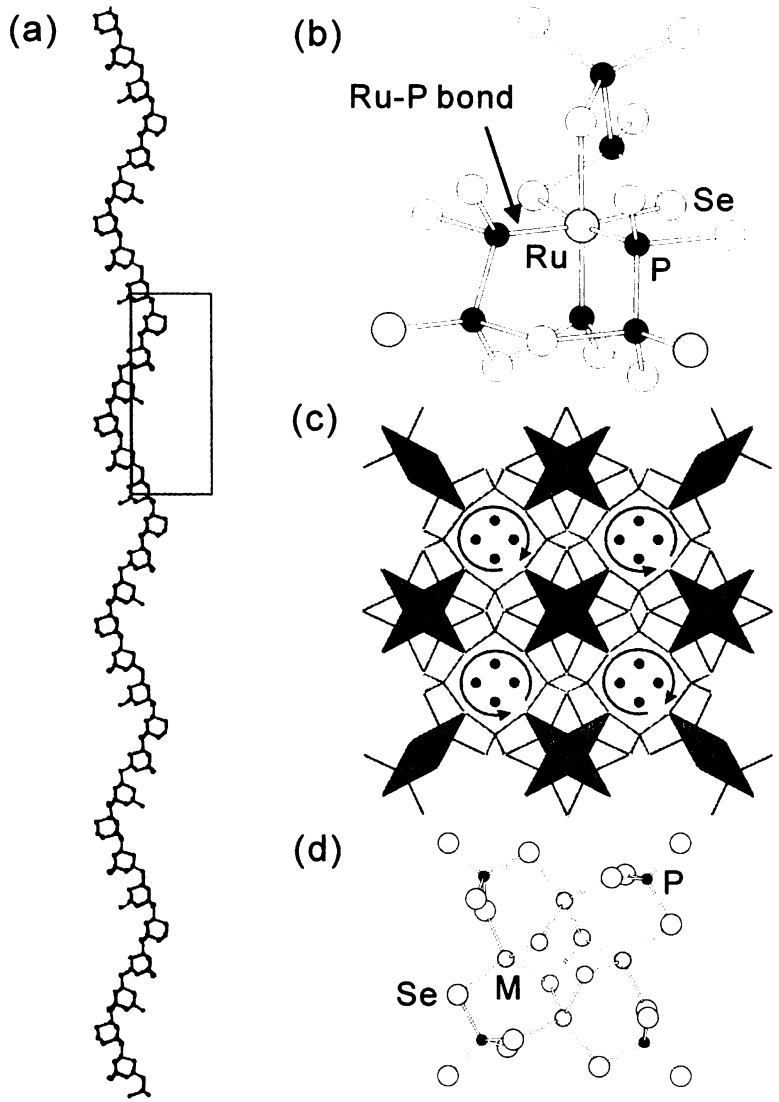

Figure 1-4. (a) View of a long filament of the infinite $[CuP_3S_9]_n^{2n-}$ chain showing the helical conformation. (b) Local geometry of $[Ru(P_2Se_6)(P_3Se_4)]_n^{3n-}$ showing Ru-P bond. (c) View of $[Nb_2P_2S_{12}]^-$ showing its helicity. (d) Tetranuclear cluster of $[M_4(Se_2)_2(PSe_4)_4]^{8-}$ (M = Hg, Cd) with a stellar-like core.

The polychalcophosphate flux served as an excellent tool to access to Ru and Os chemistry, which was elusive for a long time. $A_3MP_5Se_{10}$ (M = Ru, Os) shows significant departure from the chemistry of any other metal studied in the P/Q systems and adds a new perspective in the coordination chemistry of $[P_xQ_y]^{n-}$ anion.[36] There are two unprecedented features in these compounds: first, the mixed P/Se coordination of the Ru centers, and second, the stabilization of a novel polymeric $[P_3Se_4]_n^{n-}$ anion with P atoms in two different formal oxidation states of P^{2+} and P^{3+}. The anion binds the Ru^{2+} exclusively via P atoms which is unique because all other $[P_xQ_y]^{n-}$ units coordinate to the metal centers via the Q atoms.

$ATiPS_5$ (A = K, Rb),[37] double helix-containing $ANb_2P_2S_{12}$,[38] $K_3Cr_2(PS_4)_3$,[39] $A_2MP_2Se_6$ (A = K, Rb, Cs; M = Pd, Cd, Hg),[30] a novel, tetranuclear cluster $Rb_8[M_4(Se_2)_2(PSe_4)_4]$ (M = Cd, Hg),[40] $K_2Cu_2P_4Se_{10}$,[41] $A_2CuP_3S_9$ (A = K, Rb), $Cs_2Cu_2P_2S_6$, $K_3CuP_2S_7$,[42] unusual chiral $Cs_2CuP_3S_9$,[43] K_2AuPS_4, $KAu_5P_2S_8$,[44] $A_2AuP_2Se_6$ (A = K, Rb),[45] $K_4Pd(PS_4)_2$, $Cs_4Pd(PSe_4)_4$, $Cs_{10}Pd(PSe_4)_4$, $KPdPS_4$, and $K_2PdP_2S_6$[32a] were the product of chalcophosphate flux reaction with transition metals.

For lanthanide chemistry it is worth mentioning that $KYb_3(PS_4)_3$ surprisingly formed an interwoven framework, which is of considerable interest in the field of porous materials.[46] This architecture provides a new design to be targeted for synthesis of so-called isoreticular materials by those involved in the construction of metal organic framework and coordination solids.[47] $K_4Eu(PSe_4)_2$, highly anionic complex $Rb_9[Ce(PSe_4)_4]$,[48] $K(RE)P_2Se_6$ (RE = La, Ce, Pr, Gd, Tb),[49] $K_3CeP_2S_8$,[50] $NaYP_2S_6$, $NaSmP_2S_6$, $KSmP_2S_7$,[51] $K_2NdP_2S_7$,[52] $Cs_3Pr_5[PS_4]_6$[53] were also synthesized by flux method and characterized.

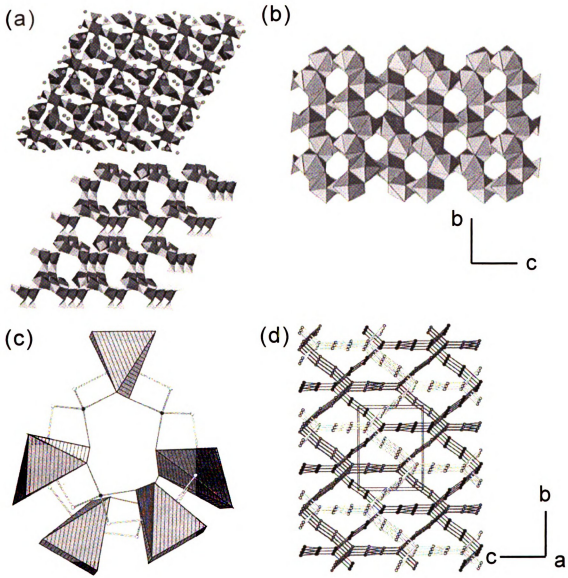

Figure 1-5. (a) Interlocked structure of $K_6Yb_3(PS_4)_5$ showing the two-dimensional interpenetrating sublattices (upper) and a single $^1/_\infty[Yb_3(PS_4)_5^{6-}]$ sublattice (lower) showing the organization of its pore system. (b) Polyhedral representation of $[U_4P_4Se_{26}]^{4-}$ down [100] direction showing the intersecting narrow tunnels. The tunnels in its Rb salt are accessible to smaller cations via ion exchange. (c) Polyhedral representation of $[U_7(PS_4)_{13}]^{11-}$ helix in $K_{11}U(PS_4)_{13}$. (d) Schematic view of the three equivalent interpenetrating diamond frameworks in UP_4S_{12}. The P_2S_6 groups are represented by rods connecting the P atoms of the P_2S_6 ligands.

The chemistry of actinide elements with polychalcophosphate flux gave the unprecedented structure of $K_2UP_3Se_9$,[54] $Rb_4U_4P_4Se_{26}$,[55] UP_4S_{12},[56] $A_{11}U_7(PS_4)_{13}$ (A = K, Rb)[57], $K_3Pu(PS_4)_3$, $APuP_2S_7$ (A = K, Rb, Cs),[58] $Cs_4ThP_6S_{18}$ and $Rb_7ThP_6S_{21}$.[59] $Rb_4U_4P_4Se_{26}$ is a novel three-dimensional, ion-exchange material containing the scarce U^{5+} ion. UP_4S_{12} adopts three interwoven polymeric diamond-type frameworks of U^{4+}. In addition to materials described above, polychalcophosphate fluxes have provided many unusual compounds with main group,[60] transition metals,[61] lanthanide and actinide elements.[62].

Although many chalcophosphate quaternary compounds have been prepared thanks to the polychalcophosphate flux method, ternary compounds $A_xP_yQ_z$, where A = alkali element, are limited. These compounds are fundamental interest because they contain $[P_xQ_y]^{n-}$ anions which are not coordinated to main group, transition metals of f-elements. Examples of these "free" chalcophosphate anionic ligands $[P_xQ_y]^{n-}$ (Q = S, Se) that have been isolated and characterized as alkali metal salts include $[PQ_4]^{3-}$,[63] $[PSe_4]^{3-}\cdot 2Se_6$,[64] $[P_2S_6]^{2-}$,[65] $[P_2Q_6]^{4-}$,[66] $[P_2Se_9]^{2-}$,[67] $[P_8Se_{18}]^{6-}$,[68] and $[P_2S_{10}]^{4-}$.[69] They are all simple discrete molecular anions mainly dependent on the classical $[PQ_4]^{3-}$ or $[P_2Q_6]^{4-}$ anion. Systematic studies of anionic building block are important. Well-defined discrete anionic fragments are potential building blocks for new three-dimensional frames or extended structural motifs. The alkali salts of $[P_xQ_y]^{n-}$ (Q = S, Se) can also be useful starting materials for solid-state reactions or coordination chemistry in solution. In addition, investigations of new $[P_xQ_y]^{n-}$ building blocks could help understand the stability ranges of these in the flux and how the observed solid-state structure motifs arise.[70]

2. Representative Properties of Chalcophosphate Compounds for Technological Application

2.1. Second Harmonic Generation Response

Nonlinear optical techniques to produce light of new wavelengths progressed fast thanks to the discovery of the laser by Maiman in 1960,[71] which provided the high-intensity coherent light essential for such processes. In 1962, Giordamaine[72] and Maker *et al.*[73] simultaneously proposed an ingenious method of matching the phase velocities of the waves at the fundamental and doubled frequencies. In 1965, Wang and Racette reported the nonlinear process in which two light beams at different wavelengths were mixed through a nonlinear crystal to produce the difference frequency of the two. This observation of difference frequency mixing stimulated the research on optical parametric generation. Giordmaine and Miller introduced a pulsed optical parametric oscillator (OPO) in the same year.[74] Byer *et al.*[75] and Smith *et al.*[76] demonstrated continuous-wave OPOs independently in 1968. The development of suitable pump lasers in the late 1980s enabled to extend these techniques to shorter time domains of pico- and femtoseconds. Despite the early introduction of basic principle of optical parametric generation,[77] full potential application should wait over 30 years for the advances of new optically nonlinear materials and their fabrication at the microstructure level. Optical parametric oscillators are rapidly extending the range of applications in, for example, spectroscopy,[78] microscopy,[79] medical diagnostics and therapies,[80] physical, chemical, biophysical and biomolecular research,[81] environmental monitoring,[82] and optical communications.[83]

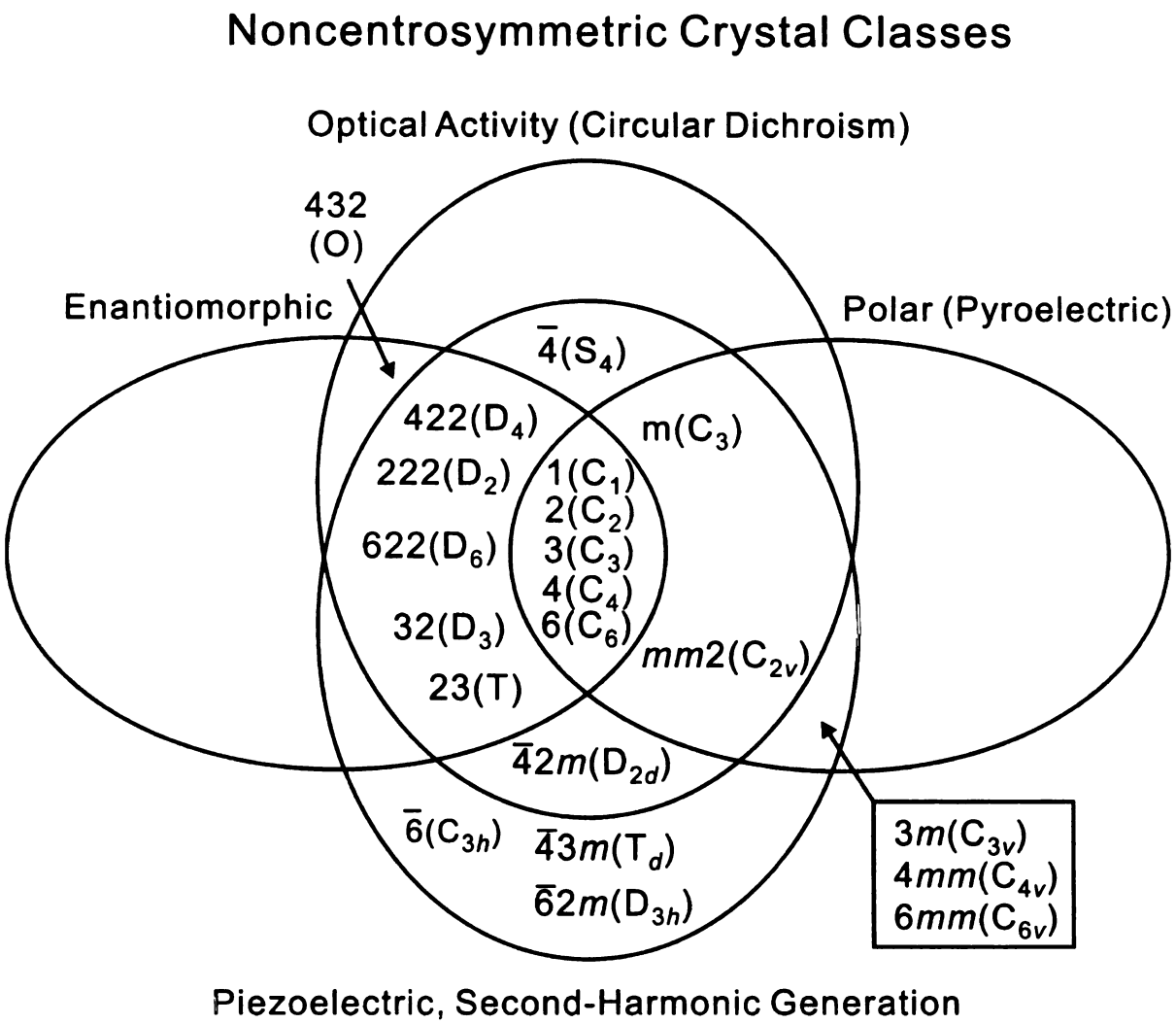

Figure 1-6. Interrelationships of noncentrosymmetric crystal classes in both Hermann-Mauguin and Schoenflies symbols.[84]

Much research attention is focused on the development of materials that can convert nonlinear optical (NLO) frequency from the near- to the mid-infrared regions for technological application. [85] NLO properties are symmetry-dependent and noncentrosymmetry of a medium is necessary. For example, all noncentrosymmetric materials except for 432(*O*) class can exhibit second harmonic generation (SHG)

materials except for 432(O) class can exhibit second harmonic generation (SHG) response.[86] Figure 1-6 demonstrates a graphical representation of crystallographic inter-relationships between physical properties and noncentrosymmetric crystal classes.[87]

When light passes through a medium, its wavelength is unchanged. Although the light goes through the colored glass and if different wavelengths are already present in the light, they may be differently absorbed to change the overall color effect. In this process, however, light that is initially of one wavelength is not converted into light of another wavelength. This is the realm of linear optics.

Second harmonic generation is a nonlinear optic process. When light of frequency ω (fundamental frequency) is irradiated onto a nonlinear crystal that adopts noncentrosymmetric space group, the vibrating electric field of the laser beam excites oscillation of the electrons bound in the atoms of the nonlinear medium. The electrons re-emit light at the fundamental frequency but also at a frequency that is double, 2ω, of incident light. This second harmonic occurs due to the anharmonicity and the asymmetry of the electric field seen by the electrons in the crystal. Optical frequency conversion in nonlinear optical crystal by second harmonic generation is an effective means of generating coherent light in wide spectral range, especially at frequencies where lasers perform poorly or are unavailable.

The most important characteristics of nonlinear crystals are (a) large SHG susceptibility $\chi^{(2)}$, which is a measure of the strength of the nonlinear interaction and is related to the degree of asymmetry of the electronic potential at the microscopic level, and (b) 'phase-matchability' because nonlinear frequency conversion is efficient only if the second harmonic waves generated by different atoms interfere constructively, or, at

least, do not extinguish each other. Following conditions are also desired for practical use. (c) The target crystal needs to be grown to a suitable size easily. (d) They are thermally stable because very strong laser is used for SHG. (e) Hygroscopic materials are less attractive for commercial use.

The representative nonlinear optic (NLO) crystals for frequency conversion include perovskite oxide $LiNbO_3$,[84a] $KTiOPO_4$ (KTP), chalcopyrite $AgGaQ_2$ (Q=S, Se) and $ZnGeP_2$, and GaAs.[88] Most of the best known and extensively studied NLO materials are oxides, which are suitable for UV-vis applications but are severely limited in IR applications due to poor transparency issues caused by M-O stretchings and their overtones. Compared to oxides, chalcogenide compounds for NLO application are still a few, despite great industrial demands for IR NLO applications, especially from the communications industry.

The chalcophosphates are an attractive class in which to search for new nonlinear optical (NLO) materials because the building units of $[PQ_4]^{3-}$ or $[P_2Q_6]^{4-}$ frequently form noncentrosymmetric arrangements, which is a structural prerequisite for NLO property. In addition, chalcogen atoms, S and Se, are much more polarizable than oxygen, consequently to give bigger second harmonic generation susceptibility. Examples are include $ANb_2P_2S_{12}$ (A=K, Rb, Cs),[38] $A_{11}U_7(PS_4)_{13}$ (A=K, Rb),[57] $Cs_2CuP_3S_9$,[43] $Na_{0.5}Pb_{1.75}PS_4$,[89] and $A_3AuP_2Se_8$,[90] $Cs_5P_5Se_{12}$,[91] $APSe_6$ (A=K, Rb),[92] and $A_2P_2Se_6$.[93] Their crystalline and glassy phase typically showed good optical transparency in the mid-IR region. Selenophosphates are transparent above ~600 cm^{-1} (16.7 μm) through mid-IR to their band edges, which are typically 1.5~2.5 eV. (0.5~0.8 μm). Currently, the number of mid-IR crystals with transparency extending well beyond 5 μm and a band edge

below 1 μm is very limited and only a few of them have really become commercially available.[94]

2.2. Glass Formation/Reversible Crystal-Glass Phase Transition

Alkali chalcophosphate compounds have shown great tendency to form glassy phase. In fact, the component elements of this class, e.g. alkali metal, phosphorus and chalcogen, are known as those which occur most commonly in non-oxidic glass system.[95] Such glasses have attracted much industrial interest due to the application for infrared-transparent optical fibers, [96] reversible conductivity switching devices, [97] semiconductors,[98] photoconductors, photoresists[99] and solid electrolytes for battery applications.[100] Generally glasses are often preferred over crystalline compounds because of their favorable mechanical and interfacing characteristics, and because their materials properties can be tailored for specific applications by continuously varying their composition or processing conditions. These glasses are commonly show moisture/air sensitivity.

Recently, interest in crystal-glass phase-change materials is growing, as a result of emerging technologies including commercially available rewritable optical media and the development of nonvolatile phase-change memory.[101] The most interesting materials are those with stoichiometric composition because they can switch between the two states without complications due to compositional changes. Several crystal-glass reversible phase-change chalcophosphates are introduced recently and examples are KMP_2Se_6 (Sb, Bi),[24] $APSe_6$ (A=K, Rb, Cs),[76] $A_2P_2Se_6$ (A = K, Rb),[77] $Cs_4P_6Se_{12}$ and $Cs_5P_5Se_{12}$.[75] Telluropolyphosphide $K_4P_8Te_4$ that composed of polyhexaphosphide with P-Te bonding showed a similar behavior. The details of these materials will be described in chapters 2,

3, 5, and 6 in this Dissertation.

3. Characterization of Amorphous Chalcophosphate Compounds.

Recent development of polychalcophosphate flux method provided new ternary and quaternary compounds in both crystalline and glass phases. Crystal-glass phase change materials that can be used for non-volatile memory application[84] exhibited crystalline to glassy states transformation or *vice-versa* by laser irradiation or thermal treatment. Chalcogenide glasses have been important in infrared optics and semiconductor technology. Structural characterization of glassy phase is essential but the lack of crystallographic long-range order makes it very difficult. For example, X-ray diffraction method, the most powerful technique for structural analysis of inorganic solids, only provides the average structure, so very limited information about local structure is available. Similarly, most of the spectroscopic techniques used are not inherently quantitative but focus on the ordered system.

3.1. Solid-state ^{31}P Nuclear Magnetic Resonance (NMR) Spectroscopy.

Because solid-state NMR is an elemental selective and inherently quantitative technique, it is uniquely suited for the structural analysis of glasses. Eckert *et al.* conducted the ^{31}P, ^{6}Li, and ^{7}Li magic angle spinning (MAS) NMR study on crystalline and glassy compositions in the $(Li_2S)_x(P_2S_5)_{1-x}$ system.[102] Various compositions were obtained by heating a mixture of $Li_2S:P_2S_5 = x:1-x$ under vacuum at 800-900 °C and quenched to ice water. NMR spectra were measured for crystalline and glassy products.

See scheme for analyzed NMR results. For glassy and crystalline phase, as x varied different types of anionic ligands were identified. In the crystalline form, $[P_2S_6]^{2-}$ (x = 0.50), $[P_2S_6]^{4-}$ (x = 0.67), and 7:3 mixture of $[PS_4]^{3-}$ and $[PS_4]^{4-}\cdot S_2$ (x = 0.75) were detected. The results demonstrated that high concentration of Li_2S (more basic condition) favors the simpler tetrahedral $[PS_4]^{3-}$ unit while less basic conditions stabilize more complex, dimeric thiophosphate species. The NMR spectra revealed the tendency of the different melts to stabilize particular thiophosphate anions. Infinite chains of $[PS_3]_n^{n-}$, which is not found in the crystalline state, were formed at x = 0.5. $[P_2S_7]^{4-}$ were stabilized at x=0.67 and when its Li salt crystallized elemental S was released.

$$Li_4P_2S_7 \text{ (glass)} \rightarrow Li_4P_2S_6 \text{ (crystal)} + 1/8\ S_8$$

Only glass at x = 0.75 agrees with crystal counterpart which possesses $[PS_4]^{3-}$, indicating the preference of tetrahedral unit at basic condition. The results from this study showed that solid-state NMR can be powerful tool to probe structural relationship between glassy and crystalline phase, which would be very helpful to develop new phase-change materials.

^{31}P solid-state MAS NMR was an important analytical tool in this Dissertation. In chapter 2, crystal-glass phase change compound $RbPSe_6$ was analyzed by this technique for its crystalline and glassy forms. High temperature ^{31}P solid-state static NMR was conducted for its melt at 350 °C. ^{31}P solid-state MAS NMR spectroscopy was also used to analyze $K_2P_2Se_6$, $Rb_4P_6Se_{12}$, $Cs_4P_6Se_{12}$, $Cs_5P_5Se_{12}$, and $K_4P_8Te_4$ compounds in Chapter 3-6.

Scheme 1

System	Glass	Crystal
$(Li_2S)_{0.5}(P_2S_5)$	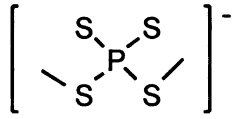	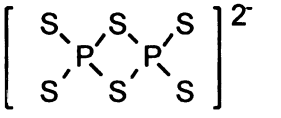
$(Li_2S)_{0.67}(P_2S_5)_{0.33}$	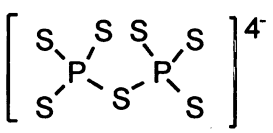	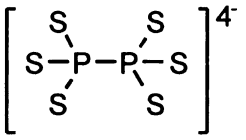
$(Li_2S)_{0.75}(P_2S_5)_{0.25}$	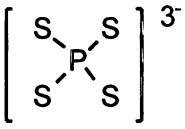	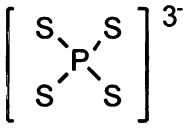

3.2 Atomic Pair Distribution Function (PDF) Analysis.

A prerequisite to a successful structural refinement is the availability of high quality single crystals or polycrystalline powders. Because glasses are not crystalline, they are not fully crystallographically periodic. The PDF analysis has been used for studying with no long-range order. The PDF technique allow the *total diffraction*, that is both the Bragg and diffuse scattering, to be analyzed together without bias, revealing the short and intermediate range order of the material regardless of the degree of disorder.[103] The Fourier relationship between measurable diffraction intensities and the real-space arrangement of pairs of atoms are used. Therefore, the technique is both a local and an extended structure probe and thus a powerful tool that can be used to identify differences in structural features between the crystalline and glassy version of phase-change materials. The pair distribution function can be defined directly in real-space in terms of atomic coordination. It can be also written as a Fourier transform of scattered X-ray or

neutron intensities. Since peaks in the PDF come directly from pairs of atoms in the solid, it is highly intuitive.

The PDF, $G(r)$ is obtained from the experimentally determined total-scattering structure function, $S(Q)$, by a sine Fourier transform

$$G(r) = \frac{2}{\pi}\int_0^\infty Q[S(Q)-1]\sin(Qr)dQ = 4\pi r[\rho(r)-\rho_0]$$

where r is the distance between two atoms, Q is the magnitude of the scattering vector, $S(Q)$ is the corrected and properly normalized powder diffraction pattern of the material (also called the structure function), $\rho(r)$ and ρ_0 are the local and average atomic number densities, respectively, and r is the radial distance.

In this Dissertation, most compounds synthesized were crystal-glass phase-change materials that include $APSe_6$ (A=K, Rb, and Cs), $A_2P_2Se_6$ (A=K, Rb), $Cs_4P_6Se_{12}$, $Cs_5P_5Se_{12}$, and $K_4P_8Te_4$. PDF analysis was used to probe the relationship between crystalline and glassy forms and suggested that the close relationship between two states possibly explains the facile restoration of crystal structure from amorphous state.

References

(1) (a) Weiss, A.; Schäfer, H. *Naturwissenschaften* **1960**, *47*, 495. (b) Weiss, A.; Schäfer, H. *Z. Naturforsch.* **1963**, *18b*, 81.

(2) (a) Hahn, H.; Klingen, W. *Naturwissenschaften* **1965**, *52*, 494. (b) Hahn, H.; Ott, R.; Klingen, W. *Z. Anorg. Allg. Chem.* **1973**, *396*, 271.

(3) (a) Garin, J.; Parthe, E. *Acta Crystallogr.* **1972**, *I28*, 3672 (b) Klingen, W.; Eulenberger, J.; Hahn, H. *Z. Anorg. Allg. Chem.* **1973**, *401*, 97.

(4) (a) Toffoli, P.; Khodadad, P.; Rodier, N. *Acta Crystallogr.* **1978**, *B34*, 1779. (b) Jandali, G.; Eulenberger, J.; Hahn, H. *Z. Anorg. Allg. Chem.* **1978**, *447*, 105.

(5) (a) Ouvard, G.; Brec, R.; Rouxel, J. *Mater. Res. Bull.* **1985**, *20*, 1181 (b) Lee, S.; Colombet, P.; Ouvard, G.; Brec, R. *Inorg. Chem.* **1988**, *27*, 1291. (c) Lee, S.; Colombet, P.; Ouvard, G.; Brec, R. *Mater. Res. Bull.* **1986**, *21*, 917. (d) Durand, E.; Ouvard, G.; Evain, M.; Brec, R. *Inorg. Chem.* **1990**, *29*, 4916.

(6) Carpentier, C. D.; Nitsche, R. *Mater. Res. Bull.* **1974**, *9*, 401.

(7) Diehl, R.; Carpentier, C. D. *Acta Crystallogr. Sect. B.* **1978**, *34*, 1097.

(8) (a) Scott, B.; Pressprich, M.; Willet, R. D.; Clearly, D. A. *J. Solid State Chem.* **1992**, *96*, 294. (b) Arnautova, E.; Sviridov, E.; Rogach, E.; Savchenko, E.; Grecov, A. *Integrated Ferroelectrics*, **1992**, *1*, 147.

(9) Wang, Z.; Willet, R. D.; Laitinen, R. A.; Clearly, D. A. *Chem. Mater.* **1995**, *7*, 856.

(10) Simon, A.; Ravez, J.; Maisonneuve, V.; Payen, C.; Cajipe, V. B. *Chem. Mater.* **1994**, *6*, 1575.

(11) (a) Etman, M.; Katty, A.; Levy-Clement, C.; Lemasson, P. *Mater. Res. Bull.* **1982**, *17*, 579. (b) Katty, A.; Soled, S.; Wold, A. *Mater. Res. Bull.* **1977**, *12*, 663.

(12) Lacroix, P. G.; Clément, R.; Nakatani, K.; Zyss, J.; Ledoux, I. *Science*, **1994**, *263*, 658.

(13) (a) Thomson, A. H.; Whittingham, M. S. *U.S. Patent* 4,049,879 **1977**. (b) Brec, R.; Le Mehaute, A. *Fr. Patent* 7,704,519 **1977**. (c) Thomson, A. H.; Whittingham, M. S. *Mater. Res. Bull.* **1977**, *12*, 741. (d) Evain, M.; Brec, R.; Whangbo, M.-H. *J. Solid State Chem.* **1987**, *71*, 244.

(14) Jansen, M.; Henseler, U. *J. Solid State Chem.* **1992**, *99*, 110.

(15) Marzik, J. V.; Hsieh, A. K.; Dwight, K.; Wold, A. *J. Solid State Chem.* **1983**, *49*, 43.

(16) Nitsche, R.; Wild, P. *Mater. Res. Bull.* **1970**, *5*, 419.

(17) Bridenbaugh, P. M. *Mater. Res. Bull.* **1973**, *8*, 1055.

(18) Post, E.; Kramer, V. *Mater. Res. Bull.* **1984**, *19*, 1607.

(19) (a) Yampol'akaya, V. V.; Serebrennikov, V. V. *Russ. J. Inorg. Chem.* **1972**, *17*, 1771. (b) Wibbelmann, C.; Brockner, W.; Eisenmann, B.; Schafer, H. *Z. Naturforsch.* **1984**, *39a*, 190. (c) Palkina, K. K.; Maksimova, S. I.; Chibiskova, N. T.; Kuvshinova, T. B.; Volodina, A. N. *Inorg. Mater. Engl. Tr.* **1984**, *20*, 1557. (d) Volodina, A. N.; Koubchinova, T. B.; Maximova, S. I.; Mouraviev, E. N.; Niazov, C. A.; Tchibiskova, N. I. *Zh. Neorg. Khim. SSSR* **1987**, *32*, 2899. (e) Le Rolland, B.; Molinie, P.; Colombet, P. *C. R. Acad. Sci. Paris Serie II* **1990**, *310*, 1201. (f) Le Rolland, B.; McMillan, P.; Molinie, P.; Colombet, P. *Eur. J. Solid State Inorg. Chem.* **1990**, *27*, 715. (g) Palkina, K. K.; Kuvshinova, T. B.; Maksimova, S. I.; Chibiskova, N. T.; Tirpolskaya, T. A. *Inorg. Mater. Engl. Tr.* **1989**, *25*, 1555. (h) Huang, Z. L.; Victoria, C.; Pilippe M. *J. Rare Earth* **1999**, *17*, 6. (i) Huang, Z. L. *J. Rare Earth* **1998**, *16*, 167. (j) Huang, Z. L.; Cajipe, V. B.; LeRolland, B.; Colombet, P.; Schipper, W. J.; Blasse, G. *Eur. J. Solid State Inorg. Chem.* **1992**, *29*, 1133.

(20) (a) Gottlieb, M.; Isaacs, T. J.; Feichtner, J. D.; Roland, G. W.; *J. Appl. Phys.* **1974**, *45*, 5145. (b) Alkire, R. W.; Vergamini, P. J.; Larson, A. C. *Acta Crystallogr.* **1984**, *C40*, 1502. (c) Alkire, R. W.; Larson, A. C.; Vergamini, P. J. *Acta Crystallogr.* **1985**, *C41*, 1709.

(21) Kanatzidis, M. G. *Curr. Opin. Solid State Mater. Sci.* **1997**, *2*, 139.

(22) McCarthy, T.; Kanatzidis, M. G. *Chem. Mater.* **1993**, *5*, 1061.

(23) McCarthy, T.; Kanatzidis, M. G. *J. Alloys Compds.* **1996**, *236*, 70.

(24) Breshears, J. D.; Kanatzidis, M. G. *J. Am.Chem. Soc.* **2000**, *122*, 7839.

(25) Malliakas, C. D.; Kanatzidis, M. G. *J. Am. Chem. Soc.* **2006**, *128*, 6002.

(26) Chondroudis, K.; Kanatzidis, M. G. *J. Chem. Soc., Chem. Commun.* **1996**, 1371.

(27) Chondroudis, K.; Kanatzidis, M. G. *J. Solid State Chem.* **1998**, *136*, 79.

(28) Chondroudis, K.; Kanatzidis, M. G. *Inorg. Chem.* **1998**, *37*, 2848.

(29) Chondroudis, K.; Kanatzidis, M. G. *Inorg. Chem.* **1996**, *35*, 840.

(30) Aitken, J. A.; Kanatzidis, M. G. *Inorg. Chem.* **2001**, *40*, 2938.

(31) Chondroudis, K.; Kanatzidis, M. G. *J. Solid State Chem.* **1998**, *138*, 321.

(32) Elder, S. H.; Van der Lee, A.; Brec. R.; Canadell, E. *J. Solid State Chem.* **1995**, *116*, 107.

(33) (a) Chondroudis, K.; Kanatzidis, M. G.; Sayettat, J.; Jobic, S.; Brec, R. *Inorg. Chem.* **1997**, *36*, 5859. (b) Coste, S.; Hanko, J.; Bujoli-Doeuff, M.; Louarn, G.; Evain, M.; Brec, R.; Alonso, B.; Jobic, S, Kanatzidis, M. G. *J. Solid State Chem.* **2003**, *175*, 133.

(34) Coste, S.; Gautier, E.; Evain, M.; Bujoli-Doeuff, M.; Brec, R.; Jobic, S.; Kanatzidis, M. G. *Chem. Mater.* **2003**, *15*, 2323.

(35) Sayettat, J.; Bull, L. M.; Gabriel, J.-C. P.; Jobic, S.; Camerel, F.; Marie, A.-M.; Fourimigué, M.; Batail, P.; Brec, R.; Inglebert, R.-L. *Angew. Chem., Int. Ed. Engl.* **1998**, *37*, 1711.

(36) Chondroudis, K.; Kanatzidis, M. G. *Angew. Chem. Int. Ed. Engl.* **1997**, *36*, 1324.

(37) Do. J.; Lee, K.; Yun, H. *J. Solid State Chem.* **1996**, *125*, 30.

(38) Gieck, C.; Derstroff, V.; Block, T.; Felser, C.; Regelsky, G.; Jepsen, O.; Ksenofontov, V.; Gutlich, P.; Eckert, H.; Tremel, W., *Chem. -Eur. J.* **2004,** 10, 382-391.

(39) Derstroff, V.; Ensling, J.; Ksenofontov, V.; Gütlich, P.; Tremel, W. *Z. Anorg. Allg. Chem.* **2002**, *628*, 1346.

(40) Chondroudis, K.; Kanatzidis, M. G. *Chem. Commun.* **1997**, 401.

(41) Chondroudis, K.; Kanatzidis, M. G. *Inorg. Chem.* **1998**, *37*, 2098.

(42) Hanko, J. A.; Sayettat, J.; Jobic, S.; Brec. R.; Kanatzidis, M. G. *Chem. Mater.* **1998**, *10*, 3040.

(43) Hanko, J. A.; Kanatzidis, M. G. J. *Solid State Chem.* **2000**, *151*, 326.

(44) Löken, S; Tremel, W. *Eur. J. Inorg. Chem.* **1998**, 283.

(45) Chondroudis, K.; McCarthy, T. J.; Kanatzidis, M. G. *Inorg. Chem.* **1996**, *35*, 3451.

(46) Aitken, J. A.; Kanatzidis, M. G. *J. Am. Chem. Soc.* **2004**, *126*, 11780.

(47) Eddaoudi, M.; Kim, J.; Rosi, N.; Vodak, D.; Wachter, J.; O'Keefe, M.; Yaghi, O. M. *Science*, **2002**, *295*, 469.

(48) Chondroudis, K.; Kanatzidis, M. G. *Inorg. Chem. Commun.* **1998**, 1, 55.

(49) Chen, J. H.; Dorhout, P. K.; Ostenson, J. E. *Inorg. Chem.* **1996**, *35*, 5627.

(50) Gauthier, G.; Jobic, S.; Brec, R.; Rouxel, J. *Inorg. Chem.* **1998**, *37*, 2332.

(51) Goh, E.-Y.; Kim, E.-J.; Kim, S.-J. *J. Solid State Chem.* **2001**, *160*, 195.

(52) Schleid, T.; Hartenbach, I.; Komm, T. *Z. Anorg. Allg. Chem.* **2002**, *628*, 7.

(53) Komm, T.; Schleid, T. *Z. Anorg. Allg. Chem.* **2004**, *630*, 712.

(54) Chondroudis, K.; Kanatzidis, M. G. *C. R. Acad. Sci. Paris*, **1996**, *322*, 887.

(55) Chondroudis, K.; Kanatzidis, M. G. *J. Am. Chem. Soc.* **1997**, *119*, 2574.

(56) Gieck, C.; Rocker, F.; Ksenofontov, V.; Gütlich, P. Tremel, W. *Angew. Chem. Int. Ed.* **2001**, *40*, 908.

(57) Gieck, C.; Tremel, W. *Chem. -Eur. J.* **2002**, *8*, 2980.

(58) Hess, R. F.;Gordon, P. L.; Tait, C. D.; Abney, K. D.; Dorhout, P. K. *J. Am. Chem. Soc.* **2002**, *124*, 1327.

(59) Chan, B. C.; Hess, R. F.; Feng, P. L.; Abney, K. D.; Dorhout, P. K. *Inorg. Chem.* **2005**, *44*, 2106.

(60) (a) McCarthy, T. J.; Kanatzidis, M. G. *J. Chem. Soc., Chem. Commun.* **1994**, 1089. (b) McCarthy, T. J.; Hogan, T.; Kannewurf, C. R.; Kanatzidis, M. G. *Chem. Mater.* **1994**, *6*, 1072. (c) Chondroudis, K.; McCarthy, T. J.; Kanatzidis, M. G. *Inorg. Chem.* **1996**, *35*, 840.

(61) (a) Do. J.; Yun, H. *Inorg. Chem.* **1996**, *35*, 3729. (b) Löken, S.; Tremel, W. *Eur. J. Inorg. Chem.* **1998**, 283. (c) Caremel, F.; Gabriel, J.-C. P.; Batail, P.; Davidson, P.; Lemaire, B.; Schmutz, M.; Gulik-Krywicki, T.; Bourgaux, C. *Nano Lett.* **2002**, *2*, 403.

(62) (a) Chen, J. H.; Dorhout, P. K. *Inorg. Chem.* **1995**, *34*, 5627. (b) Chen, J. H.; Dorhout, P. K. Ostenson, J. E. *Inorg. Chem.* **1996**, *35*, 5627. (c) Gauithier, G.; Jobic, S.; Brec, R.; Rouxel, J. *Inorg. Chem.* 1998, 37, 2332.

(63) (a) Mercier, R.; Malugani, J.-P.; Fahys, B.; Robert, G. *Acta Crystallogr. Sect. B* **1982**, *38*, 1887. (b) Schäfer, H.; Schäfer, G.; Weiss, A. *Z. Naturforsch. B: Anorg. Chem. Org. Chem.* **1965**, *20*, 811. (c) Jansen, M.; Henseler, U. *J. Solid State Chem.* **1992**, *99*, 110.

(64) Dickerson, C. A.; Fisher, M. J.; Sykora, R. E.; Albrecht-Schmitt, T. E.; Cody, J. A. *Inorg. Chem.* **2002**, *41*, 640.

(65) Brockner, W.; Becker, R.; Eisenmann, B.; Schäfer, H. *Z. Anorg. Allg. Chem.* **1985**, *520*, 51

(66) Mercier, R.; Malugani, J.-P.; Fahys, B.; Douglade, J.; Robert, G. *J. Solid State. Chem.* **1982**, *43*, 151.

(67) Chondroudis, K.; Kanatzidis, M. G. *Inorg. Chem.* **1995**, *34*, 5401.

(68) Chondroudis, K.; Kanatzidis, M. G. *Inorg. Chem.* **1998**, *37*, 2582.

(69) Aitken, J. A.; Canlas, C.; Weliky, D. P.; Kanatzidis, M. G. *Inorg. Chem.* **2001**, *40*, 6496.

(70) Canlas, C. G.; Kanatzidis, M. G.; Weliky, D. P. *Inorg. Chem.* **2003**, *42*, 3399.

(71) Maiman, T. H. *Nature*, **1960**, *187*, 493.

(72) Giordmaine, J. A. *Phys. Rev. Lett.* **1962**, *8*, 19.

(73) Maker, P. D.; Terhune, R. W.; Nicenoff, M.; Savage, C. M. *Phys. Rev. Lett.* **1962**, *8*, 21.

(74) Giordmaine, J. A.; Miller, R. C. *Phys. Rev. Lett.* **1965**, *14*, 973.

(75) Byer, R. L.; Oshman, M. K.; Young, J. F.; Harris, S. E. *Appl. Phys. Lett.* **1968**, *13*, 109.

(76) Smith, R. G.; Geusic, J. E.; Levinste, H. J.; Singh, S.; Vanuiter, L. G. *J. Appl. Phys.* **1968**, *39*, 4030.

(77) For early review: Byer, R. L. in *Treatise in Quantum Electronics*, Rabin, H. and Tang, C. L. Eds, Academic Press, New York, **1973**.

(78) Shen, Y. R. *Nature*, **1989**, *337*, 519.

(79) (a) Tang, S.; Krasieva, T. B.; Chen, Z.; Tempea, G; Tromberg, B. J. *J. Biomed. Opt.* **2006**, *11*, 020501. (b) Denk, W.; Strickler, J. H.; Webb, W. W. *Science*, **1990**, *248*, 73.

(80) Filippidis, G.; Kouloumentas, C.; Kapsokalyvas, D.; Voglis, G.; Tavernarakis, N.; Papazoglou, T. G. *J. Phys. D-Appl. Phys.* **2005**, *38*, 2625.

(81) (a) Zipfel, W. R.; Williams, R. M.; Christie, R.; Nikitin, A. Y.; Hyman, B. T.; Webb, W. W. *Proc. Natl. Acad. Sci. USA* **2003**, *100*, 7075. (b) Campagnola, P. J.; Wei, M. D.; Lewis, A.; Loew, L. M. *Biophys. J.* **1999**, *77*, 3341. (c) Freund, I.; Deutsch, M. *Opt. Commun.* **2001**, *196*, 325.

(82) (a) Gibbs-Davis, J. M.; Hayes, P. L.; Scheidt, K. A.; Geiger, F. M. *J. Am. Chem. Soc.* **2007**, *129*, 7175.

(83) S. J. B. Yoo, *J. Lightwave Technol.* **1996**, *14*, 955.

(84) Halasyamani, P.; Poeppelmeier, K. R. *Chem. Mater.* **1998**, *10*, 2753.

(85) (a) Fejer, M. M. *Phys. Today* **1994**, *40*, 25. (b) Ebrahimzadeh, M.; Dunn, M. H. *Science*, **1999**, *286*, 1513. (c) Fiore, A.; Berger, V.; Rosencher, E.; Bravetti, R.; Nagle, J. *Nature*, **1998**, *391*, 463.

(86) Glazer, A. M.; Stadnicka, K. *Acta Crystallogr.* **1989**, *A45*, 234.

(87) Hahn, T. *International Tables for Crystallography, D.* Reidel Publishing Company: Drodrecht, 1983.

(88) Rosencher E, Fiore A, Vinter B, Berger V, Bois P, Nagle J, *Science* **1996**, *271*, 168.

(89) Aitken, J. A.; Marking, G. A.; Evain, M.; Iordanidis, L.; Kanatzidis, M. G. *J. Solid State Chem.* **2000**, *153*, 158.

(90) Chondroudis, K.; Hanko, J. A.; Kanatzidis, M. G. *Inorg. Chem.* **1997**, *36*, 2623.

(91) Chung, I.; Jang, J. I.; Gave, M. A.; Weliky, D. A.; Kanatzidis, M. G. *Chem. Commun.* **2007**, 4998.

(92) Chung, I.; Do. J.; Canlas, C. G.; Weliky, D. A.; Kanatzidis, M. G. *Inorg. Chem.* **2004**, *43*, 2762.

(93) Chung, I.; Malliakas, C. D.; Jang, J. I.; Canlas, C. G.; Weliky, D. P.; Kanatzidis, M. G. *J. Am. Chem. Soc.* **2007**, *129*, 14996.

(94) (a) Petrov, V.; Rotermund, F.; Noack, F. *J. Opt. A.: Pure Appl. Opt.* **2001**, *3*, R1. (b) Isaenko, L.; Yelisseyev, A.; Lobanov, S.; Petrov, V.; Rotermund, F.; Slekys, G.; Zondy, J.-J. *J. Appl. Phys.* **2002**, *91*, 9475.

(95) (a) Hilton, A. R.; Jones, C. E.; Btau, M. *Phys. Chem. Glasses* **1966**,*7*, 108. (b) Kolomiets, B. T. *Phys. Starus Solid;* **1964**, *7*, 359 and 713. (c) Borisova, Z. U. *Semiconductors.* Plenum Press, New York 1981, and references therein.

(96) Taylor, P. C. *Mater. Res. Soc. Bull.* **1987**, 36.

(97) Ovshinsky, S. R. *Phys. Rev. Lett.* **1968**, *21*, 1450.

(98) (a) Kastner, M. *J. Non-Cryst. Solids*, **1980**, *35-36*, 807. (b) Adler, D. *J. Non-Cryst. Solids*, **1985**, *73*, 205. and references therein.

(99) Brandes, R. G.; Laming, F. P.; Pearson, A. D. *Appl. Opt.* **1970**, *9*, 1712.

(100) (a) Sahami, S.; Shea, S. W.; Kennedy, J. H. *J. Electrochem. Soc.* **1985**, *132*, 985. (b) Kennedy, J. H.; Sahami, S.; Shea, S. W.; Zhang, Z. *Solid State Ionics*, **1986**, *18/19*, 368.

(101) (a) Katoh, K.; Tsutsumi, T.; Yamada, K.; Terui, G.; Niide, Y.; Ochiai, A. *Physica B* **2006**, *373*, 111. (b) Ohta, T. *J. Optoelectr. Adv. Mater.* **2001**, *3*, 609. (c) Ohta, T.; Nishiuchi, K.; Narumi, K.; Kitaoka, Y.; Ishibashi, H.; Yamada, N.; Kozaki, T. *Jpn. J. App. Phys. Part 1.* **2000**, *39*, 770. (d) Wełnic, W.; Pamungkas, A.; Detemple, R.; Steimer, C.; Blugel, S.; Wuttig, M., *Nat. Mater.* **2006**, *5*, 56. (e) Lee, H.; Kim, Y. K.; Kim, D.; Kang, D. H. *IEEE Trans. Magn.* **2005**, *41*, 1034. (f) Kolobov, A. V.; Fons, P.; Frenkel, A. I.; Ankudinov, A. L.; Tominaga, J.; Uruga, T. *Nat. Mater.* **2004**, *3*, 703.

(102) Francisco, R. H. P.; Tepe, T.; Eckert, H. *J. Solid State Chem.* **1993**, *107*, 452.

(103) For review: Billinge, S. J. L.; Kanatzidis, M. G. *Chem. Commun.* **2004**, 749.

Chapter 2

$APSe_6$ (A=K, Rb, and Cs): Polymeric Selenophosphates with Strong Second Harmonic Generation Response and Reversible Phase-Change Properties

1. Introduction

Because complex metal chalcophosphates form readily in an alkali chalcogenide flux environment,[1] it is important to know more about what species are present during these reaction conditions. A number of free chalcophosphate anionic ligands $[P_xQ_y]^{n-}$ (Q = S, Se) have been isolated and characterized as alkali metal salts, including $[PQ_4]^{3-}$,[2] $[PSe_4]^{3-}\cdot 2Se_6$,[3] $[P_2S_6]^{2-}$,[4] $[P_2Q_6]^{4-}$,[5] $[P_2Se_9]^{2-}$,[6] $[P_8Se_{18}]^{6-}$,[7] and $[P_2S_{10}]^{4-}$.[8] They are all discrete molecular anions mainly as they do not coordinate to metals in the structure. Investigations of new $[P_xQ_y]^{n-}$ building blocks could help understand the stability ranges of these in the flux and how the observed solid-state structure motifs arise.[9] The alkali salts of $[P_xQ_y]^{n-}$ (Q = S, Se) can also be useful starting materials for solid-state reactions or coordination chemistry in solution.

Here we report on the isolation of a new polymeric $[PSe_6^-]$ anion crystallized as alkali salts $APSe_6$ (A = K, Rb, and Cs). These materials undergo an interesting reversible crystal-glass transition. Polar structural K and Rb salts exhibited remarkably strong second harmonic generation response over a wide wavelength range. In the infrared region, those materials are highly transmissive. Their SHG intensities are 60 fold stronger than that of $AgGaSe_2$, which is the top IR NLO material.

2. Experimental Section

2.1. Reagents. The reagents mentioned in this work were used as obtained: K metal (analytical reagent, Aldrich Chemical Co., Milwaukee, WI); Rb metal (analytical reagent, Johnson Matthey/AESAR Group, Seabrook, NH); Cs metal (analytical reagent, Johnson Matthey/AESAR Group, Seabrook, NH); red phosphorus powder, -100 mesh, Morton Thiokol, Inc., Danvers, MA; Se (99.9999%; Noranda Advanced Materials, Quebec, Canada); *N*,*N*-dimethylformamide (Spectrum Chemicals, ACS reagent grade); diethyl ether (Columbus Chemical Industries, Columbus WI, ACS reagent grade, anhydrous). A_2Se (A = K and Rb) starting materials were prepared by reacting stoichiometric amounts of the elements in liquid ammonia. P_2Se_5 was prepared by heating the mixture of P and Se with a stoichiometric ratio sealing in an evacuated silica tube at 460 °C for 24h.

2.2. Synthesis. Pure $APSe_6$ (A=K, Rb, Cs) were obtained in quantitative yield by heating a stoichiometric mixture of A_2Se:P_2Se_5:Se=1:1:6 in an evacuated and sealed silica tube at 350 °C for 10 days followed by cooling at a rate of 5°C h^{-1} to 250 °C, respectively. After washing with acetonitrile and ether, we obtained pure orange rod-typed single crystals. Energy dispersive spectroscopy (EDS) analysis of the crystals showed an average composition of "$KPSe_{6.2}$", "$Rb_{1.2}PSe_{6.1}$", and "$CsPSe_{6.2}$". The glassy phase of $APSe_6$ was prepared from a stoichiometric mixture of A_2Se:P_2Se_5:Se=1:1:6 placed in a silica tube and melted at 800-900 °C for 1-2 min and subsequent quenching to room temperature. All compounds are air-sensitive and begin to decompose in a week and are unstable under *N*,*N*-dimethylformamide and H_2O but relatively stable under acetonitrile.

3. Physical Measurements.

X-ray Powder Diffraction. Analyses were performed using a calibrated CPS 120 INEL X-ray powder difractometer (Cu K_α radiation) operating at 40 kV/20 mA and equipped with a position-sensitive detector with a flat sample geometry.

Electron Microscopy. Semiquantitative analyses of the compounds were performed with a JEOL JSM-35C scanning electron microscope (SEM) equipped with a Tracor Northern energy dispersive spectroscopy (EDS) detector.

Solid-state UV-vis Spectroscopy. Optical diffuse reflectance measurements were performed at room temperature using a Shimadzu UV-3101 PC double-beam, double-monochromator spectrophotometer operating in the 200-2500 nm region. The instrument is equipped with an integrating sphere and controlled by a personal computer. $BaSO_4$ was used as a 100% reflectance standard. The sample was prepared by grinding the crystals to a powder and spreading it on a compacted surface of the powdered standard material, preloaded into a sample holder. The reflectance versus wavelength data generated were used to estimate the band gap of the material by converting reflectance to absorption data.[10]

Raman Spectroscopy. Raman spectra were recorded on a Holoprobe Raman spectrograph equipped with a CCD camera detector using 633 nm radiation from a HeNe laser for excitation and a resolution of 4 cm^{-1}. Laser power at the sample was estimated to be about 5 mW, and the focused laser beam diameter was ca. 10 μm. A total of 64 scans was sufficient to obtain good quality spectra.

Infrared Spectroscopy. FT-IR spectra were recorded as solids in a CsI or KBr matrix.

The samples were ground with dry CsI or KBr into a fine powder and pressed into translucent pellets. The spectra were recorded in the far-IR region (600-100 cm^{-1}, 4 cm^{-1} resolution) and mid-IR region (500-4000 cm^{-1}, 4 cm^{-1} resolution) with the use of a Nicolet 740 FT-IR spectrometer equipped with a TGS/PE detector and silicon beam splitter.

Differential Thermal Analysis (DTA). Experiments were performed on Shimadzu DTA-50 thermal analyzer. A sample (~30 mg) of ground crystalline material was sealed in a silica ampoule under vacuum. A similar ampoule of equal mass filled with Al_2O_3 was sealed and placed on the reference side of the detector. Samples were heated to 500 °C at 10°C min^{-1}, and after 1 min it was cooled at a rate of –10 °C min^{-1} to 50 °C. Residues of the DTA experiments were examined by X-ray powder diffraction. Reproducibility of the results was checked by running multiple heating/cooling cycles. The melting and crystallization points were measured at a minimum of the endothermic peak and a maximum of the exothermic peak.

Solid-state Nuclear Magnetic Resonance (NMR) Spectroscopy. The room temperature ^{31}P Solid State NMR spectra for both crystalline and glass $RbPSe_6$ were obtained on a 9.4 T NMR Spectrometer (Varian Infinity Plus) using a double resonance magic angle spinning (MAS) probe with spinning speeds of 11 and 12 kHz using zirconia rotors of 4mm outer diameter. Bloch decay spectra were taken with a 3.75 microsecond pulse, and a relaxation delay up to 12,000 s. The spin lattice relaxation time for the crystalline phase $RbPSe_6$ is 3610 s. The chemical shifts are referenced to 85 % H_3PO_4 (0 ppm).

X-ray Crystallography. The crystal structure was determined by single-crystal X-ray diffraction methods. Preliminary examination and data collection were performed on a

SMART[11] platform diffractometer equipped with a 1K CCD area detector using graphite monochromatized Mo K_α radiation at room temperature. A hemisphere of data was collected using a narrow-frame method with scan widths of 0.30° in ω and an exposure time of 30 s frame^{-1}. The data were integrated using the SAINT[11] program. An analytical absorption correction and empirical absorption correction using the program SADABS[11] were performed. The initial positions for all atoms were obtained using direct methods, and the structures were refined with the full-matrix least-square techniques of the SHELXTL[11] crystallographic software package. Crystallographic data are given in Table 2-1. Satisfactory refinements were obtained with the noncentrosymmetric space group, $Pca2_1$ for $KPSe_6$ and $RbPSe_6$ and centrosymmetric space group $P2/n$. For $CsPSe_6$, Cs(2) site originally assigned to special position (0 0.5 -0.5) from direct methods. After the absorption correction with SADABS and final refinement followed by weight correction Cs(2) showed still large x-axis displacement of 0.09228. With the consideration of relation between Cs1 and Cs2 in centrosymmetric space group $P2/n$, Cs(2) was introduced into general position. As a result, Cs(2) location was converged into general position (-0.972682 0.494929 -0.501068) and stabilized at the refined position with small thermal parameter. But Cs(2) still exhibits the disorder near refined position leading to relatively high standard deviation of bond lengths between Cs(2) and P and Se atoms.

Nonlinear Optical Property Measurements. We used the frequency-tripled output of a passive-active mode-locked Nd:YAG laser with a pulse width of about 15 ps and a repetition rate of 10 Hz to pump an optical parametric amplifier (OPA). The OPA generates vertically polarized pulses in the ranges 400 ~ 685 nm and 737 ~ 3156 nm. In order to check the SHG efficiency as a function of the excitation energy, we tuned the

wavelength of the incident light from 1000 ~ 2000 nm. In this range, the spectral bandwidth of the linearly polarized light from the OPA is rather broad, about 2 meV full width at half maximum. However, the phase space compression phenomena ensures effective SHG where lower energy portions are exactly compensated by higher parts thereby satisfying both energy and momentum conservation. The incident laser pulse of 300 μJ was focused onto a spot 500 μm in diameter using a 3 cm focal-length lens. The corresponding incident photon flux is about 10 GW cm^{-2}. The SHG signal was collected in a reflection geometry from the excitation surface and focused onto a fiber optic bundle. The output of the fiber optic bundle is coupled to the entrance slit of a Spex Spec-One 500 M spectrometer and detected using a nitrogen-cooled CCD camera. The data collection time is 20 s.

Table 2-1. Crystallographic Data and Refinement Details for $KPSe_6$, $RbPSe_6$, and $CsPSe_6$.

Formula	$KPSe_6$	$RbPSe_6$	$CsPSe_6$
Formula Weight	543.83	590.20	647.64
Space group	$Pca2_1$ (no. 29)	$Pca2_1$ (no. 29)	$P2/n$ (no. 13)
a, Å	11.5052(7)	11.7764(17)	6.877(3)
b, Å	6.7939(6)	6.8580(10)	12.713(4)
c, Å	11.2328(7)	11.4596(16)	11.242(4)
β, deg.	90.000	90.000	92.735(7)
V, Å^3 / Z	878.01(11) / 4	925.5(2) / 4	981.8(6) / 4
crystal size, mm^3	0.020 x 0.156 x 0.015	0.028 × 0.167 × 0.037	0.139 × 0.014 × 0.014
ρ(calc), g/cm^3	4.114	4.236	4.314
μ, cm^{-1}	255.67	290.31	260.95
T, K / λ, Å	100(2) / 0.71073	293(2) / 0.71073	296(2) / 0.71073
θ range, deg	3.00 – 30.00	2.97 – 28.32	1.60 – 28.32
Total / unique reflections / parameters	8014 / 2361 / 74	2193 / 1894 / 73	2260 / 1452 / 79
Refinement method		Full-matrix least-squares on F^2	
Final R indices [$I>2\sigma(I)$], R_1[a]/wR_2 [b] (%)	5.22/6.66	2.59/4.99	3.81/8.74
R indices (all data), R_1/wR_2	6.19/6.86	3.51/5/23	8.09/9.92
Goodness-of-fit on F^2	1.257	0.977	1.024
Absolute structure parameter	0.02(1)	0.05(2)	N/A

[a] $R_1 = \Sigma \, ||F_O| - |F_C|| / \Sigma |F_O|$. [b] $wR_2 = \{\Sigma \, [w(F_O^2 - F_C^2)^2] / \Sigma [w(F_O^2)^2]\}^{1/2}$.

Table 2-2. Atomic coordinates ($\times 10^4$) and equivalent isotropic displacement parameters ($Å^2 \times 10^3$) for $RbPSe_6$ and $CsPSe_6$. U(eq) is defined as one third of the trace of the orthogonalized U_{ij} tensor.

	x	y	z	U(eq)
$RbPSe_6$				
Rb	1322(1)	6900(1)	11248(1)	39(1)
P	1660(2)	2753(2)	8181(1)	21(1)
Se(1)	-1291(1)	15638(1)	10133(1)	23(1)
Se(2)	-1461(1)	17622(1)	8467(1)	26(1)
Se(3)	-1030(1)	12440(1)	9359(1)	26(1)
Se(4)	851(1)	11790(1)	9914(1)	28(1)
Se(5)	1260(1)	5779(1)	7896(1)	27(1)
Se(6)	1344(1)	655(1)	6822(1)	29(1)
$CsPSe_6$				
Cs(1)	2500	273(1)	2500	39(1)
Cs(2)	-9727(17)	4949(15)	-5011(18)	42(2)
P(1)	-2500	-1517(3)	2500	18(1)
P(2)	-2500	3390(3)	2500	20(1)
Se(1)	-124(2)	4257(1)	1829(1)	36(1)
Se(2)	-2292(2)	-647(1)	4125(1)	31(1)
Se(3)	-88(2)	3238(1)	-753(1)	23(1)
Se(4)	138(2)	-2548(1)	2699(1)	23(1)
Se(5)	-3862(2)	1704(1)	4753(1)	22(1)
Se(6)	-1031(2)	2356(1)	3912(1)	22(1)

Table 2-3. Anisotropic displacement parameters ($Å^2 \times 10^3$) for $RbPSe_6$ and $CsPSe_6$. U(eq) is defined as one third of the trace of the orthogonalized U_{ij} tensor.

	U_{11}	U_{22}	U_{33}	U_{23}	U_{13}	U_{12}
$RbPSe_6$						
Rb	28(1)	49(1)	39(1)	-7(1)	-3(1)	7(1)
P	24(1)	18(1)	21(1)	1(1)	0(1)	0(1)
Se(1)	21(1)	26(1)	22(1)	1(1)	-1(1)	0(1)
Se(2)	24(1)	25(1)	28(1)	5(1)	-1(1)	-4(1)
Se(3)	29(1)	23(1)	27(1)	-1(1)	4(1)	-4(1)
Se(4)	32(1)	28(1)	25(1)	8(1)	4(1)	5(1)
Se(5)	31(1)	20(1)	29(1)	4(1)	6(1)	5(1)
Se(6)	36(1)	23(1)	29(1)	-4(1)	-7(1)	1(1)
$CsPSe_6$						
Cs(1)	35(1)	42(1)	39(1)	0	2(1)	0
Cs(2)	52(6)	37(3)	37(1)	-12(2)	-6(4)	-8(4)
P(1)	16(2)	17(2)	23(2)	0	4(2)	0
P(2)	21(2)	18(2)	20(2)	0	4(2)	0
Se(1)	40(1)	37(1)	31(1)	-4(1)	10(1)	-20(1)
Se(2)	40(1)	27(1)	27(1)	-9(1)	6(1)	-2(1)
Se(3)	24(1)	20(1)	26(1)	0(1)	8(1)	-2(1)
Se(4)	16(1)	31(1)	22(1)	1(1)	2(1)	4(1)
Se(5)	26(1)	19(1)	22(1)	-1(1)	5(1)	0(1)
Se(6)	21(1)	22(1)	24(1)	2(1)	3(1)	3(1)

4. Results and Discussion

Crystal Structure. $KPSe_6$ (**1**) and $RbPSe_6$ (**2**) are isostructural and adopt the polar space group $Pca2_1$. This discussion will concentrate mainly on the Rb^+ salt which consists of infinite one-dimensional chains of $^1/_\infty[PSe_6^-]$ along *a*-axis and separated by Rb^+ ions, Figure 2. The crystallographically unique anion has PSe_4 tetrahedra condensed with diselenide linkages to give the polymeric $^1/_\infty[PSe_6^-]$ chain. The PSe_4 tetrahedron is only slightly distorted from the ideal one with the Se-P-Se angles ranging from 101.46(7) to 119.79(8)°. The P-Se distances are normal at 2.1529(18) to 2.2994(17) Å. The Se-Se distances range from 2.3534(10) to 2.3859(10) Å. The dihedral angles around the bonds Se(1)-Se(2), Se(2)-Se(3), and Se(3)-Se(4) are -93.53(5)°, 112.41(4)°, and 87.35(5)°. The largest deviation from 90° gives the longest internal Se(2)-Se(3) distance as reported for disulfides[12] and leads to a bond distance alternation in the Se_4^{2-} unit. This trend is generally shown in unligated Se_4^{2-} ions.[13] Unusually short Se···Se nonbonding interactions between adjacent chains along the *c*-axis are observed at 3.217(1) to 3.350 (1) Å. Short intra- and interlayer Se···Se interactions much shorter in distance than the van der Waals radii sum of 3.80 Å[14] play a crucial role in influencing the crystal structure. In fact, other low-dimensional compounds such as $NbSe_3$ with its charge density wave

phenomenon exhibit similar Se···Se interactions of 3.30 Å.[15] In K_2Se_5, short contacts between the Se_5^{2-} ions are also observed.[16] The shorter Se···Se interactions in **3** affect the local geometry of the $^1/_\infty[PSe_6^-]$ chains to form pseudo-lamellar packing and relatively long Se-Se bonds due to the delocalization of electrons through short Se···Se contacts, Figure 2-2b.

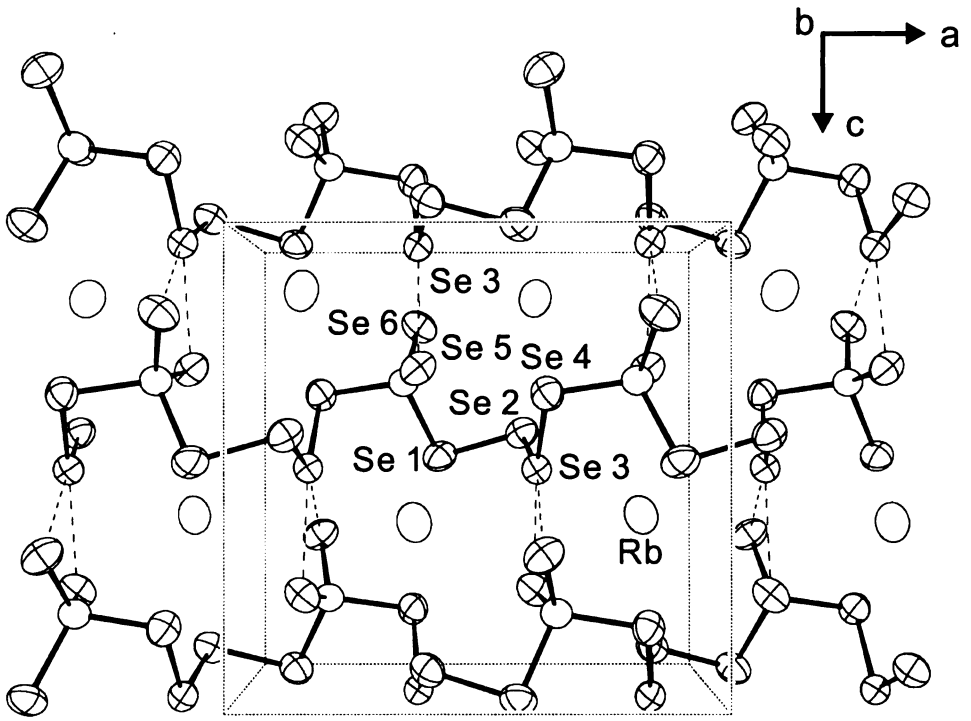

Figure 2-1. Structure of $RbPSe_6$ viewed down the *b*-axis. The Rb^+ ions are coordinated by 12 Se atoms from four selenophosphate chains. Dashed lines indicate weak Se···Se interactions (Å): Se(3)···Se(5), 3.350(1); Se(3)···Se(6), 3.217(1).

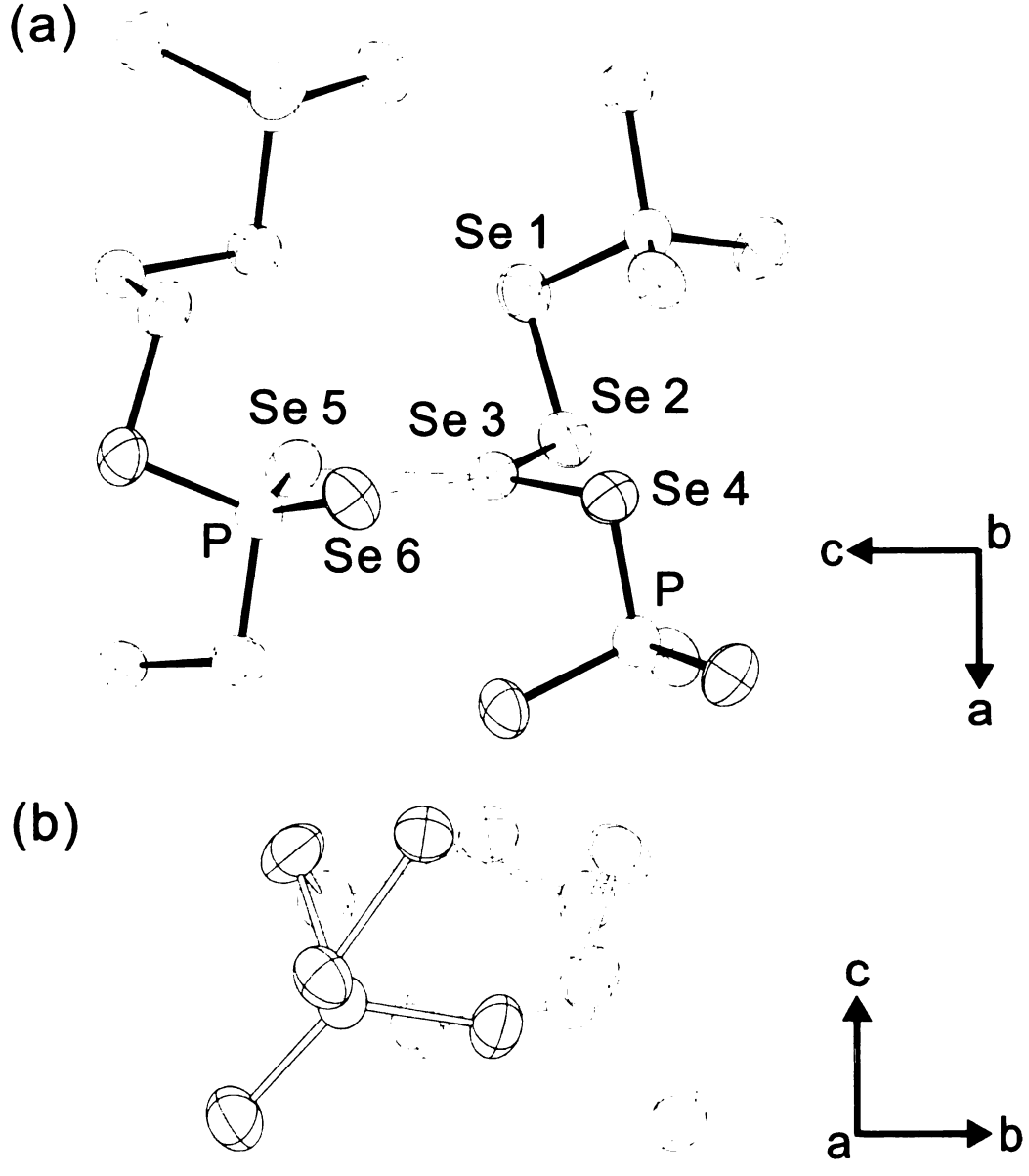

Figure 2-2. (a) Segment of the $^1/_\infty[PSe_6^-]$ anion showing the short Se···Se interactions. All thermal ellipsoids are presented with 90% probability. (b) View of a $^1/_\infty[PSe_6^-]$ chain looking down the *a*-axis, clearly showing its polar character.

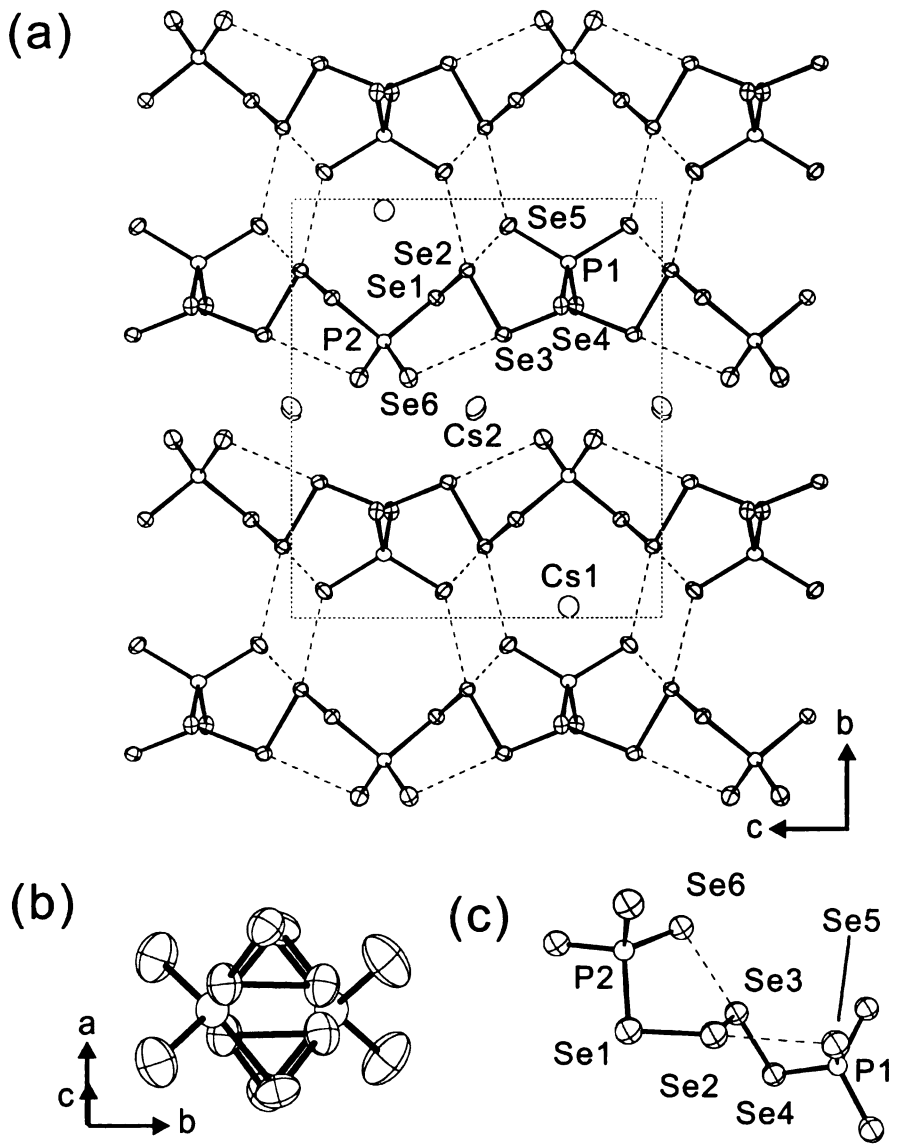

Figure 2-3. (a) Structure of $CsPSe_6$ viewed down the *a*-axis. Both Cs(1) and Cs(2) are surrounded by four different [PSe_6^-] chains. Dashed lines indicate weak Se···Se interactions (Å): Se(2) ···Se(5), 3.280(7); Se(3)···Se(6), 3.160(2); Se(2)···Se(5′), 3.248(2). (b) View of a $^1/_\infty[PSe_6^-]$ chain looking down [1 0 -1] axis. (c) Local geometry of the $^1/_\infty[PSe_6^-]$ anion in $CsPSe_6$ showing the short Se···Se interactions. All thermal ellipsoids are presented with 90% probability

Table 2-4. Selected bond distances (Å), nonbonding interaction distances (Å), and angles (deg) for $KPSe_6$ and $RbPSe_6$.

$KPSe_6$		$RbPSe_6$	
P-Se(1)	2.296(3)	P-Se(1)	2.2994(17)
P-Se(4)	2.244(3) ×2	P-Se(4)	2.2521(19) ×2
P-Se(5)	2.162(3) ×2	P-Se(5)	2.1529(18) ×2
P-Se(6)	2.161(3)	P-Se(6)	2.1530(17)
Se(1)-Se(2)	2.3473(10) ×2	Se(1)-Se(2)	2.3473(10) ×2
Se(2)-Se(3)	2.3859(10)	Se(2)-Se(3)	2.3859(10)
Se(3)-Se(4)	2.3534(10)	Se(3)-Se(4)	2.3534(10)
Se(3)···Se(5)	3.312(1)	Se(3)···Se(5)	3.350(1)
Se(3)···Se(6)	3.195(1)	Se(3)···Se(6)	3.3217(1)
Se(1)-P-Se(4)	105.70(11)	Se(1)-P-Se(4)	104.41(7)
Se(1)-P-Se(5)	108.68(11)	Se(1)-P-Se(5)	108.49(7)
Se(1)-P-Se(6)	110.62(11)	Se(1)-P-Se(6)	111.19(8)
Se(4)-P-Se(5)	109.06(11)	Se(4)-P-Se(5)	110.30(8)
Se(4)-P-Se(6)	102.02(11)	Se(4)-P-Se(6)	101.46(7)
Se(5)-P-Se(6)	119.70(12)	Se(5)-P-Se(6)	119.79(8)
P-Se(1)-Se(2)	94.46(8)	P-Se(1)-Se(2)	95.89(5)
P-Se(4)-Se(3)	95.59(8)	P-Se(4)-Se(3)	97.79(5)
Se(1)-Se(2)-Se(3)	99.60(5)	Se(1)-Se(2)-Se(3)	101.27(3)
Se(2)-Se(3)-Se(4)	102.54(5)	Se(2)-Se(3)-Se(4)	103.92(4)

Table 2-5. Selected bond distances (Å), nonbonding interaction distances (Å), and angles (deg) for $CsPSe_6$.

P(1)-Se(2)	2.135(2) ×2	Se(2)-P(1)-Se(2*)	117.54(17)
P(1)-Se(4)	2.240(2) ×2	Se(2)-P(1)-Se(4*)	114.18(4)
P(2)-Se(1)	2.138(2) ×2	Se(2*)-P(1)-Se(4*)	101.35(4)
P(2)-Se(1)	2.138(2)	Se(2)-P(1)-Se(4)	101.35(4)
P(2)-Se(6)	2.262(2) ×2	Se(2*)-P(1)-Se(4)	114.17(4)
Se(3)-Se(5)	2.3798(15)	Se(4*)-P(1)-Se(4)	108.43(15)
Se(5)-Se(6)	2.3549(16)	Se(1*)-P(2)-Se(1)	117.92(17)
		Se(1*)-P(2)-Se(6*)	102.95(5)
Se(2)···Se(5)	3.280(7)	Se(1)-P(2)-Se(6*)	112.06(5)
Se(3)···Se(6)	3.160(2)	Se(1*)-P(2)-Se(6)	112.06(5)
		Se(1)-P(2)-Se(6)	102.95(5)
		Se(6*)-P(2)-Se(6)	108.91(15)
		Se(4**)-Se(3)-Se(5*)	98.20(5)
		P(1)-Se(4)-Se(3**)	98.56(5)
		Se(6)-Se(5)-Se(3*)	100.20(5)
		P(2)-Se(6)-Se(5)	97.81(6)

Symmetry transformations used to generate equivalent atoms:

* $(-x-1/2, y, -z+1/2)$

** $(x+1, y, z+1)$

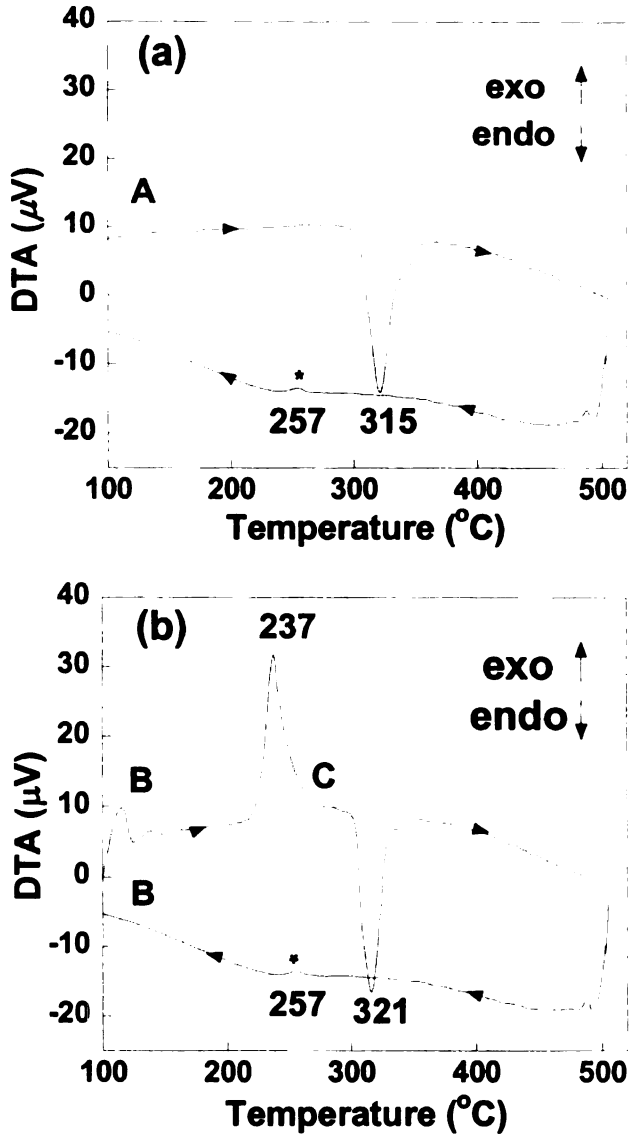

Figure 2-4. Differential thermal analysis diagrams of $RbPSe_6$ representing (a) melting in the first cycle with no crystallization upon cooling and (b) subsequent recrystallization and complete melting upon heating in the second cycle. * mark represents the vitrification upon cooling. $RbPSe_6$ is a pristine crystal at A, glass at B and restored crystal at C.

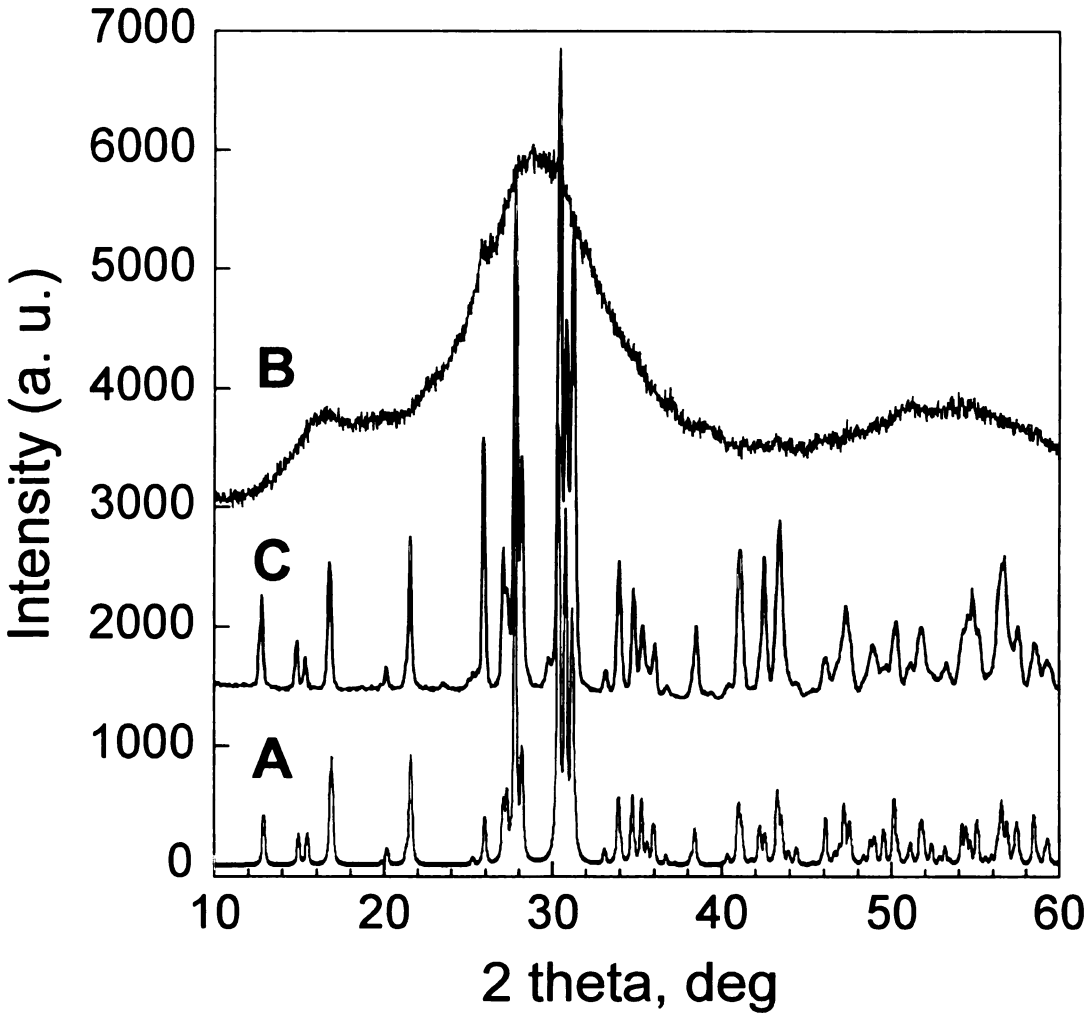

Figure 2-5. X-ray powder diffraction patterns of pristine (A), glassy (B) and recrystallized crystal 9(C)

$CsPSe_6$ (**3**) is a centrosymmetric compound also with $^1/_\infty[PSe_6^-]$ chains but of a different conformation than in the K^+ and Rb^+ analogs, Figure 2-3a. The differences in conformation are seen clearly in projection of the two chains in Figure 2-2b and 2-3b. Adjacent $^1/_\infty[PSe_6^-]$ chains along the *b*-axis are related by a 2-fold symmetry operation along the *a*-axis. P-Se distances range from 2.135(2) to 2.262(2) Å. The Se-Se distances with alteration are similar to the Rb^+ analog at 2.3549(16) to 2.3798(15) Å. The dihedral angle around the Se(2)-Se(3) bond of -121.06(1)° contributes to its longer distance than the external ones. Short Se···Se interactions are observed at 3.160(2) to 3.280(7) Å, even shorter than those of **2**. Interchain interactions generate a pseudo-lamellar packing and influence the conformation of Se_4^{2-} linkage to form straight lines of Se(1)-Se(2)···Se(5) and Se(4)-Se(3)···Se(6) connections and possibly maximize the pπ orbital overlap, Figure 2-3c.

The $[PSe_2(Se_4)^-]$ anion is a rare example of a free standing polymeric chalcophosphate with no coordinating metals. The only other reported polymeric anion is $^1/_\infty[P_3Se_4^-]$ ion which was found bound to Ru or Os atoms in $K_3RuP_5Se_{10}$,[17] $Rb_3RuP_5Se_{10}$, $K_3OsP_5Se_{10}$, and $Rb_3OsP_5Se_{10}$.[18]

Phase-Change Behavior. According to differential thermal analysis (DTA) performed at a rate of 10 °C min^{-1}, $RbPSe_6$ (**2**)[19] and $CsPSe_6$ (**3**) melt congruently at 315 and 303 °C, respectively, Figure 2-4, and form dark red glasses rather than crystals upon cooling.[20] Crystallization is only achieved on heating. The glasses recrystallize exothermically at 237 °C for **2** and 206 °C for **3** upon subsequent heating followed by melting at 321 and 310 °C for **2** and for **3**, respectively. $RbPSe_6$ showed vitrification at 257 °C on cooling to room temperature. The XRD patterns after recrystallization are the

same as those of pristine **2** and **3** indicating full recovery of the original crystal structure. Recrystallization and vitrification were repeatedly observed by repeating the DTA cycles. This clearly suggests the reversible glass-crystalline transition behavior. We may speculate that the facile crystallization of these glasses in the solid state suggest that the glass structure is somewhat related to the crystal structure, and given the polar character of the Rb salt, we may expect a similar polar nature for the precursor glass.

Spectroscopy. The solid-state diffuse reflectance UV/vis spectra of both crystalline and glassy $APSe_6$ (A = K, Rb, and Cs) reveal sharp absorption edges. The band gaps of crystalline phases **1**, **2**, and **3** revealed 2.16, 2.18, and 2.16 eV while those of glassy counterparts **4**, **5**, and **6** showed 1.82, 1.91, and 1.71 eV, respectively, which are consistent with their respective orange and dark red colors. It is noteworthy that red shifts in the absorption edge are typical in glassy phases. Glass formation in compounds with extended solid-state structures generally produces a large number of defects and mid-gap states (often called band tailing), which leads to lower band gaps compared to corresponding crystalline phases.[21] These materials show congruent melting and reversible glass-crystalline transitions accompanied with band gap shifts. This phenomenon is a key aspect of optical storage systems based on phase-change materials.[22] Furthermore, the polar K^+ and Rb^+ salts enable them to be explored for non-linear optical properties.

The far IR spectra of $RbPSe_6$ display absorption peaks at 482(s), 424(s), 386(s), 356(m), 247(m), 228(w) and 164(w) cm^{-1}, Figure 2-6. The peaks at 247 cm^{-1} are attributed to Se-Se stretching.[5,23] Those at higher energies are diagnostic of P-Se vibrations.[24] The far IR spectra of glassy $RbPSe_6$ display much broader and weaker peaks

at 507(w), 420(w), 385(sh) and 252(sh) cm^{-1}. A comparison with crystalline $RbPSe_6$ suggests that the building block $[PSe_6^-]$ unit is substantially intact in the glass but lacks long-range order. The bridging Se_4^{2-} chains seem to be severely disordered in the glassy phase according to the very weak and broad Se-Se stretching vibrations.

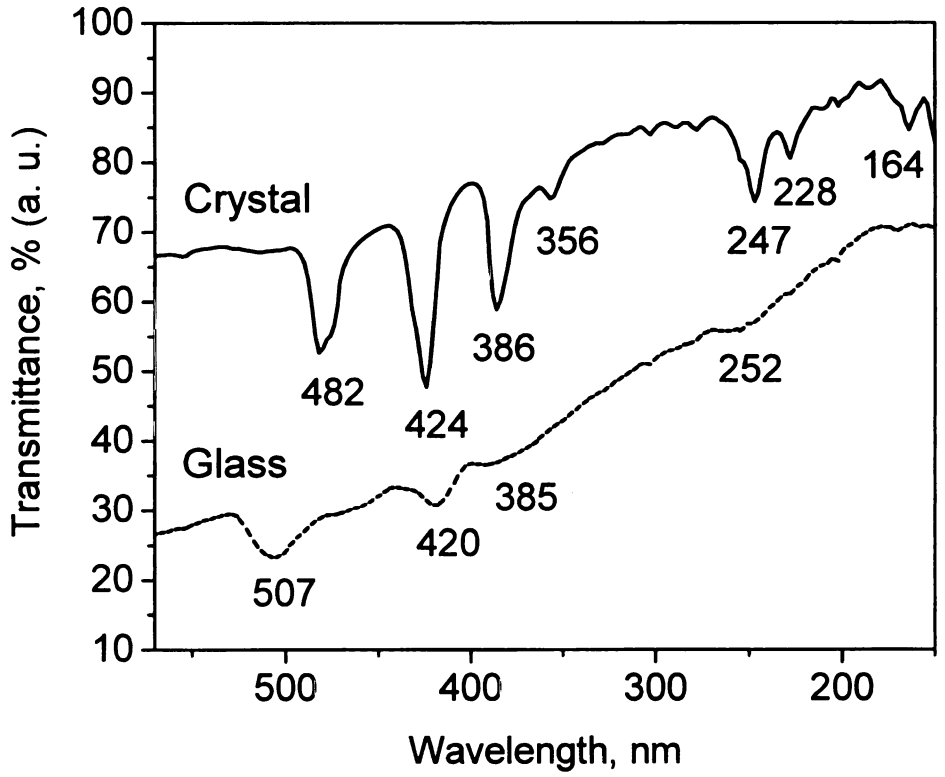

Figure 2-6. Far-IR spectra of $RbPSe_6$ crystal (upper) and glass (below).

^{31}P NMR provided further insight into bonding and structure, Figure 2-7. For crystalline $RbPSe_6$ under magic angle spinning (MAS), the major peak has an isotropic chemical shift of 4.3 ppm and a full-width at half-maximum (FWHM) linewidth of 0.5 ppm. This shift is ~40 ppm higher than a typical shift of $[P_2Se_9]^{4-}$, a comparable discrete unit with bridging Se.[9] In addition, for discrete selenophosphate units, the $\delta_{11} - \delta_{33}$

chemical shift anisotropy principal value difference correlates inversely with the degree of local symmetry about P, with ~65 ppm values observed for discrete tetrahedral $[PSe_4]^{3-}$ units and ~200 ppm values observed for $[P_2Se_9]^{4-}$ units.[9] The ~115 ppm value observed for $RbPSe_6$ fits within this correlation, with the pseudo C_2 symmetry of P in $^1/_\infty[PSe_6^-]$ chains intermediate between the high and low symmetries of P in $[PSe_4]^{3-}$ and $[P_2Se_9]^{4-}$ anions, respectively.

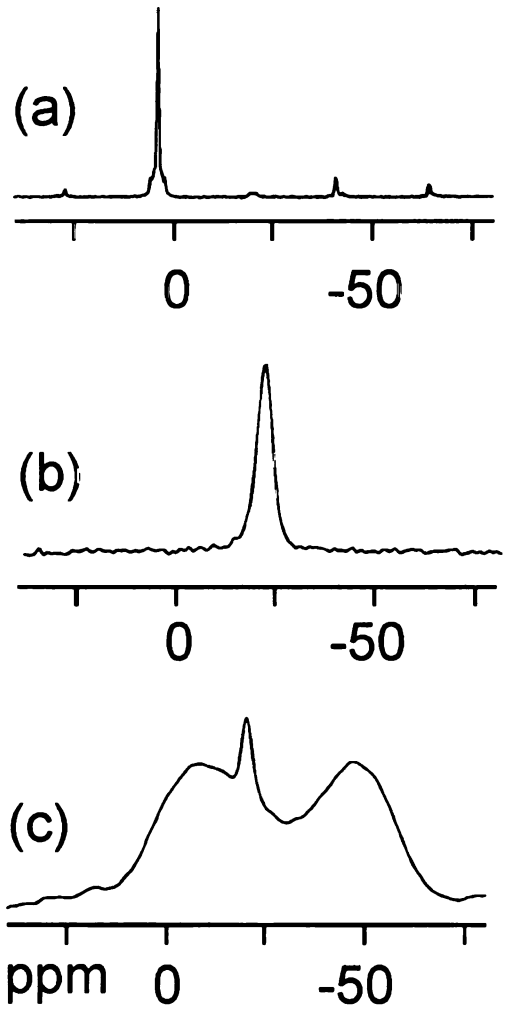

Figure 2-7. ^{31}P NMR spectra of $RbPSe_6$. Spectra (a) and (c) are for the crystalline and glassy materials, respectively, and were obtained at ambient temperature and with MAS frequency of ~11 kHz. Spectrum (b) is for the melt at 350 °C and was obtained under static conditions.

In a 350 °C melt, the static ^{31}P spectrum has a single resonance with -21 ppm peak chemical shift and 4 ppm FWHM linewidth. The shift is typical of PSe_4-type bonding,[9] and the narrow linewidth is diagnostic of rapidly tumbling small molecular species such as $[PSe_6]_m^{n-}$ ring-based molecules which would result from de-polymerization of $^1/_\infty[PSe_6^-]$ chains. In the $RbPSe_6$ glassy phase, there is a broad ^{31}P MAS signal centered at –25 ppm. The similarity of the average shifts of the melt and glass spectra and the broad width of the glass spectrum are consistent with a frozen melt model for the glass with associated conformational, packing, and possibly molecular heterogeneity. Overall, the NMR, crystallographic, and DTA data suggest that crystallization and $^1/_\infty[PSe_6^-]$ chain formation are coupled processes.

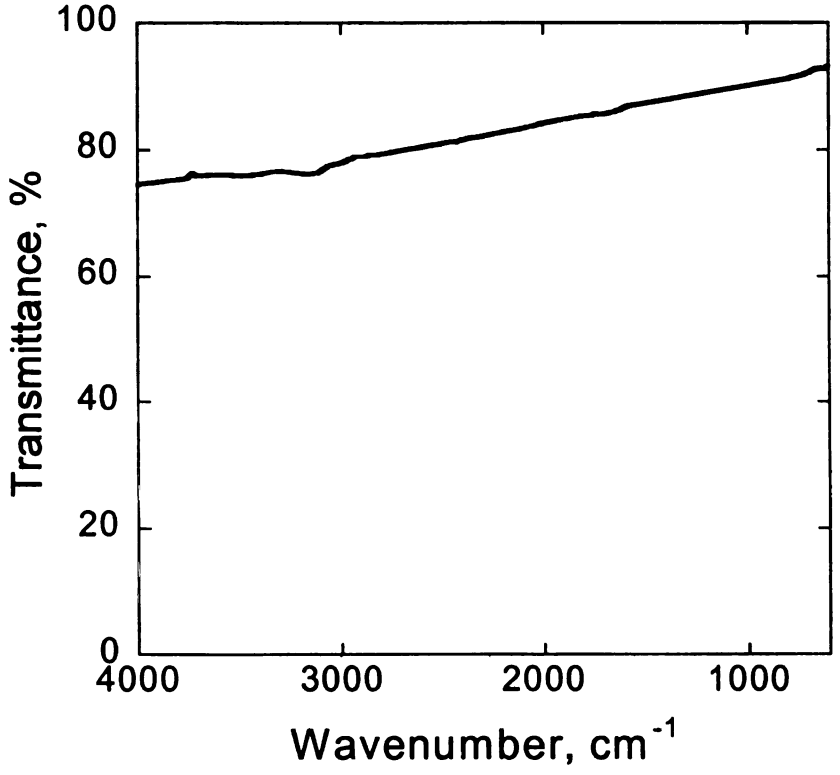

Figure 2-8. Mid-IR spectrum of glassy $KPSe_6$ showing its excellent IR transmissivity. * denotes the artifact.

Infrared Transmission. $KPSe_6$ and $RbPSe_6$ exhibit wide optical transparency ranging from long wave IR to near IR/visible light, Figure 2-8. The mid-IR transmittance spectrum showed little absorption from 4000 cm^{-1} (2 μm) to 500 cm^{-1} (20 μm). There is no light absorption below the band-gap transition suggesting uninterrupted light transmission in the compounds. Above 20 μm in the far-IR region, the compounds exhibited a complex set of absorptions, consistent with their far-IR spectrum. Optical transparency is a key feature for materials aimed at NLO applications. For example, the important NLO material for IR applications, $AgGaSe_2$,[25] shows LWIR transmission up to 17 μm.

Second Harmonic Generation Response. The polar, noncentrosymmetric chain structure of $^1/_\infty[PSe_6^-]$ composed of easily polarizable P and Se atoms linked by covalent bonding and $(Se4)^{2-}$ chain can produce large optical nonlinearity. SHG measurements were performed using a modified Kurtz powder method[26,27] with an IR light source ranging from 1000 nm to 2000 nm. SHG intensities of crystalline $KPSe_6$ and $RbPSe_6$ were directly compared with that of $AgGaSe_2$ powder. All samples were prepared in a similar fashion and the same particle size range of 45.5±7.5 μm was measured and compared. $KPSe_6$ and $RbPSe_6$ generated strong double frequency signals from the fundamental idler beam. The SHG intensity of $KPSe_6$ and $RbPSe_6$ showed a maximum at 771 and 790nm, respectively, which is ~60 times larger than that of in the same wavelength. At shorter wavelengths the $KPSe_6$ and $RbPSe_6$ outperforms the chalcopyrite material by over 200 fold, Figure 2-9a. These results demonstrate that the crystalline $KPSe_6$ and $RbPSe_6$ are very promising in IR NLO application. For comparison, the absolute nonlinear optical susceptibility at 2.12μm of $AgGaSe_2$ and $LiNbO_3$ is 67.7±13

and 29.1±5.2 pm/V, respectively.[28]

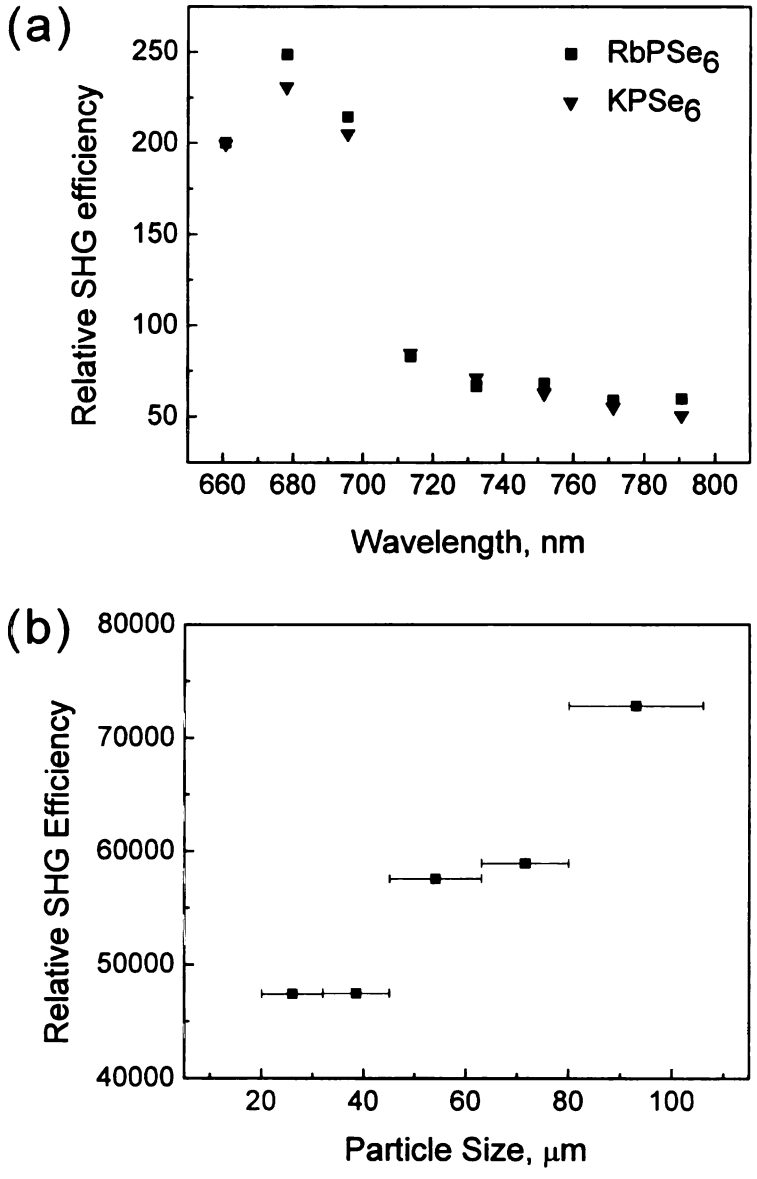

Figure 2-9. (a) SHG response of $KPSe_6$ (triangle) and $RbPSe_6$ (square) to $AgGaSe_2$ over a wide range of wavelengths. (b) Particle size to SHG intensities diagram of crystalline $RbPSe_6$ showing type-I phase-matching.

The SHG intensity of $RbPSe_6$ increased with the particle size and reached a plateau, Figure 2-9b. In principle, phase-matchable samples reach maximum intensity and then for larger average particle sizes the intensity is size-independent because of the existence of a phase-matching direction in the sample.[27] In this regard, crystalline $RbPSe_6$ is type I phase-matchable and eminently suitable for consideration in applications. $KPSe_6$ also exhibited similar behavior. These results suggest that $APSe_6$ (A=K, Rb) is of special interest for the middle and deep infrared (IR) applications due to its large nonlinear optical coefficients and high transmission in the IR region.

5. Concluding Remarks.

New compounds $APSe_6$ (A=K, Rb, Cs) composed of a rare one dimensional chain of $^1/_\infty[PSe_6^-]$. When molten the compounds can be quenched to a glassy state and exhibit reversible crystal-glass phase-change behavior. The optical absorption edge for the glassy phase is red shifted. IR spectroscopy analysis showed that the main building units are largely intact in the glassy form. This explains the rapid restoration of crystal structure from the corresponding amorphous phase. The glass forming behavior of the compounds makes them potentially valuable for producing IR optical fiber.

Polar one-dimensional compounds $APSe_6$ (A=K, Rb) showed a strong SHG response with wide optical transmittivity from 2 μm to 20 μm. The compounds are type-I phase-matchable with a response that is over 60 times larger than that of top performing NLO material $AgGaSe_2$. The remarkably stronger response is attributed to the highly polar one dimensional structure consisting of Se_4^{2-} unit that bonds to P atoms in contrast

to the weakly polar chalcopyrite structure of $AGaSe_2$.

References

(1) Kanatzidis, M. G. *Curr. Opin. Solid State & Mater. Sci.* **1997**, *2*, 139-149.

(2) (a) Jansen, M.; Henseler, U. *J. Solid State Chem.* **1992**, *99*, 110-119. (b) Mercier, R.; Malugani, J. P.; Fahys, B.; Robert, G.; Douglade, J. *Acta Crystallogr. B* **1982**, *38*, 1887-1890. (c) Schäfer, H.; Schäfer, G.; Weiss, A. *Z. Naturforsch., B: Chem. Sci.* **1965**, *B 20*, 811.

(3) Dickerson, C. A.; Fisher, M. J.; Sykora, R. E.; Albrecht-Schmitt, T. E.; Cody, J. A. *Inorg. Chem.* **2002**, *41*, 640-642.

(4) Brockner, W.; Becker, R.; Eisenmann, B.; Schafer, H. *Z. Anorg. Allg. Chem.* **1985**, *520*, 51-58.

(5) Mercier, R.; Malugani, J. P.; Fahys, B.; Douglade, J.; Robert, G. *J. Solid State Chem.* **1982**, *43*, 151-162.

(6) Chondroudis, K.; Kanatzidis, M. G. *Inorg. Chem.* **1995**, *34*, 5401-5402.

(7) Chondroudis, K.; Kanatzidis, M. G. *Inorg. Chem.* **1998**, *37*, 2582-2584.

(8) Aitken, J. A.; Canlas, C.; Weliky, D. P.; Kanatzidis, M. G. *Inorg. Chem.* **2001**, *40*, 6496-6498.

(9) Canlas, C. G.; Kanatzidis, M. G.; Weliky, D. P. *Inorg. Chem.* **2003**, *42*, 3399-3405.

(10) (a) Tandon, S. P.; Gupta, J. P. *Phys. Status Solidi* **1970**, *38*, 363-367. (b) Wendlandt, W. W.; Hecht, H. G. *Reflectance spectroscopy*; Interscience Publishers: New York, 1966. (c) Kortüm, G. *Reflectance spectroscopy. Principles, methods, applications*; Springer: Berlin, Heidelberg, New York, 1969.

(11) *SMART, SAINT, SHELXTL: Data Collection and Processing Software for the SMART-CCD System*; Siemens Analytical X-ray Instruments Inc.: Madison, WI, 1997.

(12) Hordvik, A. *Acta Chem. Scand.* **1966**, *20*, 1885-1891.

(13) Brese, N. E.; Randall, C. R.; Ibers, J. A. *Inorg. Chem.* **1988**, *27*, 940-943.

(14) Bondi, A. *J. Phys. Chem.* **1964**, *68*, 441-451.

(15) (a) Canadell, E.; Rachidi, I. E. I.; Pouget, J. P.; Gressier, P.; Meerschaut, A.; Rouxel, J.; Jung, D.; Evain, M.; Whangbo, M. H. *Inorg. Chem.* **1990**, *29*, 1401-1407. (b) Monceau, P. *Electronic Properties of Inorganic Quasi-one-dimensional Compounds*; D. Reidel; Dordrecht, Holland; Boston, MA, U.S.A., 1985.

(16) Müller, V.; Frenzen, G.; Dehnicke, K.; Fenske, D. *Z. Naturforsch., B: Chem. Sci.* **1992**, *47*, 205-210.

(17) Chondroudis, K.; Kanatzidis, M. G. *Angew. Chem., Int. Ed. Engl.* **1997**, *36*, 1324-1326.

(18) Chung, I; Kanatzidis, M. G. Unpulished results. $Rb_3RuP_5Se_{10}$, $K_3OsP_5Se_{10}$, and $Rb_3OsP_5Se_{10}$ are isostructural to $Rb_3RuP_5Se_{10}$.

(19) The thermal behavior of $KPSe_6$ showed the same patterns as that of $RbPSe_6$.

(20) The powder X-ray diffraction (XRD) patterns after each DTA cycle showed that amorphous glasses had formed.

(21) Dhingra, S.; Kanatzidis, M. G. *Science* **1992**, *258*, 1769-1772.

(22) (a) Feinleib, J.; Deneufvi.J; Moss, S. C.; R., O. S. *Appl. Phys. Lett.* **1971**, *18*, 254-257. (b) Maeda, Y.; Andoh, H.; Ikuta, I.; Minemura, H. *J. Appl. Phys.* **1988**, *64*, 1715-1719.

(23) Wachhold, M.; Kanatzidis, M. G. *J. Am. Chem. Soc.* **1999**, *121*, 4189-4195.

(24) Chondroudis, K.; Kanatzidis, M. G. *Chem. Commun.* **1996**, 1371-1372.

(25) Nikogosyan, D. N. *Nonlinear optical crystals: a complete survey*; Springer-Science: New York, 2005.

(26) Dougherty, J. P.; Kurtz, S. K. *J. Appl. Crystallogr.* **1976**, *9*, 145-158.

(27) Kurtz, S. K.; Perry, T. T. *J. Appl. Phys.* **1968**, *39*, 3798-3813.

(28) Choy, M. M.; Byer, R. L. *Phys. Rev. B* **1976**, *14*, 1693-1706.

Chapter 3

Nonlinear Optical Semiconducting Glassy Fibre Using Noncentrosymmetric Crystal-Glass Phase-Change Alkali Selenophosphate Materials $APSe_6$ (A = K, Rb)

1. Summary

Second harmonic generation (SHG) is usually forbidden in glass due to the presence of inversion symmetry at the macroscopic level. There have been numerous efforts[1] to induce SHG in glasses via poling using thermal[2], optical[3], and electron beam[4] irradiation; however the procedures are complex and/or expensive, and the resulting SHG is too small for practical applications and often non-permanent. Here we report general fabrication strategy for glassy optical fibres that yields a strong, intrinsic, second-order nonlinear optical (NLO) response based on materials which undergo a crystal-glass phase-change behaviour and adopt noncentrosymmetric space group. $APSe_6$ (A = K, Rb) compounds exhibited a strong SHG response in both the bulk crystalline and glassy phases. The optical glassy fibres of $APSe_6$ studied here were manually drawn at low temperature of 230-280 °C, to lengths of 10 or more centimetres. These as-prepared fibres exhibit coherent, continuously tuneable visible/near infrared SHG and difference frequency generation (DFG) responses over a wide range of wavelengths in centimetre long fibres. In addition they exhibit low-losses, have smooth surfaces and show

considerable mechanical flexibility. The observed SHG response was significantly enhanced simply by annealing the glassy fibre at 260 °C for a few minutes. We believe that our approach can be widely applied to prepare NLO glassy fibres by utilizing materials that undergo a phase-transition.

2. Introduction

Obtaining new coherent light sources involving different frequencies with the potential for tuneability is of great importance. Relatively few lasers prove to be practical and commercially viable and they typically generate a single or at best a few optical frequencies. Frequency conversion by a nonlinear optical (NLO) crystal is an effective way of producing coherent light at frequencies where lasers perform poorly or are unavailable. For example, when two incoming frequencies ω_1 and ω_2 are introduced in an NLO medium, they interact to produce four distinct frequencies: $2\omega_1$ and $2\omega_2$ by second harmonic generation (SHG), together with $(\omega_1 \pm \omega_2)$ by sum and difference frequency generation (SFG and DFG[5]). Demand for widely tuneable, coherent IR laser sources is emerging. Examples include: high rate (broadband) information transfer for telecommunications and internet[6] (1.3 – 1.6 μm via wavelength-division-multiplexed (WDM) all-optical networks[7]); sensing for organic and inorganic molecules[8] (including chemical warfare agents[9], biohazards[10], explosives[11] and pollutes[12]); and medical applications (in the range 2 - 12 μm)[13].

To be maximally useful NLO materials should possess: phase-matchability, high second-order nonlinearity, wide optical transparency, and thermal stability; in addition,

some applications require fibre or thin film forms. Many inorganic oxides and polymer NLO materials strongly absorb mid-IR light; in addition polymers show poor thermal stability and low damage thresholds. A crucial challenge facing many inorganic NLO crystals is the difficulty of fabricating fibres and films. Thanks to their IR transparency, high index of refraction (2.2~3.5)[14], and the excellent formability, chalcogenide glass is a promising contender for low-loss infrared optical fibre or planar waveguides; however it ordinarily lacks a second-order optical nonlinearity since a glass has inversion symmetry on a macroscopic scale. This latter fact restricts the application of glassy silica fibre, the backbone of modern telecommunication systems, to passive devices.

Our pair distribution function (PDF) analysis and Raman spectroscopic studies on the crystal-glass phase-change materials $K_2P_2Se_6$[15] and $K_{1-x}Rb_xSb_5S_8$[16] revealed that their glassy phases still largely preserved the basic building blocks that define the crystal structure but only lost long-range crystallographic order, in contrast to a common glass like silica. For the noncentrosymmetric compounds in this class, e.g. $K_2P_2Se_6$[15] and $Cs_5P_5Se_{12}$[17], we surprisingly observed significant innate SHG response from the as-prepared bulk glassy powders, plausibly by virtue of the noncentrosymmetric fragments partially intact in the glassy form of the phase-change materials. If true, optical glassy fibre exhibiting intrinsic SHG response can be drawn from the melt of noncentrosymmetric crystal-glass phase-change materials, keeping the advantages of a glassy fibre, such as mechanical flexibility, optical transparency, and low optical loss. Here we report an efficient and inexpensive way to produce nonlinear optical glassy fibre using crystal-glass phase-change materials that adopt noncentrosymmetric space group.

3. Experimental Section

3.1. Reagents. The reagents mentioned in this work were used as obtained: K metal (analytical reagent, Aldrich Chemical Co., Milwaukee, WI); Rb metal (analytical reagent, Johnson Matthey/AESAR Group, Seabrook, NH); red phosphorus powder, -100 mesh, Morton Thiokol, Inc., Danvers, MA; Se (99.9999%; Noranda Advanced Materials, Quebec, Canada); *N*,*N*-dimethylformamide (Spectrum Chemicals, ACS reagent grade); diethyl ether (Columbus Chemical Industries, Columbus WI, ACS reagent grade, anhydrous). A_2Se (A = K and Rb) starting materials were prepared by reacting stoichiometric amounts of the elements in liquid ammonia. P_2Se_5 was prepared by heating the mixture of P and Se with a stoichiometric ratio sealing in an evacuated silica tube at 460 °C for 24h.

3.2 Synthesis. Pure $APSe_6$ (A = K, Rb) was achieved by a stoichiometric mixture of A_2Se: P: Se = 1: 2: 11 under vacuum in a silica tube at 350 °C for 2 d followed by cooling at a rate of 5 °C h^{-1} to 250 °C. Energy dispersive spectroscopy analysis of the crystals showed an average composition of "$KPSe_{6.2}$" and "$Rb_{1.2}PSe_{6.1}$", respectively, for the orange rods-typed single crystals. For high purity, glassy phases of $APSe_6$ were obtained by quenching the melts of corresponding single crystals to room temperature. A glassy fibre of $APSe_6$ was drawn from the melt near melting point of each material. Crystal data for $KPSe_6$: orthorhombic $Pca2_1$, $Z = 4$; $a = 11.5052(7)$ Å, $b = 6.7939(6)$ Å, $c = 11.2328(7)$ Å, $V = 878.01(11)$ Å^3 at 100 K. Crystal data for $RbPSe_6$: orthorhombic $Pca2_1$, $Z = 4$; $a = 11.7764(17)$ Å, $b = 6.8580(10)$ Å, $c = 11.7764(17)$ Å, $V = 925.5(2)$ Å^3 at 293 K. $KPSe_6$ m.p.: ~320 °C, $RbPSe_6$ m.p.: ~315 °C.

4. Physical Measurements.

X-ray Powder Diffraction. Analyses were performed using a calibrated CPS 120 INEL X-ray powder difractometer (Cu K_α radiation) operating at 40 kV/20 mA and equipped with a position-sensitive detector with a flat sample geometry.

Electron Microscopy. Semiquantitative analyses of the compounds were performed with a JEOL JSM-35C scanning electron microscope (SEM) equipped with a Tracor Northern energy dispersive spectroscopy (EDS) detector.

Solid-State UV-vis spectroscopy. Optical diffuse reflectance measurements were performed at room temperature using a Shimadzu UV-3101 PC double-beam, double-monochromator spectrophotometer operating in the 200-2500 nm region. The instrument is equipped with an integrating sphere and controlled by a personal computer. Details are described in Chapter 2.

Raman Spectroscopy. Raman spectra were recorded on a Holoprobe Raman spectrograph equipped with a CCD camera detector using 633 nm radiation from a HeNe laser for excitation and a resolution of 4 cm^{-1}. Laser power at the sample was estimated to be about 5 mW, and the focused laser beam diameter was ca. 10 μm. A total of 64 scans was sufficient to obtain good quality spectra.

Infrared Spectroscopy. FT-IR spectra were recorded as solids in a CsI or KBr matrix. The samples were ground with dry CsI or KBr into a fine powder and pressed into translucent pellets. The spectra were recorded in the far-IR region (600-100 cm^{-1}, 4 cm^{-1} resolution) and mid-IR region (500-4000 cm^{-1}, 4 cm^{-1} resolution) with the use of a Nicolet 740 FT-IR spectrometer equipped with a TGS/PE detector and silicon beam

splitter.

Differential Thermal Analysis (DTA). Experiments were performed on Shimadzu DTA-50 thermal analyzer. A sample (~30 mg) of ground crystalline material was sealed in a silica ampoule under vacuum. A similar ampoule of equal mass filled with Al_2O_3 was sealed and placed on the reference side of the detector. Samples were heated to 500°C at 10°C min^{-1}, and after 1 min it was cooled at a rate of −10 °C min^{-1} to 50 °C. Residues of the DTA experiments were examined by X-ray powder diffraction. Reproducibility of the results was checked by running multiple heating /cooling cycles. The melting and crystallization points were measured at a minimum of the endothermic peak and a maximum of the exothermic peak.

Nonlinear Optical Property Measurements. We used the frequency-tripled output (355 nm) of a passive-active mode-locked Nd:YAG laser with a pulse width of about 15 ps and a repetition rate of 10 Hz to pump an optical parametric amplifier (OPA). The OPA generates vertically polarized pulses in the range 400 ~ 3,156 nm. In order to study the waveguided SHG response from our glass fibre, we used the idler beam (λ_{idler} = 1,240 – 1,610 nm) from the same OPA setting as above. The incident laser pulse of 0.2 mJ was focused onto the proximal surface of a fibre with a spot 300 μm in diameter using a 3 cm focal-length parabolic lens. The diameter of this fibre was about 122 ± 2 μm and its length is 10 mm. By selectively focusing the imaging lens on the opposite distal end of the fibre, the SHG signals were collected in a waveguide mode and dispersed with a Spex Spec-One 500 M spectrometer coupled to a nitrogen-cooled CCD camera. Since our monitoring range in the wavelength is rather wide, we did not use any filter but made sure that other optical components did not generate any extra SHG signals. The SHG

response from powder samples were measured using a reflection geometry under similar conditions. The detailed experimental setup is described elsewhere[18].

5. Results and Discussion.

In order to test our strategy, we chose the one-dimensional selenophosphate compounds $APSe_6$ (A=K, Rb)[19] which crystallize in the noncentrosymmetric polar space group of $Pca2_1$. Discussion here will be mainly concentrated on the K^+ salt because the Rb^+ analogue is isostructural and has similar physicochemical properties including nonlinear optical properties to K^+ salt. A one-dimensional infinite chain $^1/_\infty[PSe_6^-]$, consisting of the $[PSe_4]$ tetrahedral unit condensed with Se_2 linkage, runs along the *a*-axis, and is separated by alkali metal cations, Figure 3-1. The easily polarizable P and Se_4 chains, linked by covalent bonding, can produce a large optical nonlinearity. The compounds exhibited a reversible crystal-glass phase-change behaviour with optical contrast between the phases. $APSe_6$ exhibits wide optical transparency ranging from long-wave IR (LWIR) to near IR/visible light: 19.0 μm - 574 nm, crystalline $KPSe_6$; 19.5 μm - 681 nm, glassy $KPSe_6$; 20.2 μm - 568 nm, crystalline $RbPSe_6$; 18.9 μm - 649 nm, glassy $RbPSe_6$, Figure 3-2a. Above the complex P-Se absorptions in the far-IR region, uninterrupted light transmission continues through the mid-IR region. The optical transparency extends to an absorption edge of the compound in the visible region. The observation is consistent with characteristic IR transmittance of chalcogenide compounds. An important NLO material for IR application $AgGaSe_2$ shows LWIR transmission up to 17 μm[20].

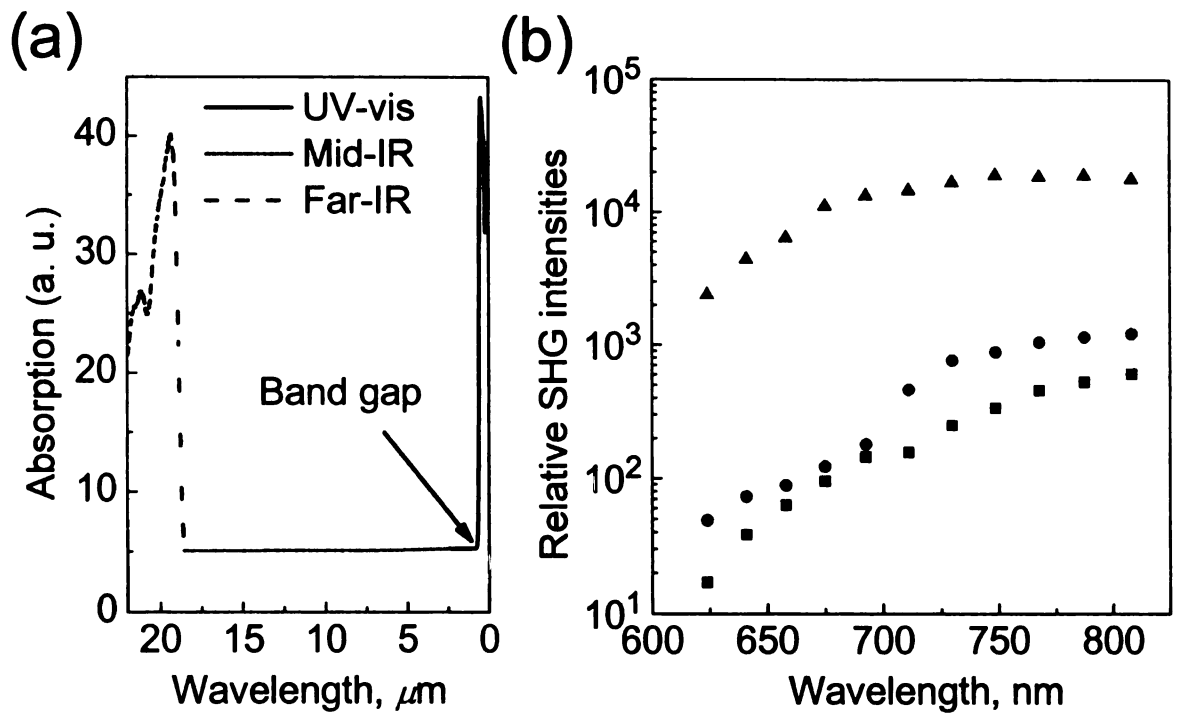

Figure 3-2. (a) Far-IR/mid-IR/visible absorption spectra of $KPSe_6$ bulk glass showing wide transparency range. (b) Relative SHG intensities of $KPSe_6$ crystal (triangle), $AgGaSe_2$ (circle), and $KPSe_6$ glass (square).

Second Harmonic Generation Response of $APSe_6$ (A=K, Rb) Bulk Crystal and Glass. $ZnGeP_2$, GaSe, and $AgGaQ_2$ (Q = S, Se) are mainstream IR NLO materials. Despite an exceptional SHG coefficient, $CdZnAs_2$ ($\chi^{(2)} \sim 434$ pm V^{-1}) is made of toxic elements and is only transparent beyond 4 μm, while optically isotropic GaAs ($\chi^{(2)} \sim 240$ pm V^{-1}) is non-birefringent and non-phase-matchable[21]. We examined the SHG response of crystalline and bulk glassy powders of $APSe_6$ compounds from 1240 to 1610 nm using a modified Kurtz powder method[22]. SHG intensities of crystalline $KPSe_6$ were directly compared with that of $AgGaSe_2$ powder. Samples prepared in a similar fashion and having the same particle size range (45.5 ± 7.5 μm) were measured and compared. Crystalline $APSe_6$ (A=K, Rb) powder generated very strong second harmonic signals

over a wide range in the visible/near infrared region. For example, $KPSe_6$ and $RbPSe_6$ crystalline powder converted 1.5 μm fundamental (lying mid way in the telecommunication band) to 0.75 μm near-infrared light with ~63 and 68 times larger intensities than that of $AgGaSe_2$ powder, Figure 3-2b. On the basis of the electronic structure, $\chi^{(2)}$ is estimated to be 151.3 pm V^{-1} and 149.4 pm V^{-1} for K^+ and Rb^+ salts[23]. SHG intensities of $APSe_6$ compounds increase with the particle sizes, indicating type-I phase-matchability. It should be noted that the calculated $\chi^{(2)}$ value of $APSe_6$ compounds are the highest among phase-matchable inorganic NLO materials with band gaps over 1.0 eV. Growing large single crystals of these compounds is in process to measure precise $\chi^{(2)}$ value. As-prepared $KPSe_6$ bulk glassy powder exhibited SHG intensities comparable to $AgGaSe_2$, Figure 3-2b.

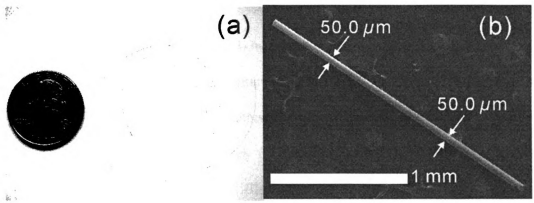

Figure 3-3. (a) Representative photograph of an optical fibre showing remarkable flexibility. (b) A representative SEM image of a fibre showing thickness uniformity at 50.0 μm and surface smoothness.

Glassy Fibre Fabrication. Based upon the strong SHG response and wide optical transparency in the IR region of both crystalline and glassy phases of $APSe_6$ (A = K, Rb) we fabricated glassy optical fibres. The Fibre drawing process was based upon the reversible thermal behaviour of crystal-glass phase-change materials: upon heating glassy phase crystallizes followed by subsequent melting, but upon cooling only vitrification occurs, instead of recrystallization. We drew $APSe_6$ glassy fibre from a viscous melt at ~230-280 °C; on cooling down from the liquid phase, and between vitrification and melting point, a continuous viscosity-temperature dependence exists which make high-speed drawing possible[24]. We note the processing temperature of the chalcogenide fibres is considerably lower than that of oxide competitors. For example, silica fibre requires approximately 2,000 K for softening[25]. Fibres with thickness ranging from a few to a hundred micrometers, having remarkable flexibility, could be prepared 'by hand' with lengths approaching a metre, Figure 3-3a. As seen in the scanning electron microscope (SEM) image of Figure 3-3b, a representative $d = 50.0$ μm fibre displays a high degree of thickness uniformity and surface smoothness; the cross-section of a fibre was continuous with no bubbles or cracks. $KPSe_6$ glassy fibre could recover its crystallinity by annealing it at 260 °C for 3 min. Crystallized fibre was slightly distorted in some regions but preserves its fibre form. An X-ray diffraction study of pristine fibre on a single crystal diffractometer showed faintly diffused scattering, confirming its amorphous nature, whereas that of annealed fibre showed remarkable crystallinity, Figure 3-4.

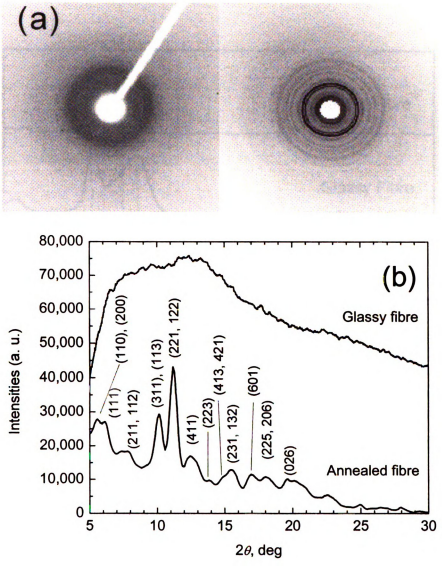

Figure 3-4. (a) X-ray diffraction ring patterns of pristine glassy (left) and annealed fibre (right) confirming their amorphous and crystalline nature, respectively. (b) X-ray diffraction patterns of the pristine glassy (upper) and annealed fibres (bottom). Diffraction profiles were regenerated from the ring patterns presented in (a), collected by STOE II single crystal diffractometer (Ag K_α). Note that the Bragg peaks from the annealed fibre are successfully indexed, indicative of the restoration of crystal structure on the fibre. (*hkl*) index on the major peak is presented.

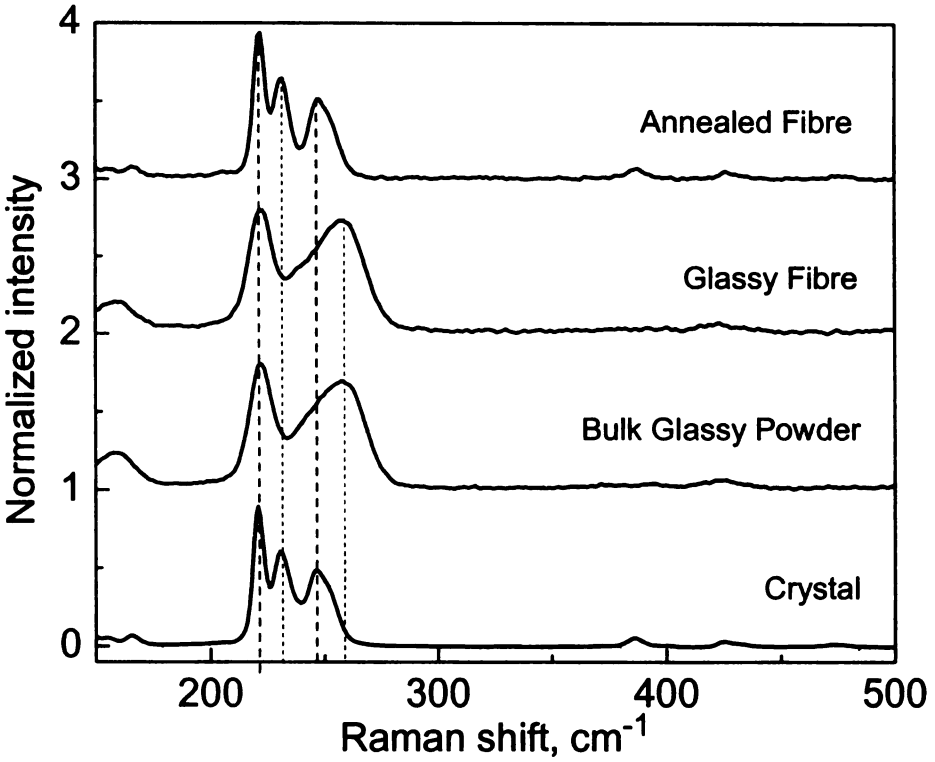

Figure 3-5. Raman spectra of $KPSe_6$ crystal, bulk glass, pristine glassy fibre, and annealed fibre.

The Raman spectrum of crystalline $KPSe_6$ at room temperature shows major shifts at 220 (s), 231 (m), and 246 (m) cm^{-1}, Figure 3-5. The shift at 220 cm^{-1} is unambiguously assigned to the PSe_4 stretching mode by comparison in the A_g stretching mode of T_d symmetry of $[PSe_4]^{3-}$ ligand. The shifts at 231 and 246 cm^{-1} can be assigned to antisymmetric and symmetric Se-Se stretching vibration modes of the diselenide group, respectively[15]. The Raman spectra of $KPSe_6$ bulk glassy powder and glassy fibre are identical, showing the broader and weaker peaks at 220 (bm) and 259 (bm) cm^{-1}, whereas the overall peak pattern is similar to that of the crystals. This suggests that the building blocks of $[PSe_4]$ and Se-Se bonds are still intact and local structural motifs are largely preserved in the bulk glass and glassy fibre but long-range crystallographic order is lost. The Raman spectrum of annealed fibre is same as that of bulk crystal, confirming the recovery of crystalline structure in the fibre form, consistent with the X-ray powder diffraction results.

The PDF analysis of $KPSe_6$ crystalline, bulk glass, and glassy fibre is also in agreement with the Raman spectroscopic data, Figure 3-6. The PDF of bulk glass and glassy fibre shows well-defined correlations up to ~8 Å with the first two at 2.3 Å (P-Se and Se-Se bonds) and 3.7 Å (K···Se and the second neighbour Se···Se distances) being very close to those of the crystalline phase. Above ~8 Å, the PDFs decays rapidly to zero, indicating the loss of the long-range order. The PDF result is consistent with that of $K_2P_2Se_6$[15]. Those observations support the facile restoration of the crystal structure from the amorphous state at the reversible crystal-glass phase transition.

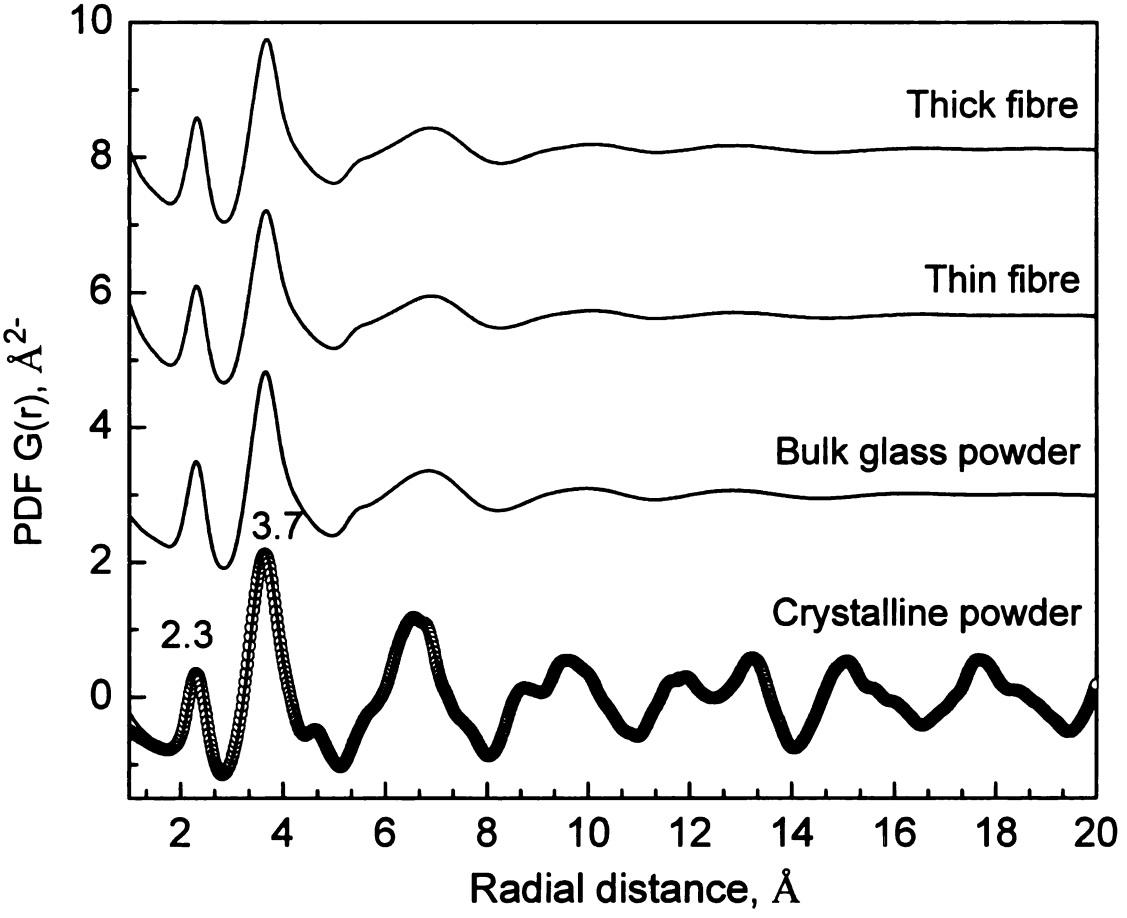

Figure 3-6. Pair distribution function (PDF) analysis for the glassy fibre, bulk glass, and crystalline powders. Fibres with different thickness at $d \sim 50$ μm and $d \sim 200$ μm were examined for comparison. Theoretical fit based upon single crystal structure refinement is plotted as black circles. The first peak at 2.3 Å corresponds to interatomic correlations of P-Se and Se-Se bonds, and the second peak at 3.7 Å K···Se and second neighbouring Se···Se. Note that PDFs of bulk glass and glassy fibres are very close to that of crystalline powder, indicating local structural order are significantly preserved in the amorphous state of bulk powder and fibre, but only lost long-range crystallographic order. This observation plausibly supports the presence of the intrinsic second-order nonlinear optic properties on the bulk glass and glassy fibre.

Second Harmonic Generation Response and Optical Loss. Since the bulk glass powder showed significant SHG response, we examined the corresponding generation and guiding of NLO light in glassy fibres. Being careful to precisely align the fibre with the laser path, we focused the tuneable incident beam (λ = 1,240 – 1,610 nm) onto the proximal end of the fibre (d = 122 μm, l = 10.0 mm); wave-guided outgoing light signal was collected from a distal end. Laser power was carefully adjusted to avoid crystallization or any laser-induced poling effect on a glassy fibre. As-prepared $APSe_6$ glassy fibre acted as a frequency convertor in a waveguide mode. It produced continuously tuneable SHG signal over a wide range of wavelengths (640 - 805 nm), Figure 3-7. The decreased SHG signal below 700 nm is due to the two-photon-induced absorption beyond the band gap. The observation of intrinsic SHG response from $KPSe_6$ glassy fibre is consistent with that found in the corresponding bulk glass powder. Note the SHG signal is generated continuously along the path, but the full path represents a macroscopic distance of 10.0 mm. Although we confirmed the amorphous nature of glassy fibre by X-ray powder diffraction, it cannot be totally ruled out that the presence of nanocrystals embedded induces the SHG response. We estimated the optical loss of $KPSe_6$ glassy fibre by measuring transmitted SHG intensities for various fibre lengths. A 10.0 mm fibre (d = 122 μm) was consecutively cut to 5.0 and 2.5 mm and the waveguided SHG intensities shown in Figure 3-8 were recorded. Rather than observing an exponential decay in the spectral region where no band gap absorption is present, the optical loss was linearly proportional to the fibre length, approximately 0.66 dB mm^{-1}, Figure 3-9. Details concerning the overall behaviour of the propagating SHG signal will require further study. Various effects including scattering from impurity, grain

boundaries, and the fibre end, as well as dispersion and inhomogeneity-induced mode conversion, all need to be considered. Regarding the materials themselves, further understanding of the temperature, surface tension and viscosity of the melt, the use of high purity starting materials, and a more sophisticated mechanical drawing process, all promise higher quality of the fibres. We note that commercial chalcogenide As_2Se_3 optical fibre has an attenuation of 10^{-2} dB mm^{-1} at 10.6 μm[24]. It should be noted that low optical loss is a prerequisite for optical fibre. Polyester sulphone (PES) showed comparable thermal properties to chalcogenide optical fibre, but the optical loss reached 30 dB mm^{-1} in the mid-IR at 10.6 μm.

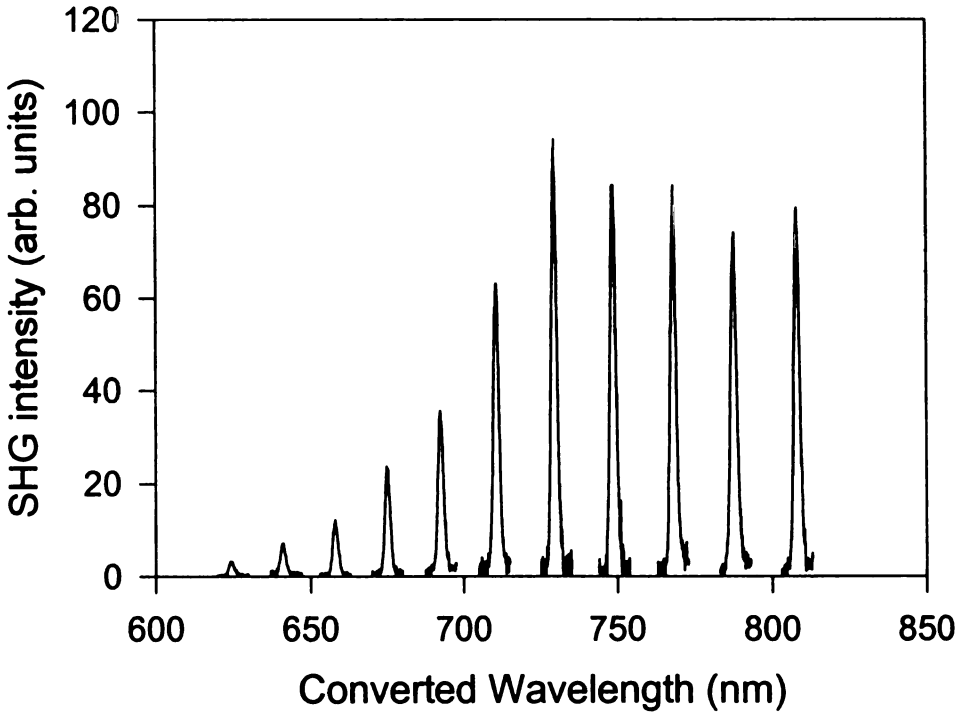

Figure 3-7. The waveguided SHG response transmitted through 10.0 mm long $KPSe_6$ glassy fibre in a wide range of vis/near IR region.

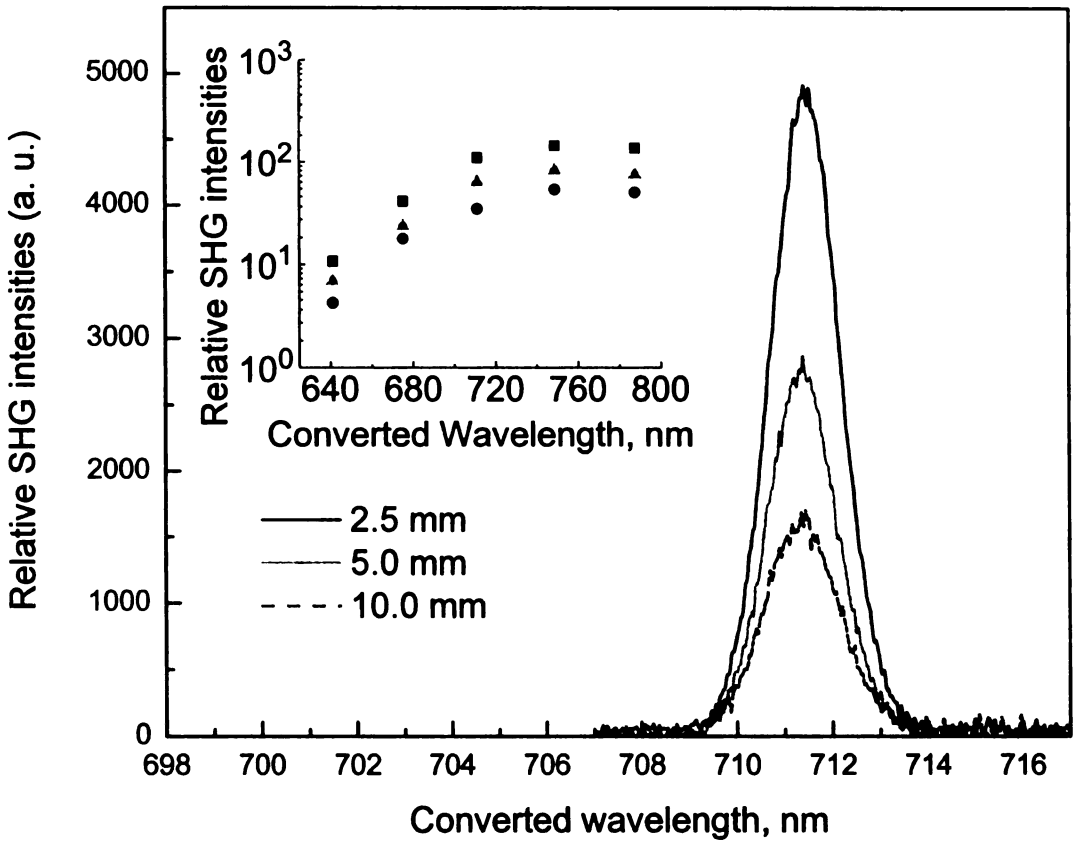

Figure 3-8. Optical loss of $KPSe_6$ glassy fibre at 711.5 nm, estimated by measuring SHG intensities for various lengths of fibres. Inset: optical loss for 640 to 788 nm SHG signals at 10.0 (circle), 5.0 (triangle), and 2.5 mm (square) long fibres.

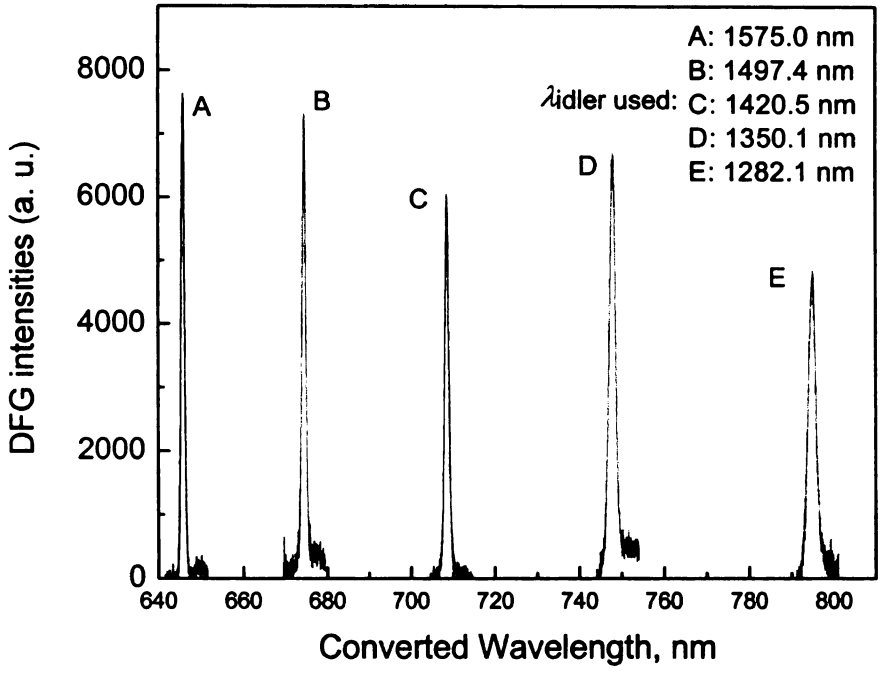

Figure 3-9. The DFG response as a function of λ_{idler}, demonstrating wave-mixing capability over a wide range of wavelengths.

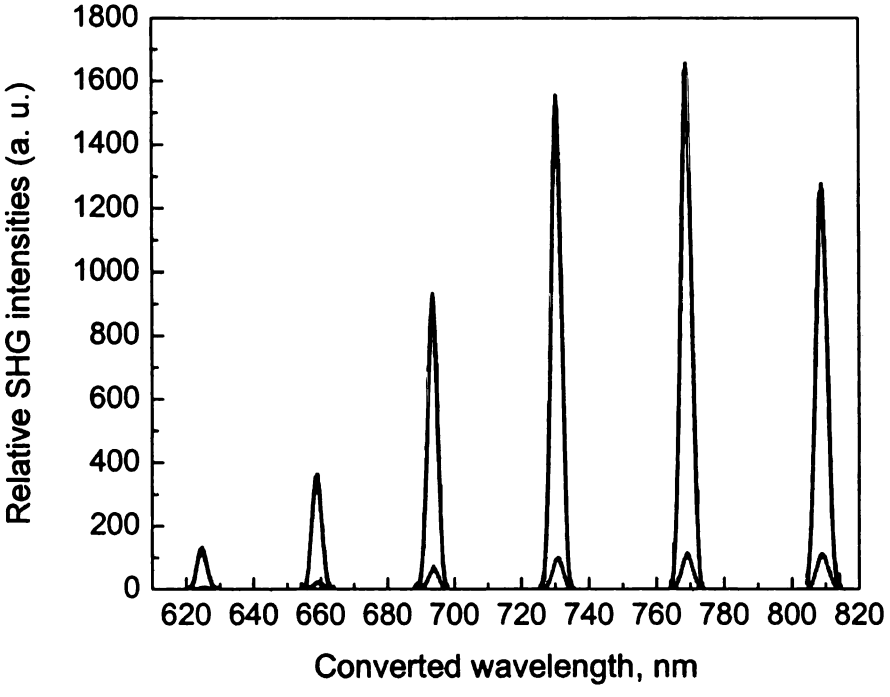

Figure 3-10. The relative SHG intensities measured from 620 to 805 nm for the pristine glassy and annealed fibres. Darker profiles represent SHG signals of the annealed fibre, and lighter profiles the pristine fibre.

Difference Frequency Generation Response. We also performed DFG experiments; this process is especially important for generating mid-IR light, and facilitates the multichannel conversion, low noise, high speed, and good transparency required for the wavelength division multiplexing (WDM) architecture[26]. Here we used both the signal and idler beams generated by an optical parametric amplifier driven by a Nd:YAG pulsed laser at 355 nm. The energy conservation among these two beams requires $1/\lambda_{signal} + 1/\lambda_{idler} = 1/355$ nm, and by definition of DFG, $1/\lambda_{signal} - 1/\lambda_{idler} = 1/\lambda_{DFG}$. Thus, for a given λ_{idler}, the expected wavelength for DFG was,

$$\lambda_{DFG} = \left(\frac{\lambda_{idler}}{\lambda_{idler} - 710nm} \right) 355nm \qquad (1)$$

By introducing different combinations of idler and signal beams, the $KPSe_6$ glassy fibre successfully generated continuously tuneable near-IR light by DFG, Figure 3-9. Deviation among DFG intensities arose from the signal beam, which was beyond the band gap. Although our detection limit (<1 μm) prohibited observing DFG at mid-IR, $APSe_6$ (A = K, Rb) should also produce tuneable coherent light throughout mid-IR region because the compounds are optically transparent there, a region where few NLO materials are available[21]. We cannot study SFG because our experimental set up produces constant λ_{SFG} at 355 nm, light that would be strongly absorbed because it is beyond the band gap.

Phase-change materials are of great interest as emerging technologies including rewritable optical media and the development of nonvolatile phase-change memory[27]. Conversion between the crystalline and glassy states can be driven by applying a voltage or heat, or irradiating appropriate laser. When they have a pronounced optical or

resistivity contrast, one state can be differentiated from the other. The stoichiometric compounds $APSe_6$ (A = K, Rb) can switch between the crystalline and glassy states without complications arising from compositional changes. One might exploit this property to switch the NLO properties of $APSe_6$ fibres. To explore this we annealed $KPSe_6$ glassy fibre at low temperature of 260 °C for 3 min and measured the waveguided SHG response. Remarkably, the annealed fibre exhibited over 10 times larger SHG intensities compared to the pristine glassy fibre in a wide range of wavelengths, Figure 3-10. This phase switching property of $APSe_6$ fibre can be utilized to periodically pole a fibre or film for quasi-phase-matching[28]. Various poling techniques developed to induce SHG on common glasses can be applied to $APSe_6$ glassy fibres[1,3,4]. By writing a grating onto a fibre with an optical standing wave the transmission of selected frequencies could be suppressed, a kind of latching optical switch.

6. Concluding Remarks

$APSe_6$ glassy fibre is in a totally different class from the conventional optical glassy fibre systems, in that it possesses strong, intrinsic, switchable, second-order NLO properties. It opens up the possibility of creating active, all-optical, broadband networks that independently modulate frequency, with no additional NLO or electronic devices. The fabrication concept suggested here is an example of combining apparently irrelevant properties (NLO + phase-change behaviour) to explore new functional materials. The discoveries and approaches described here are expected to stimulate the use of phase-change materials for NLO glassy fibres, and lead to further studies of the local structure

of glassy states in phase-change materials in order to explain the origin of their NLO properties.

References

(1) Margulis, W.; Garcia, F. C.; Hering, E. N.; Valente, L. C. G.; Lesche, B.; Laurell, F.; Carvalho, I. C. S. *MRS Bull.* **1998**, *23*, 31-35.

(2) Myers, R. A.; Mukherjee, N.; Brueck, S. R. J. *Opt. Lett.* **1991**, *16*, 1732-1734.

(3) Corbari, C.; Kazansky, P. G.; Slattery, S. A.; Nikogosyan, D. N. *Appl. Phys. Lett.* **2005**, *86*, 071106; Kityk, I. V. *J. Phys. Chem. B* **2003**, *107*, 10083-10087.

(4) Kazansky, P. G.; Dong, L.; Russell, P. S. *Opt. Lett.* **1994**, *19*, 701-703.

(5) Bloembergen, N. *Nonlinear optics*; 4th ed.; World Scientific: Singapore ; River Edge, NJ, 1996.

(6) Islam, M. N. *Phys. Today* **1994**, *47*, 34-40.

(7) Chou, M. H.; Brener, I.; Fejer, M. M.; Chaban, E. E.; Christman, S. B. *IEEE Photon. Technol. Lett.* **1999**, *11*, 653-655; Yoo, S. J. B. *J. Lightwave Technol.* **1996**, *14*, 955-966.

(8) Tittel, F. K.; Richter, D.; Fried, A. *Solid-State Mid-Infrared Laser Sources* **2003**, *89*, 445-510.

(9) Pushkarsky, M. B.; Webber, M. E.; Macdonald, T.; Patel, C. K. N. *Appl. Phys. Lett.* **2006**, *88*, 044103.

(10) Pestov, D.; Wang, X.; Ariunbold, G. O.; Murawski, R. K.; Sautenkov, V. A.; Dogariu, A.; Sokolov, A. V.; Scully, M. O. *Proc. Natl. Acad. Sci. U. S. A.* **2008**, *105*, 422-427.

(11) Pushkarsky, M. B.; Dunayevskiy, I. G.; Prasanna, M.; Tsekoun, A. G.; Go, R.; Patel, C. K. N. *Proc. Natl. Acad. Sci. U. S. A.* **2006**, *103*, 19630-19634.

(12) Pushkarsky, M.; Tsekoun, A.; Dunayevskiy, I. G.; Go, R.; Patel, C. K. N. *Proc. Natl. Acad. Sci. U. S. A.* **2006**, *103*, 10846-10849.

(13) Jean, B.; Bende, T. *Solid-State Mid-Infrared Laser Sources* **2003**, *89*, 511-544.

(14) Seddon, A. B. *J. Non-Cryst. Solids* **1995**, *184*, 44-50.

(15) Chung, I.; Malliakas, C. D.; Jang, J. I.; Canlas, C. G.; Weliky, D. P.; Kanatzidis, M. G. *J. Am. Chem. Soc.* **2007**, *129*, 14996-15006.

(16) Wachter, J. B.; Chrissafis, K.; Petkov, V.; Malliakas, C. D.; Bilc, D.; Kyratsi, T.; Paraskevopoulos, K. M.; Mahanti, S. D.; Torbrugge, T.; Eckert, H.; Kanatzidis, M. G. *J. Solid State Chem.* **2007**, *180*, 420-431.

(17) Chung, I.; Jang, J. I.; Gave, M. A.; Weliky, D. P.; Kanatzidis, M. G. *Chem. Commun.* **2007**, 4998-5000.

(18) Jang, J. I.; Ketterson, J. B. *Phys. Rev. B* **2007**, *76*, 155210.

(19) Chung, I.; Do, J.; Canlas, C. G.; Weliky, D. P.; Kanatzidis, M. G. *Inorg. Chem.* **2004**, *43*, 2762-2764.

(20) Nikogosyan, D. N. *Nonlinear optical crystals: a complete survey*; Springer-Science: New York, 2005.

(21) Fiore, A.; Berger, V.; Rosencher, E.; Bravetti, P.; Nagle, J. *Nature* **1998**, *391*, 463-466.

(22) Kurtz, S. K.; Perry, T. T. *J. Appl. Phys.* **1968**, *39*, 3798-3813.

(23) Song, J.-H.; Freeman, A. J.; Bera, T. K.; Chung, I.; Kanatzidis, M. G. *Nat. Mater.* **2008**, Submitted.

(24) Abouraddy, A. F.; Bayindir, M.; Benoit, G.; Hart, S. D.; Kuriki, K.; Orf, N.; Shapira, O.; Sorin, F.; Temelkuran, B.; Fink, Y. *Nat. Mater.* **2007**, *6*, 336-347.

(25) Tong, L. M.; Gattass, R. R.; Ashcom, J. B.; He, S. L.; Lou, J. Y.; Shen, M. Y.; Maxwell, I.; Mazur, E. *Nature* **2003**, *426*, 816-819.

(26) Park, S. K.; Do, J. Y.; Ju, J. J.; Park, S.; Kim, M. S.; Lee, M. H. *Mater. Lett.* **2005**, *59*, 2872-2875.

(27) Wuttig, M.; Yamada, N. *Nat. Mater.* **2007**, *6*, 824-832.

(28) Houé, M.; Townsend, P. D. *J. Phys. D: Appl. Phys.* **1995**, *28*, 1747-1763.

Chapter 4

The Helical Polymer $^1/_\infty[P_2Se_6^{2-}]$: Strong Second Harmonic Generation Response and Phase-Change Properties of its K and Rb Salts

1. Introduction

The chalcophosphate anions show great structural diversity and are predominantly discrete molecular species as for example the $[PSe_4]^{3-}$,[1] $[P_2Se_6]^{4-}$,[2] $[P_2Se_9]^{4-}$,[3] $[P_8Se_{18}]^{6-4}$ and the *trans*-decalin-like $[P_6Se_{12}]^{4-}$.[5] The number of infinite anions is very small and includes $^1/_\infty[PSe_6^-]$[6] and $^1/_\infty[P_5Se_{10}^{5-}]$. The latter is found bonded to transition metal atoms in $A_3MP_5Se_{10}$ (A=K, Rb; M=Ru, Os).[7] The polymeric anions show unusual structural moieties and coordination chemistry compared to the classical $[PSe_4]^{3-}$ and $[P_2Se_6]^{4-}$. All chalcophosphates are potential ligands to metal ions for building finite or extended structures.[8] The anions can be easily stabilized in polychalcogenide fluxes of suitable composition. Our experimental investigations of alkali selenophosphates provided useful insights on the relationship between structure and flux composition (A:P:Se ratio in the composition) in this class.[5] The diversity of these anions seems greater than that of the oxo-phosphate anions which are responsible for defining the enormous class of metal phosphates.[9] Therefore, the chalcogenide analogs have the potential to produce an even greater family of compounds with metal ions. One striking contrast between phosphates and chalcophosphates is the ability of the latter to couple through Q-Q bonds (Q = S, Se) forming catenated species. In principle, every simple

molecular anion $[P_xQ_y]^{z-}$ could be oxidatively coupled through its terminal P-Q bonds to form lager species linked with P-Q-Q-P moieties.

Here we describe the unique helical anion $^1/_\infty[P_2Se_6^{2-}]$ in the form of K^+ and Rb^+ salts. Although it was not formed via actual oxidative coupling chemistry, the chiral structure derives from coupling of the ethane-like $[P_2Se_6]^{4-}$ anion. Both $K_2P_2Se_6$ and $Rb_2P_2Se_6$ can be quenched from the melt to a glassy state and can undergo reversible phase-change crystal-glass transitions. Interest in phase-change materials is growing, as a result of emerging technologies including commercially available rewritable optical media and the development of nonvolatile phase-change memory.[10,11] The most interesting materials are those with stoichiometric composition because they can switch between the two states without complications due to compositional changes.

At low temperature $K_2P_2Se_6$ (but not $Rb_2P_2Se_6$) undergoes a phase transition to a structure of lower symmetry while retaining the helical structure. Polar structure $K_2P_2Se_6$ exhibits remarkably strong second harmonic generation (SHG) intensity. In the infrared region the material is highly transmissive over a wide wavelength range. Compared to the SHG intensity of the chalcopyrite compound $AgGaSe_2$, which is the top infrared NLO material used commercially, $K_2P_2Se_6$ exhibited 50-fold stronger response as well as type-I phase matching property making it a potential contender material for applications in the IR region. To our best knowledge this is one of the largest NLO SHG responses ever reported for this near and mid infrared region of the spectrum. Glassy $K_2P_2Se_6$ also exhibited SHG response. Since homogeneous glasses generally do not show SHG due to the macroscopically present inversion center, this observation is not only a rare example of amorphous NLO response with no specific treatment such as poling, it is also of

interest for further investigations in optical devices.

2. Experimental Section

2.1. Reagents.

The reagents mentioned in this work were used as obtained: K metal, analytical reagent, Aldrich Chemical Co., Milwaukee, WI; Rb metal, analytical reagent, Johnson Matthey/AESAR Group, Seabrook, NH; red phosphorus powder, -100 mesh, Morton Thiokol, Inc., Danvers, MA; Se, 99.9999%, Noranda Advanced Materials, Quebec, Canada; *N*,*N*-dimethylformamide, ACS reagent grade, Mallinckrodt Backer Inc., Paris, KY; diethyl ether, ACS reagent grade, anhydrous, Columbus Chemical Industries, Columbus WI. A_2Se (A = K and Rb) starting materials were prepared by reacting stoichiometric amounts of the elements in liquid ammonia under N_2. P_2Se_5 was prepared by heating the mixture of P and Se with a stoichiometric ratio sealing in an evacuated silica tube at 460 °C for 24h.

2.2. Synthesis

Pure $K_2P_2Se_6$ and $Rb_2P_2Se_6$ were obtained in quantitative yield by heating a mixture of K_2Se:P_2Se_5=1:1 and Rb_2Se:P:Se=1:2.4:5 in an evacuated and sealed silica tube at 450 °C for 3 d followed by cooling at a rate of 5°C h^{-1} to 250 °C, respectively. After washing with *N*,*N*-dimethylformamide (DMF) and ether, we obtained pure red/orange thick plate-typed single crystals. Energy dispersive spectroscopy (EDS) analysis of the crystals showed an average composition of "$K_2P_{1.9}Se_{5.8}$" and

"$Rb_2P_{1.9}Se_{5.9}$". The glassy phases of $K_2P_2Se_6$ and $Rb_2P_2Se_6$ were prepared from a mixture of K_2Se:P_2Se_5=1:1 and $Rb_2P_2Se_6$ crystals respectively, placed in a silica tube and melted at 800-900 °C for 1-2 min and subsequent quenching in ice water. The crystalline compounds were air-stable for at least a week and stable under polar solvents such as DMF, *N*-methylformamide, methyl and ethyl alcohol and H_2O. Glassy $K_2P_2Se_6$ and $Rb_2P_2Se_6$ were soluble in DMF and methyl alcohol without stirring to give clear light orange solution.

3. Physical Measurements

X-ray Powder Diffraction and Pair Distribution Function (PDF) Analysis. Phase purity x-ray diffraction analyses were performed using a calibrated CPS 120 INEL X-ray powder diffractometer (Cu K_α graphite monochromatized radiation) operating at 40 kV/20 mA and equipped with a position-sensitive detector with flat sample geometry.

The powder X-ray diffraction data for PDF analysis of the crystalline and glassy $K_2P_2Se_6$ were collected at room temperature using an Inel CPS 120 diffractometer. A graphite monochromatized and Rh filtered Ag K_α (0.56080 Å) radiation was used for the crystalline and glassy $K_2P_2Se_6$, respectively. The samples were ground to a fine powder under nitrogen atmosphere, loaded into 0.5 mm capillaries and flame sealed. Fluorescence due to selenium atoms was successfully filtered out by using a 0.150mm thick bronze foil in front of the CPS detector. Data reduction and the calculation of the PDF were performed as described elsewhere[12] with the PDFGetX2 software.[13]

Electron Microscopy. Semiquantitative analyses of the compounds were performed with

a JEOL JSM-35C scanning electron microscope (SEM) equipped with a Tracor Northern energy dispersive spectroscopy (EDS) detector.

Solid-State UV-vis spectroscopy. Optical diffuse reflectance measurements were performed at room temperature using a Shimadzu UV-3101 PC double-beam, double-monochromator spectrophotometer operating in the 200-2500 nm region. The instrument is equipped with an integrating sphere and controlled by a personal computer. $BaSO_4$ was used as a 100% reflectance standard. The sample was prepared by grinding the crystals to a powder and spreading it on a compacted surface of the powdered standard material, preloaded into a sample holder. The reflectance versus wavelength data generated were used to estimate the band gap of the material by converting reflectance to absorption data.[14]

Raman Spectroscopy. Raman spectra were recorded on a Holoprobe Raman spectrograph equipped with a CCD camera detector using 633 nm radiation from a HeNe laser for excitation and a resolution of 4 cm^{-1}. Laser power at the sample was estimated to be about 5 mW, and the focused laser beam diameter was ca. 10 μm. A total of 128 scans was sufficient to obtain good quality spectra.

Infrared Spectroscopy. FT-IR spectra were recorded as solids in a CsI or KBr matrix. The samples were ground with dry CsI or KBr into a fine powder and pressed into translucent pellets. The spectra were recorded in the far-IR region (600-100 cm^{-1}, 4 cm^{-1} resolution) and mid-IR region (500-4000 cm^{-1}, 4 cm^{-1} resolution) with the use of a Nicolet 740 FT-IR spectrometer equipped with a TGS/PE detector and silicon beam splitter.

Differential Thermal Analysis (DTA) Experiments were performed on Shimadzu DTA-

50 thermal analyzer. A sample (~30 mg) of ground crystalline material was sealed in a silica ampoule under vacuum. A similar ampoule of equal mass filled with Al_2O_3 was sealed and placed on the reference side of the detector. The sample was heated to 600°C at 10°C/min, and after 1 min it was cooled at a rate of −10 °C min^{-1} to 50 °C. The residues of the DTA experiments were examined by X-ray powder diffraction. Reproducibility of the results was confirmed by running multiple heating/cooling cycles. The melting and crystallization points were measured at a minimum of endothermic peak and a maximum of exothermic peak.

Solid-State Nuclear Magnetic Resonance (NMR) Spectroscopy. The room temperature solid-state NMR measurement was taken on a 9.4 T NMR Spectrometer (Varian Infinity Plus) using a double resonance magic angle spinning (MAS) probe. The sample was spun at 8.0 kHz using zirconia rotors of 6 mm outer diameter. Bloch decay spectra were taken with the excitation/detection channel tuned to ^{31}P at 161.39 MHz, a 4.5 μs 90° pulse, and a relaxation delay of 3,000 s. The spectrum was referenced using 85% H_3PO_4 at 0 ppm.

X-ray Crystallography. The crystal structure was determined by single-crystal X-ray diffraction methods. For $K_2P_2Se_6$, preliminary examination and data collection were performed on a SMART platform diffractometer equipped with a 1K CCD area detector using graphite monochromatized Mo K_α radiation at 173(2) and 298(2) K. A hemisphere of data was collected at 298(2) K using a narrow-frame method with scan widths of 0.30° in ω and an exposure time of 30s $frame^{-1}$. For the data collected at 173(2)K, 60s $frame^{-1}$ was used. The data were integrated using the SAINT program. An analytical absorption and empirical absorption correction using the program SADABS were performed for both sets. The initial positions for all atoms were obtained using

direct methods and the structures were refined with the full-matrix least-squares techniques of the SHELXTL[15] crystallographic software package. Crystallographic data are given in Table 4-1. Satisfactory refinement was obtained with the chiral space group, $P3_121$ at 298(2) K and $P3_1$ at 173(2) K. The crystals used for structure refinement were racemically and merohedrally twinned, and the twinning fractions refined to 49.5, 25.8, 23.1 and 1.6 % at 173(2) K. The racemic and merohedral twinning behavior was typical for $K_2P_2Se_6$ and their relative ratios determined for several crystals were very similar. Interestingly, flux synthesis using the mixture of K_2Se:P:Se = 1:2.4:5 significantly increased the portion of one enantiomorph compared to the crystals obtained with a direct combination reaction of K_2Se and P_2Se_5. The racemic ratio improved from 1:1 to 3:1.

Intensity data for $Rb_2P_2Se_6$ were collected at 100(2) K on a STOE IPDS II diffractometer with Mo K_α radiation operating at 50 kV and 40 mA with a 34 cm image plate. Individual frames were collected with a 5 min exposure time and a 1.0 ω rotation. The X-AREA, X-RED and X-SHAPE software package was used for data extraction and integration and to apply empirical and analytical absorption corrections. The SHELXTL software package was used to solve and refine the structure. The most satisfactory refinement was obtained with the chiral space group, $P3_121$ at 100(2) K rather than $P3_221$. The refined Flack x parameter was 0.901(96). After inversion to $P3_121$, the Flack parameter x was 0 and the BASF value was 0.89. Following refinement for racemic and merohedral twinning done at the same time, the twinning fractions refined to 89.43, 5.83, 5.59 and 2.15 % and x parameter 0.0. $Rb_2P_2Se_6$ did not show a phase transition with temperature change and its crystal structure is the same as that of $K_2P_2Se_6$ at room temperature (RT). The parameters for data collection and the details of the structural refinement are given in Table 4-1.

Fractional atomic coordinates and displacement parameters for each structure are given in Tables 4-2 - 4-4. In all cases the atoms were refined to full occupancy.

Nonlinear Optical Property Measurements. We used the frequency-tripled output of a passive-active mode-locked Nd:YAG laser with a pulse width of about 15 ps and a repetition rate of 10 Hz to pump an optical parametric amplifier (OPA). The OPA generates vertically polarized pulses in the ranges 400 ~ 685 nm and 737 ~ 3156 nm. In order to check the SHG efficiency as a function of the excitation energy, we tuned the wavelength of the incident light from 1000 ~ 2000 nm. In this range, the spectral bandwidth of the linearly polarized light from the OPA is rather broad, about 2 meV full width at half maximum. However, the phase space compression phenomena ensures effective SHG where lower energy portions are exactly compensated by higher parts thereby satisfying both energy and momentum conservation. The incident laser pulse of 300 μJ was focused onto a spot 500 μm in diameter using a 3 cm focal-length lens. The corresponding incident photon flux is about 10 GW cm^{-2}. The SHG signal was collected in a reflection geometry from the excitation surface and focused onto a fiber optic bundle. The output of the fiber optic bundle is coupled to the entrance slit of a Spex Spec-One 500 M spectrometer and detected using a nitrogen-cooled CCD camera. The data collection time is 20 s. Single crystal or glassy sample was ground and separated by various size ranges using sieves. Samples were placed in a capillary tube and measured.

Table 4-1. Crystallographic Data and Refinement Details for $K_2P_2Se_6$ and $Rb_2P_2Se_6$.

Formula	$K_2P_2Se_6$	$K_2P_2Se_6$	$Rb_2P_2Se_6$
Space group	$P3_121$ (no. 152)	$P3_1$ (no. 144)	$P3_121$ (no. 152)
a, b, Å	7.2746(8)	14.4916(7)	7.2982(5)
c, Å	18.870(4)	18.800(2)	19.002(2)
α, β (deg)	90	90	90
γ (deg)	120	120	120
Z	3	12	3
V, Å^3	864.8(2)	3419.2(4)	876.5(1)
d (calculated), mg/m^3	3.536	3.578	4.016
Temperature, K	298(2)	173(2)	101(2)
λ, Å	0.71073	0.71073	0.71073
μ, mm^{-1}	19.974	20.209	27.272
F(000)	816	3264	924
θ_{max}, deg	28.27	28.29	30.99
Total reflections	7444	21703	9968
Total unique reflections	1382	10294	1866
No. parameters	47	365	49
Refinement method	Full-matrix least-squares on F^2		
Final R indices [$I>2\sigma(I)$],			
R1[a]/wR2 [b] (%)	2.69/5.89	4.61/8.17	3.87/4.56
R indices (all data), R1/wR2	3.10/6.04	14.92/11.43	4.74/4.70
Goodness-of-fit on F^2	1.078	0.748	0.976
Absolute structure parameter	0.27(2)	0.25(1)	0.08(3)

[a] $R1 = \Sigma ||F_o| - |F_c|| / \Sigma |F_o|$. [b] $wR2 = \{\Sigma [w(F_o^2 - F_c^2)^2] / \Sigma [w(F_o^2)^2]\}^{1/2}$

Table 4-2. Atomic Coordinates ($\times 10^4$) and Equivalent Isotropic Parameters ($\times 10^3$ Å^2) for $K_2P_2Se_6$ at 298(2)K.

atom	*x*	*y*	*z*	*U*(eq)[a]
Se(1)	757(1)	2584(1)	2233(1)	27(1)
Se(2)	2769(1)	2649(1)	3957(1)	44(1)
Se(3)	4572(1)	2495(1)	801(1)	34(1)
K	5542(2)	2697(2)	2538(1)	49(1)
P	1285(2)	592(2)	548(1)	20(1)

[a] *U*(eq) is defined as one-third of the trace of the orthogonalized U_{ij} tensor.

Table 4-3. Atomic Coordinates ($\times 10^4$) and Equivalent Isotropic Parameters ($\times 10^3$ Å^2) for $K_2P_2Se_6$ at 173(2)K.

atom	*x*	*y*	*z*	*U*(eq)
Se(1)	3688(5)	9676(5)	645(4)	14(1)
Se(2)	6125(5)	2292(5)	332(4)	17(1)
Se(3)	6208(6)	9822(6)	147(4)	26(2)
Se(4)	1357(5)	4907(6)	2239(3)	20(1)
Se(5)	8603(6)	2651(5)	2076(4)	19(1)
Se(6)	9132(6)	5372(5)	1757(4)	21(2)
Se(7)	8756(5)	4608(5)	627(4)	14(1)
Se(8)	1483(5)	5153(6)	166(4)	29(2)
Se(9)	967(6)	7344(6)	324(4)	21(2)
Se(10)	6399(5)	5185(5)	2246(3)	19(1)
Se(11)	3824(6)	2740(5)	2041(4)	18(2)
Se(12)	4013(6)	5368(6)	1759(3)	17(1)
Se(13)	3654(5)	4607(5)	622(4)	14(1)
Se(14)	6081(6)	7255(5)	350(4)	17(1)
Se(15)	6201(5)	4810(5)	146(4)	22(2)
Se(16)	3598(6)	7670(5)	2049(4)	17(1)
Se(17)	6374(5)	9920(5)	2247(3)	18(1)
Se(18)	4164(6)	0437(5)	1775(4)	18(1)
Se(19)	8701(5)	9560(5)	639(4)	15(1)
Se(20)	925(6)	2310(6)	355(4)	22(2)
Se(21)	9879(6)	1305(5)	3494(4)	30(2)
Se(22)	1402(5)	0149(5)	2256(3)	19(1)
Se(23)	8845(6)	7708(5)	2070(4)	19(1)
Se(24)	8997(6)	0310(5)	1781(4)	17(1)
K(1)	6431(12)	7647(11)	2114(8)	26(3)
K(2)	1398(12)	2618(12)	2087(8)	30(4)
K(3)	1393(11)	7869(11)	2066(8)	28(3)
K(4)	8517(11)	7101(11)	339(7)	26(3)
K(5)	7876(12)	6401(11)	3684(7)	25(3)
K(6)	3789(11)	2345(10)	306(7)	19(3)
K(7)	6404(11)	2918(9)	2050(7)	28(3)
K(8)	3815(11)	7381(10)	314(7)	25(3)
P(1)	5302(13)	629(12)	79(9)	11(3)
P(2)	9693(13)	4295(13)	2324(9)	12(3)
P(3)	0372(12)	5712(13)	91(8)	13(3)
P(4)	4711(13)	4389(13)	2312(8)	12(3)
P(5)	5276(12)	5597(13)	86(9)	11(3)
P(6)	4701(12)	9309(11)	2316(8)	11(3)
P(7)	0319(13)	677(12)	105(9)	15(3)
P(8)	9724(12)	9355(12)	2344(8)	12(3)

[a] *U*(eq) is defined as one-third of the trace of the orthogonalized U_{ij} tensor.

Table 4-4. Atomic Coordinates ($\times 10^4$) and Equivalent Isotropic Parameters ($\times 10^3$ Å^2) for $Rb_2P_2Se_6$ at 101(2) K.

atom	*x*	*y*	*z*	*U*(eq)[a]
Rb	5848(1)	2708(1)	2479(1)	9(1)
Se(1)	857(1)	2488(1)	2207(1)	6(1)
Se(2)	3106(1)	2546(1)	3963(1)	10(1)
Se(3)	4272(2)	2035(1)	749(1)	7(1)
P	979(3)	238(3)	536(1)	5(1)

[a] *U*(eq) is defined as one-third of the trace of the orthogonalized U_{ij} tensor.

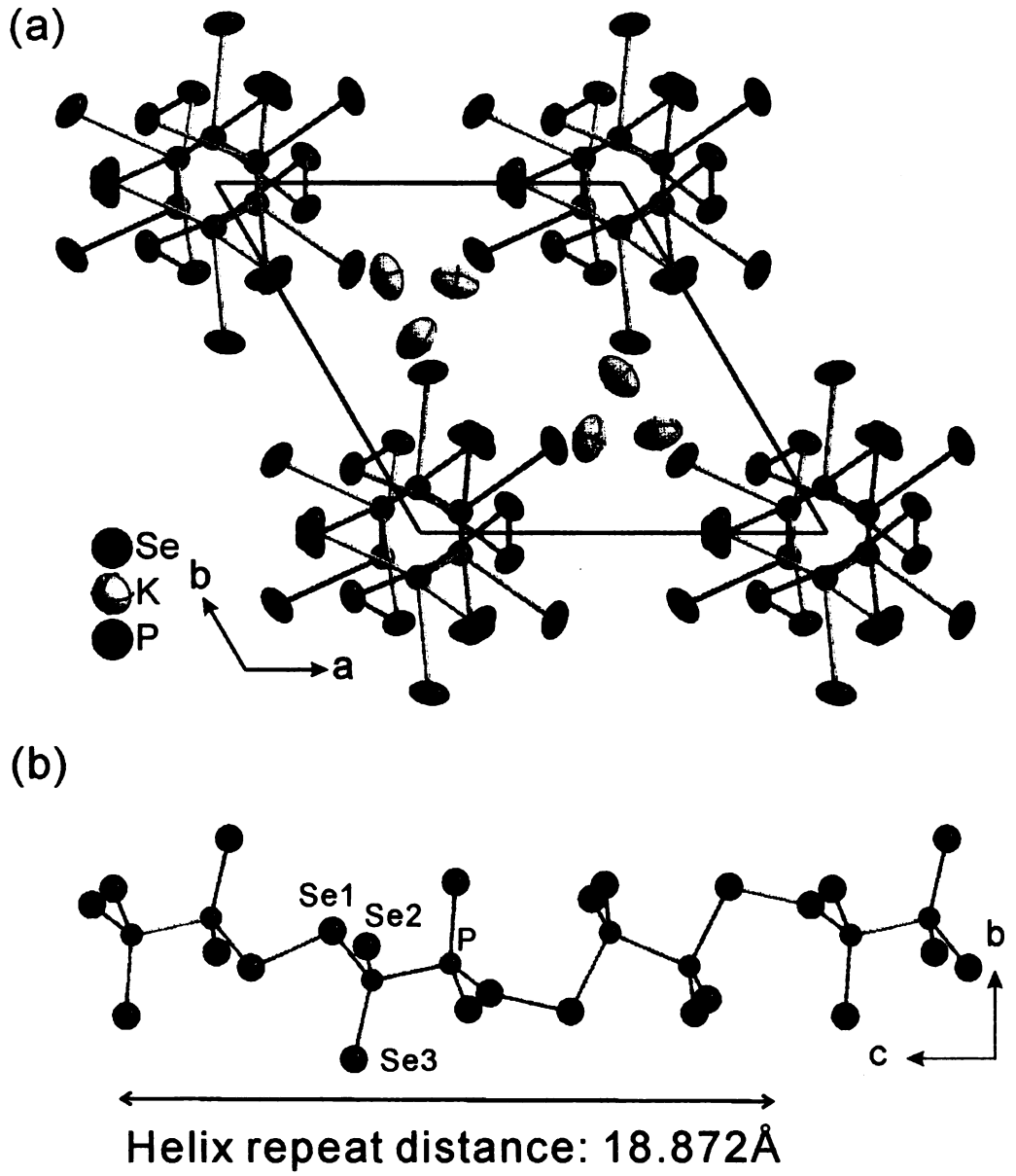

Figure 4-1. Structure of $K_2P_2Se_6$ at 298(2) K. (a) The unit cell viewed down the *c*-axis. The thermal ellipsoids with 30% probability are shown. (b) View of a $^1/_{\infty}[P_2Se_6^{2-}]$ chain looking down the *a*-axis. A helix forms by three $[P_2Se_6]$ units and repeats itself at every 18.872 Å.

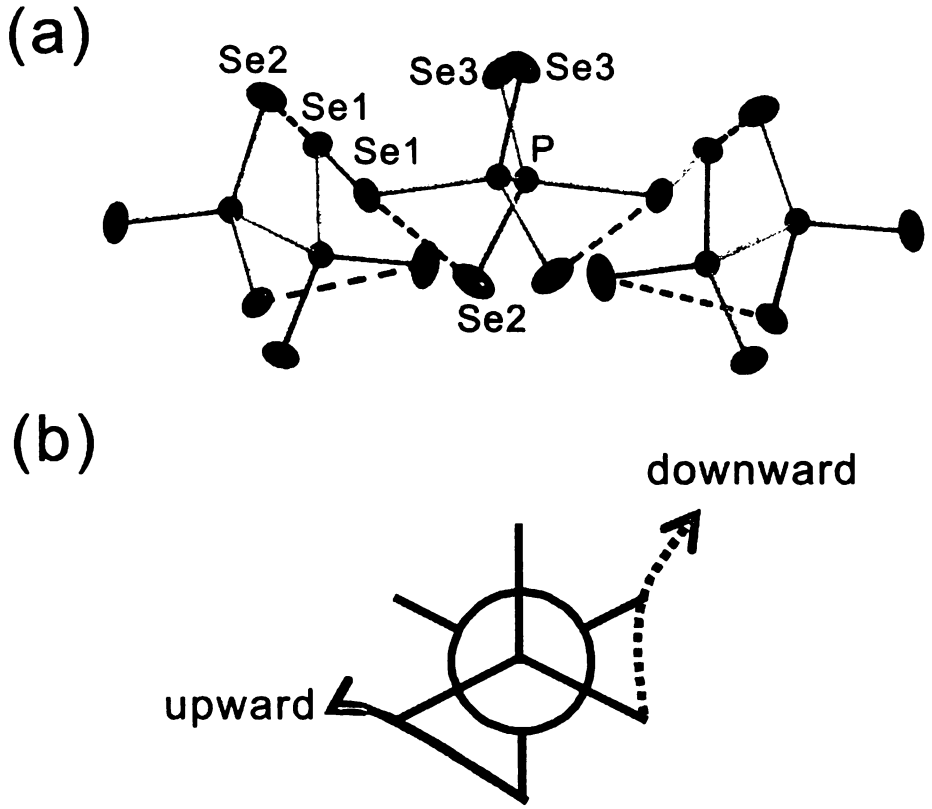

Figure 4-2. (a) Projection view of a $^{1}/_{\infty}[P_2Se_6^{2-}]$ chain slightly slanted in order to show the staggered *anti*-conformation of $[P_2Se_6]$. The role of short Se···Se nonbonding interactions (dashed line) along a helix segment is shown. Se(1)···Se(2), 3.559(1) Å. (b) Projection through P-P bonding showing the relationship between short Se···Se nonbonding interaction and chain propagation.

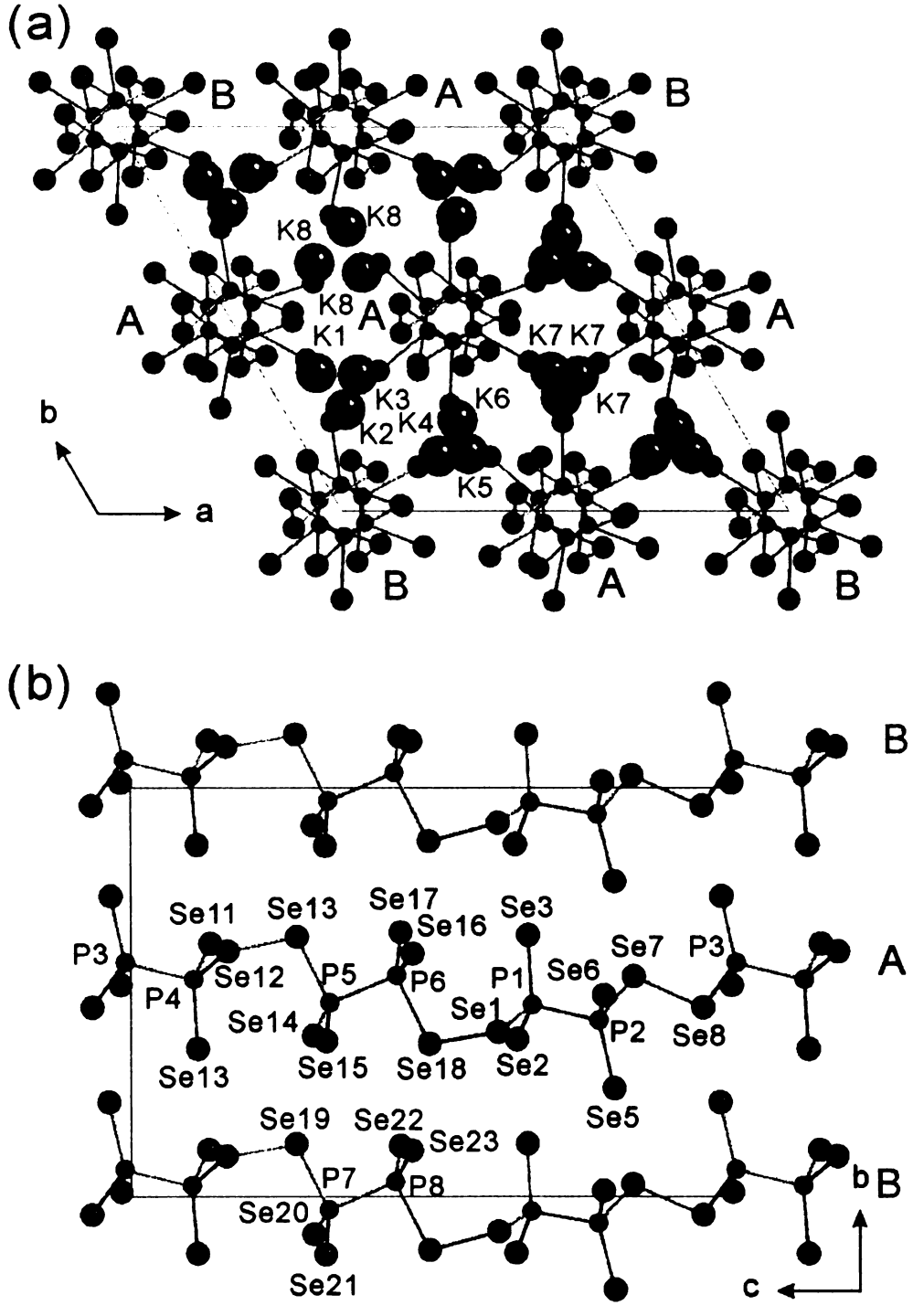

Figure 4-3. Structure of $K_2P_2Se_6$ at 173(2) K. (a) The unit cell viewed down the *c*-axis showing the superstructure. Crystallographically unique chains are differentiated as A and B. K atoms are labeled. (b) View of $^1/_\infty[P_2Se_6^{2-}]$ chains with labeling down the *a*-axis. K atoms are omitted for clarity.

4. Results and Discussion

Crystal Structure. Because at RT $K_2P_2Se_6$ and $Rb_2P_2Se_6$ are isostructural, the description that follows will be concentrated on the K salt. The structure has infinitely extended helical chains parallel to the *c*-axis, see Figure 4-1a. The chains are composed of ethane-like [P_2Se_6] repeat units that are linked via a terminal Se-Se linkages to give infinite helices of $^1/_\infty[P_2Se_6^{2-}]$, Figure 4-1b. The chirality of $K_2P_2Se_6$ is preserved in the crystal and at RT the compound adopts the chiral trigonal space group, $P3_121$. Helical features have been described in the quaternary thiophosphates $ANb_2P_2S_{12}$ (A = K, Rb, Cs)[16] and $A_{11}U_7(PS_4)_{13}$ (A = K, Rb)[17] but $K_2P_2Se_6$ is the first example to display an infinite helix structure of free standing chalcophosphate anions.

The unit cell contains a single crystallographically unique strand of the chain. Each helix runs with identical handedness along the *c*-axis. Because the helix is generated by a crystallographic 3_1 screw axis along the *c*-direction, each coil of the helix in the unit cell includes three P_2Se_6 units. There is a single crystallographic P site in the structure and pitch of the helix is 18.872(4) Å, corresponding to the unit cell repeat distance along the *c*-axis. The inter-spiral distance is equal to the *a*-lattice constant of the unit cell. Projected along its axis, a chiral 1D channel is seen with a cross-section diameter of ~1.17 Å. The P-P bond distance is normal at 2.242(2) Å. P-Se bond distances range from 2.126(1) to 2.329(1) Å comparable to known values. The P-Se-Se-P dihedral angle of 88.55(1)°, almost 90° causes a relatively short Se-Se bond distance of 2.337(1) Å compared to those in $KPSe_6$.[6] The ethane-like P_2Se_6 repeat unit adopts a local *anti*-conformation to minimize the steric hindrance around the P-P bond created by the helical geometry, Figure 4-2a. The unit is also distorted from the ideal geometry with the Se-P-

Se angles ranging from 111.88(6) to 117.95(6)°.

It is noteworthy to point out the unusually short Se···Se nonbonding interaction is observed at 3.559(1) Å for Se1···Se2, Figure 4-2a. This is shorter than the van der Waals radii sum of 3.80 Å and probably meaningful in stabilizing the crystal structure. Because the P_2Se_6 fragment is intrinsically centrosymmetric, the helical architecture results from the conformation of selenophosphate chain. In this regard, the short Se···Se contacts likely play a critical role in forming the coil by maximizing Se pπ orbital overlap through Se2···Se1-Se1···Se2 connections, Figure 4-2. To minimize the repulsion force between them, each [P_2Se_6] subunit rotates along the Se2···Se1-Se1···Se2 connection as an axis and consequently achieves the helical form. In fact, the Se3-P-P-Se3 torsion angle is severely compressed to only 36.23(1)°. Similarly short Se···Se interactions are well known in other chalcogenide systems. In $Rb_4P_6Se_{12}$[5] and $APSe_6$[6], for example, these interactions act to form pseudo one- or two-dimensional structures, respectively. The low-dimensional charge density wave compound $NbSe_3$[18] also has similar interactions.

Low Temperature Structure. We discovered that when cooled $K_2P_2Se_6$ undergoes a displacive phase transition to lower symmetry with no bond breaking at lower temperature. The $P3_121$ space group at room temperature was lowered to $P3_1$ at 173 K by losing two-fold symmetry perpendicular to *a*- and *b*-axes, Figure 4a. The new cell was enlarged to a $2a$ x $2b$ x c supercell. $P3_1$ is a maximal non-isomorphic subspace group of $P3_121$. As a result, the crystallographically unique K and P atoms and three independent Se atoms in $K_2P_2Se_6$ split to eight, eight and twenty four independent atoms, respectively. The resulting four helixes in the unit cell are differentiated

crystallographically in two groups as denoted by A and B in Figure 4-4a and 4-4b with a ratio of 3:1. It is noted that K7 and K8 still generate themselves by 3-fold screw axis surrounded by three identical strands of $^1/_\infty[P_2Se_6^{2-}]$ of type A. On the other hand, K1-K6 are crystallographically unique and generated by 3_1 screw and 2-fold rotation operation perpendicular to *a*- and *b*-axes. They are surrounded by two A and one B strands.

$Rb_2P_2Se_6$ did not show such a structural transition on cooling down to 100 K. The different behavior can be understood by the alkali metal size effect. The most notable change in going from the $P3_121$ to $P3_1$ for the K analog is found in the coordination environment of the K atoms. At room temperature K atoms are coordinated by six closely lying Se atoms whereas this expands to seven at low temperature, Figure 4-4. This is reminiscent of a pressure effect imposed on the structure as the unit cell contracts with falling temperature. Therefore the driving force for the transition seems to be the formation of the extra K···Se bonds. This effect seems to be absent in the Rb analog as the coordination environment of these atoms is already high at room temperature involving ten Se atoms. Tables 4-7 – 4-10 show a comparison of the K···Se and Rb···Se distances in the two structures for both room and low temperature.

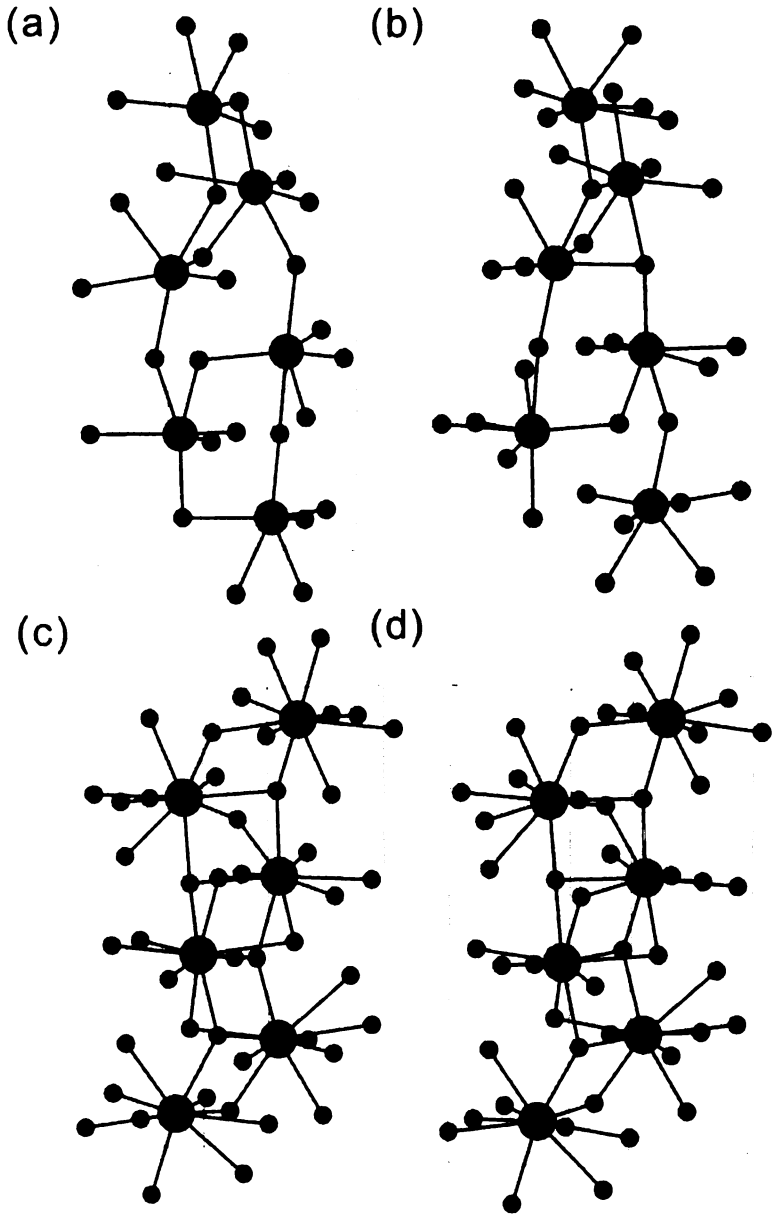

Figure 4-4. The coordination environment of K atoms in $K_2P_2Se_6$ is six at 298(2) K (a), and expands to seven at 173(2) K (b). The coordination environment of Rb atoms in $Rb_2P_2Se_6$ at (c) 298(2) K and (d) 100(2) K. It remains unchanged at both temperatures where Rb is coordinated to ten Se atoms. Large spheres are K or Rb atoms and small ones are Se atoms. P atoms are omitted for clarity.

Table 4-5. Selected Bond Distances (Å) and Angles (°) for $K_2P_2Se_6$ at 298(2) K.

P-P	2.242(2)
P-Se(1)	2.329(1)
P-Se(2)	2.131(2)
P-Se(3)	2.128(1)
Se(1)-Se(1)	2.337(1)
Se(1)-P-Se(2)	111.88(6)
Se(1)-P-Se(3)	112.29(6)
Se(2)-P-Se(3)	117.95(6)
P-Se(1)-Se(1)	100.55(4)
P-P-Se(1)	93.85(7)
P-P-Se(2)	111.42(4)
P-P-Se(3)	106.69(5)

Table 4-6. Selected Bond Distances (Å) and Angles (°) for $K_2P_2Se_6$ at 173(2) K.

P(1)-P(2)	2.227(17)	P(6)-Se(18)	2.363(17)
P(3)-P(4)	2.27(3)	P(7)-Se(19)	2.309(17)
P(5)-P(6)	2.236(18)	P(7)-Se(20)	2.125(17)
P(7)-P(8)	2.23(3)	P(7)-Se(21)	2.126(17)
P(1)-Se(1)	2.297(17)	P(8)-Se(22)	2.113(16)
P(1)-Se(2)	2.141(17)	P(8)-Se(23)	2.131(16)
P(1)-Se(3)	2.154(17)	P(8)-Se(24)	2.368(17)
P(2)-Se(4)	2.118(17)	Se(1)-Se(18)	2.334(13)
P(2)-Se(5)	2.151(17)	Se(6)-Se(7)	2.330(8)
P(2)-Se(6)	2.346(17)	Se(12)-Se(13)	2.342(7)
P(3)-Se(7)	2.305(17)	Se(19)-Se(24)	2.347(12)
P(3)-Se(8)	2.138(17)	Se(1)-P(1)-Se(2)	113.6(7)
P(3)-Se(9)	2.119(18)	Se(1)-P(1)-Se(3)	111.1(7)
P(4)-Se(10)	2.123(17)	Se(2)-P(1)-Se(3)	116.8(8)
P(4)-Se(11)	2.133(18)	Se(4)-P(2)-Se(5)	120.0(7)
P(4)-Se(12)	2.356(17)	Se(4)-P(2)-Se(6)	112.8(8)
P(5)-Se(13)	2.286(17)	Se(5)-P(2)-Se(6)	109.4(7)
P(5)-Se(14)	2.140(17)	Se(7)-P(3)-Se(8)	113.9(7)
P(5)-Se(15)	2.155(16)	Se(7)-P(3)-Se(9)	112.9(7)
P(6)-Se(16)	2.157(15)	Se(8)-P(3)-Se(9)	116.5(8)
P(6)-Se(17)	2.129(16)		

Table 4-7. K-Se distances in $K_2P_2Se_6$ at 173(2) K with standard deviation in parentheses. The maximum threshold for bond distances is 3.750Å. The coordination number of K atoms was determined to be seven.

K(1)-Se(17)	3.345(14)	K(3)-Se(22)	3.317(16)
K(1)-Se(14)	3.361(17)	K(3)-Se(3)#5	3.317(17)
K(1)-Se(8)#12	3.363(17)	K(3)-Se(9)	3.348(17)
K(1)-Se(20)#7	3.391(16)	K(3)-Se(16)	3.348(15)
K(1)-Se(23)	3.456(16)	K(3)-Se(14)#5	3.505(16)
K(1)-Se(12)#9	3.473(16)	K(3)-Se(6)	3.509(16)
K(1) Se(10)	3.554(14)	K(3)-Se(23)	3.582(15)
K(1)-Se(24)	3.842(17)	K(3)-Se(18)	3.915(16)
K(2)-Se(20)#2	3.310(17)	K(4) Se(23)	3.341(14)
K(2)-Se(4)#3	3.360(16)	K(4)-Se(22)#4	3.345(14)
K(2)-Se(11)	3.433(17)	K(4) Se(15)	3.359(15)
K(2)-Se(9)#5	3.393(17)	K(4) Se(9)	3.388(15)
K(2)-Se(21)	3.358(17)	K(4) Se(19)	3.483(15)
K(2)-Se(22)	3.595(16)	K(4)-Se(11)#4	3.509(16)
K(2)-Se(24)	3.462(16)	K(4) Se(14)	3.646(15)
K(2)-Se(12)	3.940(16)	K(4)-Se(7)	3.836(15)

Table 4.7. (Cont'd) K-Se distances in $K_2P_2Se_6$ at 173(2) K with standard deviation in parentheses. The maximum threshold for bond distances is 3.750Å. The coordination number of K atoms was determined to be seven.

K(5)-Se(5)#5	3.321(15)	K(7)-Se(10)	3.309(14)
K(5)-Se(10)	3.351(15)	K(7)-Se(2)#6	3.325(15)
K(5)-Se(20)#7	3.352(15)	K(7)-Se(15)#12	3.363(15)
K(5)-Se(3)#5	3.367(15)	K(7)-Se(5)#6	3.398(15)
K(5)-Se(23)	3.481(15)	K(7)-Se(2)#5	3.470(15)
K(5)-Se(7)#12	3.484(15)	K(7)-Se(18)#9	3.473(14)
K(5)-Se(2)#5	3.606(15)	K(7)-Se(11)#9	3.616(15)
K(5)-Se(19)#5	3.888(16)	K(7)-Se(6)	3.811(14)
K(6)-Se(11)#9	3.307(15)	K(8)-Se(8)#10	3.318(14)
K(6)-Se(17)#11	3.329(16)	K(8)-Se(16)#10	3.325(14)
K(6)-Se(21)#11	3.339(15)	K(8)-Se(4)#4	3.346(14)
K(6)-Se(5)#11	3.344(15)	K(8)-Se(14)	3.380(15)
K(6)-Se(2)#6	3.423(16)	K(8)-Se(16)#4	3.420(15)
K(6)-Se(13)	3.433(15)	K(8)-Se(1)#10	3.478(14)
K(6)-Se(15)	3.547(14)	K(8)-Se(3)	3.518(15)
K(6)-Se(1)#9	3.849(15)		

Symmetry transformations used to generate equivalent atoms:

#1 x+1, y, z #2 x+1, y+1, z #3 x, y+1, z #4 -x+y+1, -x+2, z-1/3

#5 -y+2, x-y+1, z+1/3 #6 x, y-1, z #7 -y+1, x-y+1, z+1/3

#8 -x+y+1, -x+1, z-1/3 #9 x-1, y-1, z #10 x-1, y, z

#11 -x+y, -x+1, z-1/3 #12 -y+1, x-y, z+1/3

Table 4-8. K-Se distances in $K_2P_2Se_6$ at 273(2) K with standard deviation in parentheses. The maximum threshold for bond distances is 3.750 Å. The coordination number of K atoms was determined to be six.

K-Se(2)	3.3367(18)
K-Se(3)#6	3.3388(18)
K-Se(3)#2	3.3695(19)
K-Se(2)#4	3.4263(18)
K-Se(2)#7	3.4537(17)
K-Se(1)#1	3.4834(17)
K-Se(2)#2	3.8395(19)
K-Se(1)#4	3.8731(18)
K-Se(3)#1	3.9244(19)

Symmetry transformations used to generate equivalent atoms:

#1 $-x, -x+y, -z+1/3$ #2 $-x-1, -x+y-1, -z+1/3$ #3 $-x+y-2, -x, z-1/3$

#4 $-x-1, -x+y, -z+1/3$ #5 $-x+y-1, -x+1, z-1/3$ #6 $-y+1, x-y+2, z+1/3$

#7 $-y, x-y+2, z+1/3$ #8 $x-y+1, -y+2, -z+2/3$ #9 $y-1, x+1, -z$

Table 4-9. Rb-Se distances in $Rb_2P_2Se_6$ at 100 (2) K with standard deviation in parentheses. The maximum threshold for bond distances is 4.000 Å. Rb-Se distance was not found up to 4.500 Å over the threshold. The coordination number of Rb atoms was determined to be ten.

Rb-Se(3)	3.4778(12)
Rb-Se(2)	3.5715(13)
Rb-Se(1)	3.6011(13)
Rb-Se(3)#1	3.4248(12)
Rb-Se(2)#4	3.4357(11)
Rb-Se(2)#7	3.5101(12)
Rb-Se(2)#10	3.7393(13)
Rb-Se(2)#8	3.7754(13)
Rb-Se(1)#5	3.8599(12)
Rb-Se(3)#1	3.8706(13)

Symmetry transformations used to generate equivalent atoms:

#1 $-x+1, -x+y, -z+1/3$ #2 $y, x-1, -z$ #3 $-x+2, -x+y+1, -z+1/3$

#4 $x-1, y-1, z$ #5 $x, y+1, z$ #6 $y+1, x, -z$ #7 $x+1, y, z$

#8 $y+1, x-1, -z$ #9 $x, y-1, z$ #10 $x+1, y+1, z$ #11 $x-1, y, z$

#12 $-x+1, -x+y+1, -z+1/3$

Table 4-10. Rb-Se distances in $Rb_2P_2Se_6$ at 298(2) K with standard deviation in parentheses. The maximum threshold for bond distances is 4.000 Å. Rb-Se distance was not found up to 4.500 Å over the threshold. The coordination number of Rb atoms was determined to be ten.

Rb-Se(3)	3.4714(23)
Rb-Se(2)	3.4735(25)
Rb-Se(3)#11	3.5172(22)
Rb-Se(2)#9	3.5481(23)
Rb-Se(2)#5	3.6271(23)
Rb-Se(1)	3.6545(22)
Rb-Se(2)#6	3.7805(23)
Rb-Se(1)#7	3.8185(22)
Rb-Se(1)#5	3.9055(21)
Rb-Se(3)#3	3.9302(23)

Symmetry transformations used to generate equivalent atoms:

#1 $-x+1, -x+y, -z+1/3$ #2 $y, x-1, -z$ #3 $-x+2, -x+y+1, -z+1/3$

#4 $x-1, y-1, z$ #5 $x, y+1, z$ #6 $y+1, x, -z$ #7 $x+1, y, z$

#8 $y+1, x-1, -z$ #9 $x, y-1, z$ #10 $x+1, y+1, z$ #11 $x-1, y, z$

#12 $-x+1, -x+y+1, -z+1/3$

Synthesis, Reaction Chemistry and Characterization. The alkali metal chalcophosphate ternary system is highly attractive as a model system to probe how flux conditions influence the synthetic outcome and the structure of a resulting compound.[5] A reaction medium forms by simple *in situ* fusion of A_2Q/P_2Q_5 or P/Q and this flux is conceptually defined as $A_xP_yQ_z$. The basicity of the flux is determined by the A:P:Q ratio. Higher A:P ratios impart stronger basicity to the flux. Lower A:Q ratios produce lower basicity, etc. Alternatively, for the same A:P ratio the basicity can be increased in going from the smaller to the larger alkali atoms. Therefore both the A : P ratio and the nature of the A atoms could be conveniently used as a key reaction parameter to control the formation of a product from being a simple molecular species, to being a more complex discrete or extended structure. For example to obtain the classical molecular salts A_3PSe_4 and $A_4P_2Se_6$ (A = alkali metal), high ratios of $A_2Se:P_2Se_5$ (>2:1) are required.

The polymeric $K_2P_2Se_6$ is realized under less basic conditions, namely with $K_2Se:P_2Se_5$ = 1:1, than the typical ternary alkali selenophosphates with molecular structures. In fact, less basic conditions or lower flux temperatures tend to generate longer or extended fragments.[19] This could explain why more basic Rb or Cs analogues to $K_2P_2Se_6$ could not be obtained from identical reaction conditions. The slightly higher basic character of Rb and Cs changes the reaction path to a more oxidized chalcophosphates (i.e. the P^{5+} species $RbPSe_6$ and $CsPSe_6$). $Rb_2P_2Se_6$ could be obtained however by adjusting/correcting the flux basicity by adding 0.4 mole of P to the $Rb_2Se:P_2Se_5$ = 1:1 ratio. This prevents the oxidation for P from 4+ to 5+. Thus it would appear that extended structural motifs for chalcophosphates are more likely to be

produced by weak basic fluxes with smaller less Lewis basic alkali metals such as potassium, sodium and lithium.

Conceptually, $^1/_\infty[P_2Se_6^{2-}]$ can be regarded as deriving from oxidative polymerization of the $[P_2Se_6]^{4-}$ anion, see Eq (1). Although it was not synthesized in this fashion, we speculate that an actual oxidation in solution, with e.g. I_2 as the oxidant, may in fact be successful if run under proper conditions.

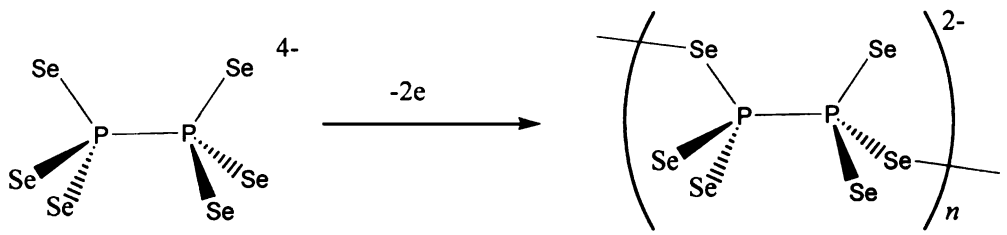

Eq. (1)

The polymeric chain is stabilized with no help of coordinating to a metal and represents a rare chalcophosphate anion. The only other example which is stabilized by alkali cations is $^1/_\infty[PSe_6^-]$.[6] The latter has PSe_4 tetrahedra condensed with diselenide (Se_2^{2-}) groups.

Finally, the existence of a single crystallographic P site in the RT structure of $K_2P_2Se_6$ is supported by solid state ^{31}P NMR spectroscopy. Under MAS at RT, crystalline $K_2P_2Se_6$ gave a single isotropic chemical shift (CS) at 54.6 ppm, Figure 4-5. The result supports the crystal structure of $K_2P_2Se_6$ at room temperature which indicates only one crystallographically unique P atom. The chemical shift value is close to that of $A_2CdP_2Se_6$ (A = K, Rb) and $K_2Cu_2P_4Se_{10}$, all of which include the P_2Se_6-type ligand.[20]

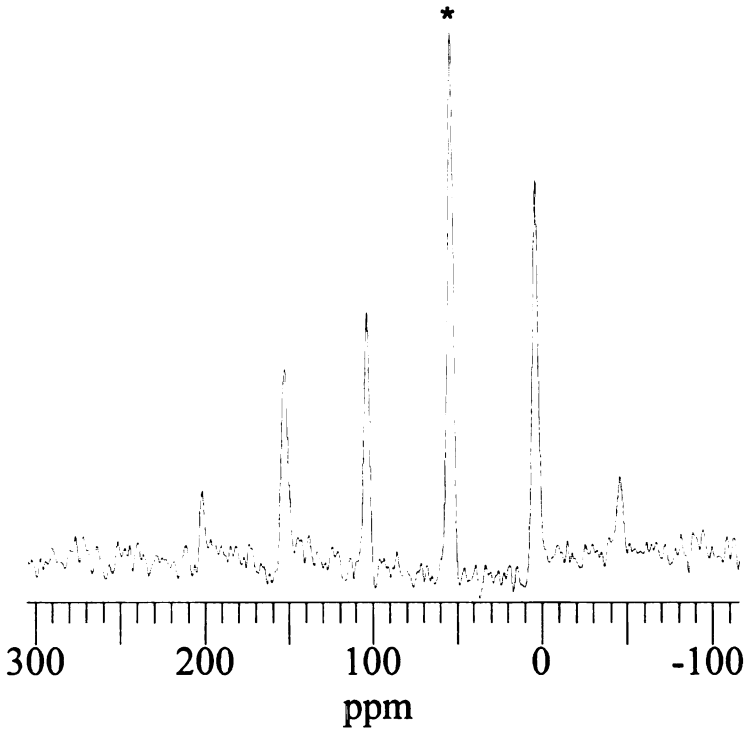

Figure 4-5. Solid state ^{31}P MAS NMR spectrum of crystalline $K_2P_2Se_6$ at room temperature. The asterisk (*) indicates the isotropic peak.

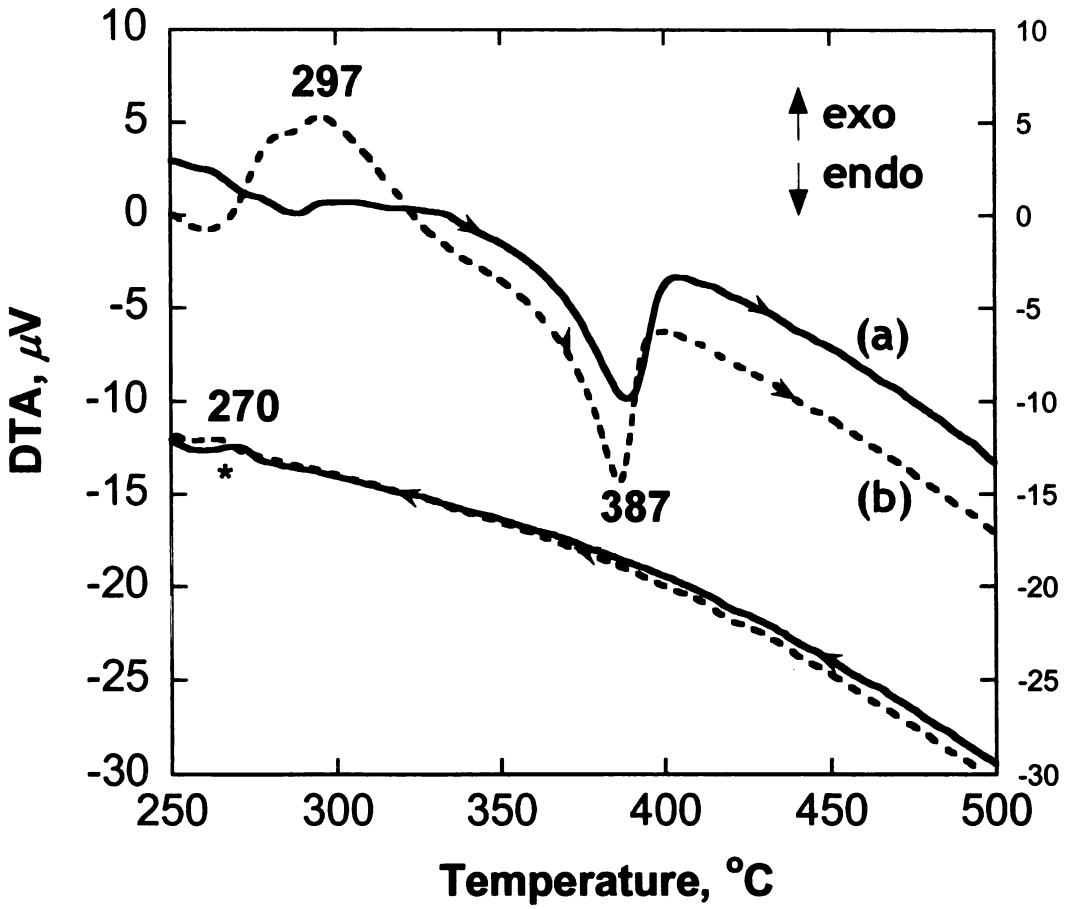

Figure 4-6. Differential thermal analysis diagram of a sample of $K_2P_2Se_6$. (a) Heating curve showing melting at 387 °C in the first heating cycle (solid line) with no crystallization upon cooling. (b) Exothermic crystallization followed by melting upon heating in the second cycle (dotted line). Asterisk indicates the vitrification event upon cooling.

Glass Formation, Phase-change Behavior and Local Structure. Both title compounds described here exhibit reversible phase change behavior. Differential thermal analysis of $K_2P_2Se_6$ performed at a rate of 10 °C min^{-1} indicates that the compound melts congruently at 387 °C, Figure 4-6. Upon cooling it forms a dark red glass at 270 °C. Crystallization is only observed on heating where the glass recrystallizes exothermically at 297 °C. The vitrification is observed again on cooling the melt to room temperature. The powder X-ray diffraction patterns (PXRD) of the pristine and recrystallized sample from DTA were identical confirming the structure recovering ability of this material.

The thermal behavior of $Rb_2P_2Se_6$ is different from that of $K_2P_2Se_6$. The DTA carried out at a rate of 10°C/min revealed the melting at 364 °C on heating and gave a dark red glass at 255 °C on cooling during a first cycle. On a second cycle, no crystallization was observed as the glass could not recover the crystal structure. The melting was observed again at 369 °C followed by vitrification at 255°C on cooling. The PXRD confirmed the amorphous nature of the glassy sample after the first and second cycles. The amorphous sample recrystallized to pristine structure only when the heating rate was lowered to less than 5°C/min. The DTA performed at a rate of 5 °C min^{-1} showed melting at 366 °C on heating and subsequent crystallization at 305 °C on cooling. The PXRD of pristine and the sample obtained after each cycle matched perfectly. These results are consistent with a greater glass forming ability of the Rb^+-salt compared to the K^+-salt. This is in agreement with a similar trend identified recently in the series $K_{1-x}Rb_xSb_5S_8$.[21c]

The solid-state optical absorption UV-vis spectra of crystalline and glassy $A_2P_2Se_6$ show sharp absorption edges, Figure 4-7. The band gap of crystalline and glassy

phases was measured at 2.08 and 1.97 eV for K^+ salt and 2.32 and 2.10 eV for Rb^+ salt, respectively. The energy gaps are consistent with dark orange/dark red color for K+ salt and orange/dark orange color for Rb^+ salt, respectively. A red shift in absorption edge in the glassy phases is a common phenomenon as glass formation generally induces substantial defects and mid-gap states to give a lower band gap than the crystalline counterpart.[22] This creates optical contrast and can be a useful feature for optical storage systems based on phase-change materials.[23]

The results of Raman spectroscopy and PDF analysis (see below) shed light on the local structure in the glass and how these materials can readily recover their crystal structure from the amorphous state. The Raman spectrum of crystalline $K_2P_2Se_6$ at room temperature shows shifts at 154(bw), 221(s), 236(m), 259(m), 388(w), 496(w), 514(vw) cm^{-1}, Figure 4-8. The shift at 221 cm^{-1} is unambiguously assigned to the P_2Se_6 stretching mode by comparison in the A_g stretching mode of D_{3d} symmetry of $[P_2Se_6]^{4-}$ ligand.[24] Other peaks at 154, 496 and 514 cm^{-1} are also related with the P_2Se_6 fragment.[25] By analogy, shifts at 236 and 259 cm^{-1} can be assigned to antisymmetric and symmetric Se-Se stretching vibration modes of the diselenide group, respectively.[26]

The Raman spectrum of glassy $K_2P_2Se_6$ shows broader and weaker peaks at 162 (bw), 218 (bm) and 258 (bw) are observed whereas the overall peak pattern is similar to that of the crystals. This suggests that the $[P_2Se_6]$ unit and Se-Se bonds are still intact and the local structural motifs are largely preserved in the glass but crystallographic long-range order is lost. This situation makes it easy to restore the crystal structure from the amorphous state for the reversible crystal-glass phase transition.

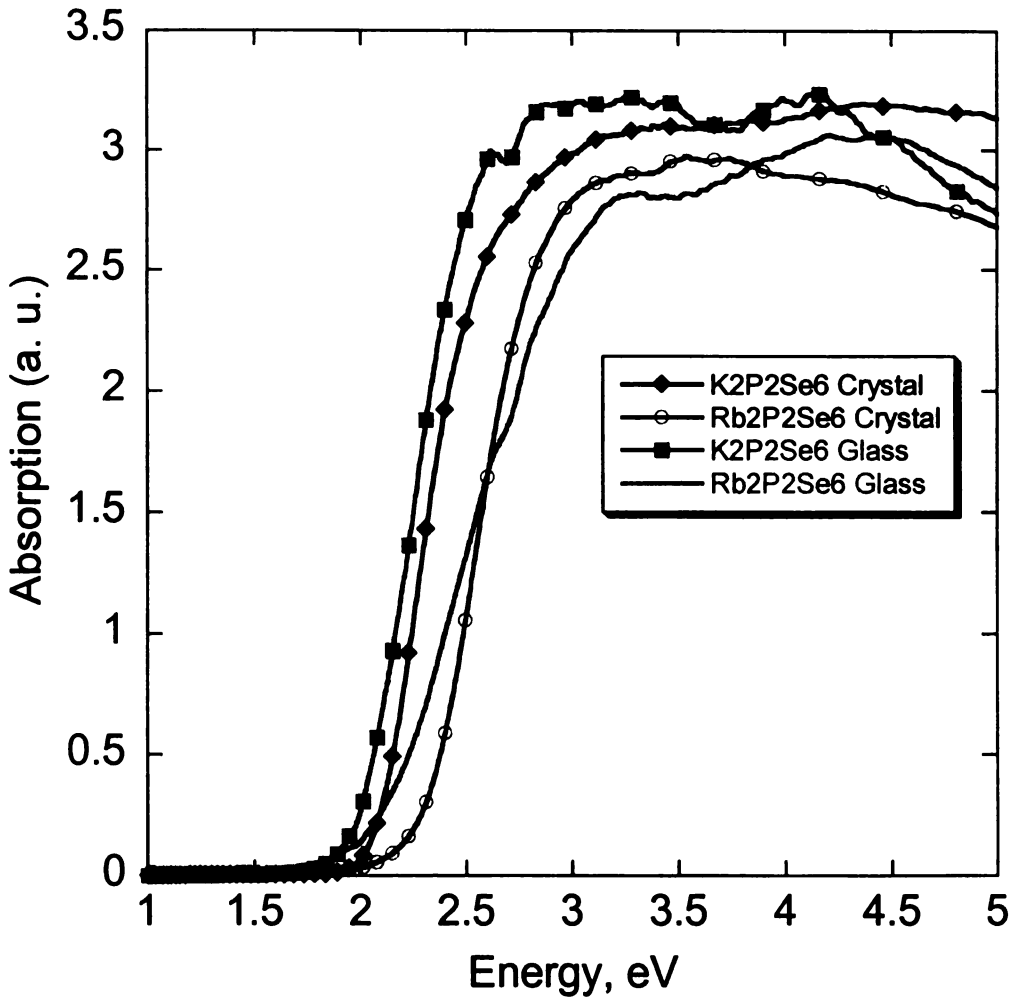

Figure 4-7. Solid state UV-vis optical absorption spectra of crystalline and glassy $K_2P_2Se_6$ and $Rb_2P_2Se_6$ showing the red shift in absorption edge in the glass samples. The band gaps are 2.09, 1.98 eV, for the K and 2.32 and 2.10 eV for Rb analogs respectively.

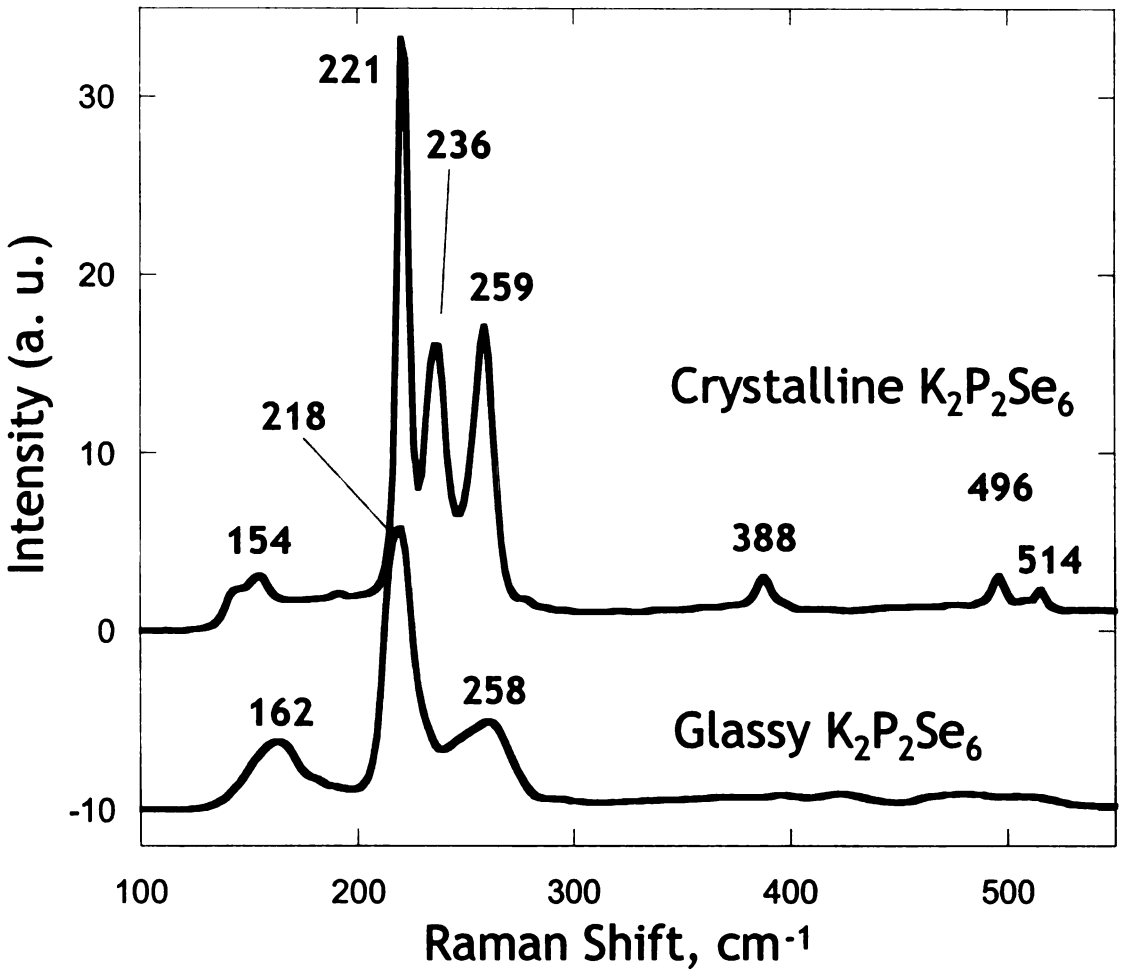

Figure 4-8. Raman spectra of crystalline (upper line) and glassy (lower line) $K_2P_2Se_6$ at room temperature. The similar but broader features in the spectrum of the glass suggest the local structure is preserved but long range order is lost.

To probe the local structure of both the glassy and crystalline forms of $K_2P_2Se_6$ we performed pair distribution function (PDF) analysis. This technique is emerging as a useful tool for the analysis of the local structure of crystalline and non-crystalline compounds.[27] The PDFs are shown in Figure 4-9. Also shown in the middle profile is the calculated PDF based on the room temperature single crystal structure model of $K_2P_2Se_6$. There appears to be good agreement between the crystal structure model and the experimentally determined PDF of $K_2P_2Se_6$. This in fact validates the correctness of the crystal structure.

The PDF of the glass shows well defined correlations up to ~8 Å with the first two at 2.2 and 3.6 Å being very similar to those of the crystalline form. The interatomic correlations in the structure disappear above ~8 Å indicating the lack of long range order periodicity. The first strong correlation at 2.2 Å is assigned to Se-Se, P-Se and P-P bonds in the structure. The second strong peak at 3.6 Å is assigned to K···Se and second neighbor Se···Se distances. The PDF data suggest that the crystalline and glassy forms of $K_2P_2Se_6$ are structurally similar which implies that the $[P_2Se_6]$ units remain intact in the glass form. This is also in agreement with the Raman spectroscopic data discussed above. The close structural relationship between crystal and glass, coupled with the stoichiometric nature of the composition, accounts for the facile congruent crystallization of the glass. Similar conclusions were reached from the PDF analysis of KSb_5S_8, another interesting phase-change material, which shows that its local structure within a radius of ~5 Å in the glass phase is clearly refined even though long range order is not observed.[21]

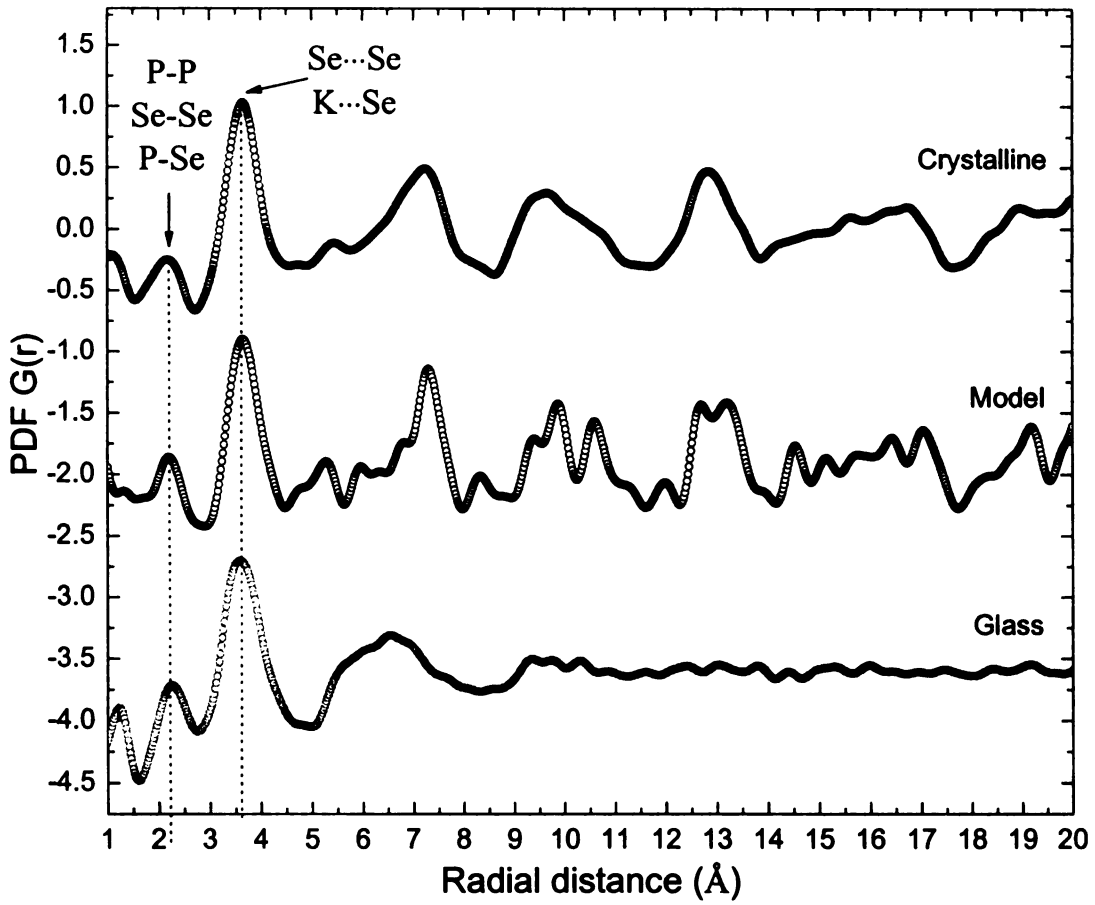

Figure 4-9. Pair distribution function G(r) of the crystalline and glassy $K_2P_2Se_6$. The calculated PDF based on the room temperature single crystal structure model of $K_2P_2Se_6$ is presented for comparison.

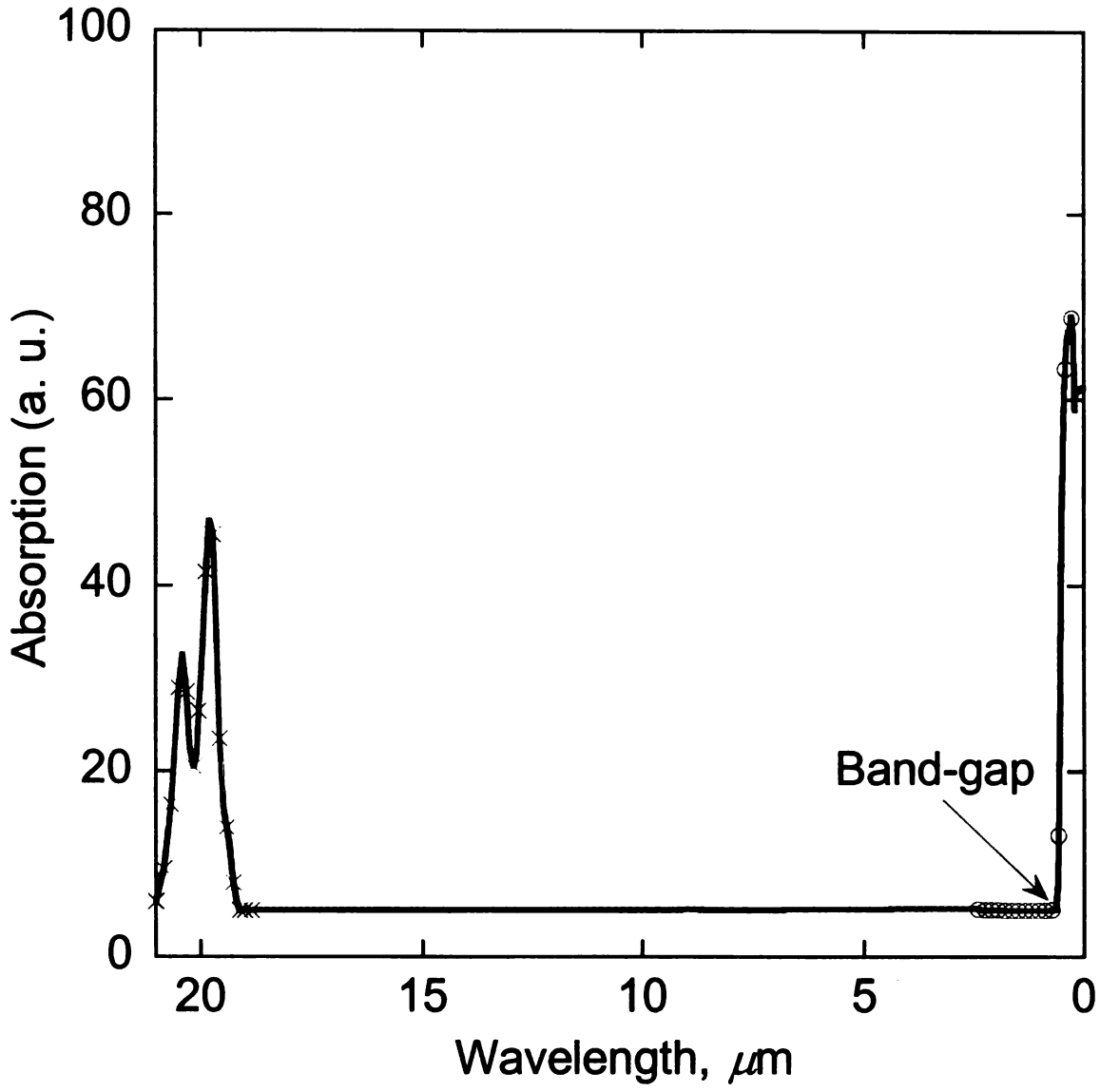

Figure 4-10. Far-IR (line with X)/mid IR (simple line)/visible (line with o) absorption spectra of crystalline $K_2P_2Se_6$. Wide transparent range of crystalline $K_2P_2Se_6$ above the absorption band at 19.8 μm at far-IR region through mid-IR to 0.596 μm at visible region is shown.

Infrared Transmission and Nonlinear Optical Properties. Materials with large NLO susceptibilities for IR application are highly sought. $AgGaQ_2$ (Q = S, Se), $ZnGeP_2$ and GaSe are main infrared materials[28] and we recently introduced the promising long wave IR NLO compound β-$K_2Hg_3Ge_2S_8$.[29] The chalcophosphates are an attractive class in which to search for new NLO materials in that basic building units of $[PQ_4]^{3-}$ or $[P_2Q_6]^{4-}$ frequently form noncentrosymmetric arrangements by coordination to central metals or polychalcogenide fragments $[Q_n]^{2-}$. Examples include $APSe_6$ (A=K, Rb),[5] $ANb_2P_2S_{12}$ (A=K, Rb, Cs),[16] $A_{11}U_7(PS_4)_{13}$ (A=K, Rb),[17] $Cs_2CuP_3S_9$,[30] $Na_{0.5}Pb_{1.75}PS_4$[31] and $A_3AuP_2Se_8$ (A=K, Rb, Cs).[32] In addition, chalcogenide compounds demonstrate better polarizability than oxide compounds, which have been predominantly studied for NLO application and wide IR transmission.

$K_2P_2Se_6$ exhibits wide optical transparency ranging from long wave IR (LWIR) to near IR (NIR)/visible light, Figure 4-10. The mid-IR transmittance spectrum showed little absorption from 505 cm^{-1} (19.8 μm) to 4000 cm^{-1} (2 μm). There is no light absorption below the band gap transition suggesting uninterrupted light transmission in the compound. The optical transparency extends over to its absorption edge of 2.08 eV (596 nm) in the visible region. Above 19.8μm in the far-IR region, the compound exhibited a complex set of absorptions, consistent with its Raman and far-IR spectra. Optical transparency is a key feature for materials aimed at NLO applications. For example, the important NLO material for IR applications, $AgGaSe_2$,[28] shows LWIR transmission up to 17 μm.

The polar, noncentrosymmetric helical chain structure of $^1/_\infty[P_2Se_6^{2-}]$ composed of easily polarizable P and Se atoms linked by covalent bonding can produce large optical

nonlinearity. SHG measurements were performed using a modified Kurtz powder method[33] with an IR light source ranging from 1000 nm to 2000 nm. SHG intensities of crystalline $K_2P_2Se_6$ were directly compared with that of $AgGaSe_2$ powder. All samples were prepared in a similar fashion and the same particle size range of 45.5±7.5 μm was measured and compared. Crystalline $K_2P_2Se_6$ generated strong double frequency signals from the fundamental idler beam. The SHG intensity of $K_2P_2Se_6$ showed a maximum at 789 nm which is ~50 times larger than that of in the same wavelength. Under the same experimental conditions $AgGaSe_2$ showed a SHG maximum at 890 nm and in this wavelength the corresponding response of $K_2P_2Se_6$ was 20-fold higher. At shorter wavelengths the $K_2P_2Se_6$ outperforms the chalcopyrite material by over 100 fold, Figure 4-11a. These results demonstrate that the crystalline $K_2P_2Se_6$ is very promising in IR NLO application. For comparison, the absolute nonlinear optical susceptibility at 2.12μm of $AgGaSe_2$ and $LiNbO_3$ is 67.7±13 and 29.1±5.2 pm V^{-1}, respectively.[34]

The SHG intensity of the crystalline phase increased with the particle size and reached a plateau, Figure 4-11b. In principle, phase-matchable samples reach maximum intensity and then for larger average particle sizes the intensity is size-independent because of the existence of a phase-matching direction in the sample.[33] In this regard, crystalline $K_2P_2Se_6$ is type I phase-matchable and eminently suitable for consideration in applications.

These results suggest that $K_2P_2Se_6$ is of special interest for the middle and deep infrared (IR) applications due to its large nonlinear optical coefficients and high transmission in the IR region. The phase matching and transmission characteristics of $K_2P_2Se_6$ should allow 3-wave interactions in the mid and near IR, particularly for optical

parametric oscillator (OPO) devices pumped with Nd:YAG laser, frequency mixing of OPO outputs pumped by Ti:Sapphire or Nd:YAG laser, as well as frequency mixing Nd:YAG laser with dye and Ti:Sapphire or other laser sources. $K_2P_2Se_6$ is also promising as an efficient frequency doubling crystal for infrared radiation such as 10.6 μm output of CO_2 lasers.

Second Harmonic Generation Response of Glassy $K_2P_2Se_6$. Surprisingly, the glassy $K_2P_2Se_6$ powder exhibited SHG response and its intensity is 38 % that of $AgGaSe_2$. Because of great optical transparency and potential formability, there have been tremendous efforts to induce SHG in glasses[35] for use in optical fibers in telecommunications. The observation of significant NLO activity in $K_2P_2Se_6$ glass could be a rare example of this property found in an amorphous material with no specific treatment such as thermal poling, electron beam irradiation and so on.[36] Since $K_2P_2Se_6$ is a phase-change material and retains its local structural motif in the glassy phase, we expect the noncentrosymmetric arrangement to be partially preserved and consequently to exhibit some SHG response. Indeed, the SHG response of the $K_2P_2Se_6$ glass started to be observed at longer wavelength than that of the crystal. This suggests that the SHG signal was generated from the glass of which the bad-gap is red-shifted relative to the crystal, and probably did not originate from traces of the recrystallized phase embedded in the glass matrix. X-ray powder diffraction patterns after the SHG measurements did not show evidence of crystallization. It cannot be completely ruled out, however, that idler beam-induced crystallization of glass may be occurring. Additional work will be necessary to better understand the NLO properties of the glass.

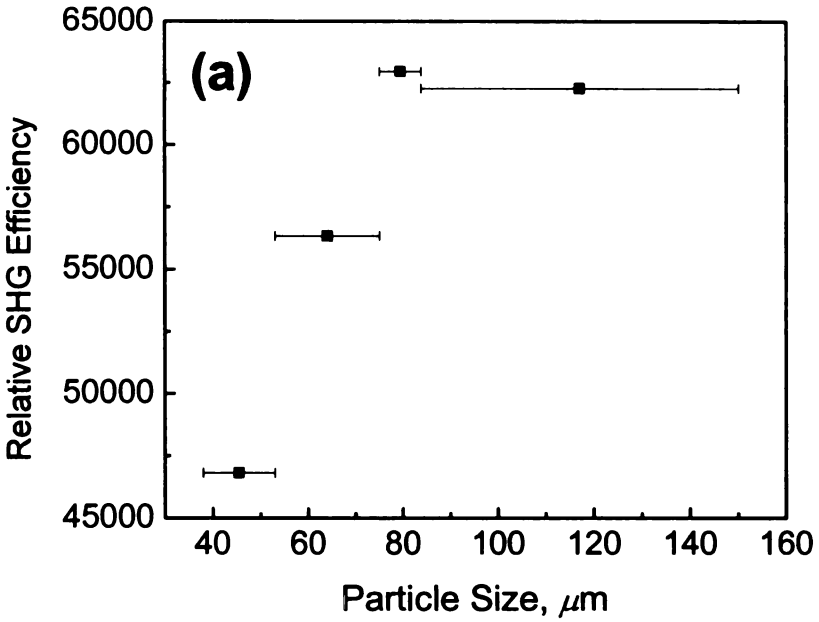

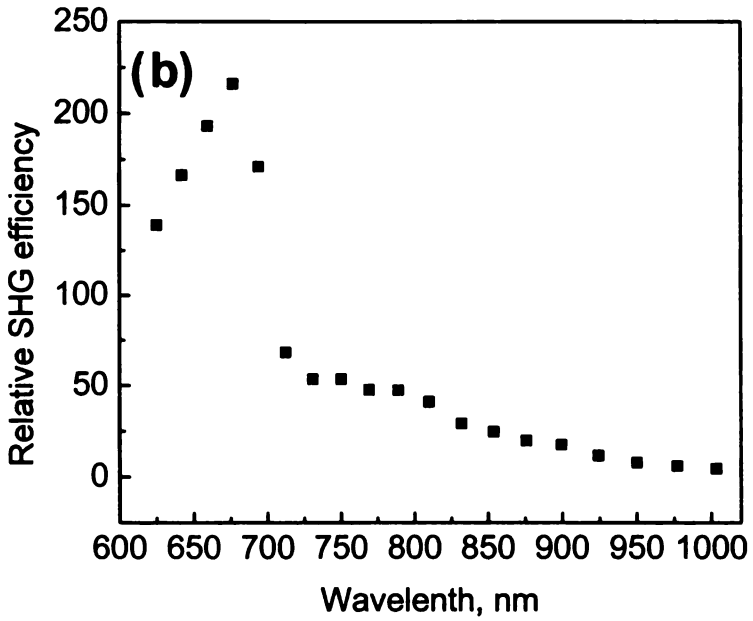

Figure 4-11. (a) Particle size to SHG intensities diagram of crystalline $K_2P_2Se_6$ showing type-I phase-matching. (b) SHG response of $K_2P_2Se_6$ relative to $AgGaSe_2$ over a wide range of wavelengths.

4.7. Thermal properties of $K_2P_2Se_6$. The thermal properties such as thermal expansion, are important properties relevant to crystal growing for NLO applications. The thermal expansion of $K_2P_2Se_6$ crystal was determined by a single crystal X-ray diffraction study in the range of 100 – 400 K, Figure 4-12. The linear (Eg. 4-2) and thermal expansion coefficients (Eg. 4-3) are defined as

$$\alpha_t = \frac{1}{L_t}\frac{dL_t}{dT} \quad \text{Eg. (2)}$$

$$\beta = \frac{1}{V}\frac{\mathrm{d}V}{\mathrm{d}T} \quad \text{Eg. (3)}$$

where L_t is the unit cell dimension along t-axis and V is the unit cell volume. Because $K_2P_2Se_6$ exhibited $2a \times 2b \times c$ supercell, a-axis distance was divided by 2 for the calculation. The thermal expansion coefficients of $K_2P_2Se_6$ were calculated to be α_a = 1.46×10^{-5} K^{-1} and α_c = 2.41 $x10^{-5}$ K^{-1}, indicating somewhat isotropic expansion. By comparison corresponding values for other relevant infrared NLO materials such as $AgGaSe_2$ ($\alpha_{\parallel c}$ = -0.81×10^{-5} K^{-1}, $\alpha_{\perp c}$ = 1.98×10^{-5} K^{-1}, 298-423 K),[37] $AgGaS_2$ ($\alpha_{\parallel c}$ = -1.32×10^{-5} K^{-1}, $\alpha_{\perp c}$ = 1.27 x 10^{-5}/K, 298-523 K)[38] and $ZnGeP_2$ ($\alpha_{\parallel c}$ = 1.59×10^{-5} K^{-1}, $\alpha_{\perp c}$ = 1.75×10^{-5} K^{-1}, 293-573 K).[39] The α of stainless steel is 1.73×10^{-5} K^{-1} at 293 K. Most importantly, $K_2P_2Se_6$ does not exhibit the anomalous behavior of $AgGaQ_2$ (Q = S, Se) which contracts along the a- and b-axes and expands along the c-direction. The latter is an anomaly which can cause thermomechanical stress in high-power applications and failure.[40]

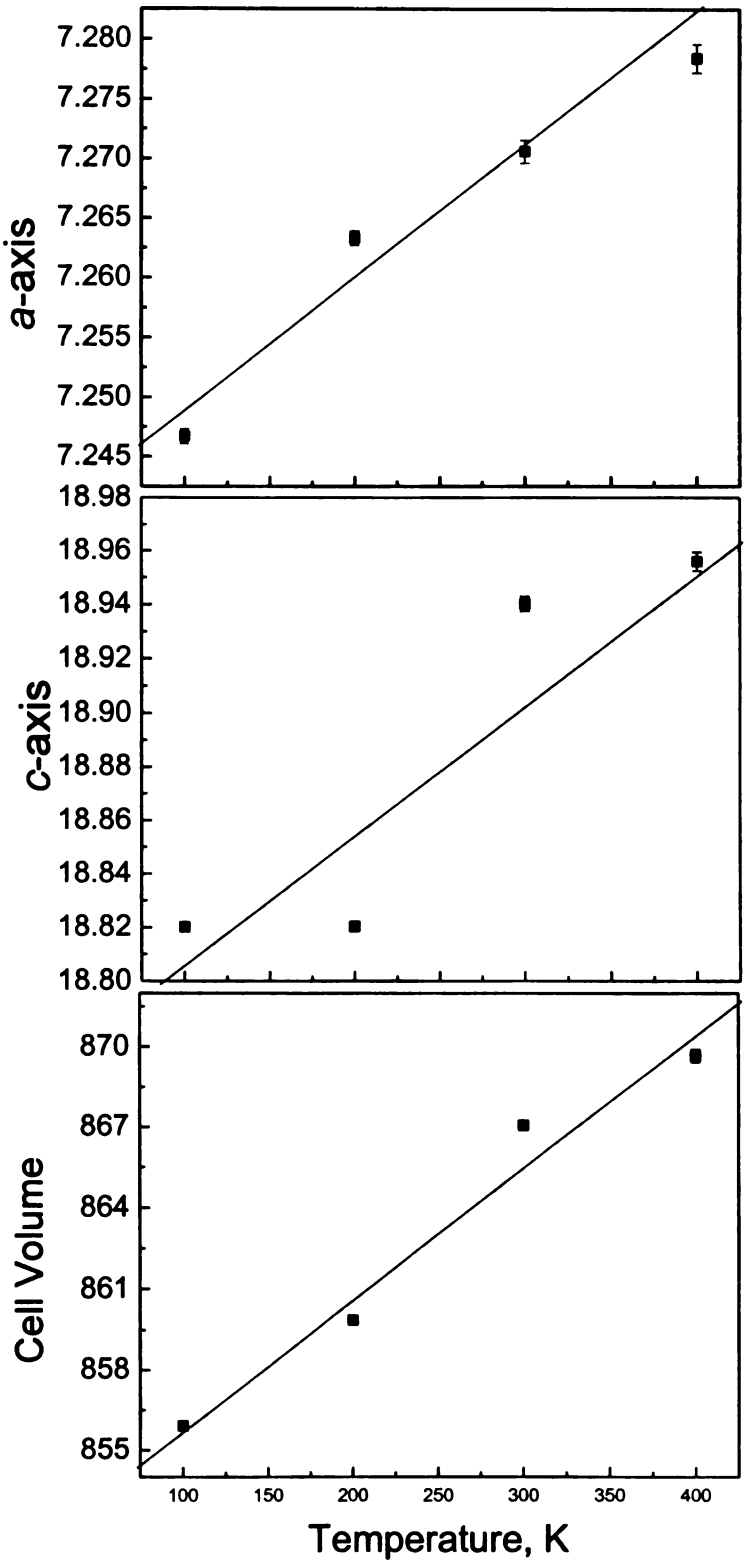

Figure 4-12. Temperature variation of the lattice parameters and cell volume for $K_2P_2Se_6$ from 100 to 400 K.

The volumetric thermal expansion coefficient of $K_2P_2Se_6$ at $\beta = 5.35 \times 10^{-5}$ K^{-1} also indicates its moderate thermal expansion. It is noteworthy that crystals of $K_2P_2Se_6$ did not show any signs of cracking or deformation when exposed to abrupt temperature change (200 K h^{-1}) or soaked at high temperature of 500 K for several days.

5. Concluding Remarks

The compounds $A_2P_2Se_6$ (A = K, Rb) have novel chiral structures composed of helices of $^1/_\infty[P_2Se_6^{2-}]$. The chirality combined with its phase-change behavior could enable $A_2P_2Se_6$ to be explored as a multi functional switchable material. On cooling $K_2P_2Se_6$ is susceptible to a displacive phase transition to a lower space group that seems to be driven by the coordination sphere expansion of the alkali ions. If correct, the phase transition could also be effected by the application of high pressure as a means of achieving coordination sphere expansion. When molten the compounds can be quenched to a glassy state and exhibit reversible crystal-glass phase change behavior. The optical absorption edge for the glassy phase is red shifted and on the basis of Raman spectroscopy and PDF analysis it appears that the main building motifs are largely intact in the glassy form. This accounts for the facile restoration of the crystal structure from the corresponding amorphous phase.

$A_2P_2Se_6$ (A = K, Rb) and the previously described $APSe_6$ (A = K, Rb, Cs) are the only reported extended structure compounds in the alkali chalcophosphate family to exhibit easy glass-formation and phase-change properties. This suggests that polymeric chalcophosphates have broad glass-forming tendencies and may constitute a fertile source

for stoichiometric chalcogenide glasses. The glass forming property of these materials makes them potentially valuable for producing IR optical glass fibers. Finally, $K_2P_2Se_6$ widely transparent in the mid-IR up to 19.2 μm that is coupled with a very large SHG response. The material is type-I phase-matchable with a response that is over 50 times larger than that of top performing NLO material $AgGaSe_2$. The remarkably stronger response is attributed to the helical structure of the selenophosphate which is highly polar, in contrast to the weakly polar chalcopyrite structure of $AgGaSe_2$. This makes $K_2P_2Se_6$ one of the best NLO materials known for non-resonant SHG. Finally, glassy form of $K_2P_2Se_6$ exhibited surprising SHG response with no poling treatment.

References

(1) Garin, J.; Parthe, E. *Acta Crystallogr. B* **1972**, *28*, 3672-3674.

(2) Francisco, R. H. P.; Tepe, T.; Eckert, H. *J. Solid State Chem.* **1993**, *107*, 452-459.

(3) Chondroudis, K.; Kanatzidis, M. G. *Inorg. Chem.* **1995**, *34*, 5401-5402.

(4) Chondroudis, K.; Kanatzidis, M. G. *Inorg. Chem.* **1998**, *37*, 2582-2584.

(5) Chung, I.; Karst, A. L.; Weliky, D. P.; Kanatzidis, M. G. *Inorg. Chem.* **2006**, *45*, 2785-2787.

(6) Chung, I.; Do, J.; Canlas, C. G.; Weliky, D. P.; Kanatzidis, M. G. *Inorg. Chem.* **2004**, *43*, 2762-2764.

(7) (a) Chondroudis, K.; Kanatzidis, M. G. *Angew. Chem., Int. Ed. Engl.* **1997**, *36*, 1324-1326. (b) Chung, I.; Kanatzidis, M. G. Unpublished work.

(8) Kanatzidis, M. G. *Curr. Opin. Solid State & Mater. Sci.* **1997**, *2*, 139-149.

(9) The chalcophosphate, for example, are capable of condensing via Q-Q polychalcogenide bonds, whereas the phosphates are not known to do so.

(10) (a) Oh, H.-R.; Cho, B.-H.; Cho, W. Y.; Kang, S.; Choi, B.-G.; Kim, H.-J.; Kim, K.-S.; Kim, D.-E.; Kwak, C.-K.; Byun, H.-G.; Jeong, G.-T.; Jeong, H.-S.; Kim, K. *IEEE J. Solid-State Circuits* **2006**, *41*, 122-126. (b) Ohta, T. *J. Optoelectron. Adv. Mat.* **2001**, *3*, 609-626. (c) Ohta, T.; Nishiuchi, K.; Narumi, K.; Kitaoka, Y.; Ishibashi, H.; Yamada, N.; Kozaki, T. *Jpn. J. Appl. Phys., Part 1* **2000**, *39*, 770-774.

(11) (a) Wełnic, W.; Pamungkas, A.; Detemple, R.; Steimer, C.; Blugel, S.; Wuttig, M. *Nat. Mater.* **2006**, *5*, 56-62. (b) Lee, H.; Kim, Y. K.; Kim, D.; Kang, D. H. *IEEE Trans. Magn.* **2005**, *41*, 1034-1036. (c) Kolobov, A. V.; Fons, P.; Frenkel, A. I.; Ankudinov, A. L.; Tominaga, J.; Uruga, T. *Nat. Mater.* **2004**, *3*, 703-708.

(12) Hwang, S. J.; Petkov, V.; Rangan, K. K.; Shastri, S.; Kanatzidis, M. G. *J. Phys. Chem. B* **2002**, *106*, 12453-12458.

(13) Qiu, X. Y.; Bozin, E. S.; Juhas, P.; Proffen, T.; Billinge, S. J. L. *J. Appl. Crystallogr.* **2004**, *37*, 110-116.

(14) (a) Kortüm, G. *Reflectance spectroscopy. Principles, methods, applications*; Springer: Berlin, Heidelberg, New York,, 1969. (b) Tandon, S. P.; Gupta, J. P. *Phys Status Solidi* **1970**, *38*, 363-367. (c) Wendlandt, W. W.; Hecht, H. G. *Reflectance spectroscopy*; Interscience Publishers: New York, 1966.

(15) *SMART, SAINT, SHELXTL: Data Collection and Processing Software for the SMART-CCD System*; Siemens Analytical X-ray Instruments Inc.: Madison, WI, 1997.

(16) Gieck, C.; Derstroff, V.; Block, T.; Felser, C.; Regelsky, G.; Jepsen, O.; Ksenofontov, V.; Gutlich, P.; Eckert, H.; Tremel, W. *Chem. Eur. J.* **2004**, *10*, 382-391.

(17) Gieck, C.; Tremel, W. *Chem. Eur. J.* **2002**, *8*, 2980-2987.

(18) (a) Canadell, E.; Rachidi, I. E. I.; Pouget, J. P.; Gressier, P.; Meerschaut, A.; Rouxel, J.; Jung, D.; Evain, M.; Whangbo, M. H. *Inorg. Chem.* **1990**, *29*, 1401-1407. (b) *Electronic Properties of Inorganic Quasi-One-Dimensional Compounds*; Monceau, P. ed.; D. Reidel Publishing Company: Dordrecht, 1985.

(19) Kanatzidis, M. G.; Sutorik, A. C. *Prog. Inorg. Chem.* **1995**, *43*, 151-265.

(20) Canlas, C. G.; Kanatzidis, M. G.; Weliky, D. P. *Inorg. Chem.* **2003**, *42*, 3399-3405.

(21) (a) Chrissafis, K.; Kyratsi, T.; Paraskevopoulos, K. M.; Kanatzidis, M. G. *Chem. Mater.* **2004**, *16*, 1932-1937. (b) Kyratsi, T.; Chrissafis, K.; Wachter, J.; Paraskevopoulos, K. M.; Kanatzidis, M. G. *Adv. Mater.* **2003**, *15*, 1428-1431. (c) Wachter, J. B.; Chrissafis, K.; Petkov, V.; Malliakas, C. D.; Bilc, D.; Kyratsi, T.; Paraskevopoulos, K. M.; Mahanti, S. D.; Torbrugge, T.; Eckert, H.; Kanatzidis, M. G. *J. Solid State Chem.* **2007**, *180*, 420-431.

(22) Dhingra, S.; Kanatzidis, M. G. *Science* **1992**, *258*, 1769-1772.

(23) (a) Maeda, Y.; Andoh, H.; Ikuta, I.; Minemura, H. *J. Appl. Phys.* **1988**, *64*, 1715-1719. (b) Feinleib, J.; Deneufvi.J; Moss, S. C.; Ovshinsk.Sr *Appl. Phys. Lett.* **1971**, *18*, 254-257.

(24) (a) Pätzmann, U.; Brockner, W. *Z. Naturforsch., A* **1987**, *42*, 515-516. (b) Brockner, W.; Ohse, L.; Pätzmann, U.; Eisenmann, B.; Schäfer, H. *Z. Naturforsch., A* **1985**, *40*, 1248-1252.

(25) Aitken, J. A.; Evain, M.; Iordanidis, L.; Kanatzidis, M. G. *Inorg. Chem.* **2002**, *41*, 180-191.

(26) (a) Choi, K. S.; Kanatzidis, M. G. *Chem. Mater.* **1999**, *11*, 2613-2618. (b) Evain, M.; Queignec, M.; Brec, R.; Sourisseau, C. *J. Solid State Chem.* **1988**, *75*, 413-431. (c) Butler, I. S.; Harvey, P. D.; Mccall, J. M.; Shaver, A. *J. Raman Spectrosc.* **1986**, *17*, 221-228.

(27) (a) Billinge, S. J. L.; Kanatzidis, M. G. *Chem. Commun.* **2004**, 749-760. (b) Petkov, V.; Billinge, S. J. L.; Shastri, S. D.; Himmel, B. *Phys. Rev. Lett.* **2000**, *85*, 3436.

(28) Nikogosyan, D. N. *Nonlinear optical crystals: a complete survey*; Springer-

Science: New York, 2005.

(29) Liao, J. H.; Marking, G. M.; Hsu, K. F.; Matsushita, Y.; Ewbank, M. D.; Borwick, R.; Cunningham, P.; Rosker, M. J.; Kanatzidis, M. G. *J. Am. Chem. Soc.* **2003**, *125*, 9484-9493.

(30) Hanko, J. A.; Kanatzidis, V. G. *J. Solid State Chem.* **2000**, *151*, 326-329.

(31) Aitken, J. A.; Marking, G. A.; Evain, M.; Iordanidis, L.; Kanatzidis, M. G. *J. Solid State Chem.* **2000**, *153*, 158-169.

(32) Chondroudis, K.; Hanko, J. A.; Kanatzidis, M. G. *Inorg. Chem.* **1997**, *36*, 2623-2632.

(33) (a) Dougherty, J. P.; Kurtz, S. K. *J. Appl. Crystallogr.* **1976**, *9*, 145-158. (b) Kurtz, S. K.; Perry, T. T. *J. Appl. Phys.* **1968**, *39*, 3798-3813.

(34) Choy, M. M.; Byer, R. L. *Phys. Rev. B* **1976**, *14*, 1693-1706.

(35) Antonyuk, B. P.; Antonyuk, V. B. *Opt. Commun.* **1998**, *147*, 143-147.

(36) (a)Fokine, M.; Saito, K.; Ikushima, A. J. *Appl. Phys. Lett.* **2005**, *87*, 171907. (b) Kityk, I. V. *J. Phys. Chem. B* **2003**, *107*, 10083-10087. (c) Qiu, M. X.; Pi, F.; Orriols, G. *Appl. Phys. Lett.* **1998**, *73*, 3040-3042. (c) Fujiwara, T.; Takahashi, M.; Ikushima, A. J. *Appl. Phys. Lett.* **1997**, *71*, 1032-1034.

(37) Iseler, G. W. *J. Cryst. Growth* **1977**, *41*, 146-150.

(38) Korczak, P.; Staff, C. B. *J. Cryst. Growth* **1974**, *24*, 386-389.

(39) Kozhina, I. I.; Borshchevskii, A. S. *Vestnik Leningradskogo Universiteta, Seriya 4: Fizika, Khimiya* **1971**, 87-92.

(40) Feigelson, R. S.; Route, R. K. *Optical Engineering* **1987**, *26*, 113-19.

Chapter 5

$[P_6Se_{12}]^{4-}$: A Phosphorus-rich Selenophosphate with Low-valent P Centers

1. Introduction

The diversity found within the class of metal chalcophosphates is extensive.[1] Typically, these are ternary (M/P/Q) and quaternary (A/M/P/Q) compounds with $[P_xQ_y]^{z-}$ anions in their structure, where M is a metal, A is an alkali metal, and Q is sulfur or selenium. The selenophosphate anions that are structurally characterized include $[PSe_4]^{3-}$,[2] $[PSe_4]^{3-}\cdot 2Se_6$,[3] $[P_2Se_6]^{4-}$,[4] $[P_2Se_9]^{4-}$,[5] $[P_2Se_{10}]^{4-}$,[6] $[P_8Se_{18}]^{6-}$,[7] $[P_2Se_8]^{2-}$,[8] and the one-dimensional polymer $^1/_\infty[PSe_6^-]$.[9] All of these are P^{5+} species except for $[P_2Se_6]^{4-}$ and $[P_8Se_{18}]^{6-}$, which are formally P^{4+} and P^{4+}/P^{3+} compounds with P-P bonds, respectively. Each anion is capable of coordinating to a metal (M) and giving rise to extended structures.[1,10] Core questions in this chemistry include the limits of structural diversity and the stabilization of species with P in even lower oxidation states. Consequent phosphorus-rich phases have been rare in this chemistry. With this in mind, we conducted experiments aimed at stabilizing alkali salts of chalcophosphate anions by employing new synthetic conditions. In the present case, we attempted reductive reactions using $P^{5+}[P_xQ_y]^{z-}$ species as starting materials with an excess of elemental P. This chemistry was carried out at ~400 °C with $RbPSe_6$ and red P and resulted in the new compound $Rb_4P_6Se_{12}$.Here we describe the new polar chalcophosphate anion $[P_6Se_{12}]^{4-}$, featuring P in two different oxidation states of 2+ and 4+. This is manifested in three parallel P-P

bonds in the molecule. Direct combination reactions of Rb_2Se, P, and Se with the correct stoichiometric ratio could not produce this compound. The result suggests a unique suitability of alkali chalcophosphates as starting materials to explore new chemistry. This is partly due to their low melting points (300-400 °C) and high reactivity.

2. Experimental Section

2.1 Reagents

The reagents mentioned in this work were used as obtained: Rb metal (analytical reagent, Johnson Matthey/AESAR Group, Seabrook, NH); red phosphorus powder, -100 mesh, Morton Thiokol, Inc., Danvers, MA; Se (99.9999%; Noranda Advanced Materials, Quebec, Canada); *N*,*N*-dimethylformamide (Spectrum Chemicals, ACS reagent grade); diethyl ether (Columbus Chemical Industries, Columbus WI, ACS reagent grade, anhydrous). Rb_2Se starting material was prepared by reacting stoichiometric amounts of the elements in liquid ammonia.

2.2. Synthesis

Pure $Rb_4P_6Se_{12}$ was achieved by a mixture of $RbPSe_6$:P=1:4 in an evacuated and sealed silica tube at 400 °C for 3 days followed by cooling at a rate of 5 °C h^{-1} to 250 °C. After washing with degassed *N*,*N*-dimethylformamide (DMF) and ether under N_2 atmosphere, we obtained pure orange irregular-shaped single crystals. Energy dispersive spectroscopy (EDS) analysis of the crystals showed an average composition of "$Rb_{3.9}P_6Se_{11.7}$" for five single crystals. The single crystals are stable in acetonitrile, DMF,

and deionized water, and they are air-stable for over 1 week.

3. Physical Measurements

X-ray Powder Diffraction. Phase purity x-ray diffraction analyses were performed using a calibrated CPS 120 INEL X-ray powder diffractometer (Cu K_α graphite monochromatized radiation) operating at 40 kV/20 mA and equipped with a position-sensitive detector with flat sample geometry.

Electron Microscopy. Semiquantitative analyses of the compounds were performed with a JEOL JSM-35C scanning electron microscope (SEM) equipped with a Tracor Northern energy dispersive spectroscopy (EDS) detector.

Solid-State UV-Vis spectroscopy. Optical diffuse reflectance measurements were performed at room temperature using a Shimadzu UV-3101 PC double-beam, double-monochromator spectrophotometer operating in the 200-2500 nm region using a procedure described in detail in Chapter 3.

Raman Spectroscopy. Raman spectra were recorded on a Holoprobe Raman spectrograph equipped with a CCD camera detector using 633 nm radiation from a HeNe laser for excitation and a resolution of 4 cm^{-1}. Laser power at the sample was estimated to be about 5 mW, and the focused laser beam diameter was ca. 10 μm. A total of 128 scans was sufficient to obtain good quality spectra.

Infrared Spectroscopy. FT-IR spectra were recorded as solids in a CsI matrix. The sample was ground with dry CsI into a fine powder and pressed into translucent pellets. The spectra were recorded in the far-IR region (600-100 cm^{-1}, 4 cm^{-1} resolution) with the

use of a Nicolet 740 FT-IR spectrometer equipped with a TGS/PE detector and silicon beam splitter.

Differential Thermal Analysis (DTA) Experiments were performed on Shimadzu DTA-50 thermal analyzer. A sample (~30 mg) of ground crystalline material was sealed in a silica ampoule under vacuum. A similar ampoule of equal mass filled with Al_2O_3 was sealed and placed on the reference side of the detector. The sample was heated to 600 °C at 10 °C min^{-1}, and after 1 min it was cooled at a rate of −10 °C min^{-1} to 50 °C. The residues of the DTA experiments were examined by X-ray powder diffraction. Reproducibility of the results was confirmed by running multiple heating/cooling cycles. The melting and crystallization points were measured at a minimum of endothermic peak and a maximum of exothermic peak.

Solid-State Nuclear Magnetic Resonance (NMR) Spectroscopy. The room temperature solid-state NMR measurement was taken on a 9.4 T NMR Spectrometer (Varian Infinity Plus) using a double resonance magic angle spinning (MAS) probe. The sample was spun at 8.0 kHz using zirconia rotors of 6 mm outer diameter. Bloch decay spectra were taken with the excitation/detection channel tuned to ^{31}P at 161.39 MHz, a 4.5 μs 90° pulse, and a relaxation delay of 3,000 s. The spectrum was referenced using 85% H_3PO_4 at 0 ppm.

X-ray Crystallography. The crystal structure was determined by single-crystal X-ray diffraction methods. Preliminary examination and data collection were performed on a SMART platform diffractometer equipped with a 1K CCD area detector using graphite monochromatized Mo K_α radiation at 293(2) K. A hemisphere of data was collected at 293(2) K using a narrow-frame method with scan widths of 0.30° in ω and an exposure time of 30s $frame^{-1}$. The data were integrated using the SAINT program. An analytical

absorption using the program SADABS was performed. The initial positions for all atoms were obtained using direct methods and the structures were refined with the full-matrix least-squares techniques of the SHELXTL[11] crystallographic software package. Crystallographic data are given in Table 1. Satisfactory refinement was obtained with the chiral space group, $Pca2_1$ at 293(2) K. Absolute structure parameter was refined at 0.07(3). The *PLATON* program[12] could not suggest additional symmetry, and the structure could not be solved in a centrosymmetric space group such as *Pbcm*

Table 5-1. Crystallographic Data and Structure Refinement for $Rb_4P_6Se_{12}$.

Formula	$Rb_4P_6Se_{12}$
Formula weight, g/mol	1475.22
Temperature, K	293(2)
Wavelength, Å	0.71073
Crystal system	Orthorhombic
Space Group	$Pca2_1$
Unit cell dimensions, Å	a = 16.409(3), b = 10.640(2), c = 15.105(3)
Volume, $Å^3$	2637.1(9)
Z, Density (calculated)	4, 3.716 g cm^{-3}
Absorption coefficient	24.296 mm^{-1}
F(000)	2584
Theta range for data collection, deg	1.91 to 28.29
Index ranges	-21<=h<=20, -14<=k<=14, -19<=l<=19
Reflections collected/unique	22687, 6163
Completeness to θ_{max}, %	96.8
Refinement method	Full-matrix least-squares on F^2
Data/restraints/parameters	6163 / 1 / 199
Goodness-of-fit on F^2	0.854
Final R indices [I>2σ(I)]	R1 [a] = 0.0463, wR2 [b] = 0.0769
R indices (all data)	R1 = 0.1726, wR2 = 0.1019
Absolute structure parameter	0.07(3)
Largest diff. peak and hole	1.451 and -1.380 e.$Å^{-3}$

[a] $R1 = \sum ||F_o| - |F_c|| / \sum |F_o|$. [b] $wR2 = \{\sum [w(F_o^2 - F_c^2)^2] / \sum [w(F_o^2)^2]\}^{1/2}$.

Table 5-2. Atomic coordinates ($\times 10^4$) and equivalent isotropic displacement parameters ($Å^2 \times 10^3$) for $Rb_4P_6Se_{12}$. U(eq) is defined as one third of the trace of the orthogonalized U_{ij} tensor.

	x	y	z	U(eq)
Rb(1)	1635(1)	7610(2)	10196(1)	33(1)
Rb(2)	-890(1)	7356(2)	8418(2)	37(1)
Rb(3)	4744(1)	7632(2)	8022(2)	37(1)
Rb(4)	-2229(1)	7211(2)	5438(2)	47(1)
Se(1)	1993(1)	2746(2)	7859(2)	33(1)
Se(2)	790(2)	5152(2)	8992(2)	33(1)
Se(3)	1100(2)	5119(2)	6601(2)	25(1)
Se(4)	79(1)	7329(2)	5537(1)	24(1)
Se(5)	3933(2)	10218(2)	6735(2)	32(1)
Se(6)	-878(2)	9625(2)	4333(2)	40(1)
Se(7)	506(1)	2393(2)	5698(2)	26(1)
Se(8)	3394(2)	9857(2)	9535(2)	34(1)
Se(9)	1386(2)	10007(2)	6939(2)	27(1)
Se(10)	2371(1)	7809(2)	7998(1)	24(1)
Se(11)	3550(2)	5297(2)	6905(2)	31(1)
Se(12)	3257(1)	5577(2)	9314(2)	29(1)
P(1)	1614(3)	4653(5)	7961(4)	19(1)
P(2)	646(3)	7102(5)	6915(4)	26(1)
P(3)	-344(3)	9376(4)	5611(4)	22(1)
P(4)	837(3)	10461(5)	5586(4)	22(1)
P(5)	1807(3)	8019(5)	6613(3)	24(1)
P(6)	2776(3)	5757(4)	8006(3)	20(1)

Table 5-3. Anisotropic displacement parameters ($Å^2 \times 10^3$)) for $Rb_4P_6Se_{12}$. The anisotropic displacement factor exponent takes the form: $-2\pi^2[h^2 a^{*2} U_{11} + ... + 2 h k a^* b^* U_{12}]$.

	U_{11}	U_{22}	U_{33}	U_{23}	U_{13}	U_{12}
Rb(1)	34(1)	33(1)	33(1)	-2(1)	-3(1)	5(1)
Rb(2)	36(1)	37(1)	37(1)	-4(1)	5(1)	1(1)
Rb(3)	32(1)	36(1)	44(1)	2(1)	-7(1)	-4(1)
Rb(4)	36(2)	52(2)	53(2)	3(1)	-7(1)	-3(1)
Se(1)	34(2)	14(1)	50(2)	5(1)	-10(1)	-1(1)
Se(2)	30(2)	36(2)	34(2)	-2(1)	8(1)	-6(1)
Se(3)	30(2)	15(2)	30(2)	-1(1)	-5(2)	0(1)
Se(4)	34(2)	13(1)	26(1)	-3(1)	-7(1)	5(1)
Se(5)	30(2)	31(2)	34(2)	2(1)	9(1)	-4(1)
Se(6)	46(2)	42(2)	31(2)	-11(1)	-15(1)	18(1)
Se(7)	33(1)	12(1)	34(1)	1(1)	-1(1)	2(1)
Se(8)	33(2)	32(2)	37(2)	6(1)	-15(1)	-9(1)
Se(9)	35(2)	17(2)	28(2)	-2(1)	-9(2)	4(1)
Se(10)	29(1)	14(1)	28(1)	0(1)	-5(1)	0(1)
Se(11)	30(2)	31(1)	32(2)	-1(1)	11(1)	-3(1)
Se(12)	34(1)	23(1)	29(1)	2(1)	-9(1)	1(1)
P(1)	19(3)	15(3)	21(3)	4(3)	-3(3)	-4(2)
P(2)	29(3)	17(3)	30(3)	-3(3)	1(3)	6(2)
P(3)	24(3)	12(3)	31(3)	2(3)	0(3)	3(2)
P(4)	24(3)	13(3)	30(3)	0(3)	1(3)	4(3)
P(5)	31(3)	15(3)	24(3)	5(2)	-1(3)	7(2)
P(6)	21(3)	12(3)	26(3)	0(2)	-1(3)	5(2)

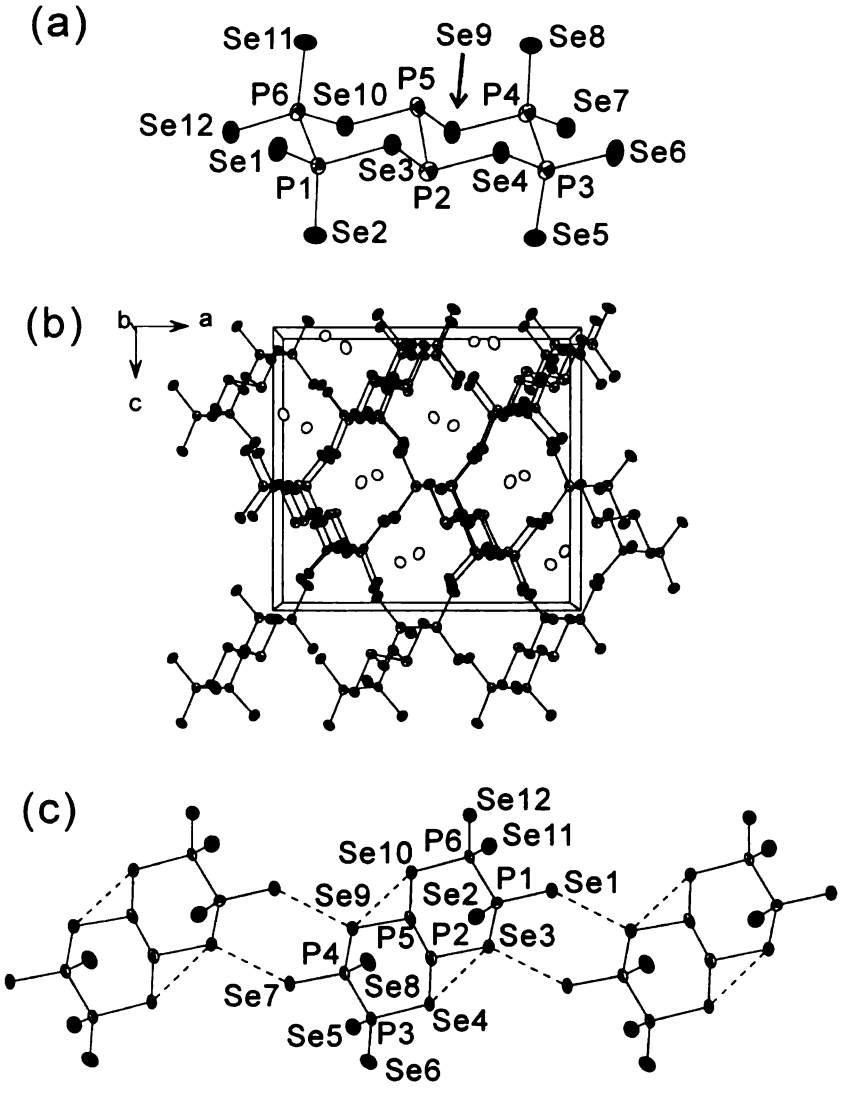

Figure 5-1. (a) $[P_6Se_{12}]^{4-}$ anion. (b) Structure of $Rb_4P_6Se_{12}$. Open circles are Cs, octants P, and black Se atoms. (c) *Pseudo*-one-dimensional chain of $[P_6Se_{12}]^{4-}$ via Se···Se nonbonding contacts. The thermal ellipsoids are shown with 50% probability. P and Se atoms are labeled in (a) and (c)

Table 5-4. Bond lengths (Å) and angles (°) for $Rb_4P_6Se_{12}$.

			2.300(6)
Se(1)-P(1)	2.128(5)	Se(10)-P(5)	
Se(2)-P(1)	2.130(6)	Se(10)-P(6)	2.282(5)
Se(3)-P(1)	2.275(6)	Se(11)-P(6)	2.148(6)
Se(3)-P(2)	2.288(5)	Se(12)-P(6)	2.136(6)
Se(4)-P(3)	2.288(5)	P(1)-P(6)	2.241(7)
Se(4)-P(2)	2.294(6)	P(2)-P(5)	2.189(6)
Se(6)-P(3)	2.136(6)	P(3)-P(4)	2.257(7)
Se(8)-P(4)#1	2.128(6)	P(3)-Se(5)#5	2.116(6)
Se(9)-P(5)	2.279(5)	P(4)-Se(7)#10	2.218(6)
Se(9)-P(4)	2.285(7)	P(4)-Se(7)#13	2.133(5)
P(5)-Se(9)-P(4)	97.0(2)	Se(8)#10-P(4)-Se(7)#13	102.1(3)
P(6)-Se(10)-P(5)	102.4(2)	Se(8)#10-P(4)-P(3)	111.6(3)
Se(1)-P(1)-Se(2)	118.4(2)	Se(7)#13-P(4)-P(3)	105.8(2)
Se(1)-P(1)-P(6)	104.7(2)	Se(8)#10-P(4)-Se(9)	111.7(2)
Se(2)-P(1)-P(6)	112.8(3)	Se(7)#13-P(4)-Se(9)	103.5(2)
Se(1)-P(1)-Se(3)	104.5(2)	P(3)-P(4)-Se(9)	102.5(3)
Se(2)-P(1)-Se(3)	111.7(2)	P(2)-P(5)-Se(9)	96.0(2)
P(6)-P(1)-Se(3)	103.2(2)	P(2)-P(5)-Se(10)	96.7(2)
P(5)-P(2)-Se(3)	94.8(2)	Se(9)-P(5)-Se(10)	90.9(2)
P(5)-P(2)-Se(4)	96.7(2)	Se(12)-P(6)-Se(11)	118.5(2)
Se(3)-P(2)-Se(4)	92.3(2)	Se(12)-P(6)-P(1)	107.2(3)
Se(5)#5-P(3)-Se(6)	118.0(2)	Se(11)-P(6)-P(1)	111.1(3)
Se(5)#5-P(3)-P(4)	113.0(3)	Se(12)-P(6)-Se(10)	101.4(2)
Se(6)-P(3)-P(4)	105.9(3)	Se(11)-P(6)-Se(10)	112.7(2)
P(4)-P(3)-Se(4)	103.0(2)	P(1)-P(6)-Se(10)	104.7(2)

Symmetry transformations used to generate equivalent atoms:

#1 $-x+1/2, y, z+1/2$ #2 $-x, -y+2, z+1/2$ #3 $-x, -y+1, z+1/2$
#4 $x-1/2, -y+1, z$ #5 $x-1/2, -y+2, z$ #6 $-x-1/2, y, z+1/2$
#7 $x+1/2, -y+1, z$ #8 $-x, -y+1, z-1/2$ #9 $-x, -y+2, z-1/2$
#10 $-x+1/2, y, z-1/2$ #11 $x+1/2, -y+2, z$ #12 $x, y-1, z$ #13 $x, y+1, z$

Table 5-5. Relationship between observed selenophosphate species and the A:P:Se ratio.

Known Compounds	Anion	A : P : Se Ratio	Color	Flux condition	Note
A_3PSe_4 (A = Na, K, Cs[16])	PSe_4^{3-}	3 : 1 : 4	Red	Basic	Molecular
$Cs_4P_2Se_{10}$[17]	$P_2Se_{10}^{4-}$	2 : 1 : 5	Red		
$A_4P_2Se_9$ (A = K, Rb, Cs)	$P_2Se_9^{4-}$	2 : 1 : 4.5	Red		
$A_4P_2Se_6$ (A = Na, K[16])	$P_2Se_6^{4-}$	2 : 1 : 3	Red		
$Cs_5P_5Se_{12}$[18]	$P_5Se_{12}^{5-}$	1 : 1 : 2.4	Orange	Intermediate	
$A_6P_8Se_{18}$ (A = K,[7] Rb[16])	$P_8Se_{18}^{6-}$	1 : 1.33 : 3	Red		
$A_4P_6Se_{12}$ (A = Rb, Cs[17])	α-$[P_6Se_{12}]^{4-}$ β-$[P_6Se_{12}]^{4-}$	1 : 1.5 : 3	Orange		Double six- membered ring
$Cs_2P_2Se_8$[8a]	$P_2Se_8^{2-}$	1 : 1 : 4	Yellow	"Acidic"	Six-membered ring
$A_2P_2Se_6$ (A = K, Rb)[19]	$^1/_\infty$ $[P_2Se_6^{2-}]$	1 : 1 : 3	Orange		One dimensional chain
$APSe_6$ (A = K, Rb, Cs)	$^1/_\infty$ $[PSe_6^-]$	1 : 1 : 6	Orange		

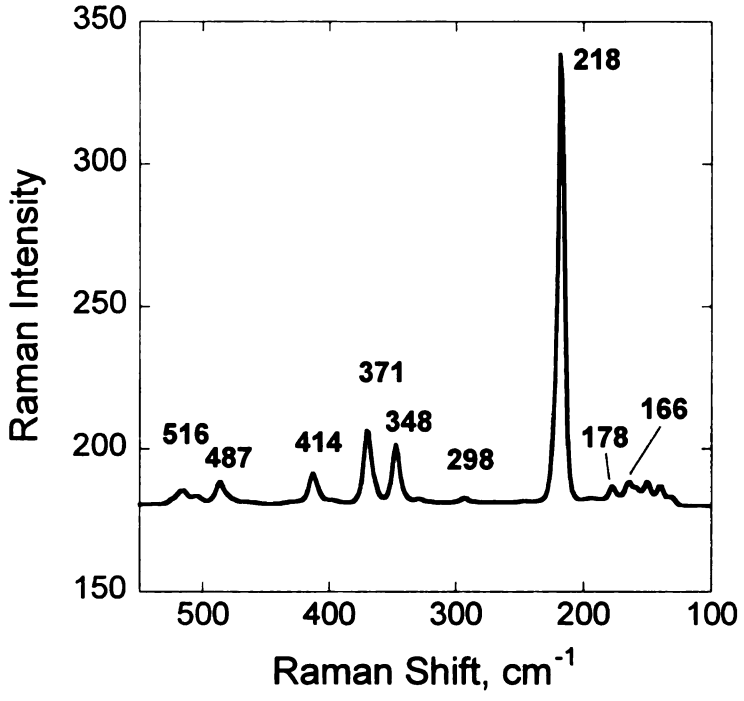

Figure 5-2. Raman Spectrum of $Rb_4P_6Se_{12}$ at room temperature.

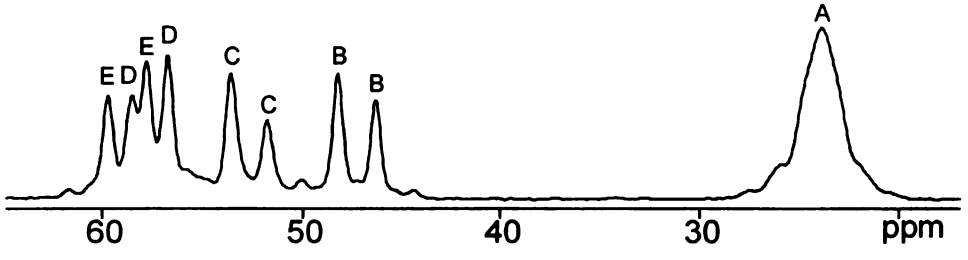

Figure 5-3. ^{31}P Bloch decay NMR spectrum of $Rb_4P_6Se_{12}$ taken at ambient temperature on a 9.4 T NMR spectrometer. Acquisition parameters included 5 μs $\pi/2$ pulse, 8000 s relaxation delay, and 13 kHz magic-angle-spinning frequency. The chemical shift reference was 85% H_3PO_4 (0 ppm). Peaks with the same letter are *J*-coupled. The average chemical shifts of peaks A-E are in order: 23.9, 47.5, 52.6, 57.6, 58.8 ppm. The *J*-couplings of doublets B-E are: 309, 292, 295, 309 Hz.

4. Results and Discussion

Crystal Structure. The new structure-type of $Rb_4P_6Se_{12}$ adopts the noncentrosymmetric space group $Pca2_1$. The compound features discrete $[P_6Se_{12}]^{4-}$ molecules, Figure 5-1a. The centrosymmetric molecule generates itself through a 2_1-screw axis along the *c* axis with no mirror plane perpendicular to the *c* axis and, consequently, crystallizes in a noncentrosymmetric fashion, Figure 5-1b. The most unusual feature of the structure is its bicyclic nature and the presence of three P-P bonds with two types of formal charges of P^{2+} and P^{4+}. The divalent formal charge is found on P2 and P5. The structure of the $[P_6Se_{12}]^{4-}$ molecule is reminiscent of the bicycloalkane *trans*-decalin. The central P_2 unit is condensed with two ethane-like $[P_2Se_6]^{4-}$ fragments to form the decalin-like skeleton.

The $[P_6Se_{12}]^{4-}$ molecule adopts the C_{2h} point group, so that the central $[P_2Se_4]$ subunit has a *trans*-C_{2h}-type configuration around the P^{2+} centers. The same *trans*-C_{2h}-type configuration is found in P_2X_4 (X = F, Cl, I).[13] The Se-P-Se angles around P2 and P5 are nearly 90° [Se3-P2-Se4, 92.3(2)°; Se9-P5-Se10, 90.9(2)°]. The dihedral angles of Se3-P2-P5-Se9 and Se4-P2-P5-Se10 are 178.76(20) and -179.74(20)°, respectively. As a result, the P2-P5 vector defines the intersection of two planes. The outer $[P_2Se_6]$ residues in the molecule represent typical anti-type conformations but are distorted. (See relevant angles in Table 5-4.) The P-Se distances are normal at 2.116(6)-2.300(6) Å. The Se-P-Se angles range from 90.9(2) to 120.1(3)°. The P2-P5 distance is 2.189(6) Å, which is only slightly shorter than the typical P-P distance of ~2.2 Å in selenophosphates. Rhombohedral black P shows a P-P distance of 2.13 Å.[14]

To the best of our knowledge, this is a unique anion. The only other anion with

formally P^{2+} centers is the polymeric $^1/_\infty[P_5Se_{10}^{5-}]$, which is strongly bound to transition-metal atoms in $A_3MP_5Se_{10}$ (A = K, Rb; M = Ru, Os).[15,16] In these compounds, the P^{2+} centers are coordinated to Ru^{2+} or Os^{2+} metal centers through the P atoms, forming P-M bonds (M = Ru, Os).

Interestingly, the atoms Se1···Se3···Se4···Se6 are collinear, which allows maximum overlap of their pπ orbitals. The Se7···Se9···Se10···Se12 atoms are similarly collinear. The intramolecular Se3···Se4, Se4···Se6, Se9···Se10, and Se10···Se12 distances range from 3.273(3) to 3.416(3) Å and indicate both nonbonding interactions and severely distorted Se-P-Se angles in the central $[P_2Se_4]$ subunit. Similar intramolecular interactions have been observed in the $[PSe_3]$ pyramidal fragment of the $[P_8Se_{18}]^{6-7}$ anion and the $^1/_\infty[PSe_6^-]$ chain in $CsPSe_6$.[9]

Another notable feature is the unusually short intermolecular Se1···Se9 and Se3···Se7 distances of 3.384(3) and 3.340(3) Å, respectively. These distances indicate nonbonding interactions, but they are much shorter than the 3.80 Å sum of the van der Waals radii.[20] They enable the molecules of $[P_6Se_{12}]^{4-}$ to organize to an infinite *pseudo*-one-dimensional structure, Figure 5-1c. Low-dimensional compounds such as $NbSe_3$[21] and $APSe_6$ (A = K, Rb, Cs) display similar Se···Se interactions. These intermolecular interactions may contribute to the compound's stability in air and polar solvents such as water and *N*,*N*-dimethylformamide.The synthesis of $Rb_4P_6Se_{12}$ adds further insight in the close relationship between the structure and the flux condition (or A:P:Se ratio) in the alkali selenophosphate ternary system. More basic fluxes (i.e., those with a high A:P ratio) or higher reaction temperatures tend to give shorter structural fragments[21] and P in the 5+ oxidation state (Table 5-5). All simple anions, e.g., $[PSe_4]^{3-}$ and $[P_2Se_9]^{4-}$, were

prepared in strongly basic fluxes (Table 5-5). As the basicity decreases, more complex species emerge, such as $[P_2Se_6]^{4-}$, $[P_8Se_{18}]^{4-}$, and $[P_2Se_8]^{2-}$. Under even less basic flux conditions, the one-dimensional polyselenide chain $^1/_\infty[PSe_6^-]$ is stabilized with K, Rb, and Cs. $Rb_4P_6Se_{12}$ is made in intermediate acidic/basic conditions, and it contains P^{2+} centers because of excess P.

Differential thermal analysis (DTA) on $Rb_4P_6Se_{12}$ at a rate of 10 °C min^{-1} showed melting at ~431 °C and crystallization upon cooling at ~384 °C. X-ray diffraction patterns for samples before and after DTA were identical. The results suggest that $Rb_4P_6Se_{12}$ could be a promising precursor in synthesis for further reaction chemistry. The UV-vis spectrum reveals a sharp absorption edge and a band gap of 2.25 eV, which is in good agreement with its orange color. By comparison, the one-dimensional $RbPSe_6$ with P^{5+} showed a gap of 2.18 eV. The Raman spectrum of $Rb_4P_6Se_{12}$ shows shifts at 218 (vs), 298 (vw), 348(w), 371 (w), 414 (w), 487 (w), and 516 (vw) cm^{-1}, Figure 5-2. The peak at 218 cm^{-1} is unambiguously assigned to the locally A_{1g} symmetric stretching mode of PSe_3.[23] The second shift at 298 cm^{-1} resembles the ν_{12} (B_g) mode in $Pb_2P_2Se_6$ having C_{2h} site symmetry.[24] The other vibrations can be attributed to PSe_3 stretching modes.[4,24] The far-IR spectrum is rather complex, showing peaks at 214 (vs), 238 (bw), 301 (vw), 319 (vw), 353 (vw), 374 (vw), 392 (vw), 408 (w), 464 (vw), 486 (vw), 514 (w), and 524 (w) cm^{-1}. The peak at 319 cm^{-1} is assigned to a P-P vibration and was not observed in the Raman spectrum. Other peaks are well matched with those of $Pb_2P_2Se_6$ and other compounds that contain the $[P_2Se_6]^{4-}$ anion.[26]

Figure 5-3 displays the ^{31}P NMR spectrum of $Rb_4P_6Se_{12}$. The narrow line widths afford resolution of most of the P sites. The ratio of the integrated intensity of the B-E

cluster of peaks to the intensity of peak A is ~2 and is generally consistent with the assignment of P1, P3, P4, and P6 to the B-E peaks and P2 and P5 to the A peak. P1/P6 and P3/P4 *J* couplings are expected, and analysis of the spectrum yielded the same *J* coupling for doublets B and E and the same *J* coupling for doublets C and D. The isotropic chemical shifts and *J* couplings were confirmed by the analysis of spectra taken on a 7-T spectrometer. It was not possible to make a more detailed assignment of P1/P6 and P3/P4 to the C/D and B/E doublets, and the P2/P5 shifts were not resolved from one another. The ^{31}P NMR chemical shifts are all >0 ppm and are consistent with the positive chemical shifts of other metal selenophosphates with P-P bonding.[27]

5. Concluding Remarks

The new selenophosphate compound $Rb_4P_6Se_{12}$ was synthesized by employing new synthetic conditions, e.g., reductive reactions using P^{5+} $[P_xQ_y]^{z-}$ species as starting materials with an excess of elemental P. This chemistry showed the high reactivity of alkali chalcophosphate ternary compounds that melt at low temperature (300-500 °C) as useful starting materials, to give new compounds. The discovery of the molecular salt $Rb_4P_6Se_{12}$ with its unique bicycloselenophosphate anion and rare combination of P^{2+} and P^{4+} centers suggests a more extensive compositional diversity in alkali chalcophosphates. The unraveling relationship between basicity and the final structure enhances the understanding of flux chemistry and the prospects of the future discovery of new materials in this class of solids.

Reference

(1) Kanatzidis, M. G. *Curr. Opin. Solid State Mater. Sci.* **1997**, *2*, 139.

(2) Garin, J.; Parthe, E. *Acta Crystallogr.* **1972**, *B28*, 3672.

(3) Dickerson, C. A.; Fisher, M. J.; Sykora, R. E.; Albrecht-Schmitt, T. E.; Cody, J. A. *Inorg. Chem.* **2002**, *41*, 640.

(4) (a) Toffoli, P. P.; Khodadad, P.; Rodier, N. *Acta Crystallogr.* **1973**, *B34*, 1779. (b) Francisco, R. H. P.; Tepe, T.; Eckert, H. *J. Solid State Chem.* **1993**, *107*, 452.

(5) Chondroudis, K.; Kanatzidis, M. G. *Inorg. Chem.* **1995**, *34*, 5401.

(6) Gave, M. A.; Canlas, C. G.; Chung, I.; Iyer, R. G.; Kanatzidis, M. G.; Weliky, D. P. *J. Solid State Chem.* **2007**, *180*, 2877.

(7) Chondroudis, K.; Kanatzidis, M. G. *Inorg. Chem.* **1998**, *37*, 2582.

(8) (a) Chung, I.; Kanatzidis, M. G. Manuscript in preparation. (b) Zhao, J.; Pennington, W. T.; Kolis, J. W. *J. Chem. Soc., Chem. Commun.* **1992**, 265.

(9) Chung, I.; Canlas, C. G.; Weliky, D. P.; Kanatzidis, M. G. *Inorg. Chem.* **2004**, *43*, 2762.

(10) (a) Do, J.; Yun, H. *Inorg. Chem.* **1996**, *35*, 3729. (b) Chen, J. H.; Dorhout, P. K.; Ostenson, J. E. *Inorg. Chem.* **1996**, *35*, 5627. (c) Gauthier, G.; Jobic, S.; Brec, R.; Rouxel, J. *Inorg. Chem.* **1998**, *37*, 2332. (d) Gieck, C.; Tremel, W. *Chem.-Eur. J.* **2002**, *8*, 2980.

(11) SHELXTL: Data collection and Processing Software for the SMART-CCD system; Siemens Analytical X-ray Instrument Inc.: Madison, WI, 1997.

(12) Spek, A. L. *J. Appl. Crystallogr.* **2003**, *36*, 7.

(13) Corbridge, D. E. C. *Phosphorus, An Outline of its Chemistry, Biochemistry and Uses*, 5th ed.; Elsevier: New York, 1995; p 143.

(14) Corbridge, D. E. C. *The Structural Chemistry of Phosphorus*; Elsevier: New York, 1974; p 16.

(15) Chondroudis, K.; Kanatzidis, M. G. *Angew. Chem., Int. Ed. Engl.* **1997**, *36*, 1324.

(16) Chung, I.; Kanatzidis, M. G. Unpublished results.

(17) Gave, M. A.; Canlas, C. G.; Chung, I.; Iyer, R. G.; Kanatzidis, M. G. Weliky, D. P. *J. Solid State Chem.* **2007**, *180*, 2877.

(18) Chung, I.; Jang, J. I.; Gave, M. A.; Weliky, D. P.; Kanatzidis, M. G. *Chem. Commun.* **2007**,4998.

(19) Chung, I.; Malliakas, C. D.; Jang, J. I.; Canlas, C. G.; Weliky, D. P.; Kanatzidis, M. G. *J. Am. Chem. Soc.* **2007**, *129*, 14996.

(20) Shannon, R. D. *Acta Crystallogr.* **1964**, *A32*, 751.

(21) (a) *Electronic Properties of Inorganic Quasi-One-Dimensional Compounds*; Monceau, P., Ed.; D. Reidel Publishing Co.: Dordrecht, The Netherlands, 1985; Part II. (b) Canadell, E.; Rachidi, E.-I.; Pouget, J. P.; Gressier, P.; Meerschaut, A.; Rouxel, J.; Jung, D.; Evain, M.; Whangbo, M.-H. *Inorg. Chem.* **1990**, *29*, 1401.

(22) Kanatzidis, M. G.; Sutorik, A. *Prog. Inorg. Chem.* **1995**, *43*, 151.

(23) Mathey, Y.; Clement, R.; Sourisseau, C.; Lucazeau, G. *Inorg. Chem.* **1980**, *19*, 2773.

(24) Becker, R.; Brockner, W. *Z. Naturforsch.* **1984**, *39a*, 357.

(25) Chondroudis, K.; Charkrabarty, D.; Axtell, E. A.; Kanatzidis, M. G. *Z. Anorg. Allg. Chem.* **1998**, *624*, 975.

(26) Parensen, M.; Brockner, W.; Cyvin, B. N.; Cyvin, S. J. *Z. Naturforsch.* **1986**, *41a*, 1233.

(27) Canlas, C. G; Kanatzidis, M. G; Weliky, D. P. *Inorg. Chem.* **2003**, *42*, 3399.

Chapter 6

Low Valent Phosphorus in the Molecular Anions $[P_5Se_{12}]^{5-}$ and β-$[P_6Se_{12}]^{4-}$: Phase Change Behavior and Near Infrared Second Harmonic Generation

1. Introduction

The structural diversity found in the chalcophosphate family is extensive. Various selenophosphate anions $[P_xQ_y]^{z-}$ (Q = S, Se) have been isolated and structurally characterized, for example, $[PSe_4]^{3-}$,[1] $[P_2Se_6]^{4-}$,[2] $[P_2Se_9]^{4-}$,[3] $[P_8Se_{18}]^{6-}$,[4] α-$[P_6Se_{12}]^{4-}$,[5] $^1/_\infty[PSe_6^-]$[6] and $^1/_\infty[P_2Se_6^{2-}]$.[7] The most common oxidation state of P in selenophosphates is P^{4+} and P^{5+}. Member of this family can exhibit technologically important properties of ferroelectric,[8] nonlinear optical,[7,9] reversible redox chemistry relevant to secondary batteries,[10] photoluminescence,[11] and phase-change properties.[6,7,12] Our experimental investigations of alkali chalcophosphate compounds provided new insights on the relationship between the structure and the flux composition (A:P:Se ratio in the composition).[5] We also found that excess phosphorus in the flux helps to produce less oxidized $P^{2+/3+/4+}$ species such as $Rb_4P_6Se_{12}$[5] and $A_6P_8Se_{18}$ (A=K, Rb, Cs).[4] With this in mind, we focused on devising rational synthetic conditions to obtain P-rich species rather than the simple classical $[PSe_4]^{3-}$ or $[P_2Se_6]^{4-}$ anions. Here we describe the novel molecular $[P_5Se_{12}]^{5-}$ and β-$[P_6Se_{12}]^{4-}$ anions. The former includes P^{3+} and P^{4+} centers and features octahedrally coordinating P. The latter is a structural isomer of α-$[P_6Se_{12}]^{4-}$,[5] and

it contains P^{2+} and P^{4+} centers. $Cs_5P_5Se_{12}$ and $Cs_4P_6Se_{12}$ exhibit reversible phase-change behavior. Both crystalline and glassy $Cs_5P_5Se_{12}$ exhibit second harmonic generation non-linear optical response.

2. Experimental Section

2.1. Reagents.

The reagents mentioned in this work were used as obtained: Cs metal (analytical reagent, Johnson Matthey/AESAR Group, Seabrook, NH); red phosphorus powder, -100 mesh, Morton Thiokol, Inc., Danvers, MA; Se (99.9999%; Noranda Advanced Materials, Quebec, Canada); *N,N*-dimethylformamide (Spectrum Chemicals, ACS reagent grade); diethyl ether (Columbus Chemical Industries, Columbus WI, ACS reagent grade, anhydrous). A_2Se (A = K and Rb) starting materials were prepared by reacting stoichiometric amounts of the elements in liquid ammonia. P_2Se_5 was prepared by heating the mixture of P and Se with a stoichiometric ratio sealing in an evacuated silica tube at 460 °C for 24h.

2.2. Synthesis

Pure orange block–shaped crystals of $Cs_5P_5Se_{12}$ were obtained by heating a mixture of Cs_2Se:P:Se=1:2.5:4 under vacuum in a silica tube at 400 °C for 3 d, followed by washing the product with degassed *N,N*-dimethylformamide (DMF) under a N_2 atmosphere to remove residual flux. The compound could be also obtained by direct combination reaction of starting materials at 400 °C for 3d. Energy-dispersive spectroscopic (EDS) microprobe analysis showed an average composition of

"$Cs_{4.8}P_5Se_{11.6}$". The single crystals are stable in DMF and alcohol and in air for several days. Pure orange block–shaped crystals $Cs_4P_6Se_{12}$ were obtained by heating a mixture of Cs_2Se:P:Se=1:4:5 under the same conditions described above. EDS microprobe analysis showed an average composition of "$Cs_{3.8}P_6Se_{11.6}$". The glassy phase of $Cs_4P_6Se_{12}$ was prepared from melting single crystals of $Cs_4P_6Se_{12}$ under vacuum in a quartz tube at 800-900 °C for 1-2 min and quenching in ice water. The crystals are stable in DMF, alcohol and water and in air for several days.

3. Physical Measurements

X-ray Powder Diffraction. Phase purity x-ray diffraction analyses were performed using a calibrated CPS 120 INEL X-ray powder diffractometer (Cu K_α graphite monochromatized radiation) operating at 40 kV/20 mA and equipped with a position-sensitive detector with flat sample geometry.

Electron Microscopy. Semiquantitative analyses of the compounds were performed with a JEOL JSM-35C scanning electron microscope (SEM) equipped with a Tracor Northern energy dispersive spectroscopy (EDS) detector.

Solid-State UV-vis spectroscopy. Optical diffuse reflectance measurements were performed at room temperature using a Shimadzu UV-3101 PC double-beam, double-monochromator spectrophotometer operating in the 200-2500 nm region. The instrument is equipped with an integrating sphere and controlled by a personal computer. $BaSO_4$ was used as a 100 % reflectance standard. The sample was prepared by grinding the crystals to a powder and spreading it on a compacted surface of the powdered standard material,

preloaded into a sample holder. The reflectance versus wavelength data generated were used to estimate the band gap of the material by converting reflectance to absorption data.[13]

Raman Spectroscopy. Raman spectra were recorded on a Holoprobe Raman spectrograph equipped with a CCD camera detector using 633 nm radiation from a HeNe laser for excitation and a resolution of 4 cm^{-1}. Laser power at the sample was estimated to be about 5 mW, and the focused laser beam diameter was ca. 10 μm. A total of 128 scans was sufficient to obtain good quality spectra.

Infrared Spectroscopy. FT-IR spectra were recorded as solids in a CsI or KBr matrix. The samples were ground with dry CsI or KBr into a fine powder and pressed into translucent pellets. The spectra were recorded in the far-IR region (600-100 cm^{-1}, 4 cm^{-1} resolution) and mid-IR region (500-4000 cm^{-1}, 4 cm^{-1} resolution) with the use of a Nicolet 740 FT-IR spectrometer equipped with a TGS/PE detector and silicon beam splitter.

Differential Thermal Analysis (DTA). Experiments were performed on Shimadzu DTA-50 thermal analyzer. A sample (~30 mg) of ground crystalline material was sealed in a silica ampoule under vacuum. A similar ampoule of equal mass filled with Al_2O_3 was sealed and placed on the reference side of the detector. The sample was heated to 600°C at 10 °C min^{-1}, and after 1 min it was cooled at a rate of –10 °C min^{-1} to 50 °C. The residues of the DTA experiments were examined by X-ray powder diffraction. Reproducibility of the results was confirmed by running multiple heating /cooling cycles. The melting and crystallization points were measured at a minimum of endothermic peak and a maximum of exothermic peak.

X-ray Photoelectron Spectroscopy. Single crystals of $Cs_5P_5Se_{12}$ and $Cs_4P_6Se_{12}$ were ground to powders and pressed to pellets. X-ray photoelectron spectroscopy (XPS) analyses were performed on the pellets with Omicron ESCA probe equipped with EA 125 energy analyzer. Photoemission was stimulated by a monochromated Al K_α radiation (1486.6 eV). Binding energies were normalized to the C 1s binding energy set at 285.0 eV. To analyze the XPS results, linear background correction was applied and photolines were fit by Gaussian-Lorentzian curves. The fitted curve was deconvoluted to reveal multiple valence states of phosphorus and their $2p_{1/2}$ and $2p_{1/3}$ spectra. The quantitative analysis of P in $Cs_5P_5Se_{12}$ and $Cs_4P_6Se_{12}$ were carried out by XPS using the integrated areas of the core-level peaks of P 2p.

Solid-State Nuclear Magnetic Resonance (NMR) Spectroscopy. Room temperature ^{31}P NMR spectra were collected on a 9.4 T spectrometer (Varian Infinity Plus) using a Varian Chemagnetics double resonance magic angle spinning (MAS) probe. The sample volume in the 4 mm diameter zirconia rotors was ~50 μL and the MAS frequency was 14 KHz. Each sample was ground to a fine powder before being packed in the rotor. The $\pi/2$ pulse width was 5.55 μs and was calibrated using H_3PO_4. Spectra were processed using 50 Hz line broadening and up to a 10th order polynomial baseline correction. Longitudinal relaxation times (T_1) were determined as described elsewhere.[14]

X-ray Crystallography. The crystal structure was determined by single-crystal X-ray diffraction methods. For $Cs_5P_5Se_{12}$, preliminary examination and data collection were performed on a SMART[15] platform diffractometer equipped with a 1K CCD area detector using graphite monochromatized Mo K_α radiation at 292(2) K. A hemisphere of data was collected at 292(2) K using a narrow-frame method with scan widths of 0.30° in ω and an

exposure time of 30s frame^{-1}. The data were integrated using the SAINT[15] program. An empirical absorption correction using the program SADABS were performed. The initial positions for all atoms were obtained using direct methods and the structures were refined with the full-matrix least-squares techniques of the SHELXTL[15] crystallographic software package. Satisfactory refinement was obtained with the noncentrosymmetric space group, *P*-4. Flack parameter was refined and absolute structure parameter is 0.06(2). Intensity data for $Cs_4P_6Se_{12}$ were collected at 100(2) K on a STOE IPDS II diffractometer with Mo K_α radiation operating at 50 kV and 40 mA with a 34 cm image plate. Individual frames were collected with a 5 min exposure time and a 1.0 ω rotation. The X-AREA, X-RED and X-SHAPE software package was used for data extraction and integration and to apply empirical and analytical absorption corrections. The SHELXTL software package was used to solve and refine the structure. The most satisfactory refinement was obtained with the space group, $P2_1/n$. The parameters for data collection and the details of the structural refinement for both compounds are given in Table 6-1. Fractional atomic coordinates and displacement parameters for each structure are given in Tables 6-2 – 6-4. In all cases the atoms were refined to full occupancy.

Nonlinear Optical Property Measurements. We used the frequency-tripled output of a passive-active mode-locked Nd:YAG laser with a pulse width of about 15 ps and a repetition rate of 10 Hz to pump an optical parametric amplifier (OPA). The OPA generates vertically polarized pulses in the ranges 400 ~ 685 nm and 737 ~ 3156 nm. In order to check the SHG efficiency as a function of the excitation energy, we tuned the wavelength of the incident light from 1000 ~ 2000 nm. In this range, the spectral bandwidth of the linearly polarized light from the OPA is rather broad, about 2 meV full

width at half maximum. However, the phase space compression phenomena ensures effective SHG where lower energy portions are exactly compensated by higher parts thereby satisfying both energy and momentum conservation. The incident laser pulse of 300 μJ was focused onto a spot 500 μm in diameter using a 3 cm focal-length lens. The corresponding incident photon flux is about 10 GW cm^{-2}. The SHG signal was collected in a reflection geometry from the excitation surface and focused onto a fiber optic bundle. The output of the fiber optic bundle is coupled to the entrance slit of a Spex Spec-One 500 M spectrometer and detected using a nitrogen-cooled CCD camera. The data collection time is 20 s.

Table 6-1. Crystallographic Data and Refinement Details for $Cs_5P_5Se_{12}$ and $Cs_4P_6Se_{12}$.

Formula	$Cs_5P_5Se_{12}$	$Cs_4P_6Se_{12}$.
Formula Weight	1766.92	1664.98
Space group	*P*-4 (no. 29)	$P2_1/n$ (no. 13)
a, Å	13.968(1)	10.836(1)
b, Å	13.968(1)	10.5437(8)
c, Å	7.546(1)	12.273(1)
β, deg.	90.000	98.661(8)
V, Å^3	1472.2(3)	1386.3(2)
Z	2	2
crystal size, mm^3	N/A	0.065 × 0.055 × 0.031
ρ_{calcd}, g cm^{-3}	3.986	3.989
μ, cm^{-1}	212.29	213.09
T, K	292(2)	100(2)
λ, Å	0.71073	0.71073
θ range, deg	1.46 – 28.25	2.33 – 29.99
Total reflections	12701	8320
Total unique reflections	3424	3961
No. parameters	73	101
Refinement method	Full-matrix least-squares on F^2	
Final R indices [$I>2\sigma(I)$], R1[a]/wR2 [b] (%)	3.00/7.27	4.29/10.36
R indices (all data), R1/wR2	3.70/8.55	7.52/14.03
Goodness-of-fit on F^2	1.159	1.077
Absolute structure parameter	0.06(2)	N/A

[a] $R1 = \sum ||F_O| - |F_C|| / \sum |F_O|$. [b] $wR2 = \{\sum [w(F_O^2 - F_C^2)^2] / \sum [w(F_O^2)^2]\}^{1/2}$

Table 6-2. Atomic coordinates ($\times 10^4$) and equivalent isotropic displacement parameters ($Å^2 \times 10^3$) for $Cs_5P_5Se_{12}$ and $Cs_4P_6Se_{12}$. U(eq) is defined as one third of the trace of the orthogonalized U_{ij} tensor.

	x	y	z	U(eq)
$Cs_5P_5Se_{12}$				
Cs(1)	3124(1)	6547(1)	2712(1)	46(1)
Cs(2)	3240(1)	355(1)	2544(1)	33(1)
Cs(3)	0	0	2477(1)	39(1)
Se(1)	-355(1)	3129(1)	2521(1)	30(1)
Se(2)	1492(1)	1856(1)	90(1)	30(1)
Se(3)	1473(1)	1780(1)	4911(1)	28(1)
Se(4)	1651(1)	4644(1)	5133(1)	32(1)
Se(5)	1275(1)	4778(1)	474(1)	26(1)
Se(6)	3466(1)	3698(1)	2132(1)	44(1)
P(1)	1125(1)	2564(1)	2537(3)	20(1)
P(2)	1994(1)	3924(1)	2678(3)	22(1)
P(3)	0	5000	2460(4)	26(1)
$Cs_4P_6Se_{12}$				
Cs(1)	4905(1)	-9(1)	2464(1)	13(1)
Cs(2)	5239(1)	4995(1)	1774(1)	15(1)
Se(5)	2385(1)	2359(1)	2759(1)	16(1)
Se(2)	2552(1)	2540(1)	7250(1)	14(1)
Se(3)	-16(1)	2876(1)	4993(1)	12(1)
Se(4)	2871(1)	-117(1)	4903(1)	14(1)
Se(6)	4914(1)	2553(1)	5048(1)	14(1)
Se(1)	2594(1)	4999(1)	5144(1)	14(1)
P(1)	1948(3)	2999(3)	5557(2)	11(1)
P(2)	2954(3)	1819(3)	4429(2)	12(1)
P(3)	4334(3)	4502(3)	4359(2)	14(1)

Table 6-3. Anisotropic displacement parameters ($Å^2 \times 10^3$) for $Cs_5P_5Se_{12}$ and $Cs_4P_6Se_{12}$. U(eq) is defined as one third of the trace of the orthogonalized U_{ij} tensor.

	U_{11}	U_{22}	U_{33}	U_{23}	U_{13}	U_{12}
$Cs_5P_5Se_{12}$						
Cs(1)	59(1)	41(1)	39(1)	-8(1)	2(1)	-13(1)
Cs(2)	30(1)	41(1)	28(1)	0(1)	4(1)	4(1)
Cs(3)	41(1)	48(1)	29(1)	0	0	-11(1)
Se(1)	22(1)	37(1)	30(1)	2(1)	0(1)	2(1)
Se(2)	42(1)	27(1)	20(1)	-6(1)	2(1)	3(1)
Se(3)	40(1)	25(1)	20(1)	4(1)	-2(1)	4(1)
Se(4)	41(1)	29(1)	26(1)	-7(1)	1(1)	2(1)
Se(5)	29(1)	26(1)	22(1)	5(1)	2(1)	2(1)
Se(6)	23(1)	64(1)	46(1)	-9(1)	2(1)	4(1)
P(1)	24(1)	18(1)	16(1)	-1(1)	1(1)	2(1)
P(2)	23(1)	21(1)	22(1)	-1(1)	0(1)	2(1)
P(3)	24(1)	36(1)	19(1)	0	0	5(1)
$Cs_4P_6Se_{12}$						
Cs(1)	30(1)	32(1)	32(1)	-3(1)	5(1)	0(1)
Cs(2)	38(1)	37(1)	30(1)	1(1)	2(1)	-7(1)
Se(1)	16(1)	28(1)	43(2)	4(1)	4(1)	3(1)
Se(2)	41(2)	37(2)	25(2)	4(1)	6(1)	12(1)
Se(3)	33(2)	17(1)	38(2)	1(1)	1(1)	2(1)
Se(4)	16(1)	31(1)	33(1)	-1(1)	2(1)	-4(1)
Se(5)	33(2)	34(2)	22(1)	-3(1)	-3(1)	1(1)
Se(6)	24(1)	18(1)	49(2)	-3(1)	12(1)	-4(1)
P(1)	19(3)	20(3)	25(3)	0(3)	4(3)	3(3)
P(2)	15(3)	18(3)	25(3)	0(3)	3(2)	-1(2)
P(3)	20(3)	22(3)	32(4)	-6(3)	7(3)	-2(3)

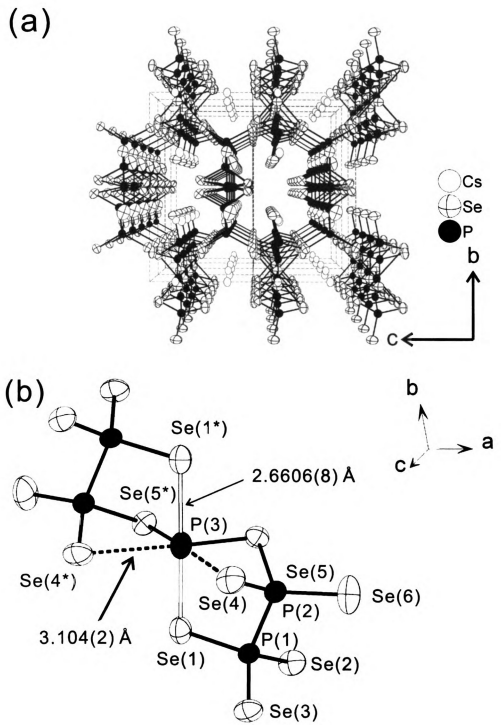

Figure 6-1. (a) The noncentrosymmetric structure of $Cs_5P_5Se_{12}$. The thermal ellipsoids are shown with 60% probability. (b) $[P_5Se_{12}]^{5-}$ anion. White lines denote long P-Se bonding at P(3)-Se(1), 2.6606(8) Å. Dashed lines indicate short Se···Se nonbonding interaction at P(3)···Se(4), 3.104(2) Å. * is defined as equivalent position (-*x*, 1-*y*, *z*).

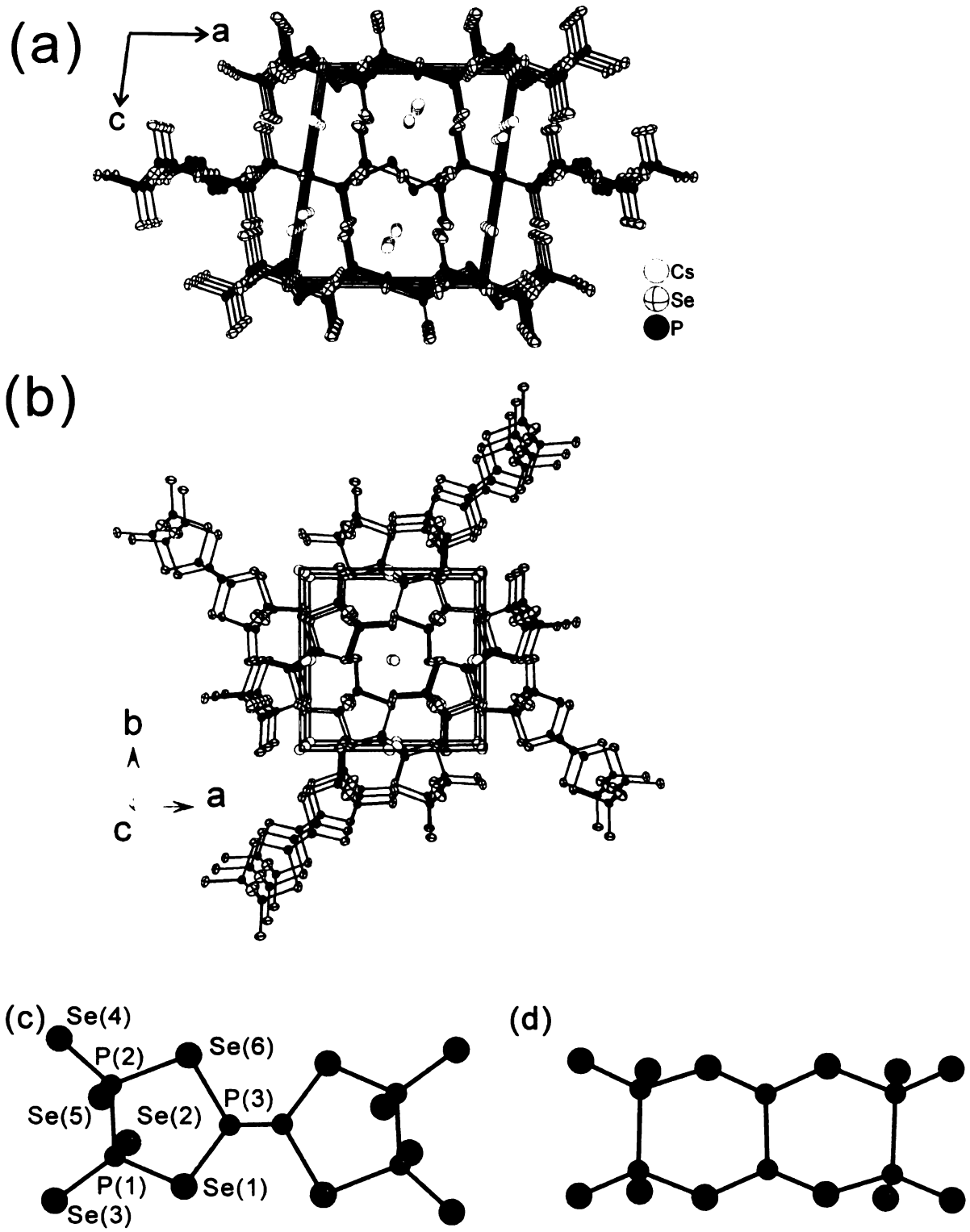

Figure 6-2. Structure of $Cs_4P_6Se_{12}$ viewed down the (a) *c*-axis and (b) *b*-axis. The thermal ellipsoids are shown with 60% probability. (c) The β-$[P_6Se_{12}]^{4-}$ anion and (d) α-$[P_6Se_{12}]^{4-}$ anion for comparison.

Table 6-4. Selected bond distances (Å) and angles (deg) for $Cs_5P_5Se_{12}$.

P(1)-Se(1)	2.2127(18)	P(2)-Se(6)	2.1207(19)
P(1)-Se(2)	2.156(2)	P(3)-Se(1)	2.6606(8) ×2
P(1)-Se(3)	2.156(2)	P(3)-Se(5)	2.349(2) ×2
P(2)-Se(4)	2.162(2)	P(1)-P(2)	2.257(2)
P(2)-Se(5)	2.280(2)		
Se(1)-P(1)-P(2)	101.72(8)	Se(5*)-P(3)-Se(5)	100.67(12)
Se(2)-P(1)-P(2)	107.36(9)	Se(5)-P(3)-Se(1*)	89.97(5)
Se(3)-P(1)-P(2)	105.49(9)	Se(5*)-P(3)-Se(1)	89.97(5)
Se(3)-P(1)-P(2)	115.14(8)	Se(5)-P(3)-Se(1)	91.29(5)
Se(3)-P(1)-P(1)	113.35(9)	Se(1*)-P(3)-Se(1)	178.02(13)
Se(2)-P(1)-P(1)	112.41(9)	P(2)-P(5)-Se(3)	86.42(7)
Se(6)-P(2)-P(1)	116.78(9)	P(1)-P(2)-Se(4)	108.22(9)
Se(6)-P(2)-P(5)	111.29(9)	P(1)-P(2)-Se(5)	99.70(9)
Se(4)-P(2)-P(5)	106.52(8)	P(1)-P(2)-Se(6)	112.80(9)

* denotes the crystallographically equivalent position by symmetry transformation of ($-x$, $-y+1$, z).

Table 6-5. Selected bond distances (Å) and angles (deg) for $Cs_4P_6Se_{12}$.

P(1)-Se(1)	2.303(2)	P(2)-Se(6)	2.281(2)
P(1)-Se(2)	2.137(2)	P(3)-Se(1)	2.303(2)
P(1)-Se(3)	2.140(2)	P(3)-Se(6)	2.274(2)
P(2)-Se(4)	2.128(2)	P(1)-P(2)	2.260(2)
P(2)-Se(5)	2.127(2)	P(1)-P(1‡)	2.232(2)
Se(1)-P(1)-Se(2)	111.26(9)	P(1)-P(2)-Se(6)	96.90(8)
Se(1)-P(1)-Se(3)	107.74(9)	P(2)-P(1)-Se(1)	100.29(8)
Se(2)-P(1)-Se(3)	116.42(8)	P(2)-P(1)-Se(2)	111.43(8)
Se(4)-P(2)-Se(5)	120.15(8)	P(2)-P(1)-Se(3)	108.43(8)
Se(4)-P(2)-Se(6)	108.07(8)	P(3‡)-P(3)-Se(1)	94.64(8)
Se(5)-P(2)-Se(6)	110.52(8)	P(3)-P(3)-Se(6)	92.84(8)
Se(1)-P(3)-Se(6)	104.36(8)	P(1)-Se(1)-P(3)	100.29(8)
P(1)-P(2)-Se(4)	108.43(8)	P(2)-Se(6)-P(3)	89.50(8)
P(1)-P(2)-Se(5)	110.26(8)		

‡ denotes the crystallographically equivalent position by symmetry transformation (-x+1, -y+1, -z+1).

4. Results and Discussion

Crystal Structure. The new compound $Cs_5P_5Se_{12}$ crystallizes in the noncentrosymmetric nonpolar space group *P*-4, Figure 6-1a. It features the discrete molecular $[P_5Se_{12}]^{5-}$ anion with two types of formal charge 3+ and 4+ on P, Figure 6-1b. The trivalent formal charge is found on P(3) which is a central P atom chelated with two ethane-like $[P_2Se_6]^{4-}$ units to form a novel octahedral complex. The octahedral coordination of the trivalent P(3) atom is very unusual and features long bond distances e.g. P(3)-Se(1) at 2.6606(8) Å and an even longer interaction of P(3)···Se(4) at 3.104(2) Å. The latter distance is much shorter than the 3.76 Å of the van der Waals radii sum.[16] The P(3)-Se(5) distance is normal at 2.349(2) Å. If the anion is to be viewed as a coordination complex, the P(3) atom plays the role of the metal and the formula can be expressed as $\{P[P_2Se_6]_2\}^{5-}$. P-Se bond distances in the chelating $[P_2Se_6]^{4-}$ ligands range from 2.121(2) to 2.280(2) Å. The $[P_2Se_6]^{4-}$ ligands in the molecule represent typical *anti*-type conformation but are distorted (See relevant angles in Table 6-4.).

It is noted that the bond angles for P(3) are close to 90° or 180°, Figure 5-1. Deviation from 90° [Se(4)-P(3)-Se(4), 98.94(2); Se(4)-P(3)-Se(5), 80.22(3); Se(5)-P(3)-Se(5), 100.67(3)] is caused by the μ_2-P(2). As a result, the octahedron around P(3) has excellent definition. The dihedral angle of Se(5)-Se(4)-Se(4)-Se(5) is only 2.35(2)° and indicates that the equatorial Se(2), Se(5), Se(5) and Se(2) atoms are nearly coplanar.

It is noteworthy that $Cs_5[P_5Se_{12}]$ is the chalcophosphate counterpart of $Cs_5[In(P_2Se_6)_2]$[17] where P(3) occupies the In^{3+} site. Generally, phosphorus is not regarded as a coordinating metal but the isolation of $\{P[P_2Se_6]_2\}^{5-}$ suggests that P itself can be such a center for $[P_xQ_y]^{n-}$, $[Ge_xQ_y]^{n-}$ or $[Sn_xQ_y]^{n-}$ ligands to produce novel complexes.

$Cs_4P_6Se_{12}$ crystallizes in the monoclinic space group $P2_1/n$, Figure 6-2a, b. The compound features the new molecule β-$[P_6Se_{12}]^{4-}$, Figure 6-2c. The central P_2 dimer is coordinated with two $[P_2Se_6]$ units to form a fulvalene-like skeleton. Both isomers α– and β-$[P_6Se_{12}]^{4-}$ anions consist of the central $[P_2]$ and two $[P_2Se_6]$ residues but they bind in a different fashion, Figure 5-2. The β-species has a center of symmetry at the middle of the P(3)-P(3*) bond and adopts the C_i point group. The formal charge on the P(3) atoms in the central $[P_2]$ is 2+. The P(3)-P(3*) distance at 2.232(2) Å but slightly longer than the corresponding distance of 2.189(6) Å found in α-$[P_6Se_{12}]^{4-}$. α- and β-$[P_6Se_{12}]^{4-}$ were isolated as Rb^+ and Cs^+ salts, respectively, but it is unclear if the different structures are due to differences in packing forces associated with the alkali metal size.

Phase-Change Behavior. Differential thermal analysis (DTA) of $Cs_4P_6Se_{12}$ performed at a rate of 10 °C min^{-1} showed reversible crystal-glass phase transition, Figure 6-3a. Upon heating the compound melted at 424 °C and upon cooling the melt solidified to a red glass. Only subsequent heating restored the crystals with an exothermic event at 263 °C followed by melting at 424 °C. Glass transition was observed at 204 °C for each cooling step. The amorphous nature of the glassy phase was confirmed with X-ray powder diffraction. The X-ray powder patterns after recrystallization were the same as those of pristine $Cs_4P_6Se_{12}$ indicating full recovery of the original crystal structure, Figure 6-3b. Recrystallization and vitrification were reversible as they could be repeatedly observed over many cycles. At cooling rates of 10 °C min^{-1} $Rb_4P_6Se_{12}$ did not glassify suggesting that its glass crystallizes faster than that of $Cs_4P_6Se_{12}$. DTA of $Cs_5P_5Se_{12}$ performed at a rate of 10 °C min^{-1} exhibited the similar reversible phase-transition behavior but it melted at 424 °C, formed a red glass at 250 °C and recrystallized at

243 °C, Figure 6-3c. The X-ray powder patterns before and after DTA of $Cs_4P_6Se_{12}$ is shown in Figure 6-4d.

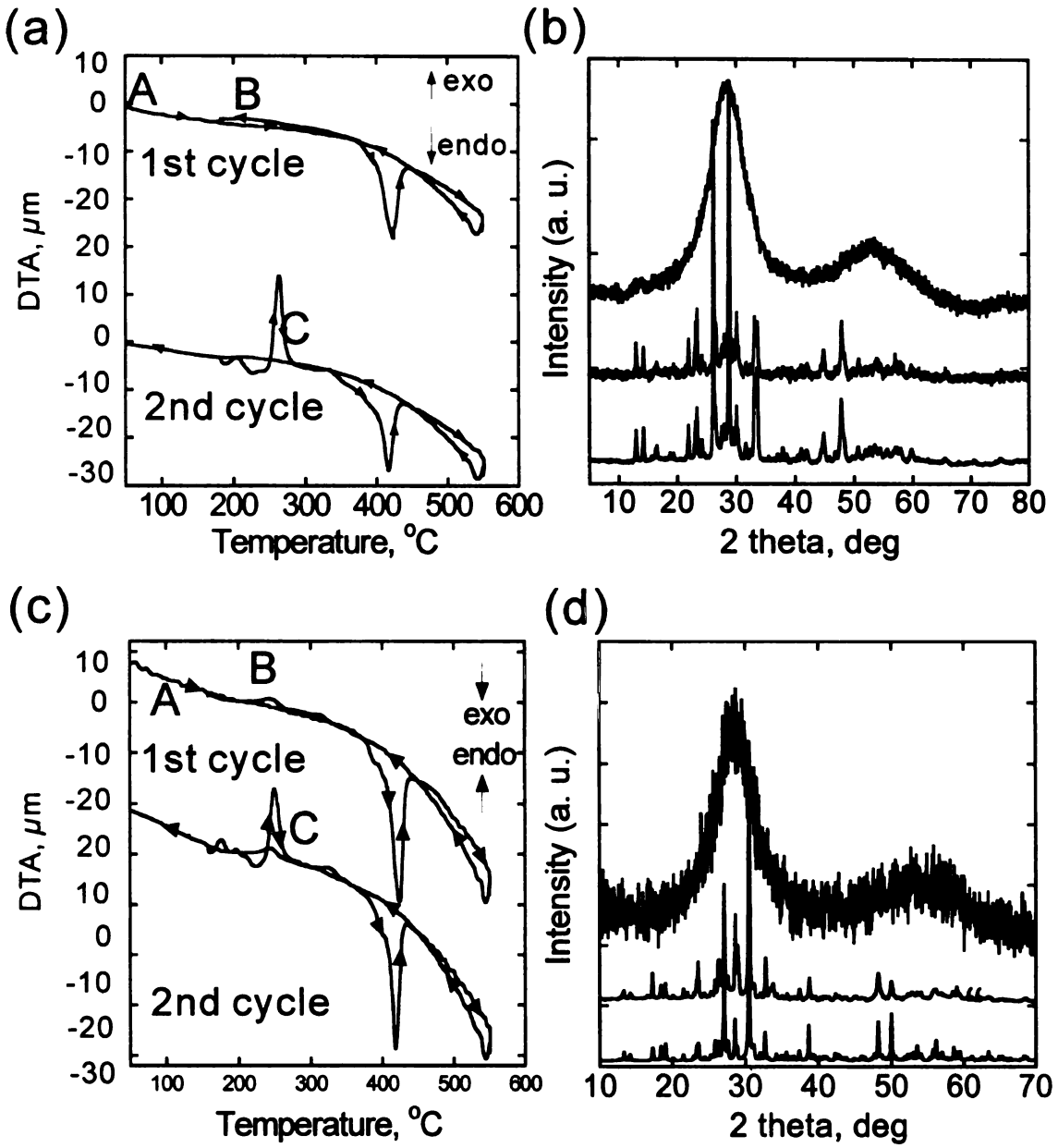

Figure 6-3. Differential thermal analysis diagrams of (a) $Cs_4P_6Se_{12}$ and (c) $Cs_5P_5Se_{12}$ showing melting in the 1st cycle with no crystallization on cooling (upper line). Glass crystallization is observed in the 2nd heating cycle. $Cs_4P_6Se_{12}$ and $Cs_5P_5Se_{12}$ are a pristine crystal at A, glass at B and restored crystal at C, respectively. X-ray powder diffraction patterns of (b) $Cs_4P_6Se_{12}$ (d) $Cs_5P_5Se_{12}$ pristine (below), glassy (upper) and recrystallized crystal(middle).

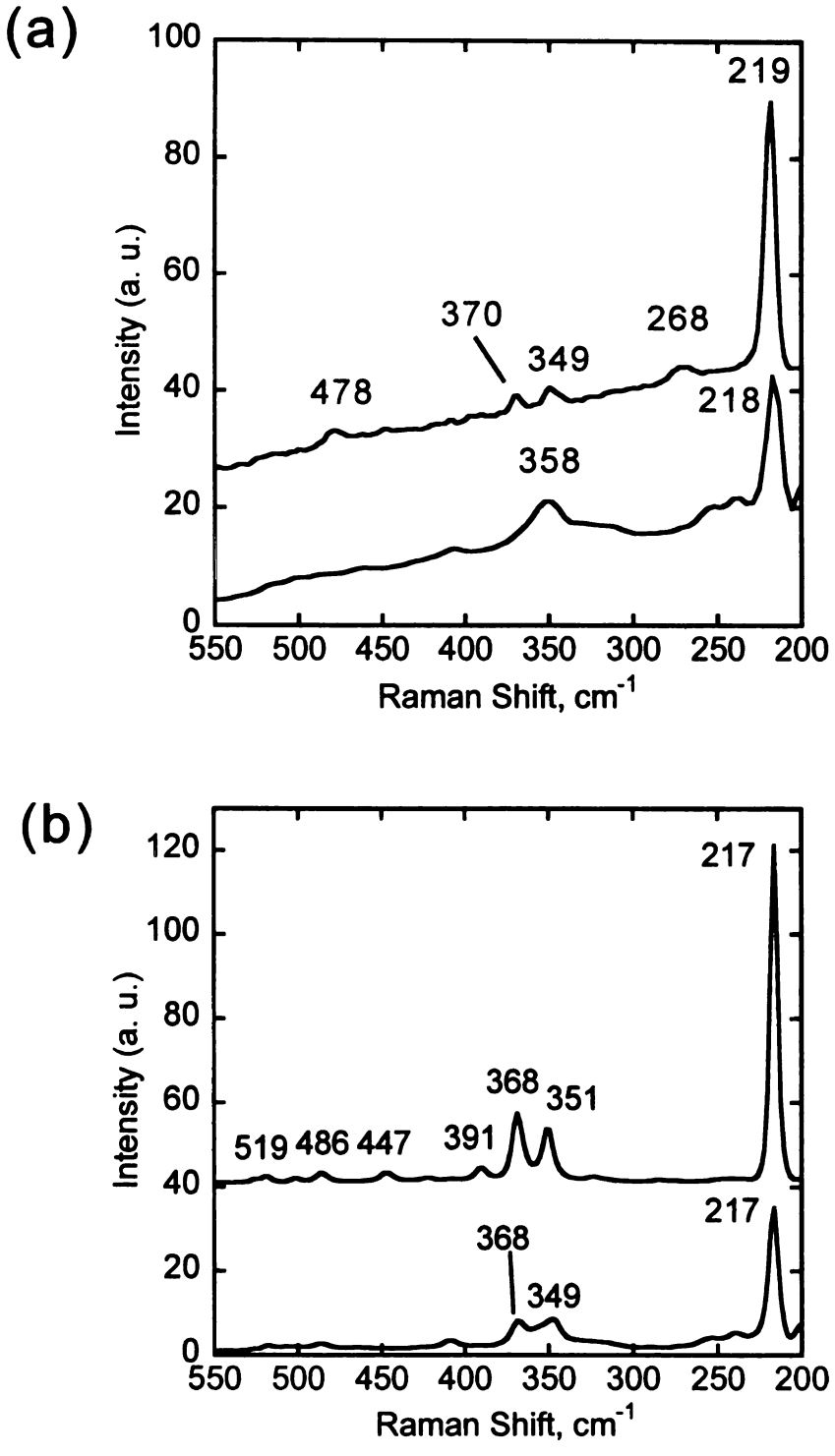

Figure 6-4. Raman spectra of crystalline (upper trace) and glassy (lower trace) of (a) $Cs_5P_5Se_{12}$ and (b) $Cs_4P_6Se_{12}$.

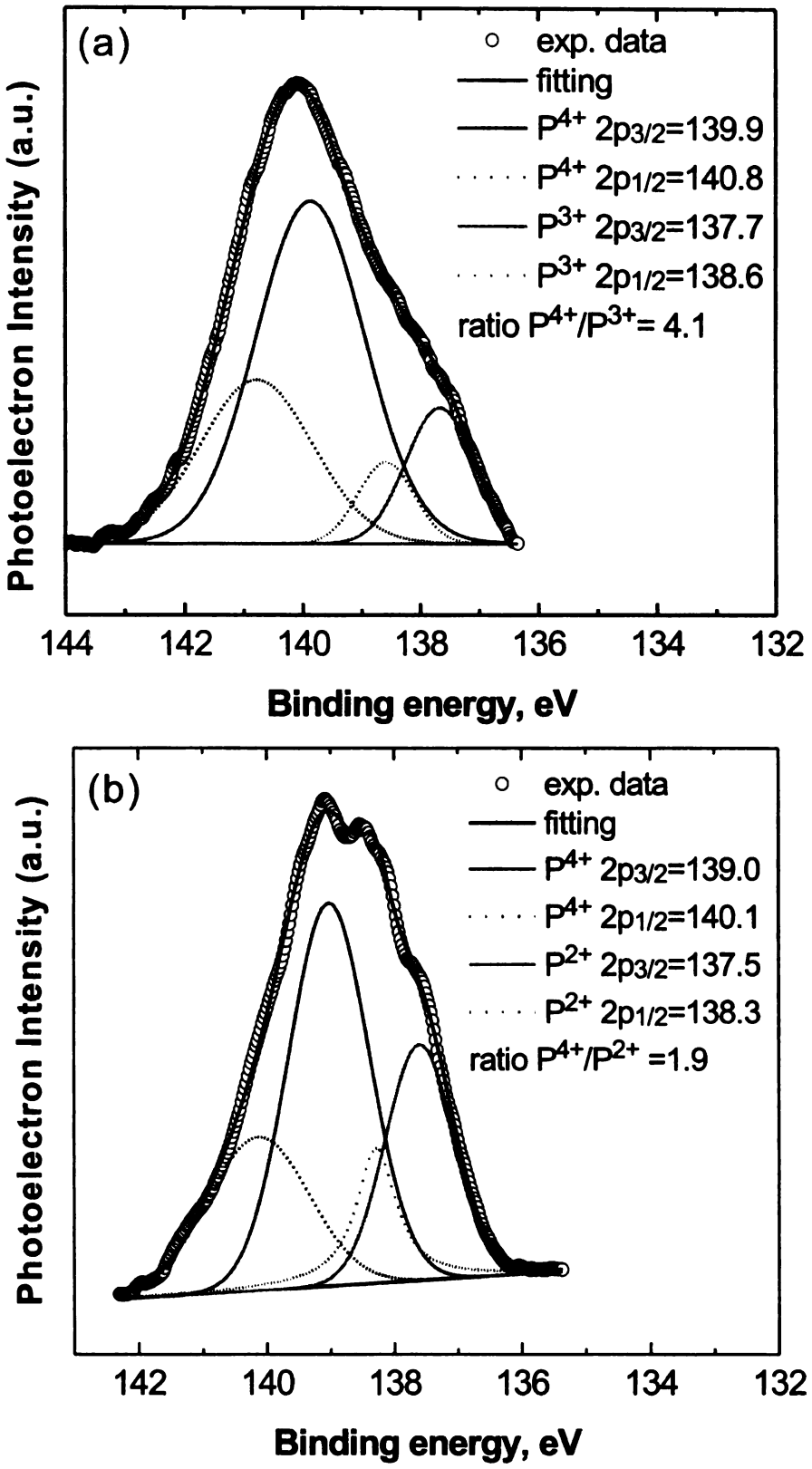

Figure 6-5. The X-ray photoelectron spectrum, peak fitting, and deconvolution profiles in the P 2p region of (a) $Cs_5P_5Se_{12}$ and (b) $Cs_4P_6Se_{12}$.

The Raman spectra of $Cs_5P_5Se_{12}$ display shifts at 219(s), 268(s), 349(w), 370(w), 478(w) and for $Cs_4P_6Se_{12}$ 221(s), 351(m), 368(m), 391(w), 447(w), 486(w) and 519(w) cm^{-1}, Figure 6-4. The spectra for both compounds were very similar. For $Cs_4P_6Se_{12}$, the shift at 221 cm^{-1} can be assigned to the P_2Se_6 stretching mode by comparison in the A_g stretching mode of D_{3d} symmetry of $[P_2Se_6]^{4-}$ ligand.[18] Other peaks at 486 and 519 cm^{-1} are also related to the P_2Se_6 fragment.[19] Peaks at 351 and 368 cm^{-1} were similarly observed in the spectrum of $Rb_4P_6Se_{12}$. The Raman spectra of glassy $Cs_5P_5Se_{12}$ and $Cs_4P_6Se_{12}$ showed broader and weaker peaks at 218 and 358 cm^{-1} for the former and 217, 349, and 368 cm^{-1} for the latter. These are at similar positions to those of the crystalline phase suggesting that local structural motif is preserved in the glass, but crystallographic long range order is lost as seen in the X-ray powder diffraction patterns of glassy $Cs_5P_5Se_{12}$ and $Cs_4P_6Se_{12}$.

The X-ray Photoelectron Spectra of $Cs_5P_5Se_{12}$ and $Cs_4P_6Se_{12}$ confirmed the presence of two different oxidation states in the compounds, Figure 6-5. Since the higher binding energy results from the higher oxidation state of a corresponding element in principle, for $Cs_5P_5Se_{12}$ peaks at higher energy (140.8, 139.9 eV) are assigned to P^{4+} centers and peaks at 138.6 and 137.7 eV are assigned to P^{3+}. The XPS analysis revealed ratio of lower/higher oxidation state of P to be 4.1 and 1.9 for $Cs_5P_5Se_{12}$ and $Cs_4P_6Se_{12}$, respectively, which supported the structural analysis: $Cs_5[P^{3+}\{P^{4+}{}_2Se_6\}_2]$ and $Cs_4[(P^{2+})_2\{P^{4+}{}_2Se_6\}_2]$.

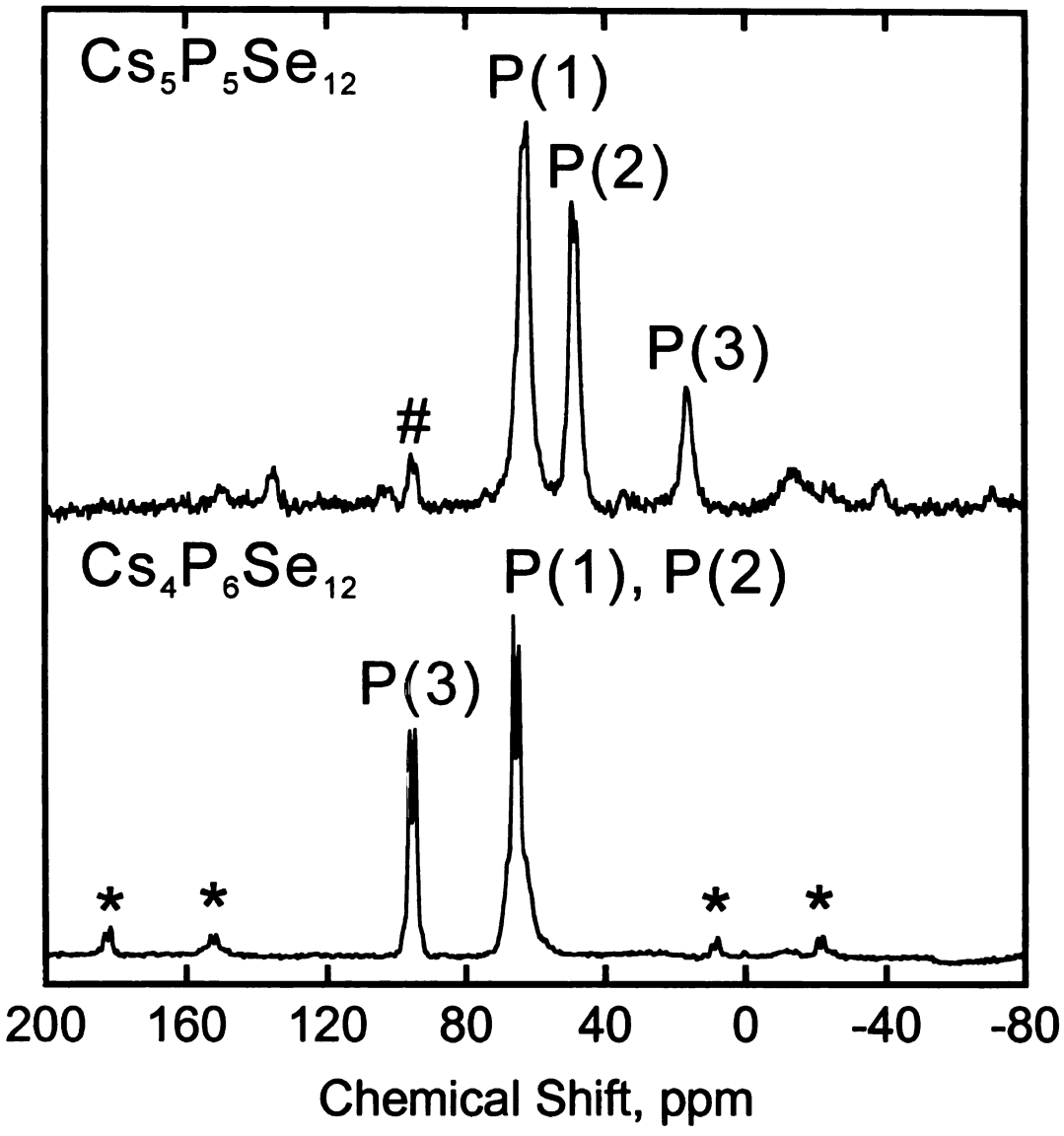

Figure 6-6. ^{31}P solid-state NMR spectra of $Cs_5P_5Se_{12}$ and $Cs_4P_6Se_{12}$ at a 14 kHz MAS frequency. * denotes spinning side bands and # $Cs_4P_6Se_{12}$ impurity.

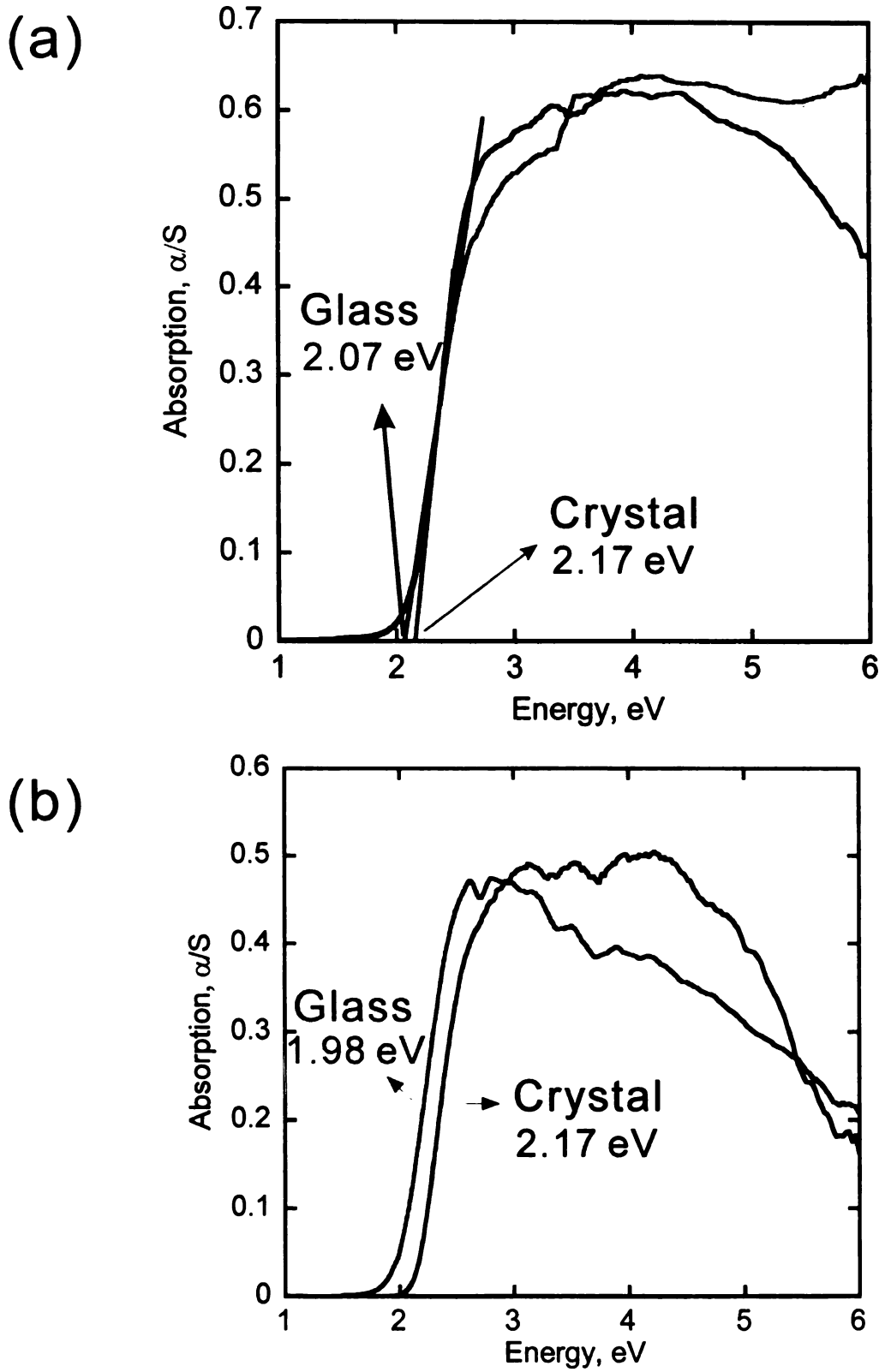

Figure 6-7. The electronic absorption spectra of crystalline and glassy (a) $Cs_5P_5Se_{12}$ and (b) $Cs_4P_6Se_{12}$.

^{31}P Solid-state NMR Spectroscopy. Room temperature solid-state ^{31}P NMR spectra of $Cs_5P_5Se_{12}$ and $Cs_4P_6Se_{12}$ were collected, Figure 6-6. The spectrum of $Cs_4P_6Se_{12}$ contained two doublets centered at 95.5 ppm and 65.5 ppm with coupling constants of J = 250 and J = 270 Hz, respectively, with an approximately 1:2 intensity ratio. Assignment of these peaks is to the P^{2+} and P^{4+} atoms, respectively. The P(1) and P(2) chemical environments are very similar, and the bond lengths and angles for each nearly agree within the error of the crystallographic refinement. It is therefore reasonable that the chemical shifts corresponding to these atoms overlap, thus accounting for the observed 1:2 ratio of the spectral peaks. One possible assignment of the observed splittings is two bond P-P J-coupling. Two bond P-P scalar coupling in the solution phase have been observed with coupling constants of ~300 Hz.[20] However, other compounds such as $KBiP_2S_7$[21] and $Rb_4P_6Se_{12}$[5] contained inequivalent ^{31}P atoms separated by two bonds and two bond P-P coupling was not observed. Another possible assignment is that the 95.5 and 65.5 ppm peaks correspond to the P(1) and P(2) atoms and the observed splitting is one-bond P(1)-P(2) J coupling. In this assignment, the P(3) signal was not detected. It is noted that the 95.5 and 65.5 ppm peaks were the only significant isotropic peaks observed under the conditions of a 5000 s delay between acquisitions and a 1200 ppm spectral window. One weakness in this assignment is that the 95.5/65.5 ppm intensity ratio is <1.

The spectrum of $Cs_5P_5Se_{12}$ showed two doublets centered at 63.1 ppm and 48.7 ppm with coupling constant of J = 200 Hz and singlet centered at 16.1 ppm, Figure 5-6. The difference in bond lengths and angles between the P(1) and P(2) coordination environments is significantly outside of the range of the error in the crystallographic refinement, and therefore distinct chemical shifts resulting from each of these sites are

predicted. Including the signal from the P(3) atom, there should therefore be three peaks in the NMR spectrum. One possible assignment is that the two doublets centered at 63.1 ppm and 48.7 ppm can be attributed to the P(1) and P(2) nuclei and the singlet at 16.1 ppm can be attributed to the P(3) nucleus. There are twice as many P(1) and P(2) atoms per formula unit than P(3) atoms, so the spectral intensity of the peaks corresponding to P(1) and P(2) should be twice that of P(3). The spectral intensity of the 63.1 ppm and 48.7 ppm peaks is ~3.5 and ~2.5-fold greater than the 16.1 ppm peak, respectively. The peak at 94.9 ppm is likely due to $Cs_4P_6Se_{12}$ impurity in the sample and this impurity would also result in a 65.5 ppm peak which would be unresolved from the 63.1 ppm peak of $Cs_5P_5Se_{12}$. The $Cs_4P_6Se_{12}$ impurity could therefore account for some of the discrepancy between the observed and predicted intensities of this assignment. The splitting of the 63.1 and 48.7 ppm peaks is attributed to one-bond P-P coupling between the crystallographically inequivalent P(1) and P(2) atoms. The two bond P(1)-P(3) or P(2)-P(3) scalar coupling was not observed. Previously, P^{4+} in selenophosphate anions with P-P bonds were observed to have positive ^{31}P chemical shifts, and P^{5+} in selenophosphate anions without P-P bonds were observed to have negative ^{31}P chemical shifts.[22] The chemical shift of the non P-P bonded P^{3+} atom in this compound, namely P(3), was assigned to a spectral feature with a positive chemical shift. The longitudinal relaxation times were ~600(100), 70(10), and 10(3) s for the 63.1, 48.7, and 16.1 ppm features, respectively. The latter two values are somewhat shorter than those of typical selenophosphates.[14] Phosphorus-containing compounds with multiple crystallographically unique ^{31}P sites typically do not have such a wide range of longitudinal relaxation times for the ^{31}P sites.

The solid state electronic absorption spectra revealed sharp absorption edges for $Cs_5P_5Se_{12}$ and $Cs_4P_6Se_{12}$ at approximately the same energy of 2.17 eV, consistent with their orange color, Figure 6-7. The energy gap of the glassy phases was measured at 2.07 and 1.98 eV, respectively. The lower energy gaps of the glasses can be attributed to structural defects that create mid-gap states and band tailing.[23] A spectral shift in the absorption edge is a key feature in creating nonvolatile memory devices.[24]

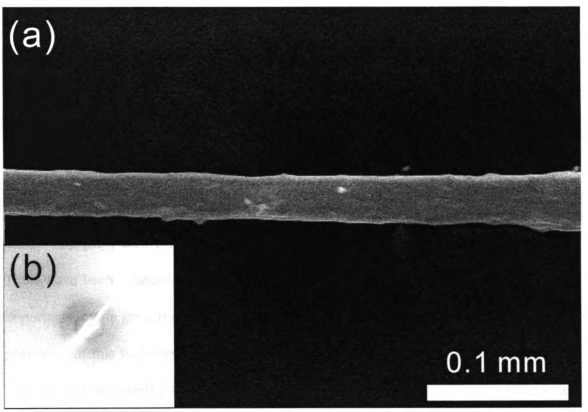

Figure 6-8. (a) Representative SEM image of $Cs_5P_5Se_{12}$ glass fiber. (b) X-ray powder diffraction pattern of $Cs_5P_5Se_{12}$ glass fiber showing its amorphous nature.

Second Harmonic Generation Response of Crystalline $CS_5P_5Se_{12}$. Because of the non-centrosymmetric crystal structure of $Cs_5P_5Se_{12}$ and its good optical transparency from the edge of the energy gap to the mid-IR region, we investigated its second

harmonic generation (SHG) response at room temperature, Figure 3d. Using a modified Kurtz powder technique we measured polycrystalline samples of 45-63 μm size using 1200-2000 nm fundamental idler radiation from a tunable laser.[25] The SHG intensities obtained were compared with those of $LiNbO_3$ and $AgGaSe_2$, which is a representative NLO material for IR applications.[26] All samples were similarly prepared, and the same particle size range and identical laser setting were used. The SHG intensity of $Cs_5P_5Se_{12}$ was approximately equal to that of $LiNbO_3$ and 25% that of $AgGaSe_2$.[24] As the particle size of $Cs_5P_5Se_{12}$ increased, the SHG intensity continuously decreased. Generally, when a powder sample is non-phase-matchable, SHG sensitivity peaks near the coherence length, which is typically 1~20 μm, and it starts to diminish through larger particle sizes. In this regard, $Cs_5P_5Se_{12}$ is type-I non-phase-matchable.[25] Despite this such materials can be useful through 'random' quasi-phase-matching.[28]

Second Harmonic Generation Response of Glassy $CS_5P_5Se_{12}$. Surprisingly, glassy $Cs_5P_5Se_{12}$ also exhibited significant SHG response, at ~ 5% that of $AgGaSe_2$. There have been tremendous efforts to induce SHG in glasses because of technological importance by its great transparency and formability, e.g. fabricating optical fibers.[29] It is possible that this is a rare example of observation of SHG response from an amorphous material with no specific treatment such as thermal poling, electron beam irradiation and so on.[30] Since $Cs_5P_5Se_{12}$ is a phase-change material and retains its local structural motif in the glassy state, as shown by Raman spectroscopy, we can expect the noncentrosymmetric arrangement to be partially preserved and plausibly give rise to some SHG response. Indeed, SHG of glass sample was observed and X-ray powder diffraction patterns taken after the measurements still showed a predominantly

amorphous nature for the sample. It cannot be completely ruled out, however, that idler beam-induced crystallization of glass may be occurring or the existence of nanocrystals embedded in glass matrix due to its phase-change property. Further investigation of the glass thin film is in progress.

$Cs_5P_5Se_{12}$ glass fibers were easily fabricated by rapid cooling extraction from the corresponding hot melt at 600 °C. Representative SEM image showed the relatively uniform formation of glass fiber and its amorphous nature was confirmed by X-ray powder diffraction patterns, Figure 6-8. When the glass fiber was heated up and annealed at 320 °C, crystallinity was fully recovered. This suggests that phase-change material with NLO property can be a potential source for facile fabrication of NLO glass fiber for IR application.

5. Concluding Remarks

The results of this study demonstrate that novel species in the chalcophosphate family can be stabilized with reduced P atoms in their structure. The low valent phosphorus in $Cs_5P_5Se_{12}$ and $Cs_4P_6Se_{12}$ is expressed with the central P^{3+} and P_2^{4+} centers playing the role of a metal center to form the unusual coordination complexes $\{P[P_2Se_6]\}^{5-}$ and $\{P_2[P_2Se_6]\}^{4-}$. Both compounds exhibit phase-change behavior by forming glasses. The crystalline and glassy $Cs_5P_5Se_{12}$ showed significant SHG response in the near infrared region of the spectrum. Glass fiber of $Cs_5P_5Se_{12}$ was easily obtained by simple rapid cooling extraction from the corresponding hot melt and its amorphous nature was confirmed.

References.

(1) Garin, J.; Parthe, E. *Acta Crystallogr., Sect. B*, **1972**, *28*, 3672-3674.

(2) Francisco, R. H. P.; Tepe, T.; Eckert, H. *J. Solid State Chem.* **1993**, *107*, 452-459.

(3) Chondroudis, K.; Kanatzidis, M. G. *Inorg. Chem.* **1995**, *34*, 5401-5402.

(4) Chondroudis, K.; Kanatzidis, M. G. *Inorg. Chem.*, **1998**, *37*, 2582-2584.

(5) Chung, I.; Karst, A. L.; Weliky, D. P.; Kanatzidis, M. G. *Inorg. Chem.*, **2006**, *45*, 2785-2787.

(6) Chung, I.; Do, J.; Canlas, C. G.; Weliky, D. P.; Kanatzidis, M. G. *Inorg. Chem.*, **2004**, *43*, 2762-2764.

(7) Chung, I.; Christos, C. D.; Jang, J. I.; Canlas, C. G.; Weliky D. P.; Kanatzidis, M. G. *J. Am. Chem. Soc.***2007**, *129*, 14996-15006.

(8) (a) Scott, B.; Pressprich, M.; Willet, R. D.; Cleary, D. A. *J. Solid State Chem.* **1992**, *96*, 294-300. (b) Carpentier, C. D.; Nitsche, R. *Mater. Res. Bull.* **1974**, *9*, 1097-1100.

(9) (a) Clement, R.; Lacroix, P. G.; Ohare, D.; Evans, J. *Adv. Mater.* **1994**, *6*, 794-797. (b) Lacroix, P. G.; Clement, R.; Nakatani, K.; Zyss, J.; Ledoux, I. *Science*, **1994**, *263*, 658-660.

(10) (a) Lemehaute, A.; Ouvrard, G.; Brec, R.; Rouxel, J. *Mater. Res. Bull.* **1977**, *12*, 1191-1197. (b) Thompson, A. H.; Whittingham, M. S. *US Pat.*, 4 049 879, **1977**.

(11) Huang, Z. L.; Cajipe, V. B.; Lerolland, B.; Colombet, P.; Schipper, W. J.; Blasse, G. *Eur. J. Solid State Inorg. Chem.* **1992**, *29*, 1133-1144.

(12) Breshears, J. D.; Kanatzidis, M. G. *J. Am. Chem. Soc.* **2000**, *122*, 7839-7840.

(13) (a) *Reflectance Spectroscopy*, Wendlandt, W. W. and Hecht, H.G.; Interscience Publishers: New York, 1966. (b) *Reflectance Spectroscopy*, Kotüm, G.; Springer-Verlag: New York, 1969. (c) Tandon, S. P.; Gupta, J. P. *Phys. Status Solidi*, **1970**, *38*, 363-367.

(14) Canlas, C. G.; Muthukumaran, R. B.; Kanatzidis, M. G.; Weliky, D. P. *Solid State Nucl. Magn. Reson.* **2003**, *24*, 110-122.

(15) SMART, SAINT, SHELXTL: Data Collection and Processing Software for the SMART-CCD system; Siemens Analytical X-ray Instruments Inc.: Madison, WI, 1997.

(16) Bondi, A. *J. Phys. Chem.*, **1964**, *68*, 441-451.

(17) Chondroudis, K.; Chakrabarty, D.; Axtell, E. A.; Kanatzidis, M. G. *Z. Anorg. Allg. Chem.*, **1998**, *624*, 975-979.

(18) (a) Brockner, W.; Ohse, L.; Pätzmann, U.; Eisenmann, B.; Schäfer, H. *Z. Naturforsch., A*, **1985**, *40*, 1248-1252. (b) Pätzmann, U.; Brockner, W. *Z. Naturforsch., A.* **1987**, *42*, 515-516.

(19) Aitken, J. A.; Evain, M.; Iordanidis, L.; Kanatzidis, M. G. *Inorg. Chem.* **2002**, 41, 180-191.

(20) (a) Pregosin, P. S.; Kunz, R. W. *^{31}P and ^{13}C NMR of Transition Metal Phosphine Complexes*. Springer-Verlag: Berlin ; New York, 1979; p 156 p. (b) Perera, S. D.; Shaw, B. L. *J. Chem. Soc. Chem. Commun.* **1995**, 865-866.

(21) (a) Gave, M.; Malliakas, C. D.; Weliky, D. P.; Kanatzidis, M. G. *Inorg. Chem.* **2007**, 46, 3632-3644. (b) McCarthy, T.; Kanatzidis, M. G. *J. Alloys Compd.* **1996**, 236, 70-85.

(22) Canlas, C. G.; Kanatzidis, M. G.; Weliky, D. P. *Inorg. Chem.* **2003**, 42, 3399-3405.

(23) (a) Marking, G. A.; Hanko, J. A.; Kanatzidis, M. G. *Chem. Mater.* 1998, **10**, 1191-1199. (b) Dhingra, S.; Kanatzidis, M. G. *Science* **1992**, *258*, 1769-1772.

(24) (a) Kyratsi, T.; Chrissafis, K.; Wachter, J. B.; Paraskevopoulos, K. M.; Kanatzidis, M. G. *Adv. Mater.* **2003**, *15*, 1428-1431. (b) Maeda, Y.; Andoh, H.; Ikuta, I.; Minemura, H. *J Appl. Phys.* **1988**, *64*, 1715-1719. (c) Maior, M. M.; Rasing, T.; Eijt, S. W. H.; Vanloosdrecht, P. H. M.; Vankempen, H.; Molnar, S. B.; Vysochanskii, Y. M.; Motrij, S. F.; Slivka, V. Y. *J. Phys.: Condens. Matter*, **1994**, *6*, 11211-11220. (c) Wachter, J. B.; Chrissafis, K.; Petkov, V.; Malliakas, C. D.; Bilc, D.; Kyratsi, T.; Paraskevopoulos, K. M.; Mahanti, S. D.; Torbrugge, T.; Eckert, H.; Kanatzidis, M. G. *J. Solid State Chem.* **2007**, *180*, 420-431.

(25) (a) Kurtz, S. K.; Perry, T. T. *J Appl. Phys.* **1968**, *39*, 3798-3813. (b) Dougherty, J. P.; Kurtz, S. K. *J. Appl. Crystallogr.* **1976**, *9*, 145-158.

(26) Nikogosyan, D. N. *Nonlinear optical crystals: a complete survey*. Springer-Science: New York, 2005.

(27) Choy, M. M.; Byer, R. L. *Phys. Rev. B* **1976**, *14*, 1693-1706.

(28) Baudrier-Raybaut, M.; Haïdar, R.; Kupecek, Ph.; Lemasson, Ph.; Rosencher, E. *Nature*, **2004**, *432*, 374-376.

(29) Antonyuk, B. P.; Antonyuk, V. B. *Opt. Commun.* **1998**, 147, 143-147.

(30) (a) Fokine, M.; Saito, K.; Ikushima, A. J. *Appl. Phys. Lett.* **2005,** *87*, 171907. (b) Fujiwara, T.; Takahashi, M.; Ikushima, A. J. *Appl. Phys. Lett.* **1997,** *71*, 1032-1034. (c) Qiu, M. X.; Pi, F.; Orriols, G. *Appl. Phys. Lett.* **1998,** 73, 3040-3042.

Chapter 7

$K_4P_8Te_4$: A New Phase-Change Compound with P-Te Bonding, Exfoliation, and Conversion to Photoluminescent Solution

1. Introduction

Solid-state materials with P-Te bonding have long been elusive although phosphorus, in general, has been known to combine with nearly all elements.[1] This is in striking contrast to the well-established metal chalcophosphate class involving the ternary (M/P/Q) and quaternary (A/M/P/Q) compounds with $[P_xQ_y]^{z-}$ anions in their structure, where M is a metal, A is an alkali metal, and Q is sulfur or selenium. The only reported P/Te containing inorganic compounds are MPTe (M = Ru, Os,[2] Ir[3]) and BaP_4Te_2.[4] The latter features P-Te bonding while only unit cell dimensions and spectroscopic data have been reported for the former. On the other hand, organometallic compounds provide some examples of P-Te bonded species, e.g. Et_3PTeX_2 (X = Cl, Br, I),[5] $TePPh_2Ch_3$[6] and $Ph_3PTe(Ph)I$.[7] The larger elements in group 15, As, Sb, and Bi, show a wealth of chemistry with Te to produce a wealth of solid-state inorganic materials.[8]

Recently, we reported rational synthetic conditions to stabilize P-rich species rather than the simple classical $[PSe_4]^{3-}$ and $[P_2Se_6]^{4-}$ anions by using excess phosphorus in the flux. Examples are $A_6P_8Se_{18}$ (A = K, Rb, Cs),[9] $Rb_4P_6Se_{12}$,[10] $Cs_4P_6Se_{12}$, and $Cs_5P_5Se_{12}$,[11] yet with the exception of BaP_4Te_2 there is a paucity of species containing P-Te bonds.

Here we report on the new alkali telluropolyphosphate compound $K_4P_8Te_4$ featuring P-Te bonding and the unique infinite anion $^1/_\infty[P_8Te_4^{4-}]$. The compound was

prepared with molten salt flux method at intermediate temperature and it shows reversible phase-change behavior. $K_4P_8Te_4$ was found to be soluble in hydrazine to give rise to colloidal solution of $^1/_\infty[P_8Te_4^{4-}]$ species. Generally it is very difficult to disperse solids in polar solvents. Because of this, very little is known about the behavior of inorganic polymers in solution, in some case these solutions have shown mesogenic liquid crystal properties e.g. $^1/_\infty[PdPS_4^-]$[12] and $^1/_\infty[Mo_3Se_3^-]$.[13] The possibility to exfoliate or even dissolve mineral compounds is of major importance because it then allows modification of the solids by solution chemistry methods and paves the way to the synthesis of new organic-inorganic hybrid and nanocomposite materials. The tellurophosphate anion can be dispersed in hydrazine solution. Nanospheres of the compound were obtained by precipitation with ethanol at room temperature. The resulting solution exhibited slightly blue-tinted white photoluminescence at room temperature when excited above the energy gap.

2. Experimental Section

2.1. Reagents. The reagents mentioned in this work were used as obtained unless noted otherwise. The reagents mentioned in this work were used as obtained: K metal (analytical reagent, Aldrich Chemical Co., Milwaukee, WI); red phosphorus powder, -100 mesh, Morton Thiokol, Inc., Danvers, MA; Te (99.999%; Noranda Advanced Materials, Quebec, Canada); *N,N*-dimethylformamide (Spectrum Chemicals, ACS reagent grade); diethyl ether (Columbus Chemical Industries, Columbus WI, ACS reagent grade, anhydrous). K_2Te starting materials was prepared by reacting

stoichiometric amounts of the elements in liquid ammonia. Anhydrous hydrazine (98 %, Aldrich) was distilled before use. **CAUTION: Hydrazine is highly toxic and should be handled proper protective equipments with special care to prevent contact with either the vapors or liquid.**

2.2. Synthesis. All sample preparation processes were carried out under inter atmosphere. Pure $K_4P_8Te_4$ was achieved by heating a mixture of K_2Te:P:Te = 3:2:5 under vacuum in a silica tube at 450 °C for 6 days, followed by cooling to 250 °C at 2 °C h^{-1}. The excess flux was dissolved with degassed *N,N*-dimethylformamide (DMF) under a N_2 atmosphere to reveal deep red-tinted black needle crystals. Energy-dispersive spectroscopy microprobe analysis on five crystals showed an average composition of "$K_{3.8}P_4Te_{3.7}$". The single crystals are stable in DMF, *N*-methylformamide and deionized H_2O and air.

3. Physical Measurements.

X-ray Powder Diffraction. Phase purity x-ray diffraction analyses were performed using a calibrated CPS 120 INEL X-ray powder diffractometer (Cu K_α graphite monochromatized radiation) operating at 40 kV/20 mA and equipped with a position-sensitive detector with flat sample geometry.

Scanning Electron Microscopy. Semiquantitative analyses of the compounds were performed with a JEOL JSM-35C scanning electron microscope (SEM) equipped with a Tracor Northern energy dispersive spectroscopy (EDS) detector.

Transmission Electron Microscopy (TEM) and High Resolution TEM. TEM sample was diluted with ethanol and irradiated by ultrasonification. TEM and HRTEM images were obtained with JEOL JEM 2200 FS Field emission TEM.

Solid-State UV-vis Spectroscopy. Optical diffuse reflectance measurements were performed at room temperature using a Shimadzu UV-3101 PC double-beam, double-monochromator spectrophotometer operating in the 200-2500 nm region. The details of the energy gap from these measurements have been discussed elsewhere.[14]

Infrared Spectroscopy. FT-IR spectra were recorded as solids in a CsI matrix. The samples were ground with dry CsI into a fine powder and pressed into translucent pellets. The spectra were recorded in the far-IR region (600-100 cm^{-1}, 4 cm^{-1} resolution) with the use of a Nicolet 740 FT-IR spectrometer equipped with a TGS/PE detector and silicon beam splitter.

Thermogravimetric Analysis. Experiments were performed on Shimadzu TGA-50 thermal analyzer by heating the samples up to 500 °C at a rate of 10 °C min^{-1} under N_2 flow of ca. 20 mL min^{-1}.

Differential Thermal Analysis (DTA). Experiments were performed on Shimadzu DTA-50 thermal analyzer. A sample (~30 mg) of ground crystalline material was sealed in a silica ampoule under vacuum. A similar ampoule of equal mass filled with Al_2O_3 was sealed and placed on the reference side of the detector. The sample was heated to 600 °C at 10 °C min^{-1}, and after 1 min it was cooled at a rate of –10 °C min^{-1} to 50 °C. The residues of the DTA experiments were examined by X-ray powder diffraction. Reproducibility of the results was confirmed by running multiple heating/cooling cycles.

The melting and crystallization points were measured at a minimum of endothermic peak and a maximum of exothermic peak.

^{31}P Solid-State NMR Spectroscopy. Room temperature ^{31}P NMR measurements were taken on a 9.4 T 400 MHz Varian Infinity Plus NMR spectrometer using a double-resonance magic angle spinning (MAS) probe using a 4 mm (outer) diameter zirconia rotor. Bloch decay spectra were taken with the excitation/detection channel tuned to ^{31}P at 161.82 MHz with a 4.5 μs, 90° pulse (calibrated to ±0.5 μs), a relaxation delay of 20 to 13,000 s, and samples were spun at frequencies between 6 and 13 kHz. All spectra were processed with up to 100 Hz of line broadening, up to a tenth-order polynomial baseline correction, and the chemical shifts (CS) were externally referenced to 85 % H_3PO_4 at 0 ppm. The spin lattice relaxation time (T_1) of each chemical shift was estimated from the exponential buildup of the peak intensity area as a function of the relaxation delay at 13 kHz between 20 and 13,000 s. The chemical shift anisotropy (CSA) principle value of each chemical shift was derived from the average of the Herzfeld-Berger fitting[15] of the MAS isotropic and sideband peak intensity areas at spinning frequencies of 8, 8.5, and 10 kHz for the peak at -4.3 ppm, at 6, 8, 8.5, 10, and 12 kHz for the peak at -16.9 ppm and at 8, 8.5, 10, 12, and 13 kHz for the peak at -34.6 ppm (outliers were excluded).

^{31}P Solution-State NMR Spectroscopy. Room temperature ^{31}P NMR measurements were taken on a 300 MHz Varian Mercoury NMR spectrometer. Spectra were taken with a 67.5° pulse and a relaxation delay of 0.6 s at a frequency of 121.53 MHz. The chemical shifts were externally refernced to 85 % H_3PO_4 at 0 ppm. Solution at a concentration of c.a. 1.25×10^{-2} mol L^{-1} was used for measurements. Preparation of $K_4P_8Te_4$/hydrazine solution will be described in Results and Discussion.

X-ray Crystallography. The crystal structure was determined by single-crystal X-ray diffraction methods. Preliminary examination and data collection was performed on a SMART[16] platform diffractometer equipped with a 1K CCD area detector using graphite monochromatized Mo K_α radiation at 173(2) K. A full sphere of data was collected at 173(2) K using narrow-frame method with scan widths of 0.30° in ω and exposure time of 50 s frame^{-1}. The SAINT software[12] was used for data extraction and integration. Semi-empirical absorption correction using the program SADABS[12] was performed. The initial positions for all atoms were obtained using direct methods, and the structure was refined with the full-matrix least-squares techniques of the SHELXTL crystallographic software package.[12] Satisfactory refinement was obtained with the centrosymmetric $P2_1/m$. All atoms were refined to full occupancy and anisotropically. ADDSYM from PLATON program[17] was used for checking out higher symmetry. The parameters for data collection, the details of the structural refinement, and fractional atomic coordinates and displacement parameters are given in Table 7-1 and 7-2.

Atomic Pair Distribution Function Analysis. Fine powder (< 40 μm) of the crystalline and glassy $K_4P_8Te_4$ was packed in a Kapton capillary with diameter of 1.0 mm. Diffraction data were collected at room temperature using the rapid acquisition pair distribution function technique.[18] Data were collected using an MAR345 image plate detector and ~ 60 keV energy X-rays (λ = 0.2128 Å) at the 11-ID-B beam line at the Advanced Photon Source. Measurements were repeated 4-5 times per sample to improve counting statistics. The data were combined and integrated using the program FIT2D.[19] Various corrections were made to the data, such as subtraction of background, Compton and fluorescence scattering, geometric corrections, absorption, and so on, as described in

reference.[20] Corrections were made using the program PDFgetX2.[21] Structural model was fit to the data using the program PDFFIT.[22]

Table 7-1. Crystallographic Data and Refinement Details for $K_4P_8Te_4$

Formula	$K_4P_8Te_4$
Crystal system	Monoclinic
Space Group	$P2_1/m$ (no.11)
Unit cell dimensions	a = 6.946(1), b= 6.555(1), c = 9.955(2), β = 90.420(3)°
Z	1
V, Å^3	453.2(2)
d (calculated), gr cm^{-3}	3.351
Crystal dimensions, mm^3	0.114 × 0.010 × 0.008
Temperature, K	173(2)
λ, Å	0.71073
μ, mm^{-1}	7.969
F(000)	404
θ_{max} (deg)	28.30
Total / unique reflections	4713 / 1167
R_{int}	0.0443
No. Parameters	46
Refinement method	Full-matrix least-squares on F^2
Final R indices [$I > 2\sigma(I)$], R_1[a]/wR_2 [b]	0.0397 / 0.0889
R indices (all data), R_1/wR_2	0.0560 / 0.0958
Goodness-of-fit on F^2	1.099

[a] $R1 = \Sigma ||F_o|- |F_c||/\Sigma|F_o|$. [b] $wR2 = \{\Sigma [w(F_o^2-F_c^2)^2]/\Sigma[w(F_o^2)^2]\}^{1/2}$

Table 7-2. Atomic coordinates ($\times 10^4$) and equivalent isotropic displacement parameters (Å $\times$ 10^4) for $K_4P_8Te_4$ at 173(2) K. *U*(eq) is defined as one third of the trace of the orthogonalized U_{ij} tensor.

	x	*y*	*z*	*U*(eq)
K(1)	261(3)	2500	3890(2)	18(1)
K(2)	2211(3)	2500	68(2)	19(1)
P(1)	3906(2)	52(3)	5802(2)	10(1)
P(2)	4918(4)	2500	2978(3)	10(1)
P(3)	4927(4)	2500	7169(3)	11(1)
Te(1)	7054(1)	2500	1014(1)	13(1)
Te(2)	8481(1)	2500	7335(1)	15(1)

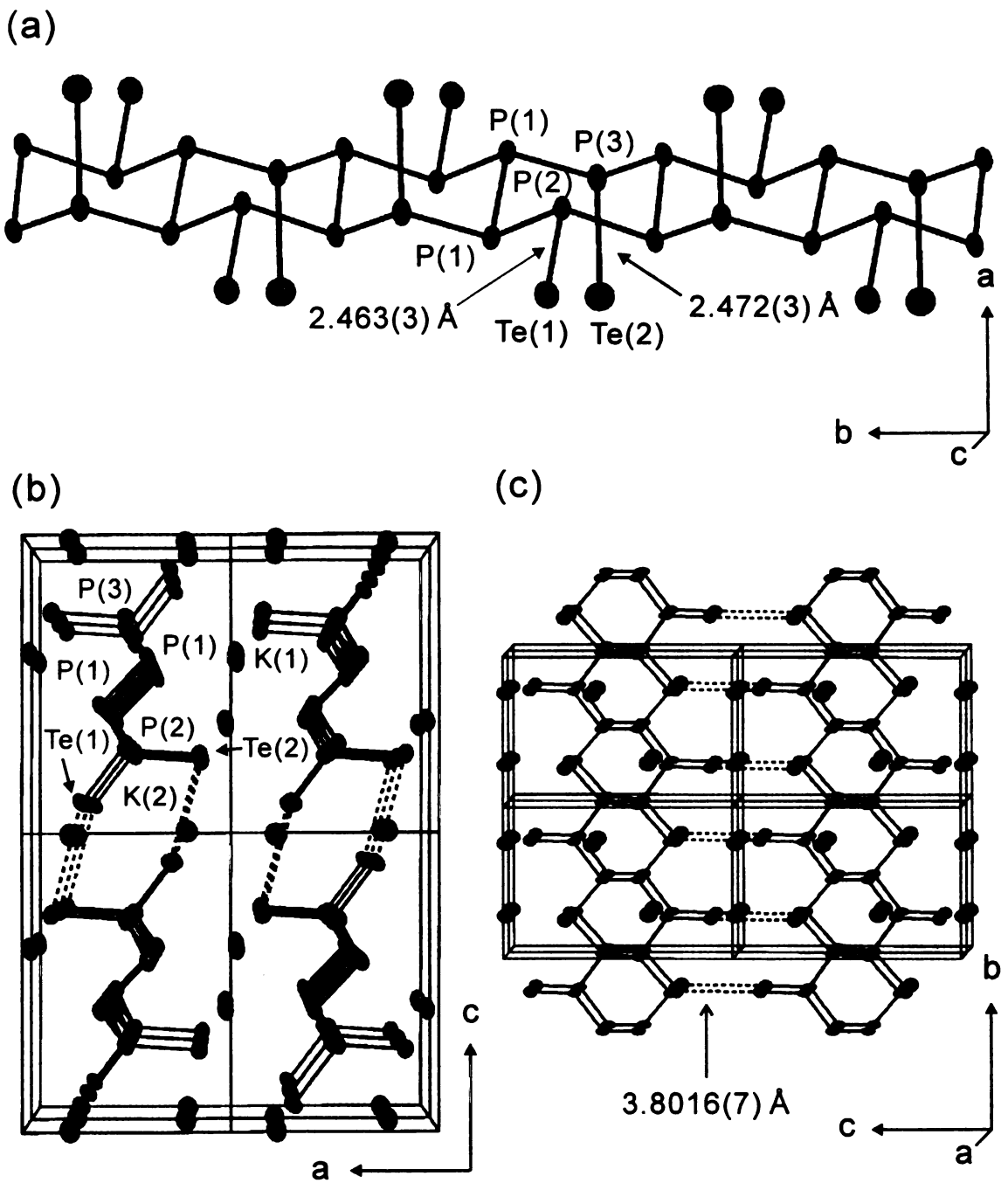

Figure 7-1. (a) View of $^{1}/_{\infty}[P_8Te_4^{4-}]$ chain. P and Te atoms are labeled. Structure of $K_4P_8Te_4$ viewed down the (b) *a*- and (c) *b*-axes. Dashed line denotes short Te···Te interaction at Te(1)···Te(2), 3.8016(7) Å. Darker large circles represent K atoms. The thermal ellipsoids are shown with 90 % in (a) and 50 % probability in (b) and (c).

4. Results and Discussion

Crystal Structure. The $K_4P_8Te_4$ adopts the $P2_1/m$ space group and features parallel infinite one-dimensional straight chains of $^1/_\infty[P_8Te_4^{4-}]$, Figure 7-1. This anion is unique in that it has no sulfur or selenium analog. The only other compound which features this species is the orthorhombic BaP_4Te_2. Due to the different number and size of counter-cation of K^+ and Ba^{2+}, the chains adopt different crystal packing. The P_8 backbone of the chain is made of six-membered P_6-rings in a chair conformation equatorially condensed via opposite edges of the hexagon defined by the P(1) atoms. This creates 3 coordinate P atoms. The equatorial and axial Te(1) and Te(2) atoms are bonded to P(2) and P(3) with distances of 2.463(3) and 2.472(3) Å, respectively. This is comparable to the sum of covalent radii at 2.47 Å.[23] Those in organometallic compounds are also similar, for example, 2.473 Å in Et_3PTeBr_2.[5] The dihedral angles in the of $^1/_\infty[P_8Te_4^{4-}]$ of P(3)-P(1)-P(1)-P(3) and P(3)-P(1)···P(2)-P(1) are -180.0(1)° and -1.8(1)°, respectively, showing the P_8 backbone chain is nearly ideal. The P-P distances at 2.214(3), 2,217(2) and 2.220(2) Å are comparable to those found in low valent chalcophosphate compounds. Selected bond distances and angles are represented in Table 7-3.

Inter-chain Te···Te nonbonding interactions, which are shorter than the sum of van der Waals radii of 4.40 Å,[24] are observed for Te(1)···Te(2) at 3.8016(7) Å, see Figure 7-1b and 1c. This weak interaction helps to organize the $^1/_\infty[P_8Te_4^{4-}]$ chains arranged side by side to form layers. K(1) atom, sandwiched by the $^1/_\infty[P_8Te_4^{4-}]$ chain, coordinates to six P and four Te atoms, whereas K(2) atom, residing at the corner of four $^1/_\infty[P_8Te_4^{4-}]$ chains, to two P and 5 Te atoms in a distorted pentagonal bipyramidal geometry, Figure 7-

2a and 2b. The distances of K to P atoms range from 3.359(3) to 3.814(3) Å, and those to Te atoms are at 3.487(2) to 3.744(3) Å, Table 3. Note that K(1)-Te(1)-K(2)-P(2) are coplanar and distance of K(1)···K(2) is 4.0483 Å, Figure 7-2c.

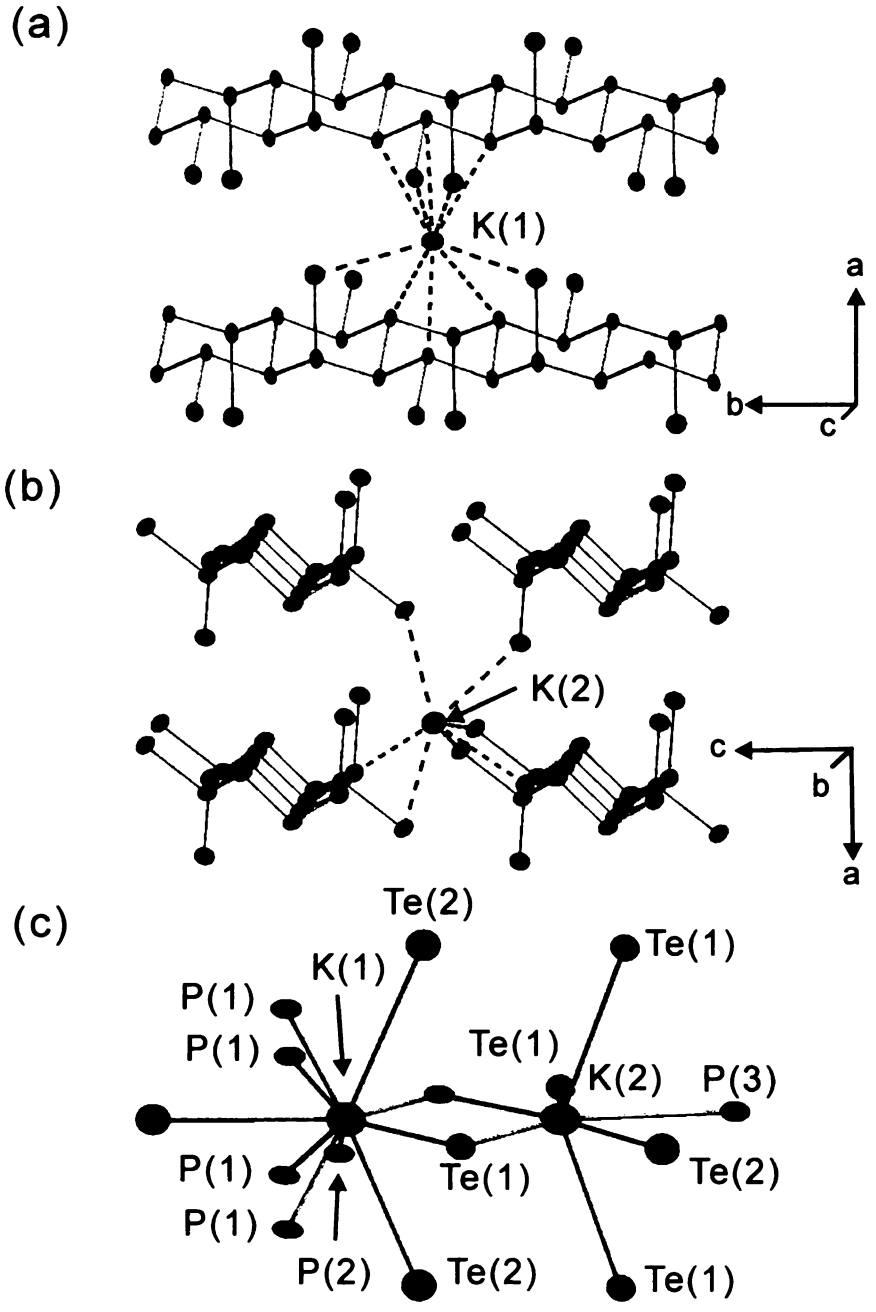

Figure 7-2. Local coordination environment of K(1) and K(2) atoms. (a) K(1) atom sandwiched by two $^1/_\infty[P_8Te_4^{4-}]$ chains, and K(2) atom surrounded by four $^1/_\infty[P_8Te_4^{4-}]$ chains are shown. Blue broken line denotes ionic bonding of K atoms to P and Te atoms in (a) and (b). (c) A K(1) and K(2) dimer is shown with K, P, and Te atoms labeled. Thermal ellipsoids are shown with 90 % probability.

Table 7-3. Selected Bond Distances (Å) and Angles (°) for $K_4P_8Te_4$ at 173(2) K.

P(1)-P(1)	2.214(3)	K(2)-P(2)	3.442(3)
P(1)-P(2)	2.220(2) ×3	K(2)-P(3)^{vii}	3.460(4)
P(1)-P(3)	2.217(2) ×2	K(2)-Te(1)	3.487(2)
P(2)-Te(1)	2.463(3)	K(2)-Te(1)^{viii}	3.489(1)
P(3)-Te(2)	2.472(3)	K(2)-Te(1)^{xi}	3.488(1)
		K(2)-P(1)^{iv}	3.710(3)
K(1)-P(1)	3.541(3)	K(2)-P(2)^{x}	3.744(3)
K(1)-P(1)^{i,ii}	3.359(3)		
K(1)-P(1)^{iii}	3.541(3)	P(1)^{v}-P(1)-P(2)^{v}	96.86(12)
K(1)-P(2)	3.366(3)	P(1)v-P(1)-P(3)	104.29(13)
K(1)-P(2)^{iv}	3.814(3)	P(1)^{iii}-P(3)-P(2)	92.72(13)
K(1)-Te(1)^{iv}	3.615(3)	P(3)-P(1)-P(2)^{v}	95.44(9)
K(1)- Te(2)^{v,vi}	3.607(1)	P(1)^{v}-P(2)-Te(1)	102.29(9)
K(1)- Te(2)^{iv}	3.653(3)	P(1)-P(3)-Te(2)	110.84(9)

Symmetry transformations used to generate equivalent atoms:

(i) $-x, y+1/2, -z+1$; (ii) $-x, -y, -z+1$; (iii) $x, -y+1/2, z$; (iv) $x-1, y, z$; (v) $-x+1, -y, -z+1$;

(vi) $-x+1$, -y+1, $-z+1$; (vii) $x, y, z-1$; (viii) $-x+1, -y, -z$; (ix) $-x+1, -y+1, -z$; (x) $x-1, y, z-1$;

(xi) $-x, -y+1, -z+1$; (xii) $-x, -y, -z$

Phase-Change Behavior. Differential thermal analysis (DTA) of $K_4P_8Te_4$ performed in a closed container at a rate of 5 °C min^{-1} showed melting at 488 °C. Upon cooling, the melt formed a black glass, Figure 7-3. On subsequent heating the glass recrystallized at 455 °C and again melted at 488 °C to form a glass upon cooling. The amorphous nature of the glassy phase was confirmed with X-ray powder diffraction. The powder diffraction patterns after recrystallization were identical to those of the pristine $K_4P_8Te_4$ indicating full recovery of the original crystal structure, Figure 7-4. The reversible crystal-glass transition was repeatedly observed in multiple DTA cycles indicating congruent melting of the substance.

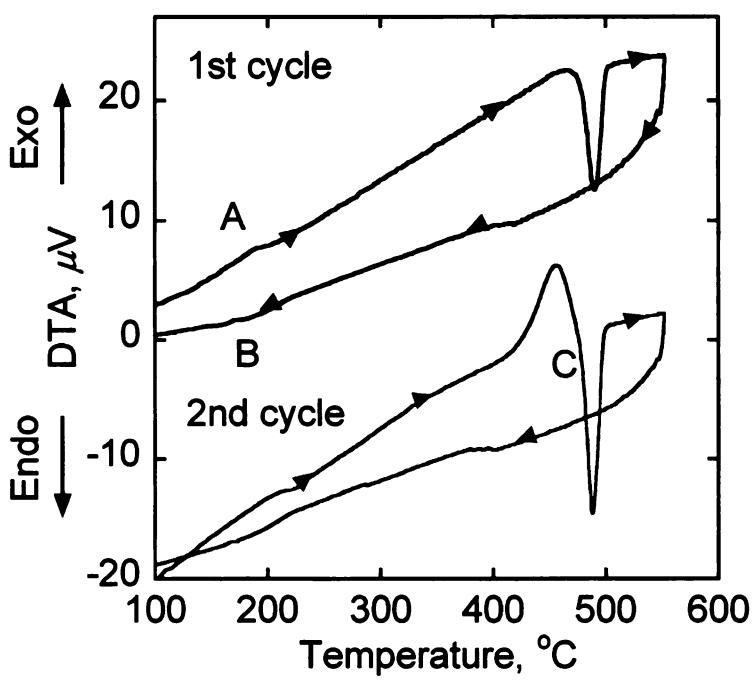

Figure 7-3. DTA diagrams of $K_4P_8Te_4$ showing melting in the 1st cycle with no crystallization on cooling (upper diagram). Glass crystallization is observed in the 2nd heating cycle (lower diagram). $K_4P_8Te_4$ is a pristine crystal at A, glass at B and restored crystal at C.

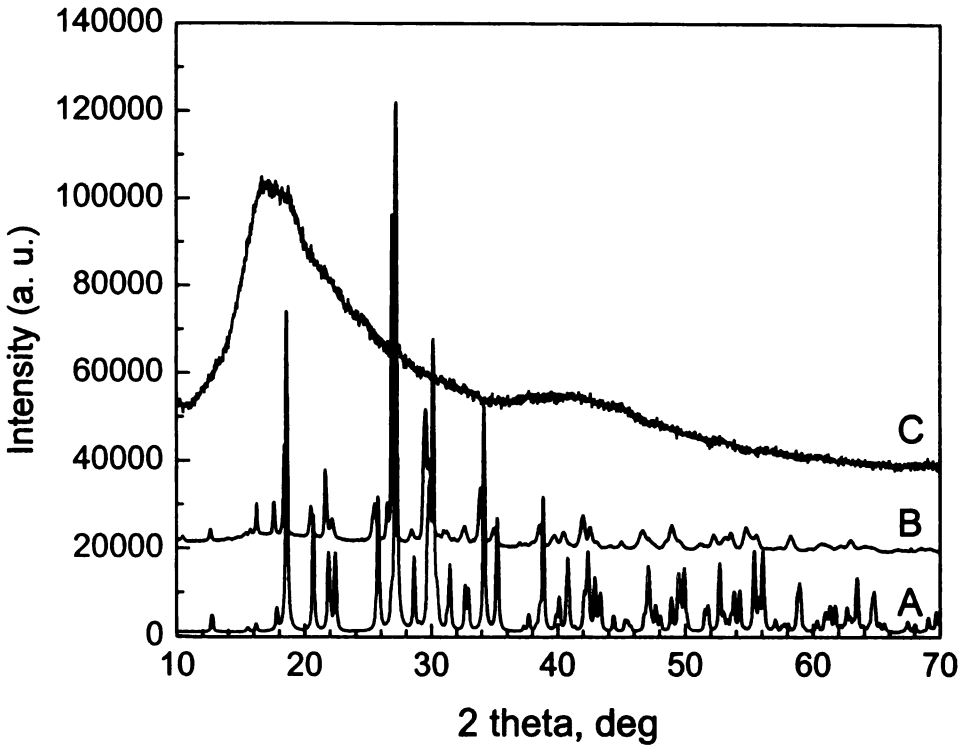

Figure 7-4. X-ray powder diffraction patterns of theoretical simulation(A), glass(B) and recrystallized crystal(C).

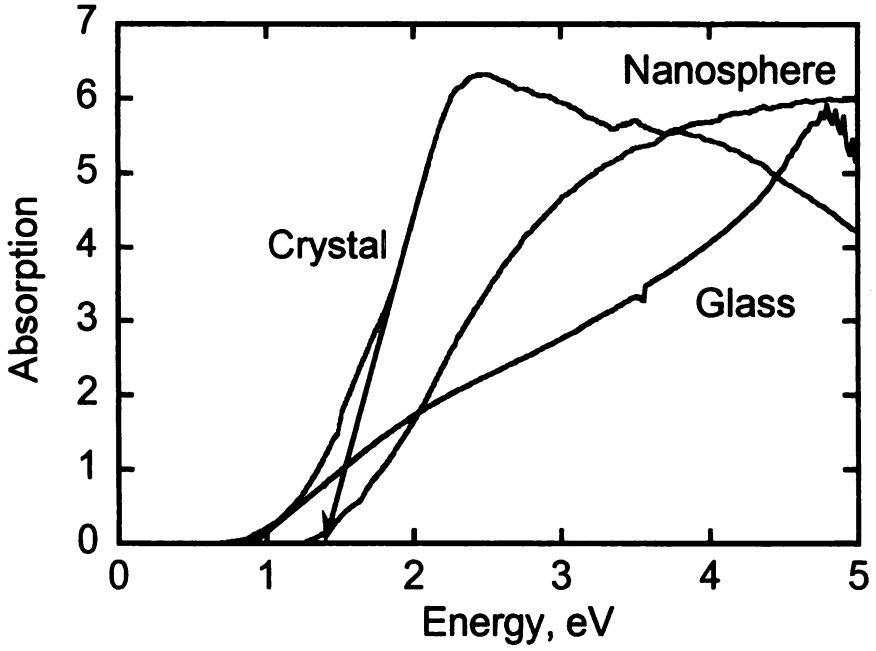

Figure 7-5. UV-vis absorption spectra of glass, pristine crystal, and nanosphere precipitated by MeOH.

Thermogravimetric analysis (TGA) at a rate of 10 °C min^{-1} showed that the compound decomposed under N_2 atmosphere from ~300 – 430 °C with a weight loss of 27.3 %. The value is in excellent agreement with the theoretical P content in the compound of 27.09 %. This suggested that the polyhexaphosphorus backbone was destroyed by heating at >300 °C. X-ray powder patterns of the black residue after TGA revealed a mixture of α-K_2Te_2, K_2Te_3 and K_5Te_3 along with a small amount of amorphous phase. The DTA and TGA results suggest that above the melting point the following equilibrium is in effect:

$$K_4P_8Te_4 \rightleftharpoons 2K_2Te_2 + 2P_4\uparrow \qquad \text{Eg.(1)}$$

The solid-state UV-vis spectra of the crystalline and glassy phases show absorption edges at 1.40 eV and 0.91 eV, respectively, Figure 7-5. The lower energy gaps of the glass can be attributed to structural defects that create midgap states and band tailing.[25] The band gap value is consistent with the black color of the materials. The infrared spectrum displays absorption peaks at 262(w), 306(s), 322(m), 417(m), 431(s), and 469(m) cm^{-1}. The peaks at 417 and 431 cm^{-1} can be assigned to P-Te by analogy to MPTe (Ru, Os),[2] and those at 323 and 469 cm^{-1} to a P-P vibration in comparison to Ba_3P_{14}.[26]

Pair Distribution Function (PDF) Analysis. To probe the local structure of both the crystalline and glassy $K_4P_8Te_4$ we performed atomic pair distribution function (PDF) analysis. This technique analyzes both the Bragg and diffuse scatterings to reveal the short and intermediate range order of a solid regardless of the degree of disorder. Peaks in the PDF directly represent the quantitative real-space interatomic distance correlation of pairs of atoms in the structure in high resolution, thus the technique is a powerful analytical tool for studying disorder and amorphous phases.[27] The experimental PDF of

crystalline $K_4P_8Te_4$ is in excellent agreement with the calculated PDF based upon the crystal structure model, validating the correctness of crystal structure refinement, Figure 7-6. The first strong correlation at 2.4 Å is assigned to the P-P and P-Te covalent bonds in the one-dimensional chain. The second peak at 3.7 Å corresponds to the distance of short Te···Te nonbonding interchain contact and that from K atom to the first neighboring P and Te atoms, defining the connectedness of $[P_8Te_4^{4-}]$ chain to K atom and the nearest chain. The third peak at 4.8 Å relates the second neighboring interchain Te···Te and K···P correlations. The peak at 7.0 Å results from the P···P distances from two neighboring P hexagons.

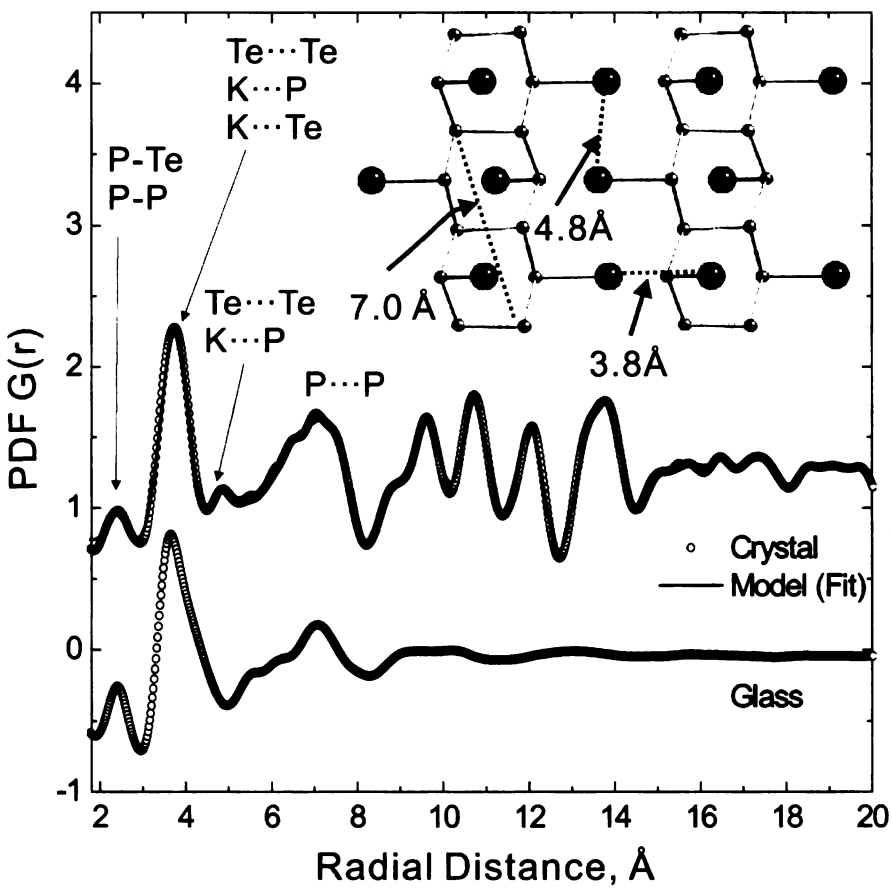

Figure 7-6. Experimental pair distribution function $G(r)$ of the crystalline (upper) and glassy (bottom) $K_4P_8Te_4$. The calculated PDF using the crystallographic coordinates is shown as red line. Selected atomic correlation distances are indicated. Atomic distances in the crystallographic model are also shown (inset).

The experimental PDF of the glass shows well-defined correlations but up to ~14 Å. The first two at 2.4 and 3.7 Å and broad feature at 7 Å are very similar to those in the crystalline form. Note that the peak at 7 Å defines the relation of two neighboring P hexagons. Beyond ~14 Å all correlations are lost reflecting the lack of long range periodicity. The structural coherence is much shorter than the crystalline phase but significantly longer than those of the conventional glasses such as silica. The PDF data suggest that the crystalline and glassy phases of $K_4P_8Te_4$ are structurally similar with respect to their local structure which is defined by a relatively large invariant fragment. This similarity indicates the rigidity of local structural unit [$P_8Te_4^{4-}$], intact in the glassy form. $K_4P_8Te_4$ is a member of a new growing class of phase change materials[28,29,30] with stoichiometric composition and mixed ionic/covalent bonding in the structure. The vast majority of chalcogenide glasses have nearly continuous compositions and all-covalent networks. Although the mechanism of switching from glass to crystalline $K_4P_8Te_4$ is not yet understood, it is likely involves the two different types of binding found in the structure, ionic (K···Te) and covalent (P-P and P-Te). Such bonding anisotropy determines glass formation tendency and in principle it could be used to control it. Detailed studies are needed to understand how the coexistence of both ionic and covalent bonding affects the phase-change and other physical properties in these materials.

Electronic Structure Calculations and Bonding. In order to explore the unusual P-Te bonding in $K_4P_8Te_4$ at a deeper level, we performed, *ab-initio* density functional calculations with the full-potential linearized augmented plane wave (FLAPW) method.[31] These calculations can also determine the nature of the band gap.

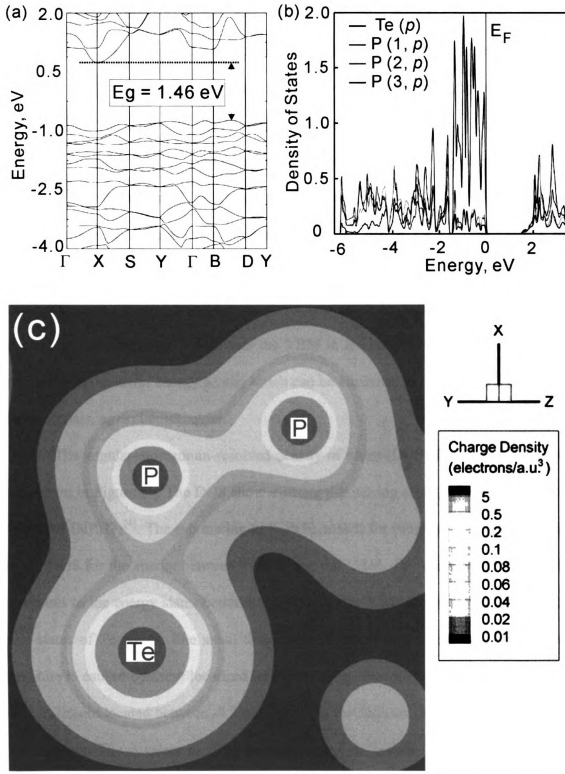

Figure 7-6. (a) The band structure of $K_4P_8Te_4$. (b) The projected density of states for *p*-orbitals of individual elements (Te and P), and (c) the contour plot of the total charge density of $K_4P_8Te_4$ calculated with the sX-LDA method.

The electronic structure of $K_4P_8Te_4$ was calculated with the fully first-principles screened-exchange local density functional approximation (sX-LDA) scheme[32] and spin-orbit coupling (SOC). The sX-LDA method is known to yield great improvements of the excited electronic states such as band gaps and band dispersion due to its better long-range description of the exchange-correlation hole compared to the local density approximation (LDA). sX-LDA calculation predicted a band gap of 1.46 eV as shown in Figure 7-7a, which is close to the experimental band gap at 1.4 eV. The valence band maximum (VBM) occurs along the B-D direction, Figure 7-7a, while the conduction band minimum (CBM) is located at the X point, which leads to an indirect band gap. The electronic states between -1.5 eV and the VBM in the band structure are less dispersed compared to the lower energy levels, which can be attributed to the localized character of these orbitals, as explained below.

The angular-momentum-resolved density of states (DOS) for Te and P *p*-orbitals are shown in Figure 5b. The DOS show a strong p-p mixing effect, which is very similar to that of BaP_4Te_2[4]. The p-p mixing in $K_4P_8Te_4$ makes for roughly three distinct regions in the DOS for the energy between -6.5 eV and the VBM. The strong contribution of Te *p*-orbitals to the energy states between -1.5 eV and the VBM are mainly due to the lone-pair states of Te atoms. The small dispersion shown in this energy range of the band structure is caused by these localized lone-pair states. The most interesting energy levels in $K_4P_8Te_4$ are located between -4.2 eV and -1.5 eV, which are derived mainly from P-Te ppσ-bonding. The covalent bonding character between Te and P can also be seen in the contour plots of the total charge density, Figure 5c. The charge densities which are relatively high along the Te-P and P-P bond axes clearly suggest a strong Te-P covalent

bonding character. The lower energy levels [at -6.5 eV ~ -4.2 eV] are mainly composed of P *p*-orbitals due to the strong covalent interactions in P-P bondings.

The ^{31}P solid-state magic angle spinning (MAS) NMR spectrum of $K_4P_8Te_4$ revealed three isotropic chemical shifts at -4.3, -16.9, and -34.6 ppm, Figure 7-7, consistent with the crystallographic analysis. Because the ratio of the integrated intensity is 1.1:2.0:1.0, the peak at -16.9 ppm can be assigned to P(1). The P(1)-P(1) fragment is shared bond between the fused cyclohexane chairs of the P_8 backbone and has no bonding with Te. The peaks at -4.3 and -34.6 ppm can be attributed to atoms P(2) or P(3). The σ_{33} - σ_{11} chemical shift anisotropy (CSA) principal value differences were ~188, 116, and 187 ppm, respectively, and also support the assignment. Because P(1) only has homoatomic bonding in contrast to P(2) and P(3) which bond to Te, it can be considered more crystallographically and magnetically symmetric than the others. For selenophosphate anions, the CSA principal value difference correlates inversely with the degree of local symmetry about P.[33] P(2) and P(3) have very similar local geometric environment and could not be individually assigned.

The ^{31}P solid-state magic angle spinning (MAS) NMR spectrum of $K_4P_8Te_4$ revealed three isotropic chemical shifts at -4.3, -16.9, and -34.6 ppm, Figure 7-7, consistent with the crystallographic analysis. Because the ratio of the integrated intensity is 1.1:2.0:1.0, the peak at -16.9 ppm can be assigned to P(1). The P(1)-P(1) fragment is shared bond between the fused cyclohexane chairs of the P8 backbone and has no bonding with Te. The peaks at -4.3 and -34.6 ppm can be attributed to atoms P(2) or P(3). The σ_{33} - σ_{11} chemical shift anisotropy (CSA) principal value differences were ~188, 116, and 187 ppm, respectively, and also support the assignment. Because P(1) only has

homoatomic bonding in contrast to P(2) and P(3) which bond to Te, it can be considered more crystallographically and magnetically symmetric than the others. For selenophosphate anions, the CSA principal value difference correlates inversely with the degree of local symmetry about P.[33] P(2) and P(3) have very similar local geometric environment and could not be individually assigned.

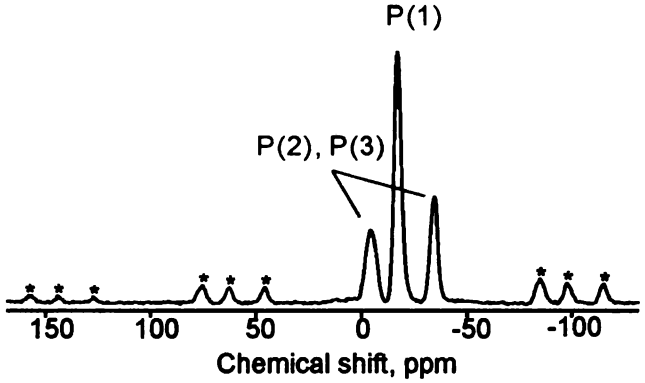

Figure 7-7. ^{31}P solid-state MAS NMR spectrum of $K_4P_8Te_4$. * denotes spinning side bands.

$K_4P_8Te_4$/hydrazine solution (10 mL) could be evaporated to dryness by blowing N_2 for 2 days to yield a sticky amorphous black solid. TGA performed at a rate of 2 °C min^{-1} demonstrated that hydrazine trapped in the structure was removed by 250 °C. The highly crystalline nanospheres were isolated by precipitation with anhydrous methanol, centrifuged, filtered and dried. X-ray powder diffraction pattern of the precipitated residue matched well with that of theoretical calculation, Figure 7-9. The band gap of the recovered $K_4P_8Te_4$ was measured at 1.62 eV, which is significantly blue shifted from 1.40 eV of the bulk pristine phase, Figure 7-5.

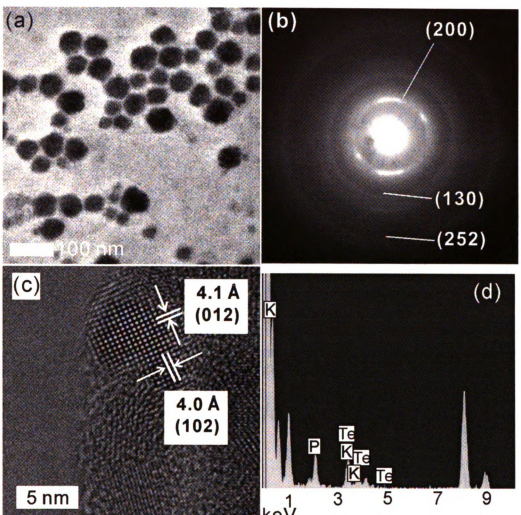

Figure 7-8. (a) TEM image of dispersed $K_4P_8Te_4$ nanosphere. (b) Selected area electron diffraction patterns of $K_4P_8Te_4$ nanosphere. (c) Lattice image on single $K_4P_8Te_4$ nanosphere by high resolution TEM, indicative of single crystalline nature in nanoscale. Lattice planes of (012) and (102) are indexed. (d) The representative EDS spectrum of single $K_4P_8Te_4$ nanosphere giving a composition of "$K_{4.8}P_8Te_{3.5}$", reasonably close to $K_4P_8Te_4$.

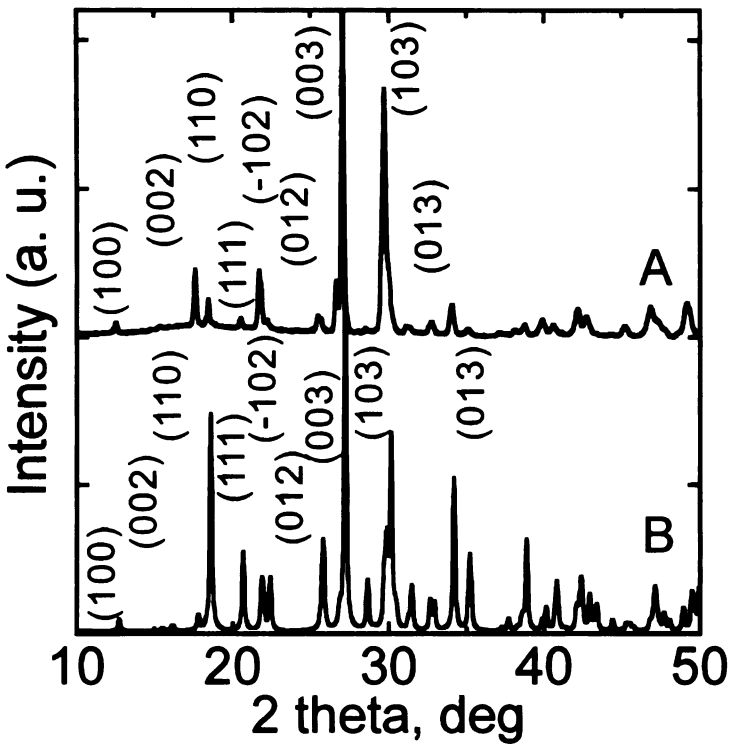

Figure 7-9. X-ray powder diffraction patterns of (A) isolated $K_4P_8Te_4$ nanosphere by methanol and (B) theoretical simulation of bulk $K_4P_8Te_4$.

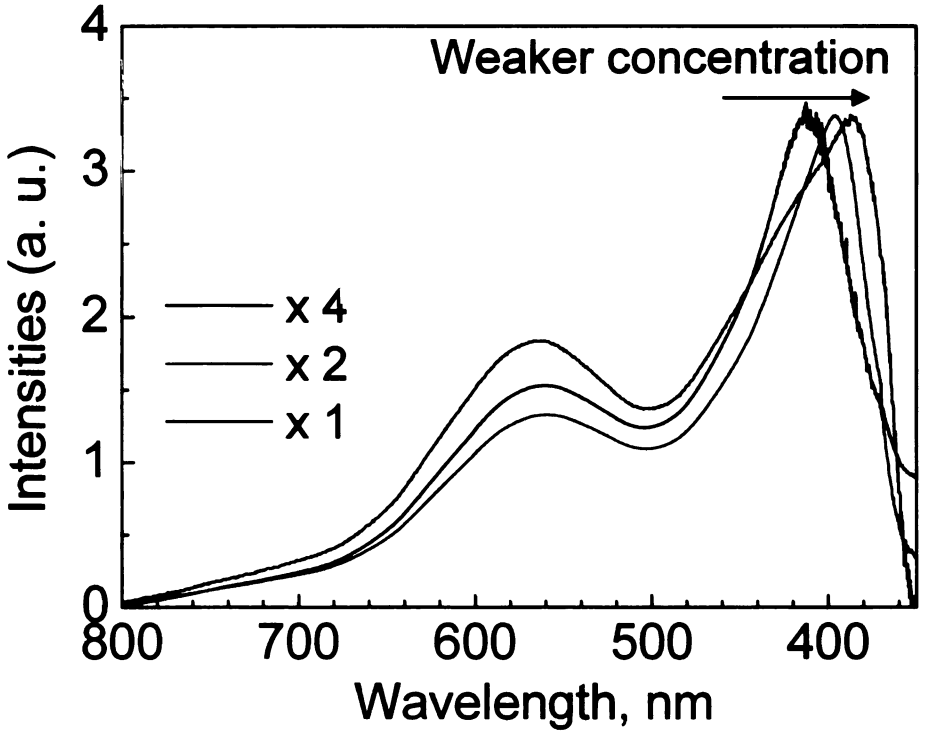

Figure 7-10. (a) Normalized UV absorbance spectra with respect to the variable concentration of dissolved $K_4P_8Te_4$ in hydrazine solution. Solution was consecutively diluted by 50 % from I to II to III.

Solution Phase Chemistry of $K_4P_8Te_4$. In order to figure out the dissolution mechanism of $K_4P_8Te_4$, we performed UV-vis absorbance in a varied concentration and ^{31}P solution-state NMR for $K_4P_8Te_4$/hydrazine solution. λ_{max} of UV-vis absorbance is dramatically blue shifted (~3.0 eV) from the band bap of the bulk crystalline phase at 1.40 eV, Figure 7-5 and Figure 7-10. Successive dilution of the solution by hydrazine to a half and a quarter concentration shifted the λ_{max} to the deeper UV region. It is understood that the observed blue shift resulted from the separation of one-dimensional chain $^1/_\infty[P_8Te_4^{4-}]$ due to the exfoliation/dissolution process of $K_4P_8Te_4$ compound to give K^+ cations and $^1/_\infty[P_8Te_4^{4-}]$ anions when loaded in highly polar hydrazine. Further λ_{max} shift resulted from the chain being further separated from one another upon dilution. Broad feature at ~500 to 650 nm possibly resulted from the hydrazine shell effect as shown in the nanoparticle/organic conjugate.[34]

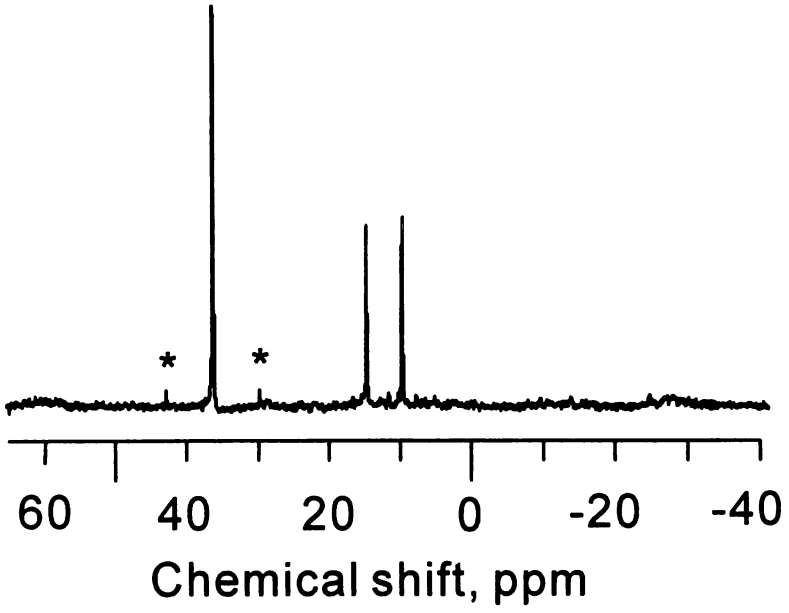

Figure 7-11. ^{31}P solution-state NMR spectrum of $K_4P_8Te_4$/hydrazine solution. * denotes spinning side bands.

^{31}P solution-state NMR spectrum of $K_4P_8Te_4$/hydrazine solution at room temperature displayed three isotropic chemical shifts at 9.6, 14.6, and 36.2 ppm with the ratio of the integrated intensity of ~1:1:2, Figure 11. Note that the NMR peak positions of the solution is close to that of black phosphorus (22.2 ppm)[35] that consists of two dimensional network of phosphorus hexagons in a chair conformation. The observed NMR peak positions of solution are different from those of the pristine solid by ^{31}P solid-state NMR. ^{31}P solution-state NMR and UV-vis absorbance results with TEM images showing nanospheres suggested that the $^1/_\infty[P_8Te_4^{4-}]$ chain was exfoliated and fragmented during solvation as found in $KNiPS_4$.[12] If the dissociated $^1/_\infty[P_8Te_4^{4-}]$ chain were intact, one-dimensional species must have been observed as previously found in $KPdPS_4$[12] and $NaNb_2PS_{10}$.[36] No major structural change or decomposition during solvation, however, is likely to have occurred because (1) "$K_4P_8Te_4$" composition on the nanosphere was confirmed by EDS and scanning TEM, and (2) rapid recovery of crystalline $K_4P_8Te_4$ phase from solution by precipitation with MeOH. Because we could not obtain crystals that possess the structure of fragmented $[P_8Te_4]_n^{n-}$ species, no structural information or assignment of ^{31}P solution-state NMR spectrum was available. Additional work will be necessary to figure out the more detailed dissolution and nanosphere formation mechanism of $K_4P_8Te_4$ and solution NMR spectrum.

The $K_4P_8Te_4$/hydrazine solution exhibited photoluminescence (PL) at room temperature, Figure 7-12. It is noteworthy that the PL entirely spans the visible region (~420 – 690 nm) with unusually large Stokes shift (~81 nm). When a 355nm Nd:YAG laser with pulse width of 15ps was introduced, white light with slight blue-tint was observed (see inset). Statistically, the PL peak should be symmetric, but the observed

peak shape is asymmetric due to reabsorption of the PL. We can approximately reproduce a symmetric peak by multiplying the observed absorption by $\exp[\alpha(E)d]$, where $d \sim 1$cm is the thickness of a cuvet. As confirmed by the superimposed Gaussian fit, the predicted peak distribution is symmetric around 2.46 eV. The PL profiles of the $K_4P_8Te_4$ nanospheres remained unchanged when hydrazine solution was diluted, suggesting the observed PL may originate from HOMO-LUMO electronic transitions in the solubilized $[P_8Te_4]_n^{n-}$ fragment rather than from impurities.

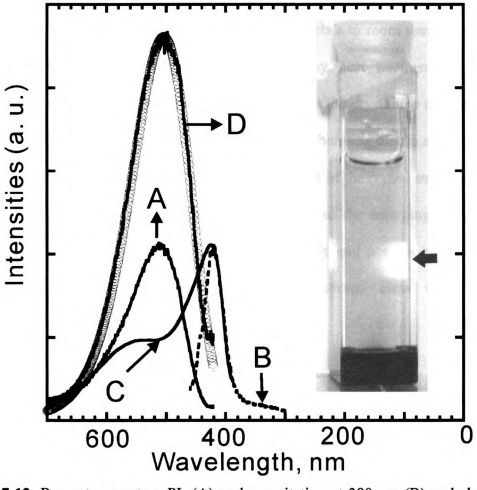

Figure 7-12. Room-temperature PL (A) under excitation at 380 nm (B) and absorption (C) spectra obtained from $K_4P_8Te_4$/hydrazine. The solid line (D) corresponds to the predicted PL after correcting the reabsorption effect, superimposed by a symmetric Gaussian fit(line with O). The inset exhibits the white emission from $K_4P_8Te_4$/hydrazine solution in a cuvet when 355 nm Nd:YAG laser was introduced at the point marked by an arrow. The nearly saturated deep reddish solution was much diluted to measure PL.

5. Concluding Remarks

Molten salt flux method was a rich source of new synthetic thio- and selenophosphate compounds. Synthesis of $K_4P_8Te_4$ exemplifies the availability of this method to phosphorus tellurides that has long elusive. The compound features a unique $^1/_\infty[P_8Te_4^{4-}]$ chain with low valent P and rare P-Te bonding. Remarkably, $K_4P_8Te_4$ compound readily forms various states of crystalline and glassy solid, nanosphere, and solution, and each state is differentiated by significant optical absorption contrast. Glassy phase is easily accessible by quenching out molten crystals to room temperature, and is switchable to the corresponding crystalline phase by heat treatment. The optical absorption edge for the glassy phase is red-shifted from the crystalline counterpart, and on the basis of the PDF analysis it appears that the basic building blocks are largely intact in the glassy state. This accounts for the facile restoration of the crystal structure from the corresponding amorphous phase. $K_4P_8Te_4$ is a member of the emerging class of phase change materials that are compositionally stoichiometric and possess alternating ionic and covalent bondings, in contrast to the conventional class that is mostly nonstoichiometric with covalent bonding networks.

Solution-state $K_4P_8Te_4$ is obtained simply by dissolving solid in hydrazine solution at room temperature. This rare behavior can open up the possibility of new chemistry: synthesis of wide range of metal tellurophosphate compound via a *chimie deuce* route, functional organic-inorganic hybrids, and nanocomposite compounds; study of gel-formation and liquid crystalline behavior. We suggested that solvation of $K_4P_8Te_4$ was driven by an exfoliation/fragmentation process by using ^{31}P NMR, UV-vis absorbance and TEM studies. The $K_4P_8Te_4$ solution exhibited highly desirable white

emission with slight blue-tint by Nd:YAG laser irradiation. Highly crystalline $K_4P_8Te_4$ nanosphere was obtained by precipitation with alcohol, giving rise to full recovery of crystal structure from solution state. In this regard, precipitation reaction with various salts is expected to produce new phosphorus tellurides in a crystalline form.

References

(1) von Schnering, H. G.; Hönle, W. *Chem. Rev.* **1988**, *88*, 243-273.

(2) Lutz, H. D.; Schmidt, T.; Waschenbach, G. *Z. Anorg. Allg. Chem.* **1988**, *562*, 7-16.

(3) Kliche, G. *Z. Naturforsch., B* **1986**, *41*, 130-131.

(4) Jörgens, S.; Johrendt, D.; Mewis, A. *Chem. Eur. J.* **2003**, *9*, 2405-2410.

(5) Konu, J.; Chivers, T. *Dalton Trans.* **2006**, 3941-3946.

(6) Dornhaus, F.; Bolte, M.; Lerner, H. W.; Wagner, M. *Eur. J. Inorg. Chem.* **2006**, 1777-1785.

(7) Boyle, P. D.; Cross, W. I.; Godfrey, S. M.; McAuliffe, C. A.; Pritchard, R. G.; Sarwar, S.; Sheffield, J. M. *Angew. Chem., Int. Ed.* **2000**, *39*, 1796-1798.

(8) Poudeu, P. F. P.; Kanatzidis, M. G. *Chem. Commun.* **2005**, 2672-2674; Hsu, K. F.; Lal, S.; Hogan, T.; Kanatzidis, M. G. *Chem. Commun.* **2002**, 1380-1381; Sheldrick, W. S.; Wachhold, M. *Coord. Chem. Rev.* **1998**, *176*, 211-322.

(9) Chondroudis, K.; Kanatzidis, M. G. *Inorg. Chem.* **1998**, *37*, 2582-2584.

(10) Chung, I.; Karst, A. L.; Weliky, D. P.; Kanatzidis, M. G. *Inorg. Chem.* **2006**, *45*, 2785-2787.

(11) Chung, I.; Jang, J. I.; Gave, M. A.; Weliky, D. P.; Kanatzidis, M. G. *Chem. Commun.* **2007**, 4998-5000.

(12) Sayettat, J.; Bull, L. M.; Gabriel, J. C. P.; Jobic, S.; Camerel, F.; Marie, A. M.; Fourmigue, M.; Batail, P.; Brec, R.; Inglebert, R. L. *Angew. Chem., Int. Ed.* **1998**, *37*, 1711-1714.

(13) Davidson, P.; Gabriel, J. C.; Levelut, A. M.; Batail, P. *Europhys. Lett.* **1993**, *21*, 317-322.

(14) Mccarthy, T. J.; Ngeyi, S. P.; Liao, J. H.; Degroot, D. C.; Hogan, T.; Kannewurf, C. R.; Kanatzidis, M. G. *Chem. Mater.* **1993**, *5*, 331-340.

(15) Herzfeld, J.; Berger, A. E. *J. Chem. Phys.* **1980**, *73*, 6021-6030.

(16) SADABS, SHELXTL, version 6; Bruker Analytical X-ray Instrumentals, Inc.: Madison, WI, 2000.

(17) Spek, A. L. *J. Appl. Crystallogr.* **2003**, *36*, 7-13.

(18) Chupas, P. J.; Qiu, X. Y.; Hanson, J. C.; Lee, P. L.; Grey, C. P.; Billinge, S. J. L. *J. Appl. Crystallogr.* **2003**, *36*, 1342-1347.

(19) Hammersley, A. P.; Svensson, S. O.; Hanfland, M.; Fitch, A. N.; Hausermann, D. *High Pressure Research* **1996**, *14*, 235-248.

(20) Egami, T.; Billinge, S. J. L. *Underneath the Bragg peaks : structural analysis of complex materials*; 1st ed.; Pergamon: Amsterdam ; Boston, 2003.

(21) Qiu, X. Y.; Bozin, E. S.; Juhas, P.; Proffen, T.; Billinge, S. J. L. *J. Appl. Crystallogr.* **2004**, *37*, 110-116.

(22) Proffen, T.; Billinge, S. J. L. *J. Appl. Crystallogr.* **1999**, *32*, 572-575.

(23) Pauling, L. The nature of the chemical bond and the structure of molecules and crystals; an introduction to modern structural chemistry; 3d ed.; Cornell University Press: Ithaca, N. Y., 1960.

(24) Cherin, P.; Unger, P. *Acta Crystallogr.* **1967**, *23*, 670-671.

(25) Marking, G. A.; Hanko, J. A.; Kanatzidis, M. G. *Chem. Mater.* **1998**, *10*, 1191-1199; Dhingra, S.; Kanatzidis, M. G. *Science* **1992**, *258*, 1769-1772.

(26) Dahlmann, W.; von Schnering, H. G. *Naturwissenschaften* **1973**, *60*, 429-429.

(27) Billinge, S. J. L.; Kanatzidis, M. G. *Chem. Commun.* **2004**, 749-760.

(28) Chung, I.; Malliakas, C. D.; Jang, J. I.; Canlas, C. G.; Weliky, D. P.; Kanatzidis, M. G. *J. Am. Chem. Soc.* **2007**, *129*, 14996-15006.

(29) Wachter, J. B.; Chrissafis, K.; Petkov, V.; Malliakas, C. D.; Bilc, D.; Kyratsi, T.; Paraskevopoulos, K. M.; Mahanti, S. D.; Torbrugge, T.; Eckert, H.; Kanatzidis, M. G. *J. Solid State Chem.* **2007**, *180*, 420-431.

(30) Kaidatzis, A.; Wachter, J. B.; Chrissafis, K.; Paraskevopoulos, K. M.; Kanatzidis, M. G. *J. Non-Cryst. Solids* **2008**, *354*, 3643-3648.

(31) Wimmer, E.; Krakauer, H.; Weinert, M.; Freeman, A. J. *Phys. Rev. B* **1981**, *24*, 864-875.

(32) Asahi, R.; Mannstadt, W.; Freeman, A. J. *Phys. Rev. B* **1999**, *59*, 7486-7492; Bylander, D. M.; Kleinman, L. *Phys. Rev. B* **1990**, *41*, 7868-7871.

(33) Canlas, C. G.; Kanatzidis, M. G.; Weliky, D. P. *Inorg. Chem.* **2003**, *42*, 3399-3405.

(34) Thakar, R.; Chen, Y. C.; Snee, P. T. *Nano Lett.* **2007**, *7*, 3429-3432.

(35) Lange, S.; Schmidt, P.; Nilges, T. *Inorg. Chem.* **2007**, *46*, 4028-4035.

(36) Camerel, F.; Gabriel, J. C. P.; Batail, P.; Davidson, P.; Lemaire, B.; Schmutz, M.; Guilk-Krzywicki, T.; Bourgaux, C. *Nano Lett.* **2002**, *2*, 403-407.

Chapter 8

Flexible Polar Nanowires of $Cs_5BiP_4Se_{12}$ from Weak Interactions between Coordination Complexes and Their Strong Second Harmonic Generation Nonlinear Optical Response.

1. Introduction

Since the discovery of WS_2[1] and MoS_2 nanotubes,[2] the synthesis of other one-dimensional inorganic nanostructures is of great interest because of promising new optical and electronic properties[3] that can be useful in technological applications. Synthetic efforts to create inorganic nanowires involve either the exploration of new compounds with nanofeatures or downsizing existing materials to the nano-scale. Examples of the former include $SbPS_4$[3] and $LiMo_3Se_3$.[4] Examples of the latter include MS_2 (M=Ti,[5] Nb, Ta,[6] Re[7]), Bi_2S_3,[8] BN,[9] V_2O_5,[10] and VS_2,[11] and the synthetic procedures to obtain such nanowires require special non-equilibrium conditions such as discharging, chemical vaporization, laser vaporization, or hydrocarbon pyrolysis. Consequently, these are limited in terms of yield, phase purity, crystallinity, and uniformity. Most of the known nanowires/-tubes are simple atomic or binary phases. More complex multinary inorganic solids in this class are still rare, yet such materials can exhibit important properties such superconductivity,[12] giant magnetoresistance,[13] ferroelectric,[14] liquid crystallinity[15] and optical nonlinearities.[16]

Here we describe the new compound $Cs_5BiP_4Se_{12}$ which intrinsically grows as nanowires. The compound is a semiconductor and shows a wide optical transparency

range through mid/near IR region and strong second harmonic generation (SHG) response at 1 μm. Integrated photonic networks with high wavelength conversion efficiency in the IR region (especially 1.3~1.5 μm) are in high demand because of the dramatic development of the broadband internet communication industry.[17] Since optical nano-waveguidance system can offer superior light confinement due a to strong index contrast, it is ideal for nonlinear optical applications.[18] In this regard, $Cs_5BiP_4Se_{12}$ can be a potential candidate for such purposes. In spite of the nanowire microstructure and fibrous nature of the material which made the selection of single crystals very challenging we succeeded in determining the structure of the material using single crystal X-ray crystallography on very thin fibers. The rather surprising finding is that the repeating unit giving rise to the nanofibers is the simple coordination complex $[Bi(P_2Se_6)_2]^{5-}$. Using the crystallographic information, *ab-initio* density functional calculations with the full-potential linearized augmetned plane wave (FLAPW) method[19] were performed to confirm the experimental band gap and to explain the nanowire nature of $Cs_5BiP_4Se_{12}$. To the best of our knowledge, the $Cs_5BiP_4Se_{12}$ presents a rare example of polar nanowires.

2. Experimental Section

2.1. Reagents. The reagents mentioned in this work were used as obtained: Cs metal, analytical reagent, Johnson Matthey/AESAR Group, Seabrook, NH; red phosphorus powder, -100 mesh, Morton Thiokol, Inc., Danvers, MA; Se, 99.9999%, Noranda Advanced Materials, Quebec, Canada; *N,N*-dimethylformamide, ACS reagent grade,

Mallinckrodt Backer Inc., Paris, KY; diethyl ether, ACS reagent grade, anhydrous, Columbus Chemical Industries, Columbus WI. The Cs_2Se starting material was prepared by reacting stoichiometric amounts of the elements in liquid ammonia under N_2.

2.2. Synthesis. The synthesis of pure $Cs_5BiP_4Se_{12}$ microfibers was achieved by reacting a mixture of Cs_2Se:Bi:P:Se=2.5:1:4:9.5 under vacuum in a fused silica tube at 850 °C for 5 d, followed by washing with degassed *N,N*-dimethylformamide (DMF) under a N_2 atmosphere (~80 % yield based on Bi). Alternatively, the title compound could be obtained by a stoichiometric mixture of the same reagents in a fused silica tube at 850 °C for 3h. Shorter reaction times produced typical tiny needles instead of microfibers. Energy dispersive spectroscopic analysis showed an average composition of "$Cs_{4.9}BiP_{3.8}Se_{11.6}$" and "$Cs_{4.8}BiP_{3.9}Se_{11.8}$" for the respective synthetic conditions. The single crystals are stable in DMF, alcohol, and air at least over a week. They are soluble in NMF to give deep orange solutions. $Cs_5BiP_4Se_{12}$ nanowires were obtained by ultrasonic irradiation of the microwire-shaped compound in EtOH for 10 min. For TEM studies, the resulting colloidal solution was centrifuged at 4000 rpm for 1 hr and filtered by a 0.2 μm syringe filter.

3. Physical Measurements.

X-ray Powder Diffraction. Phase purity X-ray diffraction analyses were performed using a calibrated CPS 120 INEL X-ray powder diffractometer (Cu K_α graphite monochromatized radiation) operating at 40 kV/20 mA and equipped with a position-

sensitive detector with flat sample geometry.

Scanning Electron Microscopy. Semiquantitative analyses and taking morphology images of the compounds were performed with a JEOL JSM-35C scanning electron microscope (SEM) equipped with a Tracor Northern energy dispersive spectroscopy (EDS) detector.

Transmission Electron Microscopy (TEM) and High Resolution TEM. TEM sample was diluted with ethanol and irradiated by ultrasonification. TEM and HRTEM images were obtained with JEOL JEM 2200 FS (Field emission TEM).

Solid-State UV-vis Spectroscopy. Optical diffuse reflectance measurements were performed at room temperature using a Shimadzu UV-3101 PC double-beam, double-monochromator spectrophotometer operating in the 200-2500 nm region. The instrument is equipped with an integrating sphere and controlled by a personal computer. $BaSO_4$ was used as a 100% reflectance standard. The sample was prepared by grinding the crystals to a powder and spreading it on a compacted surface of the powdered standard material, preloaded into a sample holder. The reflectance versus wavelength data generated, were used to estimate the band gap of the material by converting reflectance to absorption data[20] according to Kubelka-Munk equations: $\alpha/S = (1 - R)^2/(2R)$, where R is the reflectance and α and S are the absorption and scattering coefficients, respectively.

Raman Spectroscopy. Raman spectra were recorded on a Holoprobe Raman spectrograph equipped with a CCD camera detector using 633 nm radiation from a HeNe laser for excitation and a resolution of 4 cm^{-1}. Laser power at the sample was estimated to be about 5 mW, and the focused laser beam diameter was ca. 10 μm. A total of 128 scans were sufficient to obtain good quality spectra.

Infrared Spectroscopy. FT-IR spectra were recorded as solids in a CsI or KBr matrix. The samples were ground with dry CsI or KBr into a fine powder and pressed into translucent pellets. The spectra were recorded in the far-IR region (600-100 cm^{-1}, 4 cm^{-1} resolution) and mid-IR region (500-4000 cm^{-1}, 4 cm^{-1} resolution) with the use of a Nicolet 740 FT-IR spectrometer equipped with a TGS/PE detector and silicon beam splitter.

Differential Thermal Analysis (DTA) Experiments were performed on Shimadzu DTA-50 thermal analyzer. A sample (~30 mg) of ground crystalline material was sealed in a silica ampoule under vacuum. A similar ampoule of equal mass filled with Al_2O_3 was sealed and placed on the reference side of the detector. The sample was heated to 800°C at °C min^{-1}, and after 1 min it was cooled at a rate of –10 °C min^{-1} to 50 °C. The residues of the DTA experiments were examined by X-ray powder diffraction. Reproducibility of the results was confirmed by running multiple heating/cooling cycles. The melting and crystallization points were measured at a minimum of endothermic peak and a maximum of exothermic peak.

X-ray Crystallography. Since $Cs_5BiP_4Se_{12}$ crystallized as a very thin microwire form that is a bundle of individual nanowires, it was extremely hard to find suitable single crystals for X-ray diffraction studies. Most of single crystals chosen showed substantial diffused peaks. Intensity data for $Cs_5BiP_4Se_{12}$ were collected at 293(2) K on a STOE IPDS II diffractometer with Mo K_α radiation operating at 50 kV and 40 mA with a 34 cm diameter imaging plate. Data collection at lower temperature was not favorable because N_2 stream affected the very thin wire-shaped single crystal. Individual frames were collected with a 15 min exposure time and a 1.0 ω rotation. The X-AREA, X-RED and

X-SHAPE software package was used for data extraction and integration and to apply empirical and analytical absorption corrections. The SHELXTL software package was used to solve and refine the structure. The most satisfactory refinement was obtained with the polar space group, $Pmc2_1$. The Cs(8) atom was modeled as a split site to Cs(8A) and Cs(8B). Their occupancy ratio was refined to 95:5. The Flack parameter x refined to 0. The parameters for data collection and the details of the structural refinement are given in Table 8-1. Fractional atomic coordinates and displacement parameters for each structure are given in Tables 8-2 – 8-4. In all cases the atoms refined to full occupancy.

Electronic Band Structure Calculations. The electronic structure calculations were performed using the full potential linearized augmented plane wave (FLAPW) method[19] within density functional scheme. The experimental lattice parameters and atomic coordinates were employed for the calculations. The core states and the valence states were treated fully relativistically and scalar relativistically, respectively. The spin-orbit interaction was also included self-consistently by a second variational method.[21] A 5×3×1 mesh of special k-points was used in the irreducible Brillouin zone and the energy cutoffs for the interstitial plane-wave basis and the star functions were 13.0 and 144.0 Ry, respectively. The muffin-tin radii of P, Se, Cs, and Bi were 1.9, 2.0, 2.7, and 2.8 bohrs, respectively.

Nonlinear Optical Property Measurements. We used the frequency-tripled output of a passive-active mode-locked Nd:YAG laser with a pulse width of about 15 ps and a repetition rate of 10 Hz to pump an optical parametric amplifier (OPA). The OPA generates vertically polarized pulses in the ranges 400 ~ 685 nm and 737 ~ 3156 nm. In order to check the SHG efficiency as a function of the excitation energy, we tuned the

wavelength of the incident light from 1000 ~ 2000 nm. In this range, the spectral bandwidth of the linearly polarized light from the OPA is rather broad, about 2 meV full width at half maximum. However, the phase space compression phenomena ensures effective SHG where lower energy portions are exactly compensated by higher parts thereby satisfying both energy and momentum conservation. The incident laser pulse of 300 μJ was focused onto a spot 500 μm in diameter using a 3 cm focal-length lens. The corresponding incident photon flux is about 10 GW cm^{-2}. The SHG signal was collected in reflection geometry from the excitation surface and focused onto a fiber optic bundle. The output of the fiber optic bundle was coupled to the entrance slit of a Spex Spec-One 500 M spectrometer and detected using a nitrogen-cooled CCD camera. The data collection time was 20 s. Single crystal $Cs_5BiP_4Se_{12}$ sample and $AgGaSe_2$ were ground and separated by various size ranges using sieves. Samples were placed in capillary tubes and measured. The SHG intensity of $Cs_5BiP_4Se_{12}$ in a wide range of 500 – 1000 nm was compared to that of $AgGaSe_2$.

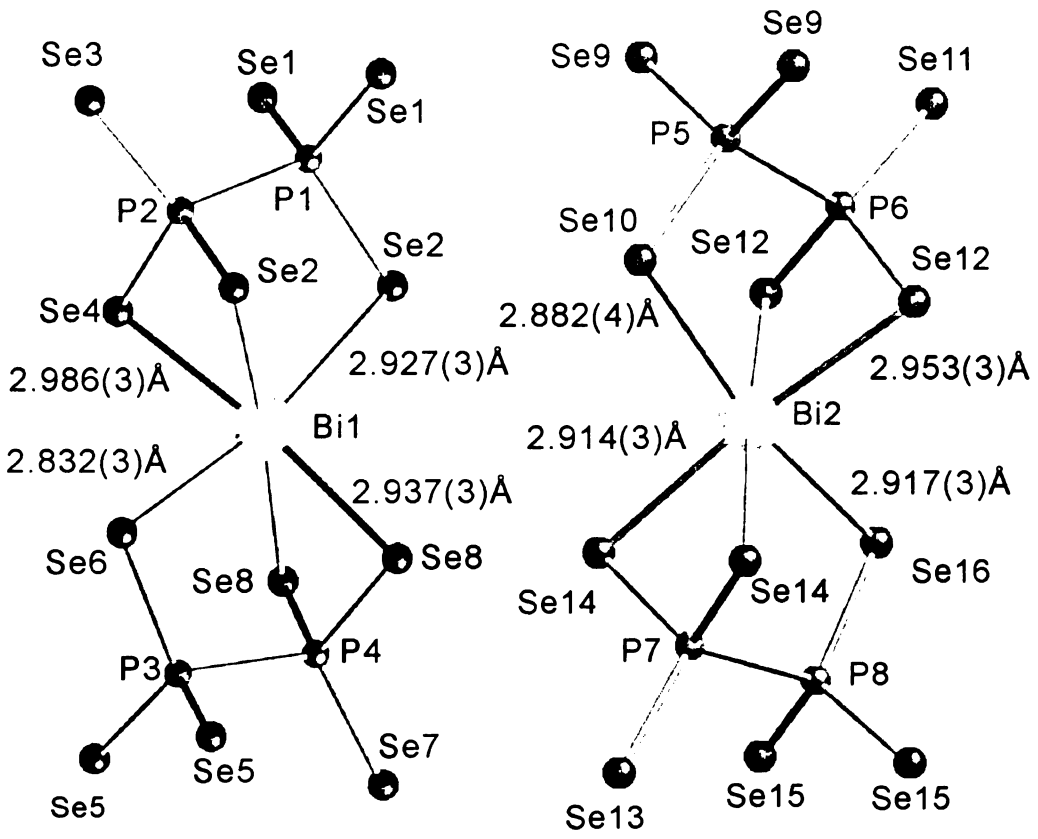

Figure 8-1. Structure of two crystallographically independent $[BiP_4Se_{12}]^{5-}$ molecules. Bi, P, and Se atoms are labeled. Bond distances (Å) are represented.

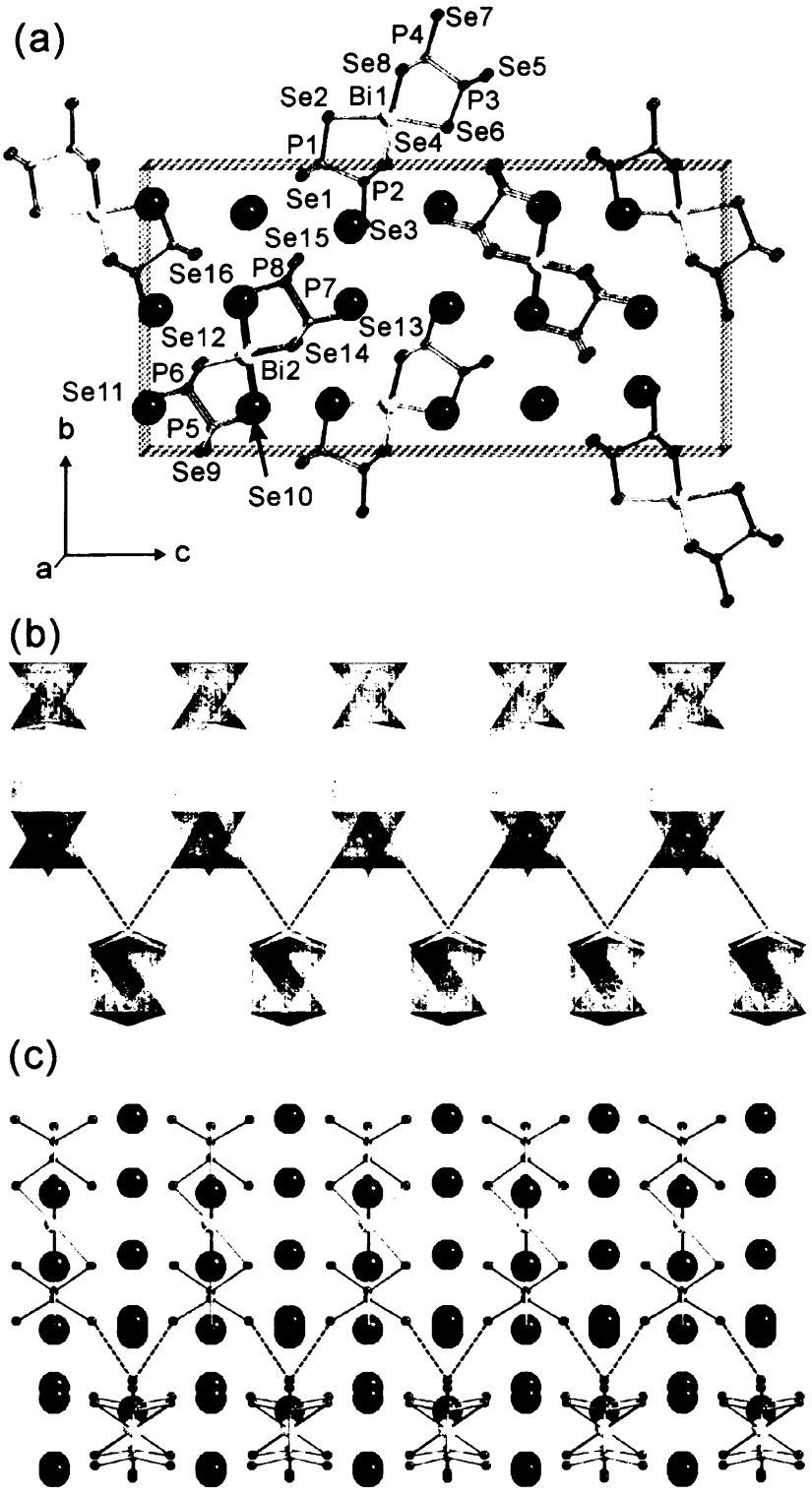

Figure 8-2. (a) Structure of $Cs_5BiP_4Se_{12}$ viewed down the *a*-axis (down the fiber direction). Bi, P, and Se atoms are labeled. Large circles are Cs atoms. (b) Polyhedral and (c) ball and stick representation of a *pseudo*-one-dimensional $[BiP_4Se_{12}]^{5-}$ chain viewed the [0 -2 1] direction. Dashed line depicts short nonbonding interaction between Se(5) and Se(16) at 3.478(3) Å. Light polyhedron depicts $[BiSe_6]$ octahedron and dark $[P_2Se_6]^{4-}$ unit with Cs atoms omitted in (b).

Table 8-1. Crystallographic Data and Refinement Details for $Cs_5BiP_4Se_{12}$

Formula	$Cs_5BiP_4Se_{12}$
Crystal system	Monoclinic
Space group	$Pmc2_1$ (no. 26)
Unit cell dimensions	a = 7.5357(2)
	b= 13.7783(6)
	c =28.0807(8)
Z	4
V, Å^3	2915.59(17)
d (calculated), gr cm^{-3}	4.431
Crystal dimensions, mm^3	0.1189 × 0.0006 × 0.0006
Temperature, K	293(2)
λ, Å	0.71073
μ, mm^{-1}	27.392
F(000)	3304
θ_{max} (deg)	27.392
Total / unique reflections	18838 / 6306
R_{int}	0.0443
No. Parameters	246
Refinement method	Full-matrix least-squares on F^2
Final R indices [$I > 2\sigma(I)$], R_1[a]/wR_2 [b]	0.0626 / 0.1151
R indices (all data), R_1/wR_2	0.0790 / 0.1207
Goodness-of-fit on F^2	1.077
Largest diff. peak and hole, e. Å^{-3}	2.198/-3.339

[a] $R1 = \Sigma \| |F_o| - |F_c| \| / \Sigma |F_o|$. [b] $wR2 = \{\Sigma [w(F_o^2 - F_c^2)^2] / \Sigma [w(F_o^2)^2]\}^{1/2}$

Table 8-2. Atomic Coordinates ($\times 10^4$) and Equivalent Isotropic Parameters ($\times 10^3$ Å^2) for $Cs_5BiP_4Se_{12}$ at 293(2) K. [a]

Atom	*x*	*y*	*z*	*U*(eq)
Cs(1)	5000	1495(2)	1862(1)	10(1)
Cs(2)	5000	1511(2)	85(1)	17(1)
Cs(3)	5000	1680(2)	6808(1)	22(1)
Cs(4)	5000	5132(2)	3542(1)	20(1)
Cs(5)	5000	5112(2)	1653(1)	21(1)
Cs(6)	0	1356(1)	5139(1)	9(1)
Cs(7)	0	1675(2)	3247(1)	20(1)
Cs(8A)	0	1680(2)	6780(1)	21(1)
Cs(8B)	-1080(60)	1710(2)	6823(1)	21(1)
Cs(9)	0	4953(2)	209(1)	71(1)
Cs(10)	0	7879(2)	3559(1)	22(1)
Bi(1)	5000	1681(1)	4219(1)	6(1)
Bi(2)	0	3406(1)	1777(1)	10(1)
P(1)	5000	50(7)	3042(1)	15(2)
P(2)	5000	594(6)	8775(1)	12(2)
P(3)	5000	2792(6)	5492(1)	7(1)
P(4)	5000	3750(6)	4835(1)	9(2)
P(5)	0	871(6)	1187(1)	8(2)
P(6)	0	2200(6)	737(1)	7(2)
P(7)	0	4521(6)	2829(1)	18(2)
P(8)	0	5922(7)	2417(1)	16(2)
Se(1)	2540(3)	382(2)	7718(1)	19(1)
Se(2)	5000	1658(3)	3155(1)	12(1)
Se(3)	5000	7873(3)	3753(1)	21(1)
Se(4)	2597(3)	24(2)	4122(1)	15(1)
Se(5)	2594(3)	3137(2)	5873(1)	12(1)
Se(6)	5000	1308(2)	5210(1)	9(1)
Se(7)	5000	4745(2)	36(2)	21(1)

Table 8-2. (Cont'd) Atomic Coordinates ($\times 10^4$) and Equivalent Isotropic Parameters ($\times 10^3$ Å^2) for $Cs_5BiP_4Se_{12}$ at 293(2) K.[a]

Se(8)	2633(3)	3322(2)	4423(1)	12(1)
Se(9)	2406(3)	83(2)	1005(1)	11(1)
Se(10)	0	1339(2)	1933(1)	10(1)
Se(11)	0	1846(3)	3(1)	22(1)
Se(12)	2378(3)	3025(2)	962(1)	13(1)
Se(13)	0	4821(4)	3564(1)	29(1)
Se(14)	2390(3)	3734(2)	2576(1)	20(1)
Se(15)	2467(3)	6631(2)	2605(1)	17(1)
Se(16)	0	5509(2)	1653(1)	11(1)

[a] The occupancy of Cs(8A) and Cs(8B) is 95 and 5 %. All other sites are fully occupied.

[b] U(eq) is defined as one-third of the trace of the orthogonalized U_{ij} tensor.

Table 8-3. Selected Bond Distances (Å) for $Cs_5BiP_4Se_{12}$ at 298(2) K.

Bi(1) – Se(2)	2.986(3)	Bi(2) – Se(10)	2.882(4)
Bi(1) – Se(4)	2.927(3) ×2	Bi(2) – Se(12)	2.953(3) ×2
Bi(1) – Se(6)	2.832(3)	Bi(2) – Se(14)	2.914(3) ×2
Bi(1) – Se(8)	2.937(3) ×2	Bi(2) – Se(16)	2.917(3)
P(1) – Se(1)	2.149(5) ×3	P(5) – Se(9)	2.175(5) ×2
P(1) – Se(2)	2.238(10)	P(5) – Se(10)	2.192(8) ×2
P(2) – Se(3)	2.114(9) ×2	P(6) – Se(11)	2.118(8)
P(2) – Se(4)	2.226(5) ×3	P(6) – Se(12)	2.214(5) ×2
P(3) – Se(5)	2.159(5) ×2	P(7) – Se(13)	2.105(10)
P(3) – Se(6)	2.193(8)	P(7) – Se(14)	2.219(7) ×2
P(4) – Se(7)	2.148(8) ×2	P(8) – Se(15)	2.165(5) ×2
P(4) – Se(8)	2.206(5) ×2	P(8) – Se(16)	2.220(9)
P(1) –P(2)	2.241(12) ×2	P(5) – P(6)	2.224(11)
P(3) - P(4)	2.268(12)	P(7) – P(8)	2.252(13)

Table 8-4. Selected Angles (°) for $Cs_5BiP_4Se_{12}$ at 298(2) K.

Se(2)-Bi(1)-Se(4)	84.21(7)	P(1)#7-P(2)-Se(3)#5	111.6(4)
Se(2)-Bi(1)-Se(6)	168.91(10)	Se(10)-Bi(2)-Se(12)	86.67(7)
Se(2)-Bi(1)-Se(8)	101.78(7)	Se(10)-Bi(2)-Se(14)	92.05(8)
Se(4)-Bi(1)-Se(4)#1	76.45(10)	Se(10)-Bi(2)-Se(16)	178.10(11)
Se(4)-Bi(1)-Se(6)	87.09(7)	Se(12)-Bi(2)-Se(12)#2	74.74(10)
Se(4)-Bi(1)-Se(8)	104.06(6)	Se(12)-Bi(2)-Se(14)	104.44(6)
Se(4)#1-Bi(1)-Se(8)	174.01(7)	Se(12)-Bi(2)-Se(14)#2	178.51(9)
Se(6)-Bi(1)-Se(8)	86.98(7)	Se(12)-Bi(2)-Se(16)	94.84(8)
Se(8)-Bi(1)-Se(8)	74.79(9)	Se(14)-Bi(2)-Se(14)#2	76.36(11)
Se(1)#3-P(1)-Se(1)#4	119.2(4)	Se(14)-Bi(2)-Se(16)	86.45(8)
Se(1)#3-P(1)-Se(2)	109.5(3)	P(1)#7-P(2)-Se(4)#7	104.5(3)
Se(3)#5-P(2)-Se(4)#6	113.3(3)	P(2)#3-P(1)-Se(2)	105.2(4)
Se(4)#6-P(2)-Se(4)#7	108.9(4)	P(3)-P(4)-Se(7)#5	110.4(4)
Se(5)-P(3)-Se(5)#1	114.3(4)	P(3)-P(4)-Se(8)	105.7(3)
Se(5)-P(3)-P(6)	112.6(2)	P(4)-P(3)-Se(5)	106.0(3)
Se(7)#5-P(4)-Se(8)#1	113.3(3)	P(4)-P(3)-Se(6)	104.5(4)
Se(8)-P(4)-Se(8)#1	107.9(3)	P(5)-P(6)-Se(11)	111.3(4)
Se(9)-P(5)-Se(9)#2	113.0(4)	P(5)-P(6)-Se(12)	105.1(3)
Se(9)-P(5)-Se(10)	111.8(3)	P(6)-P(5)-Se(9)	106.1(3)
Se(11)-P(6)-Se(12)	113.3(2)	P(6)-P(5)-Se(10)	107.5(4)
Se(12)-P(6)-Se(12)#2	108.1(4)	P(7)-P(8)-Se(15)	105.2(3)
Se(13)-P(7)-Se(14)	114.2(3)	P(7)-P(8)-Se(16)	106.1(4)
Se(14)-P(7)-Se(14)#2	108.5(5)	P(8)-P(7)-Se(13)	109.6(5)
Se(15)-P(8)-Se(15)#2	118.3(4)	P(8)-P(7)-Se(14)	104.7(3)
Se(15)-P(8)-Se(16)	110.6(3)		

Symmetry transformation used to generate equivalent atoms: (#1)-x+1, y, z; (#2)-x, y, z; (#3) –x+1, -y, z-1/2; (#4) x, -y, z-1/2; (#5) –x+1, -y+1, z+1/2; (#6) x, -y, z+1/2; (#7) –x+1, -y, z+1/2.

4. Results and Discussion

Synthesis and Crystal Structure. The new compound $Cs_5BiP_4Se_{12}$ adopts the polar space group $Pmc2_1$. It features the discrete molecular $[Bi(P_2Se_6)_2]^{5-}$ anion, Figure 8-1, which is isolated by Cs^+ cation, Figure 8-2a. The molecule is isostructural to $[In(P_2Se_6)_2]^{5-}$ [22] and $[P(P_2Se_6)_2]^{5-}$ [23] anions. There are two crystallographically unique Bi atoms and each octahedrally coordinating Bi^{3+} center is capped by two chelating tridentate $[P_2Se_6]^{4-}$ units from opposite directions. Although the respective $[Bi(P_2Se_6)_2]^{5-}$ molecules are acentric due to the distorted $[BiSe_6]$ octahedra, the polar structure arises from the noncentrosymmetric packing of Cs^+ ions. The absence of mirror plane perpendicular to the 2_1 screw axis creates the polar structural arrangement of the compound. The Bi-Se distances are normal ranging from 2.832(3) to 2.986(3) Å. The P-Se distances range from 2.114(9) to 2.241(12) Å. The P-P distances are typical at 2.224(11) to 2.252(11) Å. Noteworthy is the unusually short intermolecular nonbonding interaction of Se(5)···Se(16) at 3.478 Å, which is much shorter than the van der Waals radii sum of 3.8 Å.[24] This weak interaction is important in enabling the compound to organize in an infinite *pseudo*-one-dimensional structure along *a*-axis, Figure 8-2b. The ionic interaction of Cs^+ with $[Bi(P_2Se_6)_2]^{5-}$ is, however, also prominent as we will argue later. Low-dimensional compounds such as $NbSe_3$, $APSe_6$ (A=K, Rb, Cs),[25] $K_2P_2Se_6$,[26] and the molecular $Rb_4P_6Se_{12}$[27] display similar Se···Se interactions. The dipole associated with the noncentrosymmetric structure is parallel to the c-axis which is perpendicular to the nanowire direction. Other polar nanowire systems include the II-IV semiconductors such as ZnO, CdS, CdSe, and the III-V semiconductors GaAs, InP, etc. In these systems,

the dipole is aligned along the nanowire axis. The $Cs_5BiP_4Se_{12}$ is the first example where the dipole is perpendicular to the long axis.

Comparing polychalcophosphate flux reaction conditions that favor $Cs_5Bi(P_2Se_6)_2$ vis-à-vis $Cs_8Bi_4(P_2Se_6)_5$[28] we can gain deeper insight into the evolution of structure. The latter was synthesized in a more basic alkali polyselenophosphate flux of $Cs_2Se:P_2Se_5:Se=1:1.5:2$ at 460 °C, giving a remarkably complicated layered structure of $^2/_\infty[Bi_4(P_2Se_5)^{8-}]$. In contrast, the simpler molecular complex $[Bi(P_2Se_6)_2]^{5-}$ of the title compound was obtained by less basic flux of $Cs_2Se:P_2Se_5:Se=1:1.6:3.8$ at 850 °C. In general, less basic conditions or lower flux temperatures tend to generate longer or extended fragments.[29] Hence, we assume that the higher temperature plays a more dominant role in stabilizing $Cs_5Bi(P_2Se_6)_2$ than the flux basicity. Thus, we can expect for a given flux composition different products to form at high reaction temperature of 800-1000 °C from those formed at intermediate reaction temperatures (300-600 °C).

Nanowires. The fibrous nature of $Cs_5BiP_4Se_{12}$ is apparent by visual inspection and in scanning electron microscopic (SEM) images, Figure 8-3a. As-prepared microfibers are typically ~mm in length and submicron in thickness. The microfibers readily split to thinner fibers by physical contact. Transmission electron microscopic (TEM) images of single microfibers confirmed that they consist of individual nanowires with uniform thickness and alignment with the interval at 2.9 nm, close to the dimension of the crystallographic *c*-axis, Figure 8-3b. This creates the extreme difficulty in finding single crystals suitable for X-ray diffraction studies. Most crystals we examined showed extensive diffuse scattering normal to the a^*-axis consistent with the nanosize dimensions of the coherence length along the *b*- and *c*- axes (i.e. perpendicular to the

fiber).

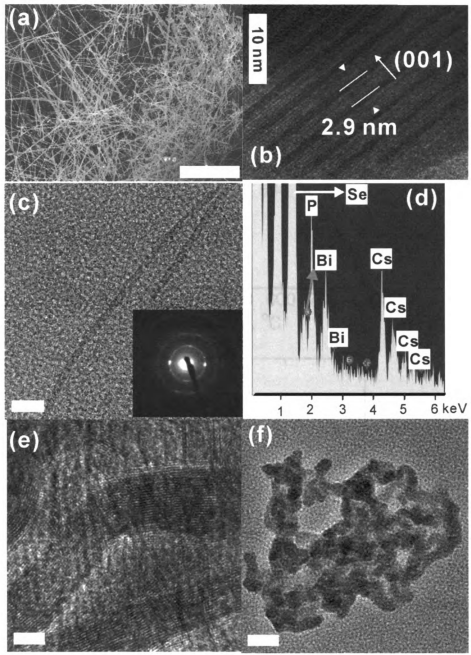

Figure 8-3. (a) Representative SEM image of $Cs_5BiP_4Se_{12}$ microfibers demonstrating their flexible texture. (b) TEM image of a bundle of nanowires showing uniform alignment of individual nanowires. The interval of each nanowire was measured at 2.9 nm, close to the crystallographic *c*-axis of 28.0807(8) Å. Inset: selected area electron diffraction pattern of $Cs_5BiP_4Se_{12}$ nanowires. (c) TEM image, (inset: selected area electron diffraction pattern of nanowires, (d) EDS analysis, and (e) HRTEM image of individual $Cs_5BiP_4Se_{12}$ nanowire dispersed in EtOH. (f) Tangled texture of $Cs_5BiP_4Se_{12}$ nanowire depicting its striking flexibility. The scale bar corresponds to (a) 500 μm, (b) 10 nm, (c) 20 nm, (e) 5 nm, and (f) 20 nm, respectively.

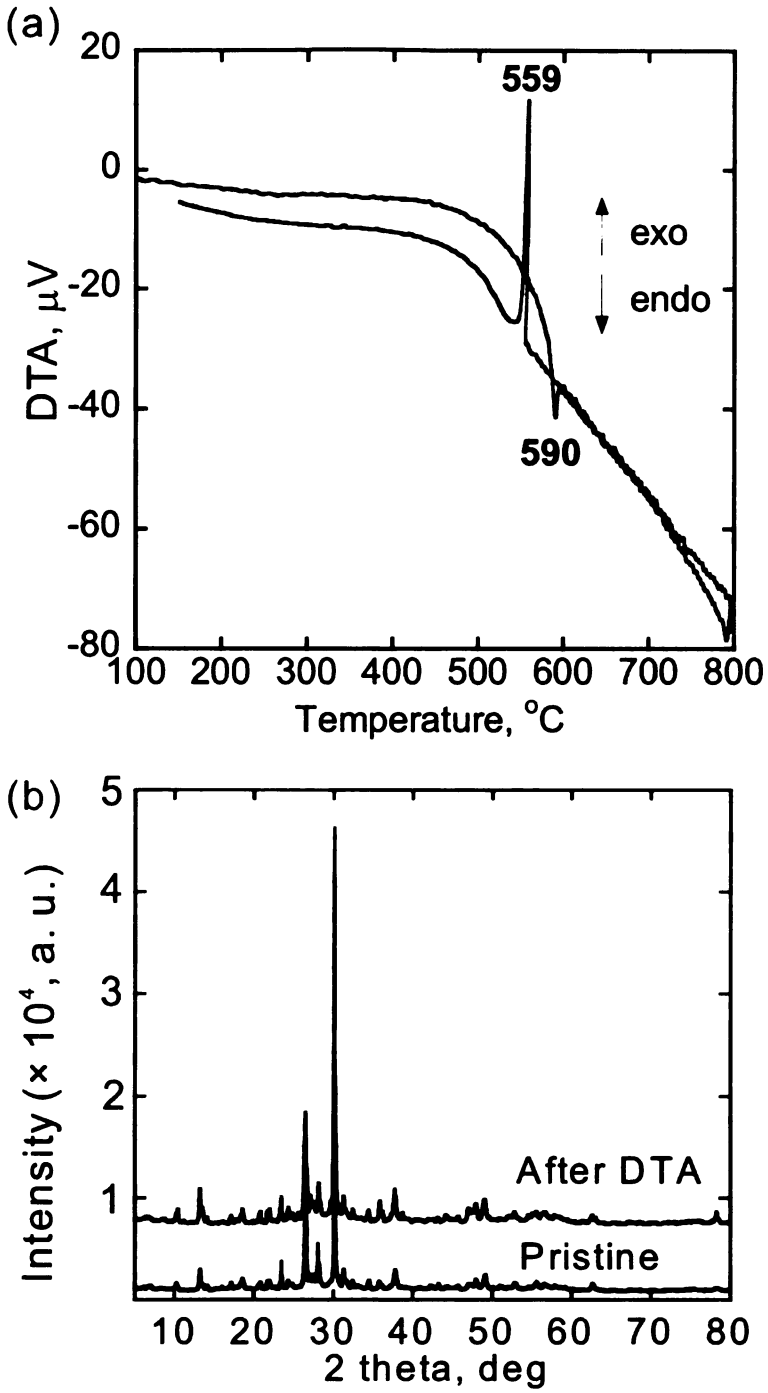

Figure 8-4. (a) Differential thermal analysis (DTA) and (b) X-ray powder diffraction patterns of pristine material and sample obtained after DTA.

The $Cs_5BiP_4Se_{12}$ microfibers can be dispersed in EtOH under N_2 atmosphere and ultrasonificated for ~10 min to form a colloidal suspension of the corresponding individual nanowires, Figure 8-3c. Selected area electron diffraction pattern showed crystalline nature of the nanowires, inset in Figure 3c. Energy dispersive spectroscopic (EDS) analysis on the sample examined by TEM showed all Cs, Bi, P, and Se to be present in the expected ratio, Figure 8-3d. The distribution in nanowire diameter is xx-yy nm. Typical long $Cs_5BiP_4Se_{12}$ nanowires show a striking flexibility and tangled texture, Figure 8-3e-f. This is extraordinary considering the single crystalline nature of the fibers. The flexible character likely arises from the weak intrachain and interchain interactions created by long nonbonding Se···Se contacts between $[Bi(P_2Se_6)_2]^{5-}$ molecules which allows them to slide past one another and bend. These weak non-bonding interactions play a key role in determining the emergent behavior in this material which is the long flexible fiber morphology from the packing of simple coordinating complexes of $[Bi(P_2Se_6)_2]^{5-}$.

Differential thermal analysis (DTA) of $Cs_5BiP_4Se_{12}$ at a rate of 10 °C min^{-1} showed melting at 590 °C and crystallization upon cooling at 559 °C, Figure 8-4a. The powder X-ray diffraction patterns before and after melting/recrystallization were identical indicating congruent melting, Figure 8-4b. The solid-state optical absorption spectrum revealed a sharp absorption edge and a band gap of 1.85 eV, which is in good agreement with its dark red color, Figure 5. The nearly vertical rise of the absorption coefficient suggests a direct bang-gap material. In comparison, $Cs_8Bi_4(P_2Se_6)_5$ compound showed a sharp optical gap at 1.44 eV.

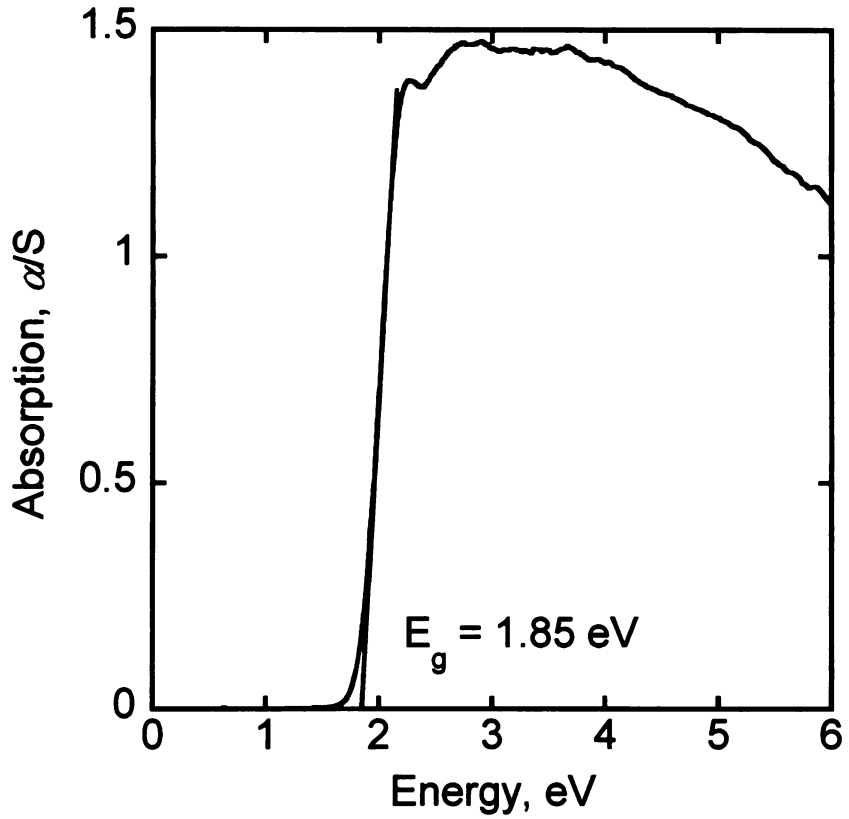

Figure 8-5. Solid-state optical absorption spectrum of $Cs_5BiP_4Se_{12}$.

Electronic Structure Calculations. To better understand the experimental findings and in particular to explore the origin and nature of the band gap result, the electronic structure was calculated using the FLAPW method with the screened-exchange local density approximation (sX-LDA) as well as the Hedin-Lundqvist[30] (LDA) forms of the exchange-correlation potential. The sX-LDA method has been successfully applied to a wide range of semiconductors, and shows great improvements of the excited electronic states in terms of correctly determining the band gaps and band dispersion.[31] While the LDA calculations yield a band gap of 1.48 eV without spin orbital coupling (SOC), Figure 8-6, and 1.15 eV with SOC included, Figure 8-7, the electronic structure calculated by the sX-LDA method with SOC determines the band gap to be 2.0 eV, which is close to the experimental band gap, 1.85 eV, Figure 8-8. The valence band maximum (VBM) and the conduction band minimum (CBM) occur along the T-Y direction and give rise to an indirect band gap, Figure 8-9. However, the almost plateau-like band dispersion ($\leq$ 5 meV) along the T-Y direction causes a large joint density of states at 2.0 eV, which is responsible for the very sharp absorption edge observed in the experiment, Figure 8-5. The narrow band dispersions (e.g. $\leq$ 0.05 eV for the valence top band along the Γ-Z-T-Y) indicate the molecular nature of the compound. The relatively strong dispersion (~0.24 eV for the valence top band) along the Γ-X direction arises from the Se···Se intermolecular interactions along the nanowire direction (*a*-axis in Figure 8-2a) compared to other directions.

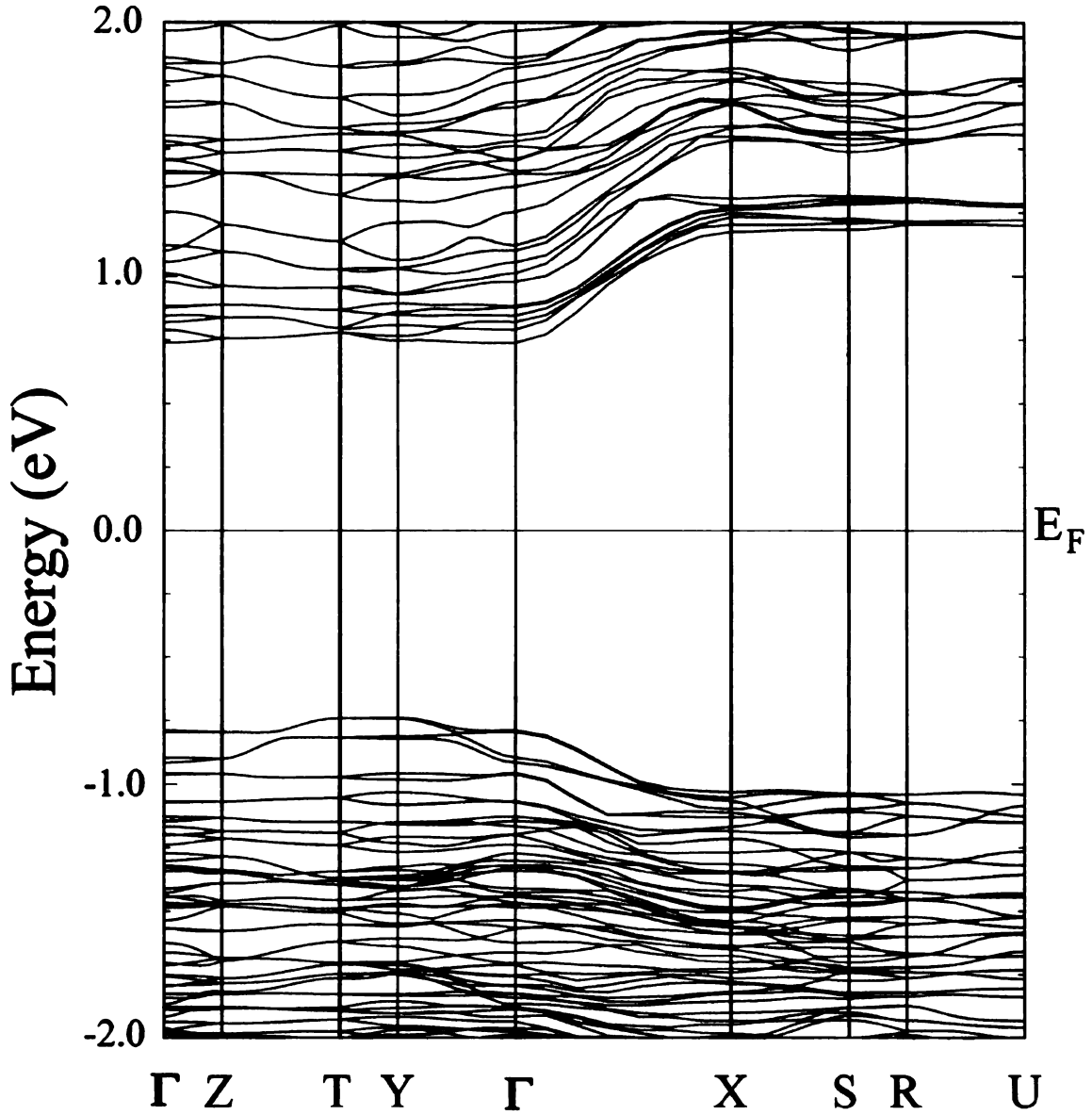

Figure 8-6. The calculated band structures using LDA (E_g = 1.45 eV).

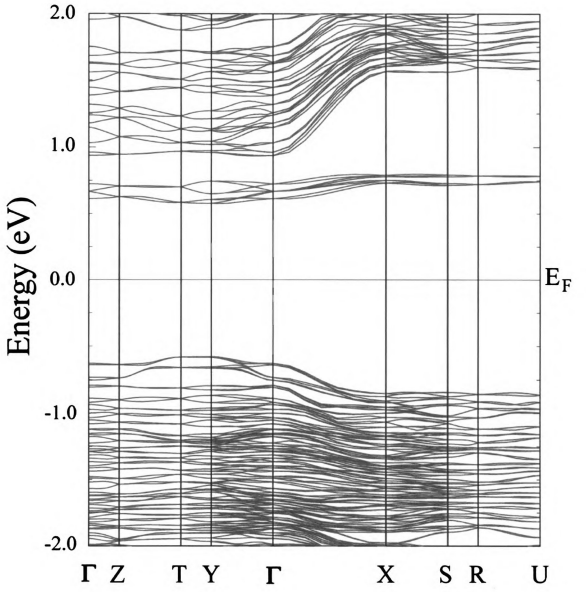

Figure 8-7. The calculated band structures using LDA with spin-orbit coupling (SOC) (E_g = 1.15 eV).

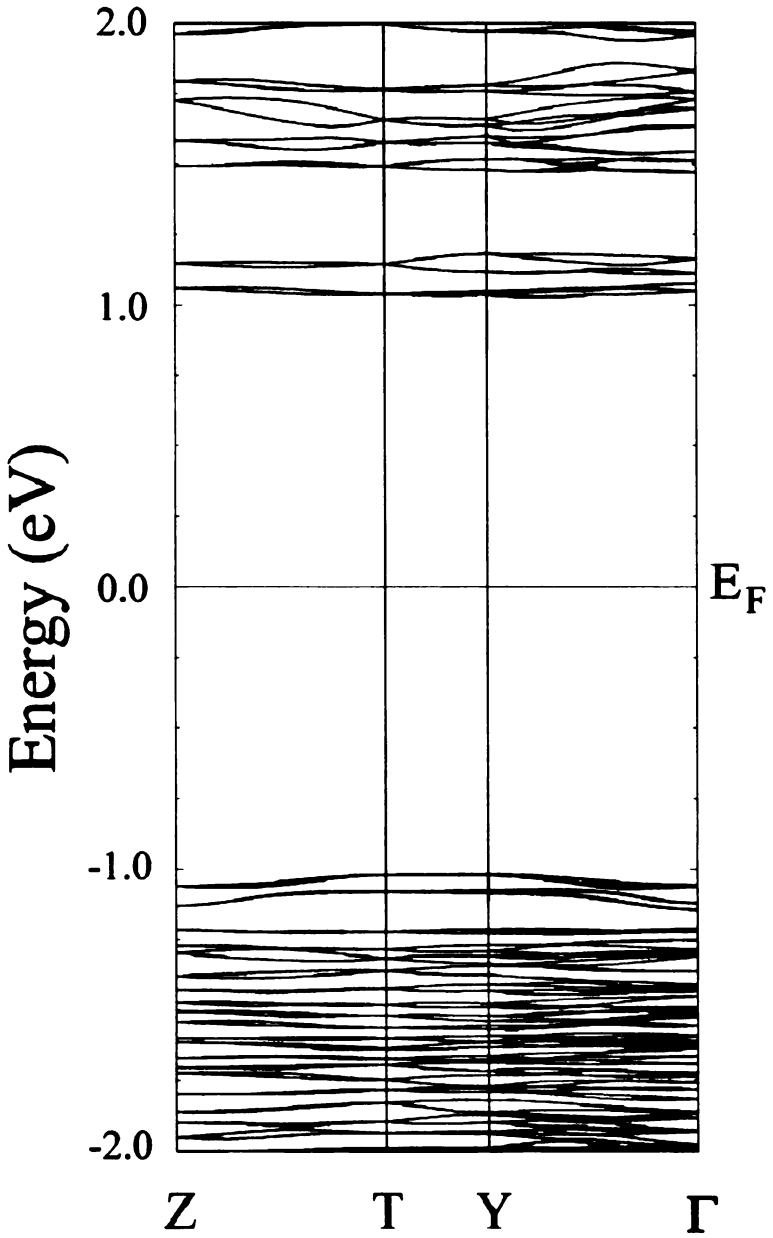

Figure 8-8. The calculated band structures sX-LDA with SOC (E_g = 2.0 eV), shown for only a small part of the Brillouin zone, namely Z-T-Y-Γ).

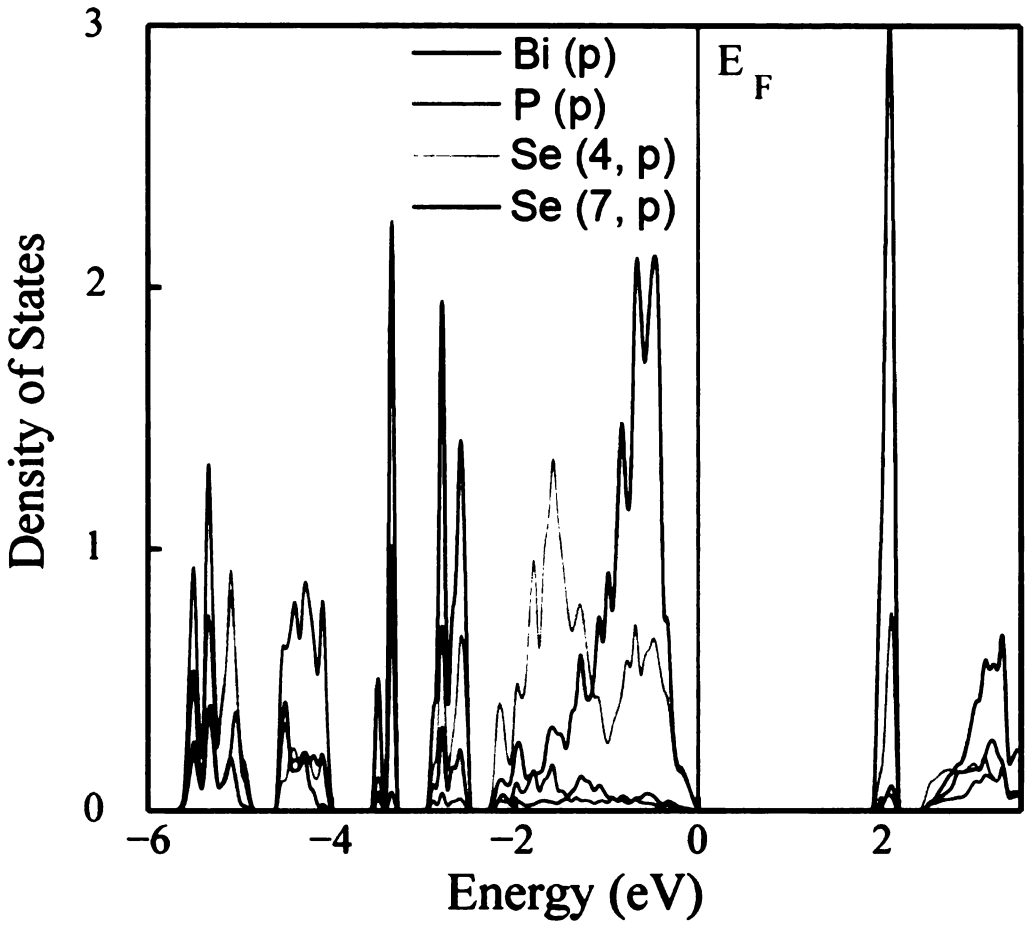

Figure 8-9. The projected density of states for *p*-orbitals of individual elements (Bi, P, Se) calculated with sX-LDA and SOC.

The angular-momentum-resolved density of states (DOS) for the individual atoms reveals that the p-p mixing has a strong effect on the electronic structure and on the energy level ordering. The strong covalent interactions between mainly P and Se *p*-orbitals forms the lower energy levels [at -6 eV ~ -4 eV] in the valence band. The energy states derived from the relatively weak hybridization between the Bi and Se *p*-orbitals are located between -4 eV and -2 eV. The dominating Se *p*-character from -2 eV to the VBM can be attributed to the lone pair states of Se and to the ionic bonding between Cs and Se. In this energy range, the *p* orbital contribution of other elements are negligibly small as shown in Figure 8-9. The conduction band minimum shows strong Bi *p*-character, which is highly affected, by the spin-orbit coupling (SOC), Figures 8-6 and 8-7. Therefore, the band gap excitation observed in the electronic spectrum of the compound shown in the Figure 5 is due to direct transitions from Se *p* to Bi *p* states.

It is unusual for discrete molecules to form nanofibers. Careful inspection of the crystal structure, Figures 8-2a and 8-10, shows that Cs atoms along the *a*-axis have more anionic Se atoms available to interact with, which gives stronger ionic interactions along the *a*-axis than those in the other directions. For instance, Figure 8-10d shows the neighbor atoms of three different molecular units (I, II, and III) around the Cs atom within 4.7 Å. Due to the larger number of neighbors in Figure 8-10d the molecular units (I) and (II) along the *a*-axis have much stronger ionic interactions with the Cs than the molecular unit (III) in the *b*-*c* plane. As a result, ionic interactions can predominantly propagate along the *a*-axis, which in turn would give better chance of crystal seeds growing along the *a*-axis, e.g. apparent nanofiber growing direction.

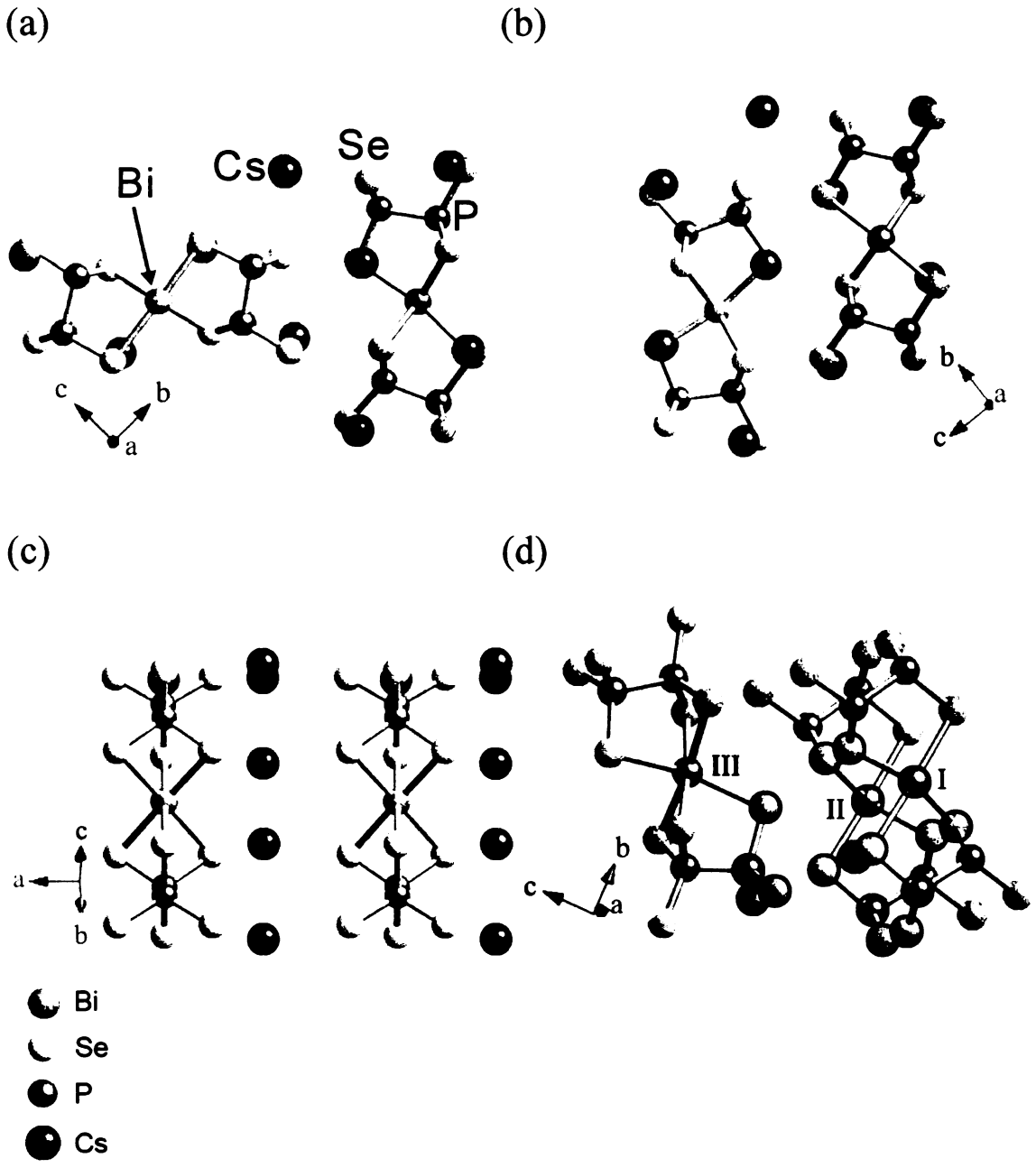

Figure 8-10. Three different models, (a), (b), and (c), taken from the original crystal structure, for the binding energy calculations (see text). The coordinates of two molecular units are taken from the original crystal structure (Figure 1a) in the *b-c* plane ((a), (b)) and along the *a*-axis (c). The neighbor atoms of three molecular $[BiP_4Se_{12}]^{5-}$ units (I, II, and III) around the Cs atom within 4.7 Å are indicated in blue circles (d).

To better understand how the discrete molecules give rise to the nanowire nature of $Cs_5BiP_4Se_{12}$, the binding energies of the molecular $[BiP_4Se_{12}]^{5-}$ units in each crystallographic direction were investigated with the LDA and the gradient-corrected Perdew, Burke, and Ernzerhof[32] (GGA) forms of the exchange-correlation potential. We prepared three different models in which the coordinates of two molecular units were taken from the original crystal structure (Figure 2a) in such a way that they have inter-molecular interactions for different orientations in the *b-c* plane, Figures 7a and 7b, and along the *a*-axis, Figure 7c. For these models, the binding energies were estimated by examining the total energy behavior in terms of the distance between two molecular units.

The LDA calculations yielded binding energies of 1.90 eV, 2.07 eV, and 4.13 eV for the 1st, 2nd, and 3rd models in Figure 8-10, respectively while the GGA calculations showed significantly smaller binding energies, namely 0.84 eV, 0.87 eV, and 3.35 eV for the 1st, 2nd, and 3rd models, respectively. The difference in the binding energies between the LDA and the GGA comes mainly from the van der Waals interactions. While the strongest interactions are the ionic interactions between the molecular units in the compound, there are also van der Waals closed-shell interactions, for which the LDA shows in general largely overestimated binding energies of the bonds. The GGA, by contrast, may give over- or underestimated or even no binding energies depending on the different GGA forms (i.e. BLYP, PBE) employed.[33] Even with the deficiency of these exchange-correlation approximations for the van der Waals interactions, both the LDA and GGA strongly showed significantly stronger bonds in the 3rd model, which is the interaction along the fiber direction. This is, therefore, the fastest growing direction which is consistent with the nanofiber nature found experimentally. The electronic

structure calculations of $Cs_5BiP_4Se_{12}$ clearly demonstrate the existence of dominating interactions along specific directions. This is indicated by the significant differences in binding energies along different crystallographic directions and explains how the ostensible molecular compound grows naturally to be nanofibers. The result suggests the possibility of theoretical modeling and prediction of what structural species can intrinsically produce nanofibers without complex preparation processes.

Spectroscopy and Nonlinear Optical Response. The Raman spectrum of $Cs_5BiP_4Se_{12}$ is very active with shifts at 118, 143, 172, 221, 300, 433 and 467 cm^{-1}, Figure 8-11. The peak at 221 cm^{-1} is unambiguously assigned to the locally A_{1g} symmetric stretching mode of the PSe_3 unit (half of the $[P_2Se_6]^{4-}$ ligand).[21] The peaks below 200 cm^{-1} are possibly related with Bi-Se stretching excitations. The other shifts can be attributed to PSe_3 stretching modes.

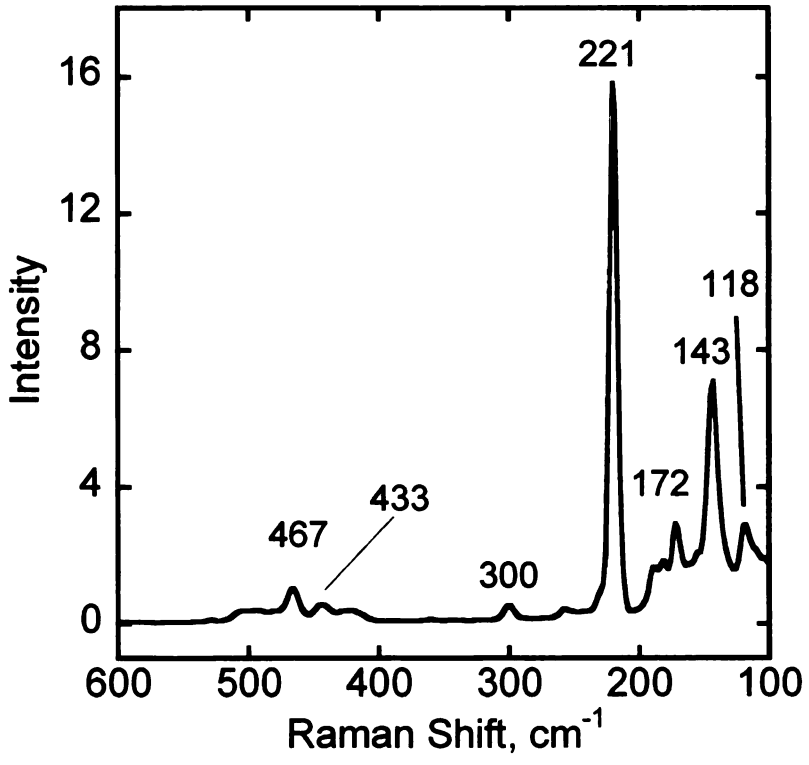

Figure 8-11. Raman spectrum of $Cs_5BiP_4Se_{12}$.

The far-IR spectrum showed peaks at 150, 181, 221, 300, 415, 440 and 502 cm^{-1}, similar to those of $KBiP_2Se_6$ which include $[P_2Se_6]^{4-}$ anion, Figure 8-12.[34] $Cs_5BiP_4Se_{12}$ is optically transparent in the far-IR through the mid-IR region to below the band edge in the visible region from 18.7 μm to 0.67 μm, corresponding to the region above the $[P_2Se_6]$ stretching absorptions, Figure 8-13. Wide optical transparency is a critical property for application of nonlinear optical (NLO) materials and optical fibers in the infrared region. NLO materials with high second harmonic generation (SHG) response is highly desirable as for example in telecommunications (near IR at 1.3-1.5 μm), as pollutant detection in the molecular fingerprint region (mid IR),[35] and medical surgery (mid IR at 10.6 μm) applications.[36]

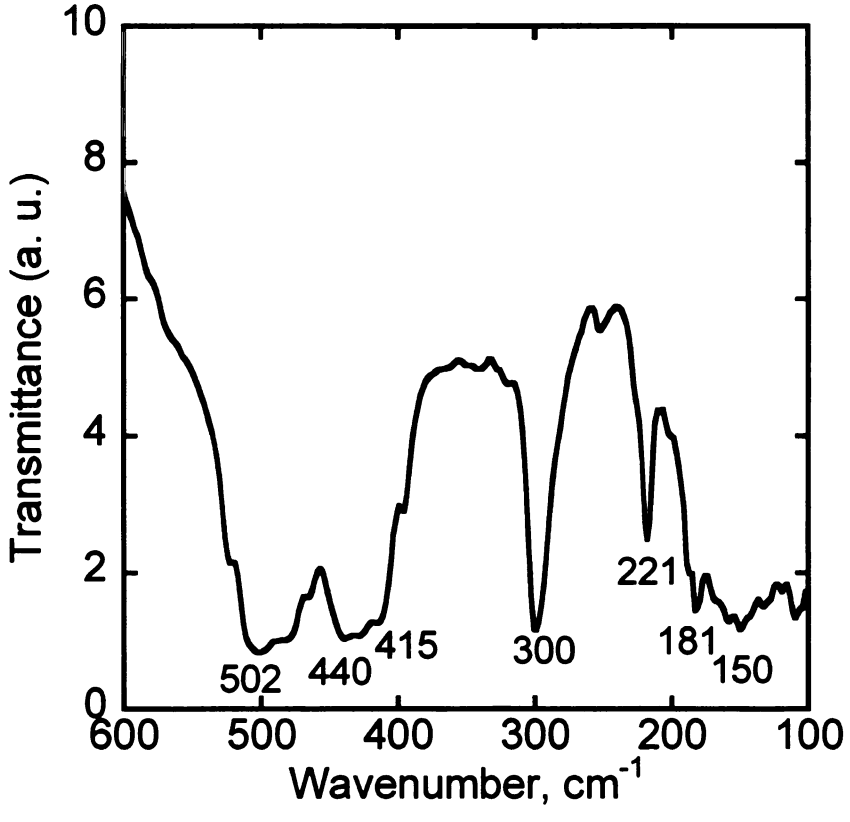

Figure 8-12. Far-IR spectrum of $Cs_5BiP_4Se_{12}$.

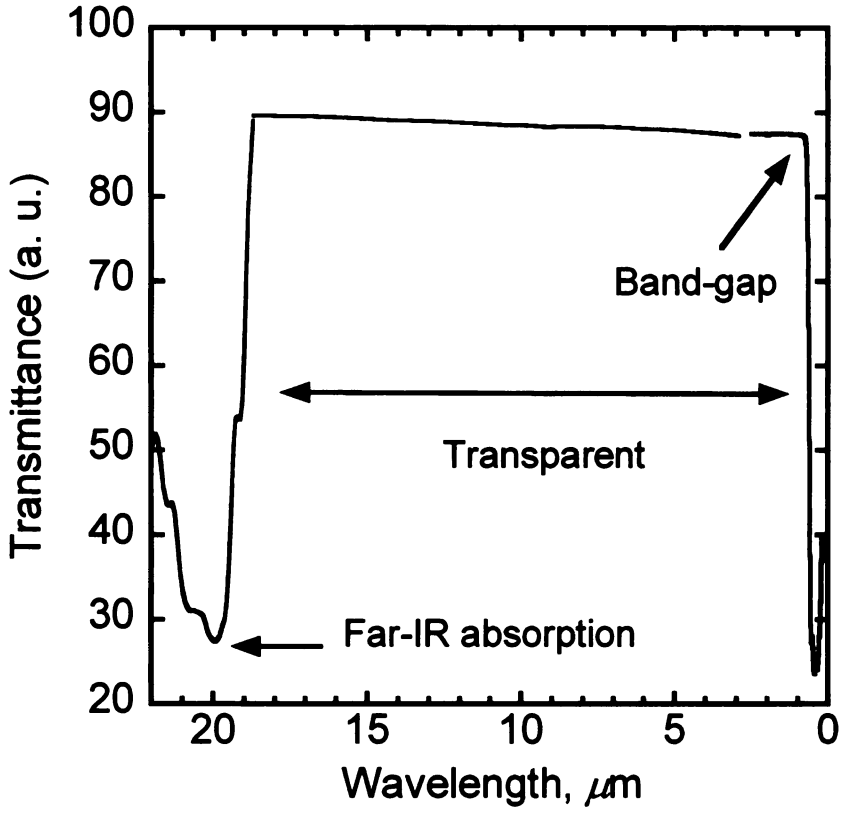

Figure 8-13. Far IR/mid IR/vis absorption spectra of $Cs_5BiP_4Se_{12}$. A wide transparency range of $Cs_5BiP_4Se_{12}$ between 18.7 μm at far-IR region and 0.67 μm at visible region is shown.

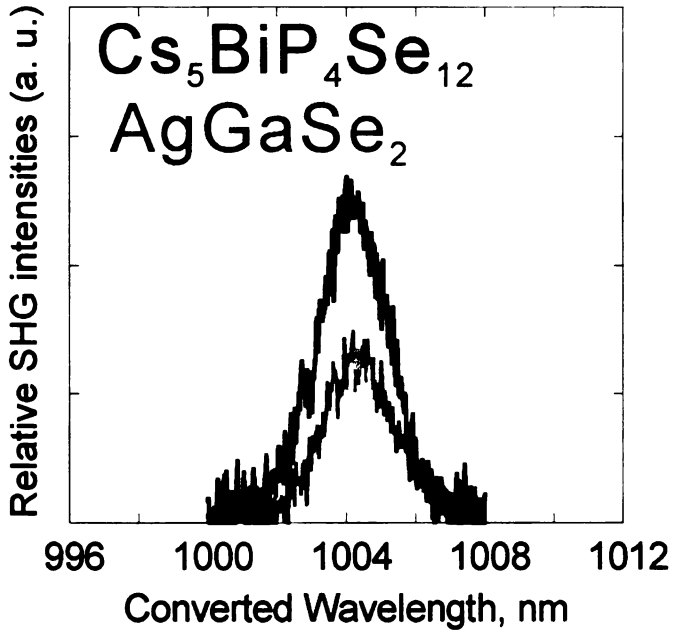

Figure 8-14. SHG response of $Cs_5BiP_4Se_{12}$ relative to $AgGaSe_2$ at 1004 nm.

Because of the polar crystal structure of $Cs_5BiP_4Se_{12}$, we investigated its NLO properties. Using a modified Kurtz powder method,[37] we measured SHG response for polycrystalline samples of 45-63 μm size with 1.2-2 μm fundamental idler radiation from a tunable laser. The second harmonic generation (SHG) response could be observed only above 0.79 μm because of the absorption beyond the band edge, and its intensity increased with wavelength up to 1 μm. The SHG intensities obtained were compared with those of $AgGaSe_2$, which is a representative NLO material for IR applications.[38] All samples were similarly prepared and the same particle size range and identical laser settings were used. The SHG intensity of $Cs_5BiP_4Se_{12}$ is ~2 times larger than that of $AgGaSe_2$ at 2 μm idler beam showing good performance in converting short wave IR, Figure 8-14. The SHG intensity reached maximum at 32-45 μm particle size and the decreased with larger sizes. Thus, $Cs_5BiP_4Se_{12}$ is type-I non-phase-matchable and the corresponding particle size of 38.5 ± 6.5 μm could be regarded as the coherence length of $Cs_5BiP_4Se_{12}$. Despite this, such materials can be useful through 'random' quasi-phase-matching.[39] It should be noted that a modified Kurtz powder method may not be suitable to determine SHG intensity for samples with microwire morphology. The Kurtz powder method deals with the relationship of SHG intensity and particle size. However, typical diameter of as prepared $Cs_5BiP_4Se_{12}$ is less than 1 μm so that sieves to differentiate the size distribution do not work well for this case. For this reason the SHG measured could be underestimated. As a result, to better understand the SHG of $Cs_5BiP_4Se_{12}$, the use of larger single crystal samples is required.

Concluding remarks

The new compound $Cs_5BiP_4Se_{12}$ forms naturally long flexible fibers. The compound reflects the rich structural chemistry of Bi with $[P_xQ_y]^{n-}$ chalcophosphate ligands. The packing mode of the $[Bi(P_2Se_6)_2]^{5-}$ molecules and the weak Se···Se interactions between molecules is responsible for the self-formed long flexible nanowires which organize into fibers. Therefore, because of this natural tendency, to obtain $Cs_5BiP_4Se_{12}$ long nanowires in high yield does not require complex chemical processes. This is a rare example of a simple phase material giving long crystalline fibers. The fiber nanowire morphology emerges from the specific intermolecular secondary interactions which could not be predicted a priori. This discovery implies that innate one- or two-dimensional nanostructures may be rationally approached under consideration of crystal structures. $Cs_5BiP_4Se_{12}$ is widely transparent in the near-/mid IR ranging from 18.8 to 0.67 μm, and it exhibits a relatively strong SHG response, which is ~2 times larger than that of $AgGaSe_2$. The compound is nearly direct band gap semiconductor with a very sharp absorption edge and melts congruently. Inherent formation of nanowires coupled with strong near IR SHG response and optical transparency enables this material to be promising for sensing noncentrosymmetric biomolecules by utilizing IR NLO signal,[40] nanowire microscopy,[41] and integrated photonic networks.[14]

References

(1) Tenne, R.; Margulis, L.; Genut, M.; Hodes, G. *Nature* **1992**, *360*, 444-446.

(2) Feldman, Y.; Wasserman, E.; Srolovitz, D. J.; Tenne, R. *Science* **1995**, *267*, 222-225.

(3) Malliakas, C. D.; Kanatzidis, M. G. *J. Am. Chem. Soc.* **2006**, *128*, 6538-6539.

(4) Davidson, P.; Gabriel, J. C.; Levelut, A. M.; Batail, P. *Europhys. Lett.* **1993**, *21*, 317-322.

(5) Chen, J.; Li, S. L.; Tao, Z. L.; Gao, F. *Chem. Commun.* **2003**, 980-981.

(6) Nath, M.; Rao, C. N. R. *J. Am. Chem. Soc.* **2001**, *123*, 4841-4842.

(7) Brorson, M.; Hansen, T. W.; Jacobsen, C. J. H. *J. Am. Chem. Soc.* **2002**, *124*, 11582-11583.

(8) Ye, C. H.; Meng, G. W.; Jiang, Z.; Wang, Y. H.; Wang, G. Z.; Zhang, L. D. *J. Am. Chem. Soc.* **2002**, *124*, 15180-15181.

(9) Chopra, N. G.; Luyken, R. J.; Cherrey, K.; Crespi, V. H.; Cohen, M. L.; Louie, S. G.; Zettl, A. *Science* **1995**, *269*, 966-967.

(10) Spahr, M. E.; Bitterli, P.; Nesper, R.; Muller, M.; Krumeich, F.; Nissen, H. U. *Angew. Chem., Int. Ed.* **1998**, *37*, 1263-1265.

(11) Therese, H. A.; Rocker, F.; Reiber, A.; Li, J. X.; Stepputat, M.; Glasser, G.; Kolb, U.; Tremel, W. *Angew. Chem., Int. Ed.* **2005**, *44*, 262-265.

(12) Cava, R. J. *Science* **1990**, *247*, 656-662; Sleight, A. W. *Science* **1988**, *242*, 1519-1527.

(13) Jin, S.; Tiefel, T. H.; Mccormack, M.; Fastnacht, R. A.; Ramesh, R.; Chen, L. H. *Science* **1994**, *264*, 413-415; Moritomo, Y.; Asamitsu, A.; Kuwahara, H.; Tokura, Y. *Nature* **1996**, *380*, 141-144.

(14) Scott, J. F.; Dearaujo, C. A. P. *Science* **1989**, *246*, 1400-1405; Dearaujo, C. A. P.; Cuchiaro, J. D.; Mcmillan, L. D.; Scott, M. C.; Scott, J. F. *Nature* **1995**, *374*, 627-629; Hemberger, J.; Lunkenheimer, P.; Fichtl, R.; von Nidda, H. A. K.; Tsurkan, V.; Loidl, A. *Nature* **2005**, *434*, 364-367.

(15) Gabriel, J. C. P.; Camerel, F.; Lemaire, B. J.; Desvaux, H.; Davidson, P.; Batail, P. *Nature* **2001**, *413*, 504-508; Miyamoto, N.; Nakato, T. *Adv. Mater.* **2002**, *14*, 1267-1270; Michot, L. J.; Bihannic, I.; Maddi, S.; Funari, S. S.; Baravian, C.; Levitz, P.;

Davidson, P. *Proc. Natl. Acad. Sci. U. S. A.* **2006**, *103*, 16101-16104; Miyamoto, N.; Yamada, Y.; Koizumi, S.; Nakato, T. *Angew. Chem., Int. Ed.* **2007**, *46*, 4123-4127.

(16) Bordui, P. F.; Fejer, M. M. *Annu. Rev. Mater. Sci.* **1993**, *23*, 321-379.

(17) Dorn, R.; Baums, D.; Kersten, P.; Regener, R. *Adv. Mater.* **1992**, *4*, 464-473; Ma, H.; Jen, A. K. Y.; Dalton, L. R. *Adv. Mater.* **2002**, *14*, 1339-1365; Yamada, H.; Shirane, M.; Chu, T.; Yokoyama, H.; Ishida, S.; Arakawa, Y. *Jpn. J. Appl. Phys., Part 1* **2005**, *44*, 6541-6545.

(18) Knight, J. C. *Nature* **2003**, *424*, 847-851.

(19) Wimmer, E.; Krakauer, H.; Weinert, M.; Freeman, A. J. *Phys. Rev. B* **1981**, *24*, 864-875.

(20) Wendlandt, W. W.; Hecht, H. G. *Reflectance spectroscopy*; Interscience Publishers: New York,, 1966; Kortüm, G. *Reflectance spectroscopy. Principles, methods, applications*; Springer: Berlin, Heidelberg, New York,, 1969; Tandon, S. P.; Gupta, J. P. *Phys Status Solidi* **1970**, *38*, 363-367; Chung, D. Y.; Choi, K. S.; Iordanidis, L.; Schindler, J. L.; Brazis, P. W.; Kannewurf, C. R.; Chen, B. X.; Hu, S. Q.; Uher, C.; Kanatzidis, M. G. *Chem. Mater.* **1997**, *9*, 3060-3071.

(21) MacDonald, A. H.; Pickett, W. E.; Koelling, D. D. *Journal of Physics C-Solid State Physics* **1980**, *13*, 2675-2683.

(22) Chondroudis, K.; Chakrabarty, D.; Axtell, E. A.; Kanatzidis, M. G. *Z. Anorg. Allg. Chem.* **1998**, *624*, 975-979.

(23) Chung, I.; Jang, J. I.; Gave, M. A.; Weliky, D. P.; Kanatzidis, M. G. *Chem. Commun.* **2007**, 4998-5000.

(24) Bondi, A. *J. Phys. Chem.* **1964**, *68*, 441-451.

(25) Chung, I.; Do, J.; Canlas, C. G.; Weliky, D. P.; Kanatzidis, M. G. *Inorg. Chem.* **2004**, *43*, 2762-2764.

(26) Chung, I.; Malliakas, C. D.; Jang, J. I.; Canlas, C. G.; Weliky, D. P.; Kanatzidis, M. G. *J. Am. Chem. Soc.* **2007**, *129*, 14996-15006.

(27) Chung, I.; Karst, A. L.; Weliky, D. P.; Kanatzidis, M. G. *Inorg. Chem.* **2006**, *45*, 2785-2787.

(28) McCarthy, T. J.; Hogan, T.; Kannewurf, C. R.; Kanatzidis, M. G. *Chem. Mater.* **1994**, *6*, 1072-1079.

(29) Kanatzidis, M. G.; Sutorik, A. C. *Prog. Inorg. Chem.* **1995**, *43*, 151-265.

(30) Hedin, L.; Lundqvist, B. I. *J. Phys. C* **1971**, *4*, 2064-2083.

(31) Asahi, R.; Mannstadt, W.; Freeman, A. J. *Phys. Rev. B* **1999**, *59*, 7486-7492; Bylander, D. M.; Kleinman, L. *Phys. Rev. B* **1990**, *41*, 7868-7871.

(32) Perdew, J. P.; Burke, K.; Ernzerhof, M. *Phys. Rev. Lett.* **1996**, *77*, 3865-3868.

(33) Montanari, B.; Ballone, P.; Jones, R. O. *J. Chem. Phys.* **1998**, *108*, 6947-6951; Wu, Q.; Yang, W. T. *J. Chem. Phys.* **2002**, *116*, 515-524.

(34) Breshears, J. D.; Kanatzidis, M. G. *J. Am. Chem. Soc.* **2000**, *122*, 7839-7840.

(35) Tittel, F. K.; Richter, D.; Fried, A. *Solid-State Mid-Infrared Laser Sources* **2003**, *89*, 445-510.

(36) Jean, B.; Bende, T. *Solid-State Mid-Infrared Laser Sources* **2003**, *89*, 511-544.

(37) Dougherty, J. P.; Kurtz, S. K. *J. Appl. Crystallogr.* **1976**, *9*, 145-158; Kurtz, S. K.; Perry, T. T. *J. Appl. Phys.* **1968**, *39*, 3798-3813.

(38) Nikogosyan, D. N. *Nonlinear optical crystals : a complete survey*; Springer-Science: New York, 2005.

(39) Baudrier-Raybaut, M.; Haidar, R.; Kupecek, P.; Lemasson, P.; Rosencher, E. *Nature* **2004**, *432*, 374-376.

(40) Zhang, D. B.; Qi, L. M.; Ma, J. M.; Cheng, H. M. *Adv. Mater.* **2002**, *14*, 1499-1502; Zipfel, W. R.; Williams, R. M.; Christie, R.; Nikitin, A. Y.; Hyman, B. T.; Webb, W. W. *Proc. Natl. Acad. Sci. U. S. A.* **2003**, *100*, 7075-7080.

(41) Johnson, J. C.; Yan, H. Q.; Schaller, R. D.; Petersen, P. B.; Yang, P. D.; Saykally, R. J. *Nano Lett.* **2002**, *2*, 279-283; Kim, J.; Song, K. B. *Micron* **2007**, *38*, 409-426.

Chapter 9

Outlooks

Chalcophosphate class is a worthy target for exploratory synthesis because, coupled with the remarkable structural and compositional diversity, they showed technologically important magnetic, electrical, and optical properties. The polychalcophosphate flux method is a proven synthetic tool during last decade. Chalcophosphate anionic building unit of $[P_xQ_y]^{n-}$ was known to combine nearly all metals to form metal chalcogenide compounds. By employing this approach, researchers produced many new ternary M/P/Q or quaternary A/M/P/Q (A=Li-Cs, M=metal, Q=S, Se) compounds.

Despite expanded registry of chalcophosphate compounds, the number of anionic ligand species $[P_xQ_y]^{n-}$ that had been structurally characterized was just a few and they are mostly simple molecular anions such as $[PQ_4]^{3-}$ and $[P_2Q_6]^{4-}$. Published works on chalcophosphate compounds were mostly regarding on synthesis of new compounds with structural characterization, but studies on their potential technological applications were left behind. Accordingly, this work started with questions of how many chalcophosphate ligands exist and which flux condition can stabilize the specific ligand, hoping to find rational synthetic conditions for desired structural species. As a result, our investigations of alkali chalcophosphate compounds provided new insights into the relationship between the structure and the flux condition (A:P:Se ratio in the composition). New one-dimensional and molecular complex chalcophosphate compounds were found based upon those understandings during this dissertation work.

1. Chalcophosphate compounds as nonlinear optical materials.

With less basic flux condition (A:Se $\leq$ 2), one-dimensional chalcophosphate compounds $APSe_6$, and $A_2P_2Se_6$ (A = K, Rb) were obtained. Both compounds crystallized in the noncentrosymmetric polar space group, and showed remarkably strong second harmonic generation. $(Se)_\chi$ chains are condensed with $[PSe_4]^{3-}$ or $[P_2Se_6]^{4-}$ units to form a highly anisotropic one-dimensional structure. Note that chalcogens (S, Se, Te) are more polarizable than oxygen atom, giving larger second-order nonlinearity. Thus, exploratory synthesis of structurally anisotropic, one- or two-dimensional compounds should be interesting for such purpose.

2. Chalcophosphate compounds as phase-change materials and rich source for glass compounds.

Prominent observation during this dissertation work was great tendency to form glassy phase of chalcophosphate compounds. Examples are $APSe_6$ (A = K, Rb, Cs), $A_2P_2Se_6$ (A = K, Rb), $Cs_4P_6Se_{12}$, $Cs_5P_5Se_{12}$, and $K_4P_8Te_4$. Glassy phases of those compounds readily recover their crystal structure upon heating near crystallization points. Note that those materials are stoichiometric and possess mixed ionic/covalent bondings, in contrast to the vast majority of chalcogenide glasses having nearly continuous compositions and all-covalent networks. Thus, switching between crystalline and glassy phases are not complicated by compositional changes. As a result, chalcophosphate compounds can be rich source for stoichiometric glasses and crystal-glass phase-change materials. It should be noted that chalcophosphate compounds synthesized in the intermediate and less basic condition frequently exhibited phase-change behavior.

In this dissertation, in order to probe the relationship between crystalline and glassy phases of phase-change materials, we performed Raman spectroscopic and pair

distribution function (PDF) analysis. However, to explain mechanism of reversible crystal-glass phase-change, further work should be necessary. This study is very important because we observed a significant second harmonic generation response in glassy phases of phase-change materials and this observation is technologically very important.

Note that chalcogenide glasses are interesting for applications for infrared transparent optical fibers, reversible conductivity switching devices, semiconductors, photoconductors, and solid electrolytes for battery materials. In this regard, physical and chemical property characterizations of glassy phases are required. Extensive exploratory synthesis of chalcophosphate compounds can provide a map of which flux conditions prefer phase-change behavior, crystalline, or glassy phases.

Finally, studies on $K_4P_8Te_4$ found the dissolution behavior of $K_4P_8Te_4$ compound in hydrazine. Since hydrazine solution can dissolve various metals with or without help of additional Te, this rare behavior can open up the possibility of new chemistry: synthesis of wide range of metal tellurophosphate compound via a *chimie deuce* route, functional organic-inorganic hybrids, and nanocomposite compounds; study of gel-formation and liquid crystalline behavior. It is also noteworthy that precipitating hydrazine/ $K_4P_8Te_4$ solution with alcohol produced nanosphere.